# Beyond the Standard Theories of Fundamental Interactions

PhD Thesis

presented to the

*Faculty of Sciences of*
*Scuola Normale Superiore di Pisa*

for the degree of

*Dottorato di Ricerca*
*(Research Doctorate)*

by

Kevin Max

born in Bonn

Pisa
December 16, 2020

PhD Thesis

submitted in partial fulfillment of the

*Corso di perfezionamento*

performed at

*Scuola Normale Superiore*
*Piazza dei Cavalieri, 7*
*56126 Pisa*

by Kevin Max
on December 16, 2020

Supervisor: Prof. Dr. Roberto Contino

**Oltre le Teorie Standard delle Interazioni Fondamentali.**
Lo status quo della fisica fondamentale è il Modello Standard (SM) e la Relatività Generale (GR). Mentre entrambe le teorie sono in grado di descrivere separatamente una vasta gamma di fenomeni nel loro rispettivo dominio di validità con elevata precisione, ci sono problemi che sorgono solo quando le due sono accoppiate. Come esempio, si consideri il problema della costante cosmologica, la bariogenesi o l'assenza di un candidato di materia oscura (DM) nello SM. In questa tesi vengono presentate e discusse diverse soluzioni. Una è la teoria di Bimetric Gravity, un'estensione naturale della gravità massiva, una modificazione della GR che modifica l'ipotesi di un gravitone di spin-2 senza massa. Saranno presentati risultati sulla fenomenologia del gravitone massivo, dove analizziamo la propagazione modificata delle onde gravitazionali e stabiliamo dei limiti competitivi sulla massa del gravitone. Inoltre, viene studiata la storia cosmologica di Bimetric Gravity, incorporando dati delle oscillazioni acustiche barioniche (BAO), dei quasar, delle supernovae e della radiazione cosmica di fondo. Come teoria concorrente, esaminiamo la Gravità Conforme, che viene sottoposta agli stessi test cosmologici. Un approccio ortogonale alla soluzione del problema della DM è un Settore Oscuro oltre lo SM. Motiviamo e presentiamo un'analisi dettagliata della fisica dei Settori Oscuri, che obbediscono ad un'invarianza approssimativa di scala. Utilizzando tecniche di teoria di campo efficace e proprietà degli operatori fissate dalla simmetria conforme, siamo in grado di porre dei limiti indipendenti dal modello su una classe di Settori Oscuri. La loro fenomenologia è testata con una vasta gamma di osservazioni terrestri e celesti.

**Beyond the Standard Theories of Fundamental Interactions.**
The status quo of fundamental physics is the Standard Model (SM) of particle physics and General Relativity (GR). While both theories separately are able to describe a wide range of phenomena in their respective domain to high accuracy, there are problems which arise solely when the two are coupled. Examples include the cosmological constant problem, baryogenesis or the absence of a suitable dark matter (DM) candidate in the SM. In this thesis, several solutions are presented and discussed. One is Bimetric Gravity, a modification of GR which breaks the assumption that one single, massless spin-2 object acts as its force carrier. Original results are presented on the phenomenology of the massive graviton, where we analyse the modified propagation of gravitational waves and set competitive bounds on the graviton mass. Furthermore, the cosmological history of the model is investigated, incorporating data from baryon acoustic oscillations, quasars, supernovae and the cosmic microwave background. As a competing theory, we review Conformal Gravity, which is put to the same cosmological tests. A complementary approach to the solution of the DM problem is a Dark Sector beyond the SM. We motivate and present a detailed analysis of the physics of Dark Sectors, which obey an approximate scale invariance. Using effective field theory techniques and properties of operators fixed by conformal symmetry, we are able to put model-independent bounds on a class of Dark Sectors. Their phenomenology is tested against a large array of terrestrial and celestial observations.

# List of Publications

This thesis contains chapters with original research performed by the thesis author, which has been previously published. Where indicated, work has been adapted from the following publications:

- *Gravitational Wave Oscillations in Bigravity* [1]
- *Decoherence of Gravitational Wave Oscillations in Bigravity* [2]
- *Probing Alternative Cosmologies through the Inverse Distance Ladder* [3]
- *Searching for Elusive Dark Sectors with Terrestrial and Celestial Observations* [4] (in preprint)

# List of Abbreviations

**AdS** anti-de Sitter (space)

**ALP** axion-like particle

**BAO** baryon acoustic oscillations

**BBH** binary black hole

**BBN** big bang nucleosynthesis

**BSM** beyond Standard Model

**CC** cosmological constant

**CFT** conformal field theory

**CG** conformal gravity

**CKM** Cabibbo-Kobayashi-Maskawa

**CMB** cosmic microwave background

**DE** dark energy

**DIS** deep inelastic scattering

**DM** dark matter

**d.o.f.** degrees of freedom

**dS** de Sitter (space)

**DS** dark sector

**EDM** electric dipole moment

**EFT** effective field theory

**EMT** energy-momentum/stress-energy tensor

**e.o.m.** equations of motion

**EW** electroweak

**EWPT** electroweak precision tests

**FLRW** Friedmann-Lemaître-Robertson-Walker

**GR** general relativity

**GW** gravitational wave

**IR** infrared

**ΛCDM** cosmological concordance model

**LDSP** lightest dark sector particle

**LEP** Large Electron-Positron Collider

**LHC** Large Hadron Collider

**LHS** left-hand side

**PDF** parton distribution function

**QCD** quantum chromodynamics

**QED** quantum electrodynamics

**QFT** quantum field theory

**RHS** right-hand side

**RS** Randall-Sundrum

**SM** Standard Model of particle physics

**SN** supernova

**s.t.** such that

**UV** ultraviolet

**vev** vacuum expectation value

**WIMP** weakly interacting massive particle

**w.r.t.** with respect to

**YM** Yang-Mills

# Contents

Habe nun, ach! Philosophie,
Juristerey und Medicin,
Und leider auch Theologie!
Durchaus studirt, mit heißem Bemühn.

Da steh' ich nun, ich armer Thor!
Und bin so klug als wie zuvor;

[...]

Daß ich erkenne, was die Welt
Im Innersten zusammenhält,

*Johann Wolfgang von Goethe*
*Faust – Der Tragödie erster Theil.*

# 1 Introduction

Fundamental physics is at a crossroads. The past century has brought immense success to the research fields of the smallest constituents of nature – particle physics – and the large scale structure of the universe – cosmology. With the advent of quantum theory and its field-theoretic extension, quantum field theory (QFT), researchers have been able to explain phenomena down to the smallest scales which can currently be probed. The interplay of theoretical and experimental observations has lead to prosperous decades of innovation, where advances in theoretical understanding have motivated experimental searches and vice versa. Major developments in the past century include the derivation of the Dirac equation in 1928 [5], swiftly followed by the detection of antiparticles (positron detection by Carl D. Anderson, 1932 [6]) and muons in 1936 [7]. While development of a consistent interpretation of quantum field theory was underway during the 1930s and 40s, this process was greatly stimulated by the measurement of the Lamb shift in 1947 by Lamb and Retherford [8]. The observation of physical effects at the loop level absolved the renormalisation program, and led to the formulation of quantum electrodynamics (QED). Armed with a comprehensive understanding of fundamental interactions between leptons and photons, the focus of the research community shifted towards the question whether quantum field theory could be able to reproduce its success by also modelling subatomic forces. With scattering experiments probing nuclei at energies of order 1 GeV/$c^2$, the 'particle zoo' of hadrons was uncovered. Simultaneously proposed by Gell-Mann and Ne'eman [9, 10], the eightfold way sought to organise the numerous mesons and baryons into group representations; this idea proved to be fundamental in the subsequent construction of the quark model. Through deep inelastic electron-proton scattering, experimentalists were able to confirm the quark hypothesis, and quantum chromodynamics (QCD) was developed as the quantum field theory of strong interactions. In the same period, the model of electroweak symmetry and spontaneous symmetry breaking was developed. With the discovery of the vector bosons, completion of the third fermion family, and finally the discovery of the Higgs boson in 2012, all efforts have culminated into the Standard Model (SM) of particle physics, currently our best understanding of the fundamental interactions of particles and forces, barring gravity.

In the meantime, and for the most parts separately, research in physical cosmology has matured the field from a driving force behind theoretical developments to a precision discipline itself. Milestones include the formulation of general relativity (GR) in 1915 [11–13], important solutions to the field equations such as the Schwarzschild and Friedmann-Lemaître-Robertson-Walker metrics, or the mounting evidence in support of dark matter (DM). A thorough narration of the history of theoretical cosmology will be given in Chapter 2, however suffice to say that observational evidence has enabled us to establish a cosmological standard model in parallelism to the SM of particle physics – the cosmological concordance or ΛCDM model.

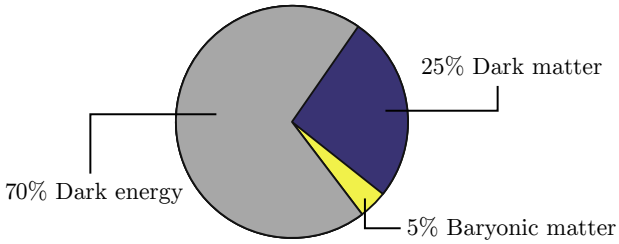


**Figure 1.1:** Energy content of the universe today according to ΛCDM.

Within the last decades, the array of precision instruments to quantify the cosmological evolution has grown, such that exclusions can be placed on alternative cosmological models. For an example, take the cosmic microwave background (CMB), which after its accidental discovery by Penzias and Wilson in 1965 [14] has grown to a precision measurement under investigation through a variety of experimental techniques. In the same manner, Supernova observations up to high redshifts lead to the discovery of the late-time acceleration of the universe. Finally, with the recent measurement of gravitational waves, approximately a century after their conceptualisation, we have truly entered the age of multi-messenger, precision cosmology.

Returning to the opening statement, we note that fundamental physics has reached a critical point in its development. While our instruments – theoretical and observational – have become ever precise, the two sectors, SM and gravity, carry long-standing, open problems. Research has been able to resolve many of the big consistency questions belonging to each field separately, such as the nature of the Higgs mechanism or the calculation of the CMB temperature; however, we seek to bring into agreement all fundamental descriptions of natural phenomena. In particular, some of the most important remaining questions are at the interface of particle physics and cosmology, that is, only if both fields are considered in combination.

Examples are plenty, such as the unknown nature of dark matter, or the form of the energy density governing the current expansion of the universe ('dark energy'). Interpreting observational data from various sources using the cosmological concordance model, the energy budget of the universe in its current state is approximately 25 % dark matter, 70 % dark energy, while only about 5 % is accounted for by ordinary baryonic matter (see Fig. 1.1). While the inclusion of an additional matter component within cosmological analyses is trivial, to explain such a matter distribution with SM physics does not seem to be viable. As another example, we find the cosmological constant problem, where the inclusion of particle loops on a curved space-time grossly fails to predict the current vacuum energy density. We also take note of the baryon asymmetry, or the unclear nature of a UV-complete theory of quantum gravity.

Note that the problems mentioned above arise only when the theoretical framework employed in the description of particles is combined with general relativity, and one seeks to simultaneously explain cosmological, astrophysical and particle physics observations. Due to the nature of these problems, we can expect that they require solutions which are not isolated to one sector (particles or gravity). Instead, an ansatz which combines both the particle physics point of view and an understanding of the cosmological background may prove useful for the development of a coherent description of nature. The research presented in this thesis has been conducted with this paradigm in mind. This shift in perspective follows an ongoing trend in fundamental physics research. It brings about some obvious considerations, such as whether a proposed dark matter candidate can correctly reproduce the observed dark matter abundance, all the while being compliant with constraints from big bang nucleosynthesis (BBN) or the bullet cluster, but also with collider and beam dump experiments. But the interplay of particle physics and cosmology also has more subtle implications. For example, consider Bimetric Gravity (bigravity), an extension to general relativity which will be discussed in detail in Chapters 2–5. The integral point to the construction of Bimetric Gravity is

to extend GR to accommodate a massive graviton. The search for a consistent theory of a massive spin-2 particle can clearly be motivated from a particle physics point of view, but as the study presented in Chapter 5 will show, Bimetric Gravity is also able to provide a viable cosmological history, while retaining its most attractive feature, i.e. a solution to the 'new' cosmological constant problem (see also the discussion in Sec. 2.3).

This manuscript is separated into two major parts, which approach the interface of particle physics and cosmology from different angles. Chapters 2–5 are oriented towards the astrophysical implications of a modified gravity sector. In Chapter 2, we begin with a review of the current status of the cosmological concordance model, and discuss in depth the dark matter and dark energy problems. Motivated by these issues, we introduce the theories of Massive Gravity and Bimetric Gravity. We review the construction of the consistent theory of interacting spin-2 objects in the remainder of Chapter 2.

The following Chapters 3–5 are dedicated to the investigation of the phenomenology of Bimetric Gravity. In Chapter 3, original research on this topic is presented in the form of the first consistent derivation of gravitational wave oscillations – a mixing phenomenon between the two metrics, much akin to two-flavour neutrino oscillations. This possible detection signature is further explored in Chapter 4, where the decoherence regime of gravitational waves is employed to set bounds on the graviton mass.

In Chapter 5, the astrophysical tests of Bimetric Gravity are complemented by a statistical analysis of the theory, based on data sourced from a variety of cosmological observations. We expect any modification of GR not only to ameliorate the theoretical inconsistencies of ΛCDM, but also to improve the agreement with existing observations. In the analysis featured in this chapter, Bimetric Gravity is therefore put to the test against the concordance model and some of its iterations ($k\Lambda$CDM, $\omega\Lambda$CDM). We also introduce a more radical modification of gravity in the form of Conformal Gravity. This theory implements a gravitational sector which is invariant under conformal transformations (we will revisit conformal symmetry in a particle physics application in Chapter 7). The sum of models is tested against a list of precise cosmological observations, extending over a wide range of redshifts. We use Supernova and quasar data at high redshift, as well as input from BBN, the CMB and baryon acoustic oscillations (BAO). The statistical analysis is discussed in detail, and we draw conclusions on the viability of the various modifications to GR.

We switch gears in Chapters 6 and 7, where the question of the nature of dark matter is investigated through a particle physics approach. Motivated by the sheer abundance of possible dark matter models, we study a class of models beyond the SM (BSM) based on general symmetry arguments. Using effective field theory (EFT) and qualities of particle propagators determined by conformal symmetry, we are able to calculate physical effects for models in this class without the need to specify the theories explicitly. We do however give concrete examples, e.g. pure Yang-Mills theories or Randall-Sundrum inspired models. The phenomenology of such dark sectors (DS) is tested against an extensive array of experimental observations. We consider high-energy collider searches for missing energy and displaced vertex events performed at LEP and LHC, as well as electroweak precision tests and modifications of Higgs physics. These results are accompanied by searches using the fixed-target beam dump experiments NA64 and E137, where high-intensity beams are employed in the search for new physics effects, as well as hadron decays from related experimental setups such as BESIII. We include further laboratory tests in the form of precision experiments at lower energies, such as the lifetime of positronium. These terrestrial constraints are flanked by celestial observations, where we are able to set bounds on an approximately conformal dark sector through stellar evolution and the observation of supernova SN1978A.

This manuscript is concluded in Chapter 8 with a summary of the results obtained, and an outlook on future paths in particle physics and cosmology.

**Conventions.** Natural units and the Einstein sum convention are used throughout this manuscript. We define the Planck mass as $8\pi\, G_N = M_{\rm Pl}^{-2}$. Square brackets denote a trace, $[\mathbb{X}] = \mathbb{X}^{\mu}{}_{\mu}$. For the metric, we use the GR convention with the flat metric $\eta = \text{diag}(-1, 1, 1, 1)$ in Chapters 2–5, whereas in the more particle physics oriented Chapters 6 and 7, we define the Minkowski metric as $\eta = \text{diag}(1, -1, -1, -1)$ such that $p^2 = +m^2$. $A \supset B$ with $A$ and $B$ terms in equations means that $B$ is only one addend comprising $A$, i.e. $A = B + ...$ The brackets of the anti-commutator are defined as $[A, B] = AB - BA$, and we extend this notation to the anti-commuting of indices, $A_{[\mu}B_{\nu]} = A_\mu B_\nu - A_\nu B_\mu$. Similarly, $A_{(\mu}B_{\nu)} = A_\mu B_\nu + A_\nu B_\mu$.

# 2 | Going Beyond: General Relativity

## 2.1 Charted Territory: ΛCDM

Just over a century ago, Albert Einstein published his theory of General Relativity (GR). As a key concept, he introduced the notion of the metric as a dynamical field, whose dynamics are determined from the Einstein field equations (EFE),

$$R_{\mu\nu} - \frac{R}{2} g_{\mu\nu} + \Lambda\, g_{\mu\nu} = 8\pi G\, T_{\mu\nu}. \tag{2.1.1}$$

Here, the left hand side is constructed purely from the metric tensor (with the inclusion of a cosmological constant $\Lambda$), while the right hand side of the above equation is given by the energy-momentum tensor (EMT) $T_{\mu\nu}$. In this way, the EFE describe the dynamics of gravity as a coupled system: non-zero energy densities (due to mass or radiation) generate local distortions of the metric, whereas the metric determines the geodesics of particle motion.

Shortly after the inception of GR, two important solutions to the equations of motion were found. In 1916, the Schwarzschild metric was published [15], which solves the EFE in vacuum, and which describes the gravitational field outside of a spherically symmetric mass. Notably, the Schwarzschild solution reduces to Newton's law of gravity for weak gravitational fields. Other efforts were concentrated on finding a cosmological solution, i.e. a metric which (to a certain degree of approximation) could describe the universe as a whole. Over the course of the next years, several authors contributed to this search; the endeavour culminated in the Friedmann-Lemaître-Robertson-Walker metric (FLRW) solution, laying the groundwork for the modern concordance cosmology model, including its dynamic history of expansion and the big bang hypothesis.

The FLRW metric is constructed from the assumption that space is isotropic and homogeneous on cosmological scales; an explicit time-dependence enters only via the scale factor $a(t)$. This greatly simplifies the equations of motion, yielding the Friedmann equation

$$H(t)^2 + \frac{k}{a(t)^2} = \sum_i \frac{\rho_i(t)}{3M_{\mathrm{Pl}}^2},$$

with the Hubble function $H(t) \equiv \dot{a}/a$, which contains all information on the cosmological expansion rate. It is modified by the presence of the curvature term $k$, and energy densities $\rho_i$ such as radiation ($i = r$) and non-relativistic matter ($i = m$). By defining the energy densities with respect to their values observed today, this can be cast into the form

$$H(z)^2 = H_0^2 \left[\Omega_r^0 (1+z)^4 + \Omega_m^0 (1+z)^3 + \Omega_k^0 (1+z)^2 + \Omega_\Lambda\right], \tag{2.1.2}$$

with $\Omega_i^0 \equiv \frac{\rho_i(z=0)}{\rho_c}$. Here, we have introduced the redshift parameter $z \equiv a^{-1} - 1$ and the critical density $\rho_c \equiv 3H_0^2 M_{\mathrm{Pl}}^2$, defined such that

$$\Omega_m(z) + \Omega_r(z) + \Omega_k(z) + \Omega_\Lambda = 1.$$

This makes it clear that the evolution of the universe is governed by its energetic composition. It is our goal to determine the different components which enter Eq. (2.1.2), in order to understand to which degree the FLRW ansatz is able to describe the universe on cosmological scales.

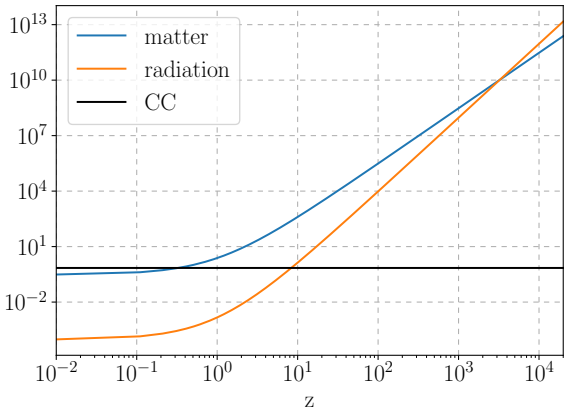


**Figure 2.1:** Energy densities $\rho_i(z)/\rho_c(z=0)$ in the concordance cosmology model (where curvature $k=0$) as a function of redshift.

One key component we need to take into consideration is dark matter (DM), arguably one of the most-researched topics in contemporary (astro-) particle physics and cosmology. There is ample evidence for the existence of DM as an additional component to the observed baryonic matter density $\Omega_b$. On astrophysical scales, the DM hypothesis explains well the shape of galactic rotation curves [16–18] and their velocity dispersion [19], the observation of the bullet cluster and similar events [20, 21], and gravitational lensing [22, 23]. While several of these phenomena can also be explained individually by theories of modified gravity, currently DM is the only framework addressing all phenomena simultaneously. In particular, the comparison of mass distributions of colliding galaxy clusters before and after the event is incompatible with modifications of Newton's law, but well-explained by a dark matter component [24].

On cosmological scales, evidence for the existence of DM is provided by the observation of the cosmic microwave background (CMB), structure formation, and a wide range of tests of cosmological distances which probe the Hubble function (2.1.2). In the early universe, structure is formed from small inhomogeneities in the matter distribution, which act as gravitational wells and grow over time. In order to reproduce the observed structures on large scales (filaments and voids) and small scales (galaxies), the mass of the dominant DM component plays a crucial role. For hot dark matter with a mass of order eV and below, galaxy superclusters form first and then fragment into galaxies. This top-down paradigm has been challenged, as the characteristic length scales of superclusters are not seen in galaxy surveys [25]; e.g. in the N-body simulation of Ref. [26], light neutrinos are excluded as hot dark matter. The remaining viable alternative is that the dominant contribution to DM is either warm (with a mass of order keV) or cold; such DM leads to hierarchical structure formation, where small structures are formed first, which then grow by accretion of matter. We conclude that except for the formation of structures, the requirement of DM can be compressed into the statement that there exists an additional non-relativistic matter component.[1]

*In passing, we also note that all evidence for DM is purely gravitational.*

The final piece we add to our standard cosmological model is the late-time acceleration of the expansion of the universe. Through Eq. (2.1.2), it is apparent that a sizeable cosmological constant can become the dominant energy density component for low $z$. This leads to an exponential growth of the scale factor with time, $a(t) \propto \exp(\sqrt{\Lambda/3}\,t)$, implying an accelerated expansion at late times.

First evidence for a non-zero cosmological constant appeared in 1998 with the analysis of observations of Type Ia Supernovae (SNe) [27, 28]. With the SN data, it was possible to determine

[1] In fact, in the standard term 'cold dark matter' of the ΛCDM model, it is understood that both warm and cold dark matter are considered.

| $\Omega_\Lambda$ | $\Omega_k$ | $\Omega_m^0$ | $100\,\Omega_b^0$ | $N_{\text{eff}}$ | $H_0$ / $\frac{\text{km/s}}{\text{Mpc}}$ |
|---|---|---|---|---|---|
| $1-\Omega_m^0$ | zero | $0.315 \pm 0.007$ | $4.93 \pm 0.08$ | $2.99 \pm 0.17$ | $67.4 \pm 0.5$ |

**Table 2.1:** Summary of fixed parameters and current best fits in ΛCDM from Planck 2018 results [29]. $N_{\text{eff}}$ is the effective number of light degrees of freedom at CMB, where the SM predicts the value 3.046.

the deceleration parameter $q_0 \equiv -(\dot{H}/H^2+1)|_{z=0}$ to be negative, implying a sizeable dark energy contribution. Over the last twenty years, a wide range of observations has been found to be in agreement with this, such as measurements of the CMB or baryon acoustic oscillations (BAO). This topic, including a re-analysis using an updated and largely augmented SNe sample, will be discussed at length in Chapter 5.

*Gathering all of these components, we have constructed the ΛCDM or 'concordance' model, the current standard model of cosmology.*

We conclude our review of ΛCDM with a brief summary of its cosmological history: after the very early universe, the initial conditions of primordial matter distribution have been set.[2] The universe is in a state of a hot, dense plasma of elementary particles (radiation-dominated era). As the universe expands, temperature falls with $a(t) \propto 1/T$, and at around $T = \mathcal{O}(1\text{ MeV})$, nuclei start to form in what is known as big bang nucleosynthesis (BBN). As the universe cools further and reaches energies of order eV, the electrons undergo recombination, i.e. they bind with nuclei to form neutral atoms. Finally, as hydrogen atoms form, photons – which so far have been in thermal equilibrium with matter – obtain a drastically increased scattering length, and become free-streaming. The last scattering of photons occurs at $z_* \approx 1100$, and this radiation is observed today as the CMB. In parallel, the matter distribution undergoes the process of baryon acoustic oscillations (BAO): before recombination, as photons and baryons are still in thermal equilibrium, the baryonic matter densities oscillate under the forces of radiation pressure and gravity. The dominant perturbation to a homogeneous matter distribution is a single spherical acoustic wave; at recombination, the photons decouple and the acoustic oscillations are frozen-in as a characteristic length scale. We observe this BAO length today in the distribution of galaxies and quasars. In the late universe, after galaxies have formed, the dominant energy density is given by dark energy, which causes an accelerated expansion.

## 2.2 Towards a theory of Massive Gravity

### 2.2.1 The cosmological constant problem

While ΛCDM is able to explain most data reasonably well and provides a consistent cosmological history, perhaps its major issue is the *cosmological constant problem*. On the grounds of gravity alone, we understand the EFE, Eq. (2.1.1), as the equation of a classical field, the metric $g_{\mu\nu}$. The right-hand side however is comprised of the known SM physics, whose dynamics are governed by a quantum field theory. To current precision of gravity measurements, this semi-classical approximation is valid, even while it is unclear how it embeds into a UV complete theory of quantum gravity. Following the QFT description of the matter content, quantum corrections to the vacuum energy predict a large cosmological constant in the vacuum. For example, at one-loop order, a scalar $\phi$ of

[2] The homogeneity of these primordial fluctuations requires an additional mechanism, such as cosmic inflation.

mass $m$ induces the vacuum energy contribution[3]

$$\rho_{\text{vac}}^{\text{1-loop}} = \quad = -\frac{m^4}{(8\pi)^2}\Big[-\frac{2}{\epsilon} - \log\frac{\mu^2}{m^2} + \gamma - \frac{3}{2}\Big]. \tag{2.2.1}$$

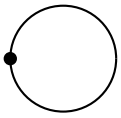

Naively, the finite piece constitutes a very large value, for the SM has masses of $\mathcal{O}(100\text{ GeV})$, and we expect BSM physics to introduce even higher masses. However, having the tools of QFT at hand, we understand that we need to renormalise the vacuum energy at the cost of giving up its prediction. By this procedure, we fix the one-loop contribution to the observed value $\rho_{\text{vac}}^{\text{obs}} \approx (2 \times 10^{-3}\text{ eV})^4$. Advancing to higher loop orders however, this needs to be repeated at all orders of the perturbative series; the vacuum energy proves to be extremely sensitive to UV dynamics.

The issue is further complicated by the electroweak and QCD phase transitions of the SM, due to which some operators in its spectrum acquire a vacuum expectation value (vev). If we set the vacuum energy in any phase of our model to its measured value today, we obtain an additional contribution due to $\rho_{\text{vac}}^{\text{QCD}} \sim (100\text{ MeV})^4$ and/or $\rho_{\text{vac}}^{\text{EW}} \sim (100\text{ GeV})^4$ in the other phases.

*We stress that this fine-tuning problem appears precisely at the intersection of GR and SM physics, that is, only when both theories are combined.*

We conclude that if the QFT prediction is true, the vacuum energy due to matter fields must not gravitate in the way that GR predicts. This continues to be one of the main driving forces for consistent theories of gravity beyond GR. One such candidate theory is Massive Gravity (MG) and the related theory of Bimetric Gravity (bigravity). The introduction of a (small) graviton mass leads to modified IR physics, while both theories still behaves like GR at small scales due to strong coupling effects of the additional modes. By introducing a potential for the metric, MG tackles the cosmological constant problem in twofold ways: it implements degravitation of the dark energy component, that is a screening of a potentially large cosmological constant. On the other hand, if one accepts that the vacuum energy due to ordinary matter does not gravitate at all, it also provides a radiatively stable and arbitrarily small dark energy component in the form of the graviton mass. Apart from dark energy, the development of Massive Gravity theories has lead to a plethora of interesting phenomena, which we will detail in the following.

### 2.2.2 The Fierz-Pauli Lagrangian

*Returning to the formulation of GR in terms of the equations of motion (2.1.1), let us take a step back, and assume a particle physicist's point of view on the construction of Massive Gravity.*

In quantum field theory on a flat space-time manifold, particles are constructed as unitary, irreducible representations of the Poincaré group $\text{ISO}(1,3)$. As demonstrated by Wigner in 1939 [30], such representations are classified by two numbers: their mass $m \geq 0$ and spin $J = 0, \frac{1}{2}, 1, ...$ For representations with $J = 0$, he showed that there is one independent d.o.f., while for $J > 0$, each representation carries $2J + 1$ polarisations if $m$ is non-zero and exactly two polarisations if $m = 0$. Across different fields of physics, we have found that a vast range of natural phenomena can be well described by these properties (with the inclusion of additional quantum numbers). In particular, the SM of particle physics is constructed from massless as well as massive representations of spin $0$, $\frac{1}{2}$, and $1$.[4]

Experimental observations tell us that no fundamental particle with spin beyond 1 is required in particle physics. However, we know of such a field as the mediator of gravity. The EFE can be

[3] An identical, but formally correct result is also obtained by an evaluation of the effective action $W$, which extends the calculation of the bubble diagram to curved space-time.

[4] The scalar representation – the Higgs field – acquires a mass due to the electroweak phase transition.

derived from the Einstein-Hilbert action,

$$S_{\rm EH} = \frac{M_{\rm Pl}^2}{2}\int d^4x\sqrt{|\det g_{\mu\nu}|}\,(R-2\Lambda) \tag{2.2.2}$$

which makes the underlying diffeomorphism invariance of the theory apparent. Recall that Wigner's classification is only defined on a Minkowski background metric; indeed, if we linearise Eq. (2.2.2), we see that the metric perturbations are described by a two-index field with two propagating helicities. Thus, expressed in modern particle physics terms, we understand GR to be the unique theory of a massless particle of spin-2.

It is a natural question to ask whether we can formulate a consistent theory of a *massive* spin-2 field. We will elaborate this question in the following along the lines of the reviews [31, 32].

We start out at the level of linear perturbations to the Minkowski metric, $g^{\mu\nu} = \eta^{\mu\nu} - h^{\mu\nu} + \mathcal{O}(h^2)$. The kinetic term is the same as in GR, Eq. (2.2.2). The linearised Einstein-Hilbert Lagrangian is

$$\mathcal{L}_{\text{lin-GR}} = \frac{1}{4}h_{\mu\nu}\Box h^{\mu\nu} - \frac{1}{2}h_{\mu\nu}\partial^\mu\partial_\alpha h^{\nu\alpha} + \frac{1}{2}h\,\partial_\mu\partial_\nu h^{\mu\nu} - \frac{1}{4}h\,\Box\, h.$$

By choosing an appropriate gauge, one can show that this describes two propagating d.o.f., as we expect for a massless particle of helicity-2. To this kinetic term we now add a mass term in the form of all possible contractions of $h_{\mu\nu}$,

$$\mathcal{L}_{\rm mass} = m^2[a(h_{\mu\nu})^2 + b\,h^2]. \tag{2.2.3}$$

Already at the linear level of Massive Gravity, we need to be wary of ghost modes, as can be seen by the decomposition of $h_{\mu\nu}$ into the transverse helicity-2 and -1 modes $h^T_{\mu\nu}, A^T_\mu$, and the longitudinal scalar mode $\pi_L$.[5] Inserting $h_{\mu\nu} \supset \partial_\mu\partial_\nu\pi_L/m^2$ yields four-derivative terms of the form

$$\mathcal{L}_{\rm mass} = \frac{1}{m^2}[a+b]\pi_L\Box^2\pi_L. \tag{2.2.4}$$

While not immediately apparent, this Lagrangian encompasses two propagating degrees of freedom. Crucially, it introduces an Ostrogradsky instability, i.e. one of these modes always has a kinetic term with an opposite sign. We can see this by introducing a Lagrangian multiplier[6] [32],

$$\mathcal{L}_{\rm mass} = \frac{1}{m^2}[a+b]\left(\tilde\chi\Box\pi_L - \frac{1}{4}\tilde\chi^2\right)$$

subject to the e.o.m. of $\tilde\chi$, which is $2\Box\pi_L = \tilde\chi$. The two modes can now be made manifest by transforming $\pi_L = (\phi_1+\phi_2)$ and $\tilde\chi = (\phi_1-\phi_2)$, whereupon

$$\mathcal{L}_{\rm mass} = \frac{1}{m^2}[a+b]\left(\phi_1\Box\phi_1 - \phi_2\Box\phi_2 - \frac{1}{4}(\phi_1-\phi_2)^2\right)$$

after integrating by parts twice. As is now apparent, the kinetic energy of one scalar mode contributes negatively, and there is no stable ground state.

The instability is cured by fixing $a=-b$, which yields the linearised action

$$\mathcal{L}_{\rm FP} = \mathcal{L}_{\text{lin-GR}} - \frac{1}{8}m^2[h^2_{\mu\nu} - h^2], \tag{2.2.5}$$

known as the Fierz-Pauli Lagrangian [33, 34], proposed already in 1939.

[5] In the following, we will focus on the modes $h^T_{\mu\nu}$ and $\pi_L$, as $A^T_\mu$ is not excites directly (there is no quantity it can be coupled to in a gauge-invariant way).

[6] The analysis described here presupposes that $h_{\mu\nu}$ is a dynamical field, such that a counting of d.o.f. is applicable.

Note that the mass term breaks linearised coordinate invariance, under which $h_{\mu\nu} \mapsto h_{\mu\nu} + \frac{1}{2}\,\partial_{(\mu}\,\xi_{\nu)}$. This is problematic, as we have set out to give the graviton a mass without breaking Poincaré symmetry. However, similar to the Proca action for a massive vector field exhibiting a $U(1)$ symmetry, this can easily be accommodated by the introduction of Stückelberg fields. We add four fields $\chi_\mu$, such that the Fierz-Pauli mass term becomes

$$m^2[(h_{\mu\nu} + \partial_{(\mu}\chi_{\nu)})^2 - \,(h + 2\,\partial_\mu\chi^\mu)^2] \tag{2.2.6}$$

which is invariant under the transformation $\chi_\mu \mapsto \chi_\mu - \frac{1}{2}\xi_\mu$.

### 2.2.3 vDVZ discontinuity

We will now define the propagator of the massive graviton and compare to the massless case. Coupled to a source, the linearised Lagrangian (2.2.5) implies the e.o.m.

$$\hat{\mathcal{E}}^{\alpha\beta}_{\mu\nu} h_{\alpha\beta} + \frac{m^2}{2}(h_{\mu\nu} - \eta_{\mu\nu}\,h) = \frac{T_{\mu\nu}}{M_{\rm Pl}} \tag{2.2.7}$$

with the Lichnerowicz operator $\hat{\mathcal{E}}^{\alpha\beta}_{\mu\nu} h_{\alpha\beta} \equiv -\frac{1}{2}[\Box h_{\mu\nu} - \partial_{(\mu}\partial_\alpha h^\alpha{}_{\nu)} + \partial_\mu\partial_\nu h - \eta_{\mu\nu}(\Box h - \partial_\alpha\partial_\beta h^{\alpha\beta})]$. The e.o.m. can be rewritten in the form

$$(\Box - m^2)h_{\mu\nu} = \big[\frac{1}{2}\tilde{\eta}_{\mu\alpha}\tilde{\eta}_{\nu\beta} + \frac{1}{2}\tilde{\eta}_{\mu\beta}\tilde{\eta}_{\nu\alpha} - \frac{1}{3}\tilde{\eta}_{\alpha\beta}\tilde{\eta}_{\mu\nu}\big]\frac{T_{\alpha\beta}}{M_{\rm Pl}} \equiv f^{\rm massive}_{\mu\nu\alpha\beta}\frac{T_{\alpha\beta}}{M_{\rm Pl}}$$

where $\tilde{\eta}_{\mu\nu} \equiv \eta_{\mu\nu} - \partial_\mu\partial_\nu/m^2$. This is solved by the propagator

$$G^{\rm massive}_{\mu\nu\alpha\beta}(x,x') \propto \frac{f^{\rm massive}_{\mu\nu\alpha\beta}}{\Box - m^2}.$$

A well-known issue arises in the computation of the amplitude of a gravitational exchange between two sources,

$$\mathcal{A}^{\rm massive} = \frac{1}{M_{\rm Pl}^2}\int d^4x\, T'^{\mu\nu} G^{\rm massive}_{\mu\nu\alpha\beta}(x,x')\, T^{\alpha\beta}, \tag{2.2.8}$$

which in the limit $m \to 0$ takes the form

$$\lim_{m\to 0}\mathcal{A}^{\rm massive} = -\frac{2}{M_{\rm Pl}^2}\int d^4x\, T'^{\mu\nu}\frac{1}{\Box}\,(T^{\mu\nu} - \frac{1}{3}T\eta_{\mu\nu}), \tag{2.2.9}$$

where we have assumed that the sources are conserved.

This result is to be compared to the genuinely massless case of GR. By use of the de Donder gauge $\partial_\mu h^\mu{}_\nu = \frac{1}{2}\partial_\nu h$, the linearised EFE can be written as

$$\Box h_{\mu\nu} = -\frac{2}{M_{\rm Pl}}(T_{\mu\nu} - \frac{1}{2}T\eta_{\mu\nu}), \tag{2.2.10}$$

and the propagator is

$$G^{\rm massless}_{\mu\nu\alpha\beta}(x,x') = \frac{f^{\rm massless}_{\mu\nu\alpha\beta}}{\Box}.$$

with $f^{\rm massless}_{\mu\nu\alpha\beta} \equiv \frac{1}{2}\eta_{\mu\alpha}\eta_{\nu\beta} + \frac{1}{2}\eta_{\mu\beta}\eta_{\nu\alpha} - \frac{1}{2}\eta_{\alpha\beta}\eta_{\mu\nu}$. The gravitational amplitude in this case is

$$\mathcal{A}^{\rm massless} = -\frac{2}{M_{\rm Pl}^2}\int d^4x\, T'^{\mu\nu}\frac{1}{\Box}\,(T^{\mu\nu} - \frac{1}{2}T\eta_{\mu\nu}). \tag{2.2.11}$$

Let us compare this result to the $m \to 0$ case of massive linearised gravity, Eq. (2.2.9). Assuming two massive, non-relativistic test bodies as sources with components $T^{00} = m_1$ and $T'^{00} = m_2$, we recover Newton's law of gravitation [35],

$$V^{\text{massless}}(r) = \frac{G_N\, m_1\, m_2}{r}, \qquad V^{m\to 0}(r) = \frac{4}{3}\frac{G_N\, m_1\, m_2}{r}, \tag{2.2.12}$$

where we find the potential induced by the massive graviton to deviate from the genuinely massless case independent of how small $m$ is. This is the well-known van Dam-Veltman-Zakharov (vDVZ) discontinuity of Fierz-Pauli massive gravity [36, 37]. A modified potential of such form is excluded already by tests within the solar system.[7] The origin of the discrepancy lies in the additional helicity-0 mode, which obtains non-linearly growing field values in the vicinity of matter. The resolution to the vDVZ discontinuity will thus become apparent once we generalise Fierz-Pauli massive gravity to the non-linear level.

### 2.2.4 Reintroducing non-linear diffeomorphism invariance

As GR is a theory of a *non-linearly* realised gauge symmetry – diffeomorphism invariance – it is clear that we must undo the linearisation and seek a generalisation of the mass term (2.2.6). Attempting to form a potential term from $g_{\mu\nu}$ alone, we find that the only gauge-invariant contraction is $g^{\mu\nu}g_{\mu\nu} = 4$, i.e. a cosmological constant term. Thus, we are required to introduce a secondary two-index field, a 'reference metric' $\tilde{g}_{\mu\nu}$ [38]. In order to implement diffeomorphism invariance, the Stückelberg fields are promoted to a non-linear representation: with the use of four scalar auxiliary fields $\phi^a$, we construct

$$\tilde{g}_{\mu\nu} \equiv \partial_\mu\phi^a\partial_\nu\phi^b\eta_{ab},$$

which evidently transforms as a tensor under diffeomorphisms [39–41]. The auxiliary fields are related to the linear Stückelberg fields via $\phi^a = x^a - \eta^{a\mu}\chi_\mu/M_{\text{Pl}}$.

We can now form the scalar quantity $g^{-1}\tilde{g} \equiv g^{\mu\alpha}\tilde{g}_{\alpha\nu}$, and use it to write down a potential for $g_{\mu\nu}$. As the simplest ansatz, we may choose to extend Eq. (2.2.6) by writing

$$S \supset -m^2M_{\text{Pl}}^2\int d^4x\sqrt{-g}\left\{[(\mathbb{I} - g^{-1}\tilde{g})^2] - [\mathbb{I} - g^{-1}\tilde{g}]^2\right\} \tag{2.2.13}$$

with $\mathbb{I} = \delta^\mu_\nu$. It is easy to see that this reproduces the Fierz-Pauli term, e.g. by choosing a gauge where the reference metric is Minkowski ('unitary gauge'). However, this also reintroduces higher derivative terms, and thus an Ostrogradsky instability. We see this by writing explicitly the modes of the Stückelberg fields as[8]

$$\chi_\mu = \frac{1}{m}A^T_\mu + \frac{1}{m^2}\partial_\mu\pi_L.$$

Extracting the scalar mode $\pi_L$ only,

$$(g^{-1}\tilde{g})^\mu{}_\nu \supset \delta^\mu_\nu - \frac{2}{M_{\text{Pl}}m^2}\partial^\mu\partial_\nu\pi_L + \frac{1}{M_{\text{Pl}}^2m^4}(\partial^\mu\partial_\gamma\pi_L)(\partial^\gamma\partial_\nu\pi_L) + \mathcal{O}(\pi_L^3) \tag{2.2.14}$$

and therefore Eq. (2.2.13) becomes [32]

$$-\int d^4x\Big\{\frac{4}{m^2}\big([\Pi^2] - [\Pi]^2\big) - \frac{4}{M_{\text{Pl}}m^4}\big([\Pi^3] - [\Pi][\Pi^2]\big) + \frac{1}{M_{\text{Pl}}^2m^6}\big([\Pi^4] - [\Pi^2]^2\big)\Big\} \tag{2.2.15}$$

[7] Solar system bounds can be accommodated by a redefinition of $G_N$, however the discontinuity will then reappear in other observations, such as gravitational lensing.

[8] In this gauge, the Stückelberg fields describe the helicity-1 and -0 modes, while $h_{\mu\nu}$ is the transverse traceless mode.

where we have defined $\Pi^{\mu\nu} \equiv \partial_\mu\partial_\nu\pi_L$. As per construction, at quadratic order in $\pi_L$ the higher derivative terms cancel up to a total derivative,

$$[\Pi^2] - [\Pi]^2 = \partial^\mu\partial_\alpha\pi_L\,\partial^\alpha\partial_\mu\pi_L - (\partial^\mu\partial_\mu\pi_L)^2 \overset{\text{IP}}{=} 0. \tag{2.2.16}$$

At higher order in $1/M_{\rm Pl}$ however, we find no such cancellation, as can be seen by expanding $\pi_L$ about a background configuration, $\pi_L = \pi_L^0 + \delta\pi_L$. The cubic term becomes [32]

$$\begin{aligned}[\Pi^3] - [\Pi][\Pi^2] = Z^{\mu\nu\alpha\beta}\,[\partial_\mu\partial_\nu\delta\pi_L][\partial_\alpha\partial_\beta\delta\pi_L] + \mathcal{O}\big((\pi_L^0)^3, (\pi_L^0)^2\delta\pi_L, \delta\pi_L^3\big) \\ \text{with } Z^{\mu\nu\alpha\beta} = 3\eta^{\nu\alpha}\partial^\mu\partial^\beta\pi_L^0 - \Box\pi_L^0\eta^{\mu\alpha}\eta^{\nu\beta} - 2\partial^\alpha\partial^\beta\pi_L^0\eta^{\mu\nu}.\end{aligned} \tag{2.2.17}$$

We see that the simple ansatz (2.2.13) leads to an inconsistency on arbitrary backgrounds; the appearing negative-norm state at the non-linear level is known as a Boulware-Deser (BD) ghost [42]. Historically, this constituted the main obstacle to the construction of a consistent theory of Massive Gravity. Nowadays, avoiding the BD ghost can be seen as a guiding principle for the construction of the unique ghost-free theory of Massive Gravity, the 'dRGT theory' due to de Rham, Gabadadze and Tolley [43–45].

The appearance of the BD ghost is also apparent when counting the number of degrees of freedom (d.o.f.). In GR in $D = 4$, the metric has 10 d.o.f. The Bianchi constraint equations eliminate four of these, and with an appropriate coordinate transformation we remove four additional d.o.f.; this leaves two propagating d.o.f. for the graviton, in agreement with a massless spin-2 representation of the Lorentz group. On the other hand, in the linearised construction of Massive Gravity, we have restored coordinate invariance at the cost of introducing four additional d.o.f. (the Stückelberg fields $\phi^a$) – the mismatch between these six modes and the five physical polarisations of a massive spin-2 field signals the appearance of the BD ghost. It shows that we must render one mode non-dynamical to *all orders in non-linearities* by setting the coefficients appropriately.

In order to construct the ghost-free potential of $g$ and $\tilde{g}$, three approaches are known: the metric formulation, the Vielbein (or Tetrad) formalism, and deconstruction of an extra dimension. We will briefly describe the metric formulation and its historic development, while we will work out the Vielbein formulation of Massive Gravity in detail. This is followed by a summary of the deconstruction approach.

### 2.2.5 Metric formulation

Starting from the Einstein-Hilbert action, the immediately apparent approach is to extend the Fierz-Pauli term non-linearly in the metric formulation. As we have noted, the principal difficulty lies in identifying those terms which produce higher derivatives of $\pi_L$. These modes are isolated in the *decoupling limit*, where one takes $M_{\rm Pl} \to \infty$ and $m \to 0$ such that the scale[9]

$$\Lambda_3 \equiv (m^2 M_{\rm Pl})^{1/3} \tag{2.2.18}$$

remains constant. This keeps all orders in $\pi_L$, which scale with $1/\Lambda_3^3$, while decoupling non-linear powers of the helicity-2 mode. One can now perform an EFT expansion in powers of $\pi_L$ – which is what we have done to quadratic order when setting the coefficients $a$ and $b$ in Eq. (2.2.4). In a series of seminal papers in 2010–11, it was shown that this cancellation can be extended to higher orders: in Ref. [43], de Rham and Gabadadze showed that at each order in $\Pi_{\mu\nu}$, there exists a unique combination of contractions of $\Pi_{\mu\nu}$ such that the sum is a total derivative. By choosing the coefficients of the EFT series appropriately, the potential (up to quartic order) can be rewritten as these total derivatives, and the BD ghost is eliminated. Furthermore, it was shown that orders

[9] In a general theory of Massive Gravity, interactions of $\pi_L$ arise already at order $\Lambda_5 \equiv (m^4 M_{\rm Pl})^{1/5}$, but one can show that these are always pathological [46].

at the quintic level in $\Pi_{\mu\nu}$ and beyond vanish identically. This construction of a potential for Massive Gravity was extended to full non-linear covariance in Ref. [44] by making the replacement $\Pi^\mu_\nu \mapsto \mathbb{I} - g^{-1}\tilde{g}$. The final missing piece was the proof that the potential remains ghost-free away from the decoupling limit, as demonstrated in Refs. [45, 47–51]. Briefly, the proof consists of showing the existence of a Hamiltonian constraint, which eliminates one d.o.f. from the theory. To this end, the action is rewritten using the ADM formalism, see also Sec. 2.2.6.

The fully non-linear, ghost-free potential will be given in Eq. (2.2.75) and is discussed in detail in Sec. 2.2.8.

### 2.2.6 Vielbein formulation

However, the derivation of dRGT theory in the metric formulation is cumbersome and the cancellation of terms which introduce the BD ghost must be set by hand. As it turns out, the construction of the potential is most easily formulated with the use of Vielbeins. For any object to be evaluated at a point $x^\mu$ in spacetime, we define a set of coordinates $\xi^A$ which span a local inertial frame in $x^\mu$. This defines the Vielbein $e^A(x)$,

$$e^A_\mu \equiv \frac{\partial \xi^A(x)}{\partial x^\mu}, \qquad e^A \equiv e^A_\mu \, dx^\mu. \tag{2.2.19}$$

We also define the inverse Vielbein with inverted indices, $(e^A_\mu)^{-1} \equiv e^\mu_a$. The Vielbein is related to the metric via

$$g_{\mu\nu} dx^\mu dx^\nu = ds^2 = e^A e^B \eta_{AB} \quad \Rightarrow \quad g_{\mu\nu}(x) = e^A_\mu(x) e^B_\nu(x) \, \eta_{AB}. \tag{2.2.20}$$

$e^A_\mu(x)$ carries two types of indices: the Greek letter $\mu$ indicates the usual index of a vector under general coordinate transformations in curved space, while Roman $A$ is a 'flat' index in a local Lorentz frame. Crucially, we note that the Vielbeins span a different tangent space in different points $x^\mu$. Therefore, the Lorentz transformations are local,

$$e^A_\mu(x) \overset{\text{LL}}{\longmapsto} \Lambda(x)^A{}_B \, e^B_\mu(x) \tag{2.2.21}$$

where we stress that $\Lambda = \Lambda(x)$. This admits an analogy with gauge theories of spin-1 particles, where $e^\mu_a$ transforms in a fundamental representation of diffeomorphism, and as fundamental of an 'internal' symmetry (local Lorentz transformations).

We will now review the construction of the Einstein-Hilbert Lagrangian in the Vielbein formalism, following closely Refs. [52] and [53].

#### Essentials of the Vielbein formulation of GR

In the Vielbein language, the Ricci scalar can be expressed solely by $e^A$ and its first derivatives. In the subsequent analysis of the d.o.f., this fact will be of great use. To derive this form, we define two separate covariant derivatives: for a mixed index object $\lambda^{\beta,A}$ (one index of general coordinate transformations $\beta$, one local Lorentz index $A$), let

$$\mathcal{D}_\alpha \lambda^{\beta,A} \equiv \partial_\alpha \lambda^{\beta,A} + \Gamma^\beta{}_{\alpha\gamma} \lambda^{\gamma,A} + \omega_\alpha{}^A{}_B \lambda^{\beta,B} \tag{2.2.22}$$

$$\nabla_\alpha \lambda^{\beta,A} \equiv \partial_\alpha \lambda^{\beta,A} + \Gamma^\beta{}_{\alpha\gamma} \lambda^{\gamma,A}. \tag{2.2.23}$$

Here, $\Gamma^\beta{}_{\alpha\gamma}$ is the usual connection in curved space and $\omega_\alpha{}^A{}_B$ the spin-connection. As we note, $\mathcal{D}_\alpha$ is the covariant derivate w.r.t. both types of indices, while $\nabla_\alpha$ remains agnostic to the presence

of local Lorentz indices. We require the Vielbein postulate, i.e. the covariant derivatives to be compatible with the metric and the Vielbein,

$$\mathcal{D}_\alpha e_{\beta,A} = 0 \tag{2.2.24}$$

$$\nabla_\alpha g_{\beta\gamma} = 0 \quad \Rightarrow \quad \mathcal{D}_\alpha g_{\beta\gamma} = 0. \tag{2.2.25}$$

Analogously to vector gauge theories, one can define the Riemann tensor from the anti-commutator of the covariant derivative acting on a generic representation. As we now have both $\mathcal{D}_\alpha$ and $\nabla_\alpha$ at our disposal, we define the mixed index Riemann tensor

$$R_{\alpha\beta A}{}^B \lambda_B \equiv [\mathcal{D}_\alpha, \mathcal{D}_\beta]\lambda_A \tag{2.2.26}$$

and equivalently

$$R_{\alpha\beta\mu}{}^\nu \lambda_\nu \equiv [\nabla_\alpha, \nabla_\beta]\lambda_\mu. \tag{2.2.27}$$

The two definitions are related via $R_{\alpha\beta A}{}^B e^\delta_B e^A_\gamma = R_{\alpha\beta\gamma}{}^\delta$, as can be seen by setting $\lambda_A = e^\alpha_A \lambda_\alpha$:

$$\begin{aligned} R_{\alpha\beta A}{}^B e^\mu_B \lambda_\mu &= [\mathcal{D}_\alpha, \mathcal{D}_\beta] e^\mu_A \lambda_\mu \\ &= e^\mu_A [\nabla\alpha, \nabla_\beta]\lambda_\mu = e^\nu_A R_{\alpha\beta\nu}{}^\mu \lambda_\mu \end{aligned} \tag{2.2.28}$$

where in passing to the second line we have made use of Eqs. (2.2.24) and (2.2.27). Given this, the Ricci scalar is expressed in terms of the Vielbeins as

$$R = g^{\alpha\gamma} R_{\alpha\beta\gamma}{}^\beta = g^{\alpha\gamma} e^\beta_A R_{\alpha\beta\gamma}{}^\delta e^A_\delta = e^{\beta,A}[\nabla_\alpha, \nabla_\beta] e^\alpha_A \tag{2.2.29}$$

As is apparent, the Ricci scalar written in this form is still a function of second derivatives on the Vielbein. We now make use of the definition of $\mathcal{D}_\alpha$ and the compatibility of the Vielbein, Eq. (2.2.24),

$$0 = \mathcal{D}_\alpha e_{\beta,A} = \nabla_\alpha e_{\beta,A} + \omega_{\alpha,AB} e^B_\beta. \tag{2.2.30}$$

By solving for $\nabla_\alpha e_{\beta,A}$ and inserting twice into Eq. (2.2.29), we have

$$R = \left[\nabla_\alpha (e^{\beta,A} \nabla_\beta e^\alpha_A) - \omega_\alpha{}^{AJ} e^\beta_J \omega_{\beta,AI} e^{\alpha,I}\right] + \quad (\alpha \leftrightarrow \beta). \tag{2.2.31}$$

The first term is a total derivative, which we neglect in the following. In order to simplify our calculations further, we define

$$\Omega^{ABC} \equiv e^{\alpha,A} e^{\beta,B} \partial_{[\alpha} e^C_{\beta]} \tag{2.2.32}$$

$$\Rightarrow \quad \omega_\alpha{}^{AB} = \frac{1}{2} e_{\alpha,C} \left(\Omega^{CAB} + \Omega^{BCA} - \Omega^{ABC}\right)$$

and thus, the Einstein-Hilbert Lagrangian takes the form

$$\mathcal{L}_{\text{EH}} = e\, R = e \left(\Omega_A{}^{BA} \Omega_{CB}{}^C - \frac{1}{2}\Omega^{ABC}\Omega_{ACB} - \frac{1}{4}\Omega^{ABC}\Omega_{ABC}\right). \tag{2.2.33}$$

We will also make use of the exterior product notation,

$$e^A \wedge e^B \equiv e^A_\mu e^B_\nu \, dx^\mu \wedge dx^\nu \tag{2.2.34}$$

where $dx^{\mu_1} \wedge ... \wedge dx^{\mu_D}$ is defined as the volume element in $D$ dimensions, $d^D x$. In this notation, the mixed-index Riemann tensor is

$$R^{AB}_{\mu\nu} = \partial_\mu \omega^{AB}_\nu - \partial_\nu \omega^{AB}_\mu + \omega^A_{\mu,C} \omega^{CB}_\nu - \omega^A_{\nu,C} \omega^{CB}_\mu. \tag{2.2.35}$$

Furthermore, we define the Levi-Civita symbol $\tilde{\varepsilon}_{ABCD}$ as the pseudotensor in a local Lorentz frame, and its generalisation to curved spacetime,

$$\epsilon^{\mu\nu\rho\sigma} = e\,\tilde{\varepsilon}^{KLMN} e^{\mu}_{K} e^{\nu}_{L} e^{\rho}_{M} e^{\sigma}_{N}, \tag{2.2.36}$$

where the factor $e \equiv \det e^{A}_{\mu}$ ensures that $\epsilon^{\mu\nu\rho\sigma}$ transforms as a tensor.

We will also translate the Vielbein formulation to the metric formalism. To this end, a useful relation is $\sqrt{\det g_{\mu\nu}} = \det e^{A}_{\mu}$. This can be shown with the definition of the Vielbein determinant,

$$\det e^{A}_{\mu} = \frac{1}{4!}\epsilon^{\mu\nu\rho\sigma}\tilde{\varepsilon}_{ABCD}\, e^{A}_{\mu} e^{B}_{\nu} e^{C}_{\rho} e^{D}_{\sigma}. \tag{2.2.37}$$

The determinant of the metric is

$$\begin{aligned}
\sqrt{\det g_{\mu\nu}} &= \big[\frac{1}{4!}\epsilon^{\mu\nu\rho\sigma}\epsilon^{\alpha\beta\gamma\delta}\, g_{\mu\alpha} g_{\nu\beta} g_{\rho\gamma} g_{\sigma\delta}\big]^{1/2} \\
&= \big[\frac{1}{4!}\, e\,\tilde{\varepsilon}^{KLMN} e^{\mu}_{K} e^{\nu}_{L} e^{\rho}_{M} e^{\sigma}_{N}\, \epsilon^{\alpha\beta\gamma\delta}\, e^{A}_{\mu} e_{\alpha,A} e^{B}_{\nu} e_{\beta,B} e^{C}_{\rho} e_{\gamma,C} e^{D}_{\sigma} e_{\delta,D}\big]^{1/2} \\
&= \big[\frac{1}{4!}\, e\,\tilde{\varepsilon}_{ABCD}\, \epsilon^{\alpha\beta\gamma\delta}\, e^{A}_{\alpha} e^{B}_{\beta} e^{C}_{\gamma} e^{D}_{\delta}\big]^{1/2} = [e\cdot e]^{1/2} = e.
\end{aligned} \tag{2.2.38}$$

**Constructing a potential of Vielbeins**

With the definition of the Ricci scalar in terms of the Vielbeins, the kinetic term of the metric is

$$S_{\rm EH} = \frac{M_{\rm Pl}^2}{2}\int d^4x\, e\,(R[e] - 2\Lambda) \tag{2.2.39}$$

In this alternative language, we now proceed with the construction of Massive Gravity. We define a secondary Vielbein $f^{A}_{\mu}(x)$, in complete analogy with the reference metric $\tilde{g}_{\mu\nu}$. We also let $f^{A}_{\mu}$ transform independently of $e^{A}_{\mu}$ under both local Lorentz and general coordinate transformations.

Now we may ask: which is the unique ghost-free potential of two Vielbeins $e^{A}$ and $f^{A}$? We can motivate an ansatz by evaluating terms which need to be present. For example, the only term in the Einstein-Hilbert action without derivatives is the cosmological constant term $\Lambda$. Rewritten explicitly in terms of the Vielbein $e^{A}$, it is

$$\int d^4x\, e\,\Lambda = \frac{1}{4!}\Lambda\int \tilde{\epsilon}_{ABCD}\, e^{A}\wedge e^{B}\wedge e^{C}\wedge e^{D}. \tag{2.2.40}$$

To see this, we use Eqs. (2.2.34) and (2.2.36),

$$\begin{aligned}
\tilde{\varepsilon}_{ABCD}\, e^{A}\wedge e^{B}\wedge e^{C}\wedge e^{D} &= \tilde{\varepsilon}_{ABCD}\, e^{A}_{\mu} e^{B}_{\nu} e^{C}_{\rho} e^{D}_{\sigma}\, dx^{\mu}\wedge dx^{\nu}\wedge dx^{\rho}\wedge dx^{\sigma} \\
&= \tilde{\varepsilon}_{ABCD}\, \epsilon^{\mu\nu\rho\sigma}\, e^{A}_{\mu} e^{B}_{\nu} e^{C}_{\rho} e^{D}_{\sigma}\, d^4x \\
&= e\,\tilde{\varepsilon}_{ABCD}\,\tilde{\varepsilon}^{KLMN}\, e^{A}_{\mu} e^{B}_{\nu} e^{C}_{\rho} e^{D}_{\sigma} e^{\mu}_{K} e^{\nu}_{L} e^{\rho}_{M} e^{\sigma}_{N}\, d^4x \\
&= e\,\tilde{\varepsilon}_{ABCD}\,\tilde{\varepsilon}^{ABCD}\, d^4x = 4!\, e\, d^4x.
\end{aligned} \tag{2.2.41}$$

Equivalently, we expect a similar term in $f^{A}$ to be present,

$$\int d^4x\, f \propto \int \tilde{\epsilon}_{ABCD}\, f^{A}\wedge f^{B}\wedge f^{C}\wedge f^{D}. \tag{2.2.42}$$

with $f \equiv \det f^{A}_{\mu}$. Extension to mixing terms in $e^{A}$ and $f^{A}$ is now highly suggestive, and thus it was conjectured by Hinterbichler and Rosen [54] that the unique ghost-free potential for $\mathcal{N}$ Vielbeins $e_{(1)},\ldots,e_{(\mathcal{N})}$ in $D=4$ takes the form

$$V(e_{(1)},\ldots,e_{(\mathcal{N})}) = \sum_{I_1,I_2,I_3,I_4=1}^{\mathcal{N}} T^{I_1 I_2 I_3 I_4}\,\tilde{\epsilon}_{ABCD}\, e^{A}_{(I_1)}\wedge e^{B}_{(I_2)}\wedge e^{C}_{(I_3)}\wedge e^{D}_{(I_4)}. \tag{2.2.43}$$

Here, $T^{I_1 I_2 I_3 I_4}$ is a totally symmetric tensor of constant coefficients. We see that Eq. (2.2.43) breaks the $\mathcal{N}$ local Lorentz and $\mathcal{N}$ general coordinate transformations down to the 'diagonal' subgroup, where all Vielbeins transform simultaneously, such that $(e^A_{(I_1),\mu})^{-1} e^A_{(I_2),\mu}$ is invariant.

In the two-Vielbein case $\mathcal{N} = 2$, Eq. (2.2.43) produces five terms for the potential. Going back to the notation $e^A_{(1)} = e^A$ and $e^A_{(2)} = f^A$, these are

$$\begin{aligned} V(e,f) = \quad & \alpha_0 \, \tilde{\epsilon}_{ABCD} \, e^A \wedge e^B \wedge e^C \wedge e^D \\ & + \alpha_1 \, \tilde{\epsilon}_{ABCD} \, e^A \wedge e^B \wedge e^C \wedge f^D \\ & + \alpha_2 \, \tilde{\epsilon}_{ABCD} \, e^A \wedge e^B \wedge f^C \wedge f^D \\ & + \alpha_3 \, \tilde{\epsilon}_{ABCD} \, e^A \wedge f^B \wedge f^C \wedge f^D \\ & + \alpha_4 \, \tilde{\epsilon}_{ABCD} \, f^A \wedge f^B \wedge f^C \wedge f^D \end{aligned} \tag{2.2.44}$$

with constants $\alpha_i$.

In order to accept this proposal, we need to examine $V(e,f)$ for two qualities:

1. Does its construction ensure ghost-freeness?
2. Is it the *unique* ghost-free potential of two Vielbeins?

In order to demonstrate that the potential (2.2.44) is ghost-free, we review the analysis performed in Ref. [54] (see also Refs. [53, 55]). To this end, the Lagrangian of Massive Gravity is examined in terms of the ADM parametrisation [56].

### ADM analysis

The ADM programme consists of deriving the Hamiltonian to the action in a (3+1)-decomposition of space-time, and examining which d.o.f. propagate. We will begin with an analysis of the kinetic term, the Einstein-Hilbert Lagrangian, following Ref. [53].

In the ADM formalism, instead of using a general form of the metric $g_{\mu\nu}$, which treats all space-time dimensions equally, the time coordinate is singled out: space-time is foliated into surfaces of equal times, and one can show that the ten components of the metric are decomposed as

$$ds^2 = -N^2 dt^2 + \gamma_{ij} \, (dx^i + N^i dt)(dx^j + N^j dt). \tag{2.2.45}$$

$N$ is known as the lapse function, and the three-vector $N^i$ is conventionally called the shift. In terms of the Vielbein, this corresponds to [53]

$$e_{\mu,A} = \begin{pmatrix} N \, N_0 + N^i e_{i,0} & N \, N_a + N^i e_{i,a} \\ e_{i,0} & e_{i,a} \end{pmatrix} \tag{2.2.46}$$

$$e^{\mu,A} = \begin{pmatrix} -\frac{N^0}{N} & -\frac{N^a}{N} \\ e^{i,0} & e^{i,a} \end{pmatrix} \tag{2.2.47}$$

where $a = 1,2,3$ is a flat index, and $i = 1,2,3$ an index of general coordinate transformations.[10] The metric (2.2.45) is reproduced with the conditions

$$N^A e_{i,A} = 0 \qquad N^A N_A = -1 \qquad e_{i,A} \, e^A_j = \gamma_{ij}. \tag{2.2.48}$$

In this decomposition, the determinant of the metric is $\det g_{\mu\nu} = -N^2 \det \gamma_{ij}$, equivalent to $e = N \det e^a_i$. We define the determinant of the spatial Vielbein, ${}^{(3)}e \equiv \det e^a_i$.

[10] In the following, $a, b, c$ denote flat spatial indices, while $i, j, k$ denote curved spatial indices.

By a local Lorentz transformation, we can bring the generic Vielbein $e^A_\mu$ into an upper triangular form [54, 57]. This corresponds to the choice $N^A = (1,0,0,0)$, upon which we obtain

$$\hat{e}^A_\mu = \begin{pmatrix} N & N^i e^a_i \\ 0 & e^a_i \end{pmatrix} \tag{2.2.49}$$

$$\hat{e}^{\mu,A} = \begin{pmatrix} -\frac{1}{N} & 0 \\ \frac{N^i}{N} & e^{i,a} \end{pmatrix}. \tag{2.2.50}$$

To show how $\hat{e}^A_\mu$ is related to the general Vielbein $e^A_\mu$, we make use of a standard Lorentz boost with a three-vector $v^a$ as gauge parameter,

$$\Lambda(v)^A{}_B = \begin{pmatrix} \gamma & v^a \\ v_b & \delta^a_b + \frac{1}{1+\gamma} v^a v_b \end{pmatrix}, \tag{2.2.51}$$

with $\gamma \equiv \sqrt{1 + v^a v_a}$. Under this Lorentz boost, $\hat{e}^A_\mu$ transforms as

$$\Lambda(v)^A{}_B \, \hat{e}^B_\mu = \begin{pmatrix} N\gamma + N^i e^a_i v_a & N v^a + N^i e^b_i (\delta^a_b + \frac{1}{1+\gamma} v^a v_b) \\ e^a_i v_a & e^b_i (\delta^a_b + \frac{1}{1+\gamma} v^a v_b) \end{pmatrix}. \tag{2.2.52}$$

Comparison with Eq. (2.2.46) shows that this is a mere reparametrisation of a generic Vielbein. Furthermore, the Ricci scalar can be written as a function purely of the metric, and thus is agnostic towards the Lorentz structure of the Vielbein. It is therefore sufficient to use the gauge-fixed upper triangular Vielbein $\hat{e}^A_\mu$ to calculate $R$.

We thus proceed to evaluate $\Omega^{ABC}$, see Eq. (2.2.33), for which we find

$$\begin{aligned} \Omega^{0ab} &= -\frac{1}{N} e^{j,a} \partial_{[0} e^b_{j]} + \frac{N^i}{N} e^{j,a} \partial_{[i} e^b_{j]} \\ \Omega^{0a0} &= \frac{1}{N} e^{j,a} \partial_j N \\ \Omega^{ab0} &= 0 \\ \Omega^{abc} &= e^{i,a} e^{j,b} \partial_{[i} e^c_{j]} \end{aligned} \tag{2.2.53}$$

Inserting this into the Einstein-Hilbert Lagrangian (2.2.33), we obtain

$$\mathcal{L}_{\text{EH}} = N \, {}^{(3)}e \left[ {}^{(3)}R + 2\,\Omega^b{}_0{}^0 \Omega_{ba}{}^a + \Omega_a{}^{0a} \Omega_{b0}{}^b - \frac{1}{2} \Omega^{0bc} \Omega_{0(bc)} \right] \tag{2.2.54}$$

where we have defined the spatial Ricci scalar ${}^{(3)}R$, which can be derived straightforwardly through the spatial covariant derivative $\nabla_a$. Again, additional surface terms have been dropped.

Analogously to classical mechanics, the canonical momenta are defined from the Lagrangian through the variation w.r.t. the components of $\dot{e}^A_\mu$, and we have

$$\begin{aligned} \pi^{i,a} \equiv \frac{\delta \mathcal{L}_{\text{EH}}}{\delta \dot{e}_{i,a}} &= {}^{(3)}e \left( \Omega^{0(ba)} e^i_b - 2\,\Omega^0{}_b{}^b e^{i,a} \right) \\ p \equiv \frac{\delta \mathcal{L}_{\text{EH}}}{\delta \dot{N}} = 0 \qquad & p^i \equiv \frac{\delta \mathcal{L}_{\text{EH}}}{\delta \dot{N}_i} = 0. \end{aligned} \tag{2.2.55}$$

Crucially, we immediately see from Eqs. (2.2.53) that the momenta of the lapse $N$ and shift $N^i$ are zero, rendering these d.o.f. non-propagating. By noting that the combination $e^b_i \pi^{i,a}$ is symmetric in $a, b$, we are able to construct a set of primary constraints:[11]

$$\mathcal{P}^{ab} \equiv e^{[b}_i \pi^{i,a]} = 0. \tag{2.2.56}$$

[11] We recall that a primary constraint is an equation connecting phase-space variables; a secondary constraint is a set of constraint equations evolved in time using the e.o.m.

To enforce these three constraints, we add the term $\lambda_{ab}\mathcal{P}^{ab}$ to the action, where $\lambda_{ab}$ is an arbitrary Lagrangian multiplier. By inverting $\pi^{i,a}$ in terms of $\Omega^{abc}$, we can express $\mathcal{L}_{\rm EH}$ fully as a function of $\pi^{ab} \equiv \pi^{i,a}e^b_i$, ${}^{(3)}e$ and ${}^{(3)}R$, and are now in the position to assemble the Hamiltonian $\mathcal{H}_{\rm EH}$ [52]:

$$\begin{aligned}\mathcal{H}_{\rm EH} &= \pi^{i,a}\dot{e}_{i,a} - \mathcal{L}_{\rm EH} + \frac{1}{2}\lambda_{ab}\mathcal{P}^{ab} \\ &= \frac{N}{2\,{}^{(3)}e}\big[\pi_{ab}\pi^{ab} - \frac{1}{2}(\pi^a{}_a)^2 - 2\,{}^{(3)}e^2\,{}^{(3)}R,\big] - N^i e_{i,a}\,{}^{(3)}\mathcal{D}_j\pi^{j,a} + \frac{1}{2}\lambda_{ab}\mathcal{P}^{ab},\end{aligned} \tag{2.2.57}$$

where ${}^{(3)}\mathcal{D}_i$ is defined as the covariant derivative w.r.t the spatial Vielbein, i.e. such that $\mathcal{D}_i e_{j,a} = 0$. This Hamiltonian can be abbreviated as

$$\begin{aligned}\mathcal{H}_{\rm EH} &= N\,\mathcal{C}_{\rm EH} + N^i\mathcal{C}^{\rm EH}_i + \frac{1}{2}\lambda_{ab}\mathcal{P}^{ab} \\ \text{where}\quad C_{\rm EH} &= \frac{1}{2\,{}^{(3)}e}\big[\pi_{ab}\pi^{ab} - \frac{1}{2}(\pi^a{}_a)^2 - 2\,{}^{(3)}e^2\,{}^{(3)}R\big], \\ C^{\rm EH}_i &= -e_{i,a}\,{}^{(3)}\mathcal{D}_j\pi^{j,a}.\end{aligned} \tag{2.2.58}$$

With the Hamiltonian in this form at hand, it is now easy to determine the number of propagating d.o.f. As $p = p^i = 0$, we find $C_{\rm EH} \approx 0$ and $C^{\rm EH}_i \approx 0$ upon use of the equations of motion. Therefore, the lapse produces one constraint equation, while the shift provides three constraints. One can show that these conditions respectively correspond to the diffeomorphism invariance of the system under time re-parametrisations and spatial transformations modulo $SO(3)$ rotations [53]; similarly, $\mathcal{P}_{ab}$ is the generator of $SO(3)$ rotations. Therefore, each constraint equation eliminates two d.o.f. – one due to the constraint equation itself, one due to the associated symmetry.

The d.o.f. counting is thus

$$\underbrace{2\times 9}_{e^i_a} - \underbrace{(2\times 1)}_{\mathcal{C}_{\rm EH}} - \underbrace{(2\times 3)}_{\mathcal{C}^{\rm EH}_i} - \underbrace{(2\times 3)}_{\mathcal{P}^{ab}} = 2\times 2 \text{ d.o.f. in phase space,} \tag{2.2.59}$$

which is the correct number of d.o.f. for a massless spin-2 field.

We now turn to case of multiple Vielbeins. For $\mathcal{N}'$ *dynamical* Vielbeins[12] $e^a_{(I),i}$, the derivation of the kinetic term goes through as above; we define the conjugate momentum $\pi^{i,a}_{(I)}$, and by a Lorentz transformation with the parameter $v^a_{(I)}$, we can express each Vielbein in an upper-triangular form. Thus, the kinetic terms are $\mathcal{N}'$ copies of the Einstein-Hilbert action,

$$\mathcal{S}^{(I)}_{\rm EH} = \int d^4x\big[\pi^{i,a}_{(I)}\dot{e}^{(I)}_{i,a} - N_{(I)}\mathcal{C}^{(I)}_{\rm EH} - N^i_{(I)}\mathcal{C}^{\rm EH}_{(I),i} - \frac{1}{2}\lambda^{(I)}_{ab}\mathcal{P}^{ab}_{(I)}\big]. \tag{2.2.60}$$

Crucially, we stress that each copy of the Einstein-Hilbert action is independent of the parameter $v^a_{(I)}$.

We now append the potential $V(e_{(1)},\dots,e_{(\mathcal{N})})$ of Eq. (2.2.43) to the Hamiltonian,

$$\mathcal{H}_{\rm MG} = \mathcal{H}_{\rm EH} + V(e_{(1)},\dots,e_{(\mathcal{N})}). \tag{2.2.61}$$

The Vielbeins are now written in terms of the parametrisation (2.2.52),

$$e^A_{(I),\mu} = \begin{pmatrix} N_{(I)}\,\gamma_{(I)} + N^i_{(I)}e^a_{(I),i}v_{(I),a} & N_{(I)}v^a_{(I)} + N^i_{(I)}e^b_{(I),i}(\delta^a_b + \frac{1}{1+\gamma_{(I)}}v^a_{(I)}v_{(I),b}) \\ e^a_{(I),i}v_{(I),a} & e^b_{(I),i}(\delta^a_b + \frac{1}{1+\gamma_{(I)}}v^a_{(I)}v_{(I),b}) \end{pmatrix}. \tag{2.2.62}$$

[12] The total number of Vielbeins $\mathcal{N}$ does not necessarily coincide with the number of dynamical Vielbeins. See the discussion of Massive Gravity vs. Bimetric Gravity, Sec. 2.2.8.

We recall that the potential breaks the $\mathcal{N}$ local Lorentz symmetries of the $e^A_{(I)}$ down to one Lorentz invariance. We use this residual symmetry to set one of the Vielbeins, say $e^A_{(1),\mu}$, to its upper-triangular form. Crucially, this means that it is independent of $v^a_{(1)}$.

To show the ghost-freedom of $V(e_{(1)},\dots,e_{(\mathcal{N})})$, we now show the existence of the appropriate number of constraints, such that only physical d.o.f. remain. We observe that $e^A_{(I),\mu}$ is linear in the lapse and shift functions $N_{(I)}$ and $N^i_{(I)}$; in particular, they only appear in the first row. Combine this with the fact that the potential by construction is antisymmetric in all indices, it is guaranteed that $V$ can be rewritten as a sum of terms proportional to $N_{(I)}$ or $N^i_{(I)}$. Explicitly, a generic term in the potential is

$$\begin{aligned}&\tilde{\epsilon}_{ABCD}\, e^A_{(I_1)} \wedge e^B_{(I_2)} \wedge e^C_{(I_3)} \wedge e^D_{(I_4)} \\ &= \tilde{\epsilon}_{ABCD}\, \epsilon^{\mu\nu\rho\sigma}\, e^A_{(I_1),\mu}\, e^B_{(I_2),\nu}\, e^C_{(I_3),\rho}\, e^D_{(I_4),\sigma}\, d^4x\,. \end{aligned} \tag{2.2.63}$$

Picking e.g. $\mu = 0$, we see that all terms are lead by either $N_{(I_1)}$ or $N^i_{(I_1)}$, and $\nu,\rho,\sigma \neq 0$, hence there are no other lapse or shift functions in this term. We are thus able to write the potential as [54]

$$V(e_{(1)},\dots,e_{(\mathcal{N})}) = \sum_{I=1}^{\mathcal{N}} \left(N_{(I)}\mathcal{C}^m_{(I)} + N^i_{(I)}\mathcal{C}^m_{(I),i}\right) \tag{2.2.64}$$

where $\mathcal{C}^m_{(I)}$ and $\mathcal{C}^m_{(I),i}$ are functions of the spatial Vielbeins $e^a_{(I),i}$ and the boost parameters $v^a_{(I)}$. The complete action is now

$$\mathcal{S}_{\rm tot} = \int d^4x \sum_{I=1}^{\mathcal{N}} \left\{ \pi^{i,a}_{(I)} \dot{e}^{(I)}_{i,a} - N_{(I)}\left[\mathcal{C}^{\rm EH}_{(I)} + \mathcal{C}^m_{(I)}\right] - N^i_{(I)}\left[\mathcal{C}^{\rm EH}_{(I),i} + \mathcal{C}^m_{(I),i}\right] - \frac{1}{2}\lambda^{(I)}_{ab}\mathcal{P}^{ab}_{(I)} \right\} \tag{2.2.65}$$

Even though the potential in the form of Eq. (2.2.64) already suggests the presence of Hamiltonian constraints, we need to eliminate the gauge parameter $v^a_{(I)}$ in $\mathcal{C}^m_{(I)}$ and $\mathcal{C}^m_{(I),i}$ before counting d.o.f. To this end, we need $(\mathcal{N}-1)$ equations of three-vectors (recall that we have used the one unbroken Lorentz symmetry to set $v^a_{(1)} = 0$). We use the constraint equations

$$\frac{\delta \mathcal{L}_{\rm tot}}{\delta N^i_{(J)}} = \mathcal{C}^{\rm EH}_{(J),i}(e,\pi) + \mathcal{C}^m_{(J),i}(e,v) = 0 \qquad \text{for } J = 2,\dots,\mathcal{N}. \tag{2.2.66}$$

We need not calculate the explicit solution for the $v^a_{(J)}$, but suffice to assume that the above expression can be inverted. We can then immediately plug the above equation back into the action, which gives us

$$\mathcal{S}_{\rm tot} = \int d^4x \left[ \sum_{I=1}^{\mathcal{N}} \left\{ \pi^{i,a}_{(I)} \dot{e}^{(I)}_{i,a} - N_{(I)}\left[\mathcal{C}^{\rm EH}_{(I)} + \mathcal{C}^m_{(I)}\right] - \frac{1}{2}\lambda^{(I)}_{ab}\mathcal{P}^{ab}_{(I)} \right\} - N^i_{(1)}\left[\mathcal{C}^{\rm EH}_{(1),i} + \mathcal{C}^m_{(1),i}\right] \right], \tag{2.2.67}$$

which is the appropriate action to count the number of d.o.f. In doing so, we find

$$\begin{aligned} \underbrace{2\times\mathcal{N}\times 9}_{e^i_{(I),a}} - \underbrace{(2\times\mathcal{N})}_{\mathcal{C}^{\rm EH}_{(I)}+\mathcal{C}^m_{(I)}} - \underbrace{(2\times\mathcal{N}\times 3)}_{\mathcal{P}^{ab}_{(I)}} - \underbrace{(2\times 3)}_{\mathcal{C}^{\rm EH}_{(1),i}+\mathcal{C}^m_{(1),i}} &= 2\times(5\mathcal{N}-3) \\ &= 2\times(5\,(\mathcal{N}-1)+2), \end{aligned} \tag{2.2.68}$$

which is exactly the number of d.o.f. of $\mathcal{N}-1$ massive and one massless spin-2 fields. We note that the existence of $\mathcal{N}-1$ primary constraints is only a necessary condition to ghost-freedom. For the proof of the existence of secondary constraints in the Vielbein formulation, see Ref. [58].

Finally, we comment on the uniqueness of Eq. (2.2.43) as the ghost-free potential of $\mathcal{N}$ Vielbeins. As we have seen, its construction implies ghost-freedom at the fully non-linear order. In order to claim that this is unique, one must invert the statement; this has been shown within the metric reformulation in Ref. [59].

### 2.2.7 Dimensional deconstruction formulation

A posteriori, we know of another way to construct the Massive Gravity potential: the introduction of an auxiliary dimension – an approach known as *dimensional deconstruction*. Starting from a theory of gravity in five dimensions, the extra dimension is discretised in position space (as opposed to the usual KK mode decomposition in momentum space). The motivation for this approach is clear: a massless spin-2 particle in 5D has five polarisations, exactly matching the number of d.o.f. of a massive graviton in 4D. Furthermore, instead of resumming perturbations to the background metric order by order, the deconstruction approach is a covariant formulation from the start.

We briefly sketch the deconstruction approach as proposed in Refs. [60–62] and reviewed in [32]. The starting point is the Einstein-Hilbert action in 5D,

$$S_{5\mathrm{D}} = \frac{M_5^3}{2}\int d^4x\, dy\, \sqrt{-g}\ {}^{(5)}R[g] \tag{2.2.69}$$

where $g_{MN}$ is the metric of five-dimensional space-time, and ${}^{(5)}R[g]$ is the associated Ricci-scalar. As we only intend to retain four-dimensional diffeomorphism invariance, we gauge fix such that

$$G_{MN}(x,y)\, dx^M dx^N = dy^2 + g_{\mu\nu}(x,y) dx^\mu dx^\nu. \tag{2.2.70}$$

As it turns out, the deconstruction approach also benefits from a reformulation using Vielbeins.[13] We decompose the five-dimensional Vielbein $e^{\mathbf{a}}$ with $\mathbf{a} = 1, \dots, 5$ as

$$e^{\mathbf{a}} = \begin{pmatrix} e^A_\mu dx^\mu \\ dy \end{pmatrix}. \tag{2.2.71}$$

and by further gauge fixing set the spin connection $\omega$ associated to $e^{\mathbf{a}}$ to $\omega_y^{AB} = 0$. The discretisation of the $y$-dimension means replacing

$$\begin{aligned} y &\mapsto y_i \\ e^A_\mu(x,y) &\mapsto {e_i}^A_\mu(x) \equiv e^A_\mu(x,y_i) \\ \partial_y e^A_\mu(x,y) &\mapsto m\,({e_{i+1}}^A_\mu(x) - {e_i}^A_\mu(x)). \end{aligned} \tag{2.2.72}$$

We can evaluate Eq. (2.2.69) using this procedure. For example, a two-site discretisation yields the mass term [32]

$$S_{\mathrm{mass}} = \frac{m^2 M_{\mathrm{Pl}}^2}{4}\int \tilde{\epsilon}_{ABCD}\,(f^A - e^A)\wedge(f^B - e^B)\wedge e^C \wedge e^D \tag{2.2.73}$$

which we known from the Vielbein formulation to be part of the ghost-free potential. The full potential is obtained by a weighted discretisation, i.e.

$$e^A_\mu(x,y) \quad \mapsto \quad r\, {e_i}^A_\mu(x) + (1-r)\, {e_{i+1}}^A_\mu(x) \tag{2.2.74}$$

with arbitrary, real weight $r$. One can show that this reproduces the Vielbein potential of Eq. (2.2.43).

Note that ghost-freedom is not guaranteed automatically by deconstruction of a healthy five-dimensional theory. It is possible that such a theory leads to an inconsistent 4D description; e.g. performing a naive discretisation on the metric level reintroduces the BD ghost. It is only because we arrive at Eq. (2.2.43), which has been shown to be ghost-free, that the formulation is consistent.

[13] A straightforward discretisation of the metric leads to a mass term of the form (2.2.13), which carries a ghost mode [32].

### 2.2.8 The non-linear, ghost-free Massive Gravity potential

We now have at our disposal the fully non-linear, ghost-free potential of coupled metric objects. As we have seen, the construction is most easily accomplished in the Vielbein language. Nevertheless, as we are passing to the phenomenological aspects of this theory, it will be more adequate to work in the metric formulation.

A more practical form of the potential (2.2.43) for the case $\mathcal{N} = 2$ is given by [63]:

$$S_{\rm MG} = \frac{M_g^2}{2}\int d^4x\sqrt{-g}\; R(g) + m^2 M_g^2 \int d^4x\sqrt{-g}\sum_{n=0}^{4}\beta_n e_n(\sqrt{g^{-1}\tilde{g}}). \tag{2.2.75}$$

This is the action of the dRGT theory of Massive Gravity. The potential contains the constants $\beta_i$ and is a function of the five elementary polynomials

$$e_0(\mathbb{X}) = 1\,, \quad e_1(\mathbb{X}) = [\mathbb{X}]\,, \quad e_2(\mathbb{X}) = \frac{1}{2}\left([\mathbb{X}]^2 - \left[\mathbb{X}^2\right]\right), \tag{2.2.76}$$

$$e_3(\mathbb{X}) = \frac{1}{6}\left([\mathbb{X}]^3 - 3\,[\mathbb{X}]\left[\mathbb{X}^2\right] + 2\left[\mathbb{X}^3\right]\right), \quad e_4(\mathbb{X}) = \det\mathbb{X}\,. \tag{2.2.77}$$

For phenomenological reasons which will be detailed in Sec. 2.3, we will focus on the theory of $\mathcal{N} = 2$ metrics which are both dynamical. We therefore add to the action Eq. (2.2.75) a kinetic term for the reference metric $\tilde{g}$.

The coupling of the metric(s) to matter can be accommodated in several ways, not all of which retain ghost-freeness [64]. In analogy to GR, we introduce a matter coupling of the form $\sqrt{-g}\,\mathcal{L}_{\rm matter}$. This choice is motivated as for this coupling, stable cosmological solutions are known to exist [65–68].

These additional ingredients define the theory of bimetric gravity (bigravity) we will work with in the following. The action is

$$S_{\rm bigravity} = S_{\rm MG} + \frac{M_{\tilde{g}}^2}{2}\int d^4x\sqrt{-\tilde{g}}\;\tilde{R}(\tilde{g}) + \int d^4x\sqrt{-g}\;\mathcal{L}_{\rm matter}. \tag{2.2.78}$$

For convenience, we replace the scale which multiplies the potential by the effective mass scale $M_{\rm eff} \equiv (M_g^{-2} + M_{\tilde{g}}^{-2})^{-1/2}$.

The equations of motion w.r.t. $g$ and $\tilde{g}$ are

$$R_{\mu\nu} - \frac{1}{2}g_{\mu\nu}R + B_{\mu\nu}(g,\tilde{g}) = \frac{1}{M_g^2}T_{\mu\nu}\,, \tag{2.2.79a}$$

$$\tilde{R}_{\mu\nu} - \frac{1}{2}\tilde{g}_{\mu\nu}\tilde{R} + \tilde{B}_{\mu\nu}(g,\tilde{g}) = 0\,, \tag{2.2.79b}$$

where we have defined $\sin^2(\theta) = \frac{M_{\rm eff}^2}{M_g^2}$, $\cos^2(\theta) = \frac{M_{\rm eff}^2}{M_{\tilde{g}}^2}$ and $\tilde{R}_{\mu\nu}$ the Ricci tensor constructed from $\tilde{g}$. The coupling terms $B_{\mu\nu}$ and $\tilde{B}_{\mu\nu}$ are obtained from the variation of the potential in the action w.r.t. $g$ and $\tilde{g}$ [63],

$$B_{\mu\nu}(g,\tilde{g}) = \frac{m^2\sin^2(\theta)}{2}\sum_{n=0}^{3}(-1)^n\beta_n\left[g_{\mu\lambda}\mathbb{Y}^{\lambda}_{(n)\,\nu}(\sqrt{g^{-1}\tilde{g}}) + g_{\nu\lambda}\mathbb{Y}^{\lambda}_{(n)\,\mu}(\sqrt{g^{-1}\tilde{g}})\right], \tag{2.2.80a}$$

$$\tilde{B}_{\mu\nu}(g,\tilde{g}) = \frac{m^2\cos^2(\theta)}{2}\sum_{n=0}^{3}(-1)^n\beta_{4-n}\left[\tilde{g}_{\mu\lambda}\mathbb{Y}^{\lambda}_{(n)\,\nu}(\sqrt{\tilde{g}^{-1}g}) + \tilde{g}_{\nu\lambda}\mathbb{Y}^{\lambda}_{(n)\,\mu}(\sqrt{\tilde{g}^{-1}g})\right], \tag{2.2.80b}$$

with the functions

$$\begin{aligned}
&\mathbb{Y}_0(\mathbb{X}) = \mathbb{1}\,, \qquad \mathbb{Y}_1(\mathbb{X}) = \mathbb{X} - \mathbb{1}\,[\mathbb{X}]\,,\\
&\mathbb{Y}_2(\mathbb{X}) = \mathbb{X}^2 - \mathbb{X}[\mathbb{X}] + \frac{1}{2}\mathbb{1}([\mathbb{X}]^2 - \left[\mathbb{X}^2\right])\,,\\
&\mathbb{Y}_3(\mathbb{X}) = \mathbb{X}^3 - \mathbb{X}^2[\mathbb{X}] + \frac{1}{2}\mathbb{X}([\mathbb{X}]^2 - \left[\mathbb{X}^2\right]) - \frac{1}{6}\mathbb{1}\left([\mathbb{X}]^3 - 3\,[\mathbb{X}]\left[\mathbb{X}^2\right] + 2\left[\mathbb{X}^3\right]\right).
\end{aligned} \tag{2.2.81}$$

By applying the covariant derivatives to Eqs. (2.2.79), we obtain the conservation laws,

$$\nabla_\mu B^\mu{}_\nu = 0, \qquad \tilde{\nabla}_\mu \tilde{B}^\mu{}_\nu = 0, \qquad \nabla_\mu T^\mu{}_\nu = 0, \tag{2.2.82}$$

where $\tilde{\nabla}_\mu$ is the covariant derivative constructed from $\tilde{g}$. The first two equations are known as Bianchi constraints.

We point out the symmetric structure of the equations of motion in bigravity, determined by its construction through the diagonal subgroup of two independent diffeomorphism invariances. Setting aside the matter coupling, this theory of bigravity is invariant under the simultaneous exchange

$$g \leftrightarrow \tilde{g} \qquad M_g \leftrightarrow M_{\tilde{g}} \qquad \beta_n \leftrightarrow \beta_{4-n}. \tag{2.2.83}$$

Note also that the e.o.m. of $g_{\mu\nu}$ completely decouple from the dynamics of $\tilde{g}_{\mu\nu}$ for $\sin\theta \to 0$. In this limit, GR is fully recovered; this is indeed the correct limit to decouple the additional modes, as opposed to taking $m \to 0$. On the other hand, in the limit $\cos\theta \to 0$, the dynamics induced by one of Einstein-Hilbert terms is smoothly shut off, while the metric potential remains non-zero; we have thus re-obtained dRGT Massive Gravity from bigravity.

### 2.2.9 Strong coupling and Vainshtein mechanism

We will now discuss the resolution of the vDVZ discontinuity in the strong coupling regime of the dRGT theory and bigravity. The central claim is that the strong coupling of the scalar mode effectively restores the gravitational interactions to those of GR below a certain distance $r_V$ – a screening effect known as Vainshtein mechanism. The task is thus to obtain a spherically symmetric solution to the field equations including the potential of metrics. Historically, a closed form solution has been obtained first in the decoupling limit, where the non-linear coupling of the scalar mode $\pi_L$ to the helicity-2 mode is isolated. One can then obtain algebraic solutions to the field equations. By an appropriate choice of the branch of solutions one then recovers the Newtonian gravitational potential at scales below the Vainshtein radius $r_V$ (to be defined below), see Refs. [69–71].

Instead of going to the decoupling limit, we choose to work in the weak field limit of the full theory. We will follow the analysis in [72] (see also Refs. [73, 74]), where the ansatz is made

$$\begin{aligned} g_{\mu\nu}dx^\mu dx^\nu &= -e^{\nu_1(r)}dt^2 + e^{\lambda_1(r)}dr^2 + r^2 d\Omega^2\,, \\ \tilde{g}_{\mu\nu}dx^\mu dx^\nu &= -e^{\nu_2(r)}dt^2 + e^{\lambda_2(r)}(r + r\,\mu(r))'^2 dr^2 + (r + r\,\mu(r))^2 d\Omega^2\,, \end{aligned} \tag{2.2.84}$$

where a prime denotes a derivative w.r.t. the radial variable $r$. The ansatz has been chosen such that both metrics are recovered as flat in the weak field limit $\{\lambda_1, \lambda_2, \nu_1, \nu_2, \mu\} \ll 1$. Note also that this is not the most general spherically symmetric ansatz; in particular, non-diagonal solutions are possible [75]. However, this ansatz is sufficient to demonstrate the effects of strong coupling.

We will now show how this spherically symmetric ansatz demonstrates the Vainshtein mechanism at work. In order to do, we evaluate the EFE (2.2.79) using Eqs. (2.2.84) in two regimes: first, we use the weak field approximation (linear regime), corresponding to the large distance limit. We will show that the gravitational potential does not resemble GR and bears the vDVZ discontinuity. We will then relax the linear approximation to a degree which easily allows us to see the modification of the gravitational potential at short distances, restoring GR.

**Linear regime**

Evaluating the field equations far removed from a mass distribution, we find a system of coupled equations. The non-zero components of the e.o.m of $g_{\mu\nu}$, written as $G_{\mu\nu} = -B_{\mu\nu}$, are

$$tt: \quad \frac{\lambda_1}{r^2} + \frac{\lambda_1'}{r} = \Lambda\,(1+\nu_1) + \frac{m_g^2 \sin^2\theta}{2}(-\lambda_1 + \lambda_2 + 6\mu + 2\mu' r)\,, \tag{2.2.85a}$$

$$rr: \quad \frac{\lambda_1}{r^2} - \frac{\nu_1'}{r} = \Lambda\,(1+\lambda_1) + \frac{m_g^2 \sin^2\theta}{2}(-\nu_1 + \nu_2 + 4\mu)\,, \tag{2.2.85b}$$

$$\theta\theta: \quad \frac{1}{2}\Big(\frac{\lambda_1'}{r} - \frac{\nu_1'}{r} - \nu_1''\Big) = \Lambda + \frac{m_g^2 \sin^2\theta}{2}(-\lambda_1 + \lambda_2 - \nu_1 + \nu_2 + 4\mu + 2\mu' r)\,. \tag{2.2.85c}$$

We have defined $\Lambda \equiv m^2 \sin^2\theta\,(\beta_0 + 3\beta_1 + 3\beta_2 + \beta_3)$ and $m_g^2 \equiv m^2(\beta_1 + 2\beta_2 + \beta_3)$. As we will see in Sec. 3.3, these quantities correspond to a cosmological constant and the physical mass of the massive graviton.[14] The corresponding equations for $\tilde{g}_{\mu\nu}$ are

$$tt: \quad \frac{\lambda_2}{r^2} + \frac{\lambda_2'}{r} = \tilde{\Lambda}\,(1+\nu_2) - \frac{m_g^2 \cos^2\theta}{2}(-\lambda_1 + \lambda_2 + 6\mu + 2\mu' r)\,, \tag{2.2.86a}$$

$$rr: \quad \frac{\lambda_2}{r^2} - \frac{\nu_2'}{r} = \tilde{\Lambda}\,(1+\lambda_2 + 2\mu + 2\mu' r) - \frac{m_g^2 \cos^2\theta}{2}(-\nu_1 + \nu_2 + 4\mu)\,, \tag{2.2.86b}$$

$$\theta\theta: \quad \frac{1}{2}\Big(\frac{\lambda_2'}{r} - \frac{\nu_2'}{r} - \nu_2''\Big) = \tilde{\Lambda}\,(1+2\mu) - \frac{m_g^2 \cos^2\theta}{2}(-\lambda_1 + \lambda_2 - \nu_1 + \nu_2 + 4\mu + 2\mu' r)\,, \tag{2.2.86c}$$

where we additionally have defined $\tilde{\Lambda} \equiv m^2 \sin^2\theta\,(\beta_4 + 3\beta_3 + 3\beta_2 + \beta_1)$. The Bianchi identities (2.2.82) yield one constraint equation,

$$\lambda_1 - \lambda_2 = \frac{r}{2}(\nu_1' - \nu_2')\,. \tag{2.2.87}$$

We now choose $\beta_0$ and $\beta_4$ s.t. $\Lambda$ and $\tilde{\Lambda}$ are set to zero; this simplifies our analysis and restricts the solutions to be asymptotically Minkowski [74].

To obtain the first solution to this system of equations, we define $\nu_- \equiv \nu_1 - \nu_2$ and $\lambda_- \equiv \lambda_1 - \lambda_2$. The steps to obtain the solution are these: we subtract the $rr$ equations and solve for $\lambda_-$, the solution of which we insert into Eq. (2.2.87). By this means, we obtain $\mu(\nu_-, \nu_-')$, which we insert into the $tt$ equations, Eqs. (2.2.85a) − (2.2.86a). Combined with the Bianchi constraint, this yields a second order differential equation for $\nu_-$,

$$\nu_-'' + \frac{2\,\nu_-'}{r} - m_g^2\,\nu_- = 0\,. \tag{2.2.88}$$

This is solved by

$$\nu_-(r) = \frac{C_1}{r} e^{-m_g r} \tag{2.2.89}$$

where we have dropped the unphysical exponentially growing solution. For the remaining functions, we find

$$\lambda_-(r) = -\frac{C_1}{2}\frac{1 + m_g r}{r}\, e^{-m_g r}\,, \tag{2.2.90}$$

$$\mu(r) = \frac{C_1}{4\,m_g^2 r^3}\,(1 + m_g r + m_g^2 r^2)\, e^{-m_g r}\,. \tag{2.2.91}$$

[14] We point out that we obtain an additional contribution on the RHS compared to Ref. [74]. As we will set both $\Lambda$ and $\tilde{\Lambda}$ to zero, this does not affect the conclusions.

The orthogonal solution is defined by $\nu_+ \equiv \cos^2\theta\,\nu_1 + \sin^2\theta\,\nu_2$ and $\lambda_+ \equiv \cos^2\theta\,\lambda_1 + \sin^2\theta\,\lambda_2$. Eqs. (2.2.85) and (2.2.86) are solved by

$$\nu_+(r) = -\frac{C_2}{r} + C_3\,, \tag{2.2.92}$$

$$\lambda_+(r) = \frac{C_2}{r}\,. \tag{2.2.93}$$

We are now able to assemble the full solution in the linear regime:[15]

$$\nu_1(r) = -\frac{C_2}{r} + \sin^2\theta\,\frac{C_1}{r}e^{-m_g r} + C_3\,, \tag{2.2.94}$$

$$\lambda_1(r) = \frac{C_2}{r} - \sin^2\theta\,\frac{C_1}{2}\frac{1+m_g r}{r}\,e^{-m_g r}\,, \tag{2.2.95}$$

$$\nu_2(r) = -\frac{C_2}{r} - \cos^2\theta\,\frac{C_1}{r}e^{-m_g r} + C_3\,, \tag{2.2.96}$$

$$\lambda_2(r) = \frac{C_2}{r} + \cos^2\theta\,\frac{C_1}{2}\frac{1+m_g r}{r}\,e^{-m_g r}\,, \tag{2.2.97}$$

$$\mu(r) = \frac{C_1}{4\,m_g^2 r^3}\,(1 + m_g r + m_g^2 r^2)\,e^{-m_g r}\,. \tag{2.2.98}$$

As is apparent from the above solution, we have re-obtained the vDVZ discontinuity in the linear regime. In fact, taking the limit $m_g \to 0$, we see that $\mu(r)$ develops a singularity. Inverting this statement, we recall that the linear approximation is defined by $|\mu(r)| \ll 1$, i.e. when $C_1 \ll m_g^2 r^3$. We will now determine the exact behaviour as well as the radius of the onset of the strong coupling regime.

### Non-linear regime

As Eqs. (2.2.94) – (2.2.98) show, the only function in the large scale solution of the metrics which exhibits problematic behaviour as $m_g \to 0$ is $\mu(r)$. It is therefore suggestive that we only need to extend the non-linear analysis to $\mu$, while keeping $\{\lambda_1, \lambda_2, \nu_1, \nu_2\} \ll 1$. We will in fact see that this is sufficient to recover the correct potential at small scales.

Let us first evaluate the Bianchi identities in the non-linear regime of $\mu$. The only non-trivial equation can be written as [74]

$$\frac{2\,\{r(1+\mu)\}'(\lambda_1 - \lambda_2)}{\{r(1+\mu)\}'\,\nu_1' - \nu_2'} = r\,\frac{(\beta_1 + 2\beta_2 + \beta_3) + 2\mu(\beta_2 + \beta_3) + \mu^2\beta_3}{(\beta_1 + 2\beta_2 + \beta_3) + \mu(\beta_2 + \beta_3)}. \tag{2.2.99}$$

We note that we are able to find an algebraic equation for $\mu(r)$ if we can determine all other functions in the above equation as functions purely of $\mu$. Fortunately, this is in fact possible in the regime we are interested in: assuming $\mu(r)$ to be sizeable at low scales, the EFE, Eqs. (2.2.79), are significantly simplified, as all powers of $\nu_1, \nu_2, \lambda_1$ and $\lambda_2$ can be dropped in the interaction terms $B_{\mu\nu}$, $\tilde{B}_{\mu\nu}$. The equation $G_{tt} = -B_{tt} + \rho/{M_g}^2$ can be readily integrated, and we obtain the solution

$$\lambda_1 = \frac{r_S}{r} + m^2\sin^2\theta\,r^2\mu\left\{(\beta_1 + 2\beta_2 + \beta_3) + \mu(\beta_2 + \beta_3) + \mu^2\frac{\beta_3}{3}\right\} \tag{2.2.100}$$

outside of the mass distribution $\rho$. The Schwarzschild radius $r_S$ has been defined in the conventional way, where $r_S = M/(4\pi M_g^2) = 2\,M\,G_N$ with $M$ the total mass. In a similar fashion, we find from $G_{rr} = -B_{rr}$ that

$$\nu_1' = \frac{r_S}{r^2} + m^2\sin^2\theta\,r\,\mu\left\{-(\beta_1 + 2\beta_2 + \beta_3) + \mu^2\frac{\beta_3}{3}\right\}, \tag{2.2.101}$$

[15] Note that this solution is not exactly the result we have anticipated in Sec. 2.2.3. The corresponding expression is obtained in Massive Gravity rather than bigravity, and the ansatz (2.2.84) needs to be modified by dropping $\nu_2$ and $\lambda_2$ such that $\nu_1 = \sin^2\theta\,\nu_-$; one may then choose $C_1 = -\frac{4}{3}r_S$ to find an exact matching with Eq. (2.2.12) [72].

and from $\tilde{G}_{tt} = -\tilde{B}_{tt}$

$$\lambda_2 = -\frac{m^2\cos^2\theta}{1+\mu}\, r^2\mu\left\{(\beta_1+2\beta_2+\beta_3)+\mu(\beta_1+3\beta_2+2\beta_3)+\mu^2(\frac{\beta_3}{3}+\beta_2+\beta_3)\right\}. \tag{2.2.102}$$

Finally, the equation $\tilde{G}_{rr} = -\tilde{B}_{rr}$ yields

$$\nu_2' = \frac{\{r(1+\mu)\}'}{r(1+\mu)^2}\left[m^2\cos^2\theta\, r^2\,\mu\right]\left\{(\beta_1+2\beta_2+\beta_3)+2\mu(\beta_1+2\beta_2+\beta_3)+\mu^2(\frac{2}{3}\beta_1+2\beta_2+\beta_3)\right\}. \tag{2.2.103}$$

As anticipated, inserting these results into Eq. (2.2.99) gives an *algebraic* equation for $\mu(r)$. It is of seventh order, and the spectrum in general consists of a wide range of possible solutions, several of which allow for physically sound interpretations. For a thorough analysis of the different branches of solutions, we refer to [72] and references therein. Following this analysis, we will examine the non-linear regime by choosing the solution

$$\mu = -\frac{1}{\sqrt{\beta_3}} + \delta\mu, \qquad \text{with } |\delta\mu| \ll 1. \tag{2.2.104}$$

Plugging back into (2.2.100) and (2.2.101), we find[16]

$$\nu_1 = -\frac{r_S}{r} + m^2r^2\sin^2\theta\, r^2\,\frac{3(\beta_1+2\beta_2+\beta_3)-1}{6\sqrt{\beta_3}} \equiv -\frac{r_S}{r} - r^2\frac{\Lambda_{\text{eff}}}{3} \tag{2.2.105}$$

$$\lambda_1 = \frac{r_S}{r} - m^2r^2\sin^2\theta\, r^2\,\frac{(1+3(\beta_1+2\beta_2+\beta_3))\sqrt{\beta_3}-3(\beta_2+\beta_3)}{3\beta_3} \equiv \frac{r_S}{r} + r^2\frac{\Lambda'_{\text{eff}}}{3} \tag{2.2.106}$$

Note that we were able to regroup the constant terms into two effective cosmological constants, a result very similar to the standard Schwarzschild solution of GR. The solutions for $\nu_2$ and $\lambda_2$ can be obtained similarly and are found to be $\mathcal{O}(m^2r^2)$.

We stress that these solutions are only valid in the range where $\mu$ remains sizeable. We are now ready to define the Vainshtein radius $r_V$ as the characteristic length of the transition between the non-linear regime and the linear solution, valid at large $r$. By matching the linear solution, Eqs. (2.2.94) – (2.2.98), to the non-linear solution at $r_V$, we find $C_1 \sim m^2r_V^3 = r_S$ as well as $C_2 \sim r_S$. The Vainshtein radius is therefore set to

$$r_V \equiv \left(\frac{r_S}{m^2}\right)^{1/3}. \tag{2.2.107}$$

**Discussion**

By examining the field equations of bigravity in a spherically symmetric configuration, we have found that there indeed exist solutions which offer a split phenomenology. For the metric coupling to matter, we find a gravitational potential which features the effects of the additional degrees of freedom (compared to GR) at large distances, given by Eq. (2.2.94); at short scales $r \ll r_V$, we have the complementary solution

$$2\,\Phi(r) = \nu_1 = -\frac{r_S}{r} - r^2\frac{\Lambda_{\text{eff}}}{3}. \tag{2.2.108}$$

This concludes the resolution of the vDVZ discontinuity, as evidently, bigravity is able to mimic the effects of GR at small scales.[17] Notice that we have obtained a correction term which acts like a cosmological constant of size $\mathcal{O}(m^2)$. The two sectors of $g$ and $\tilde{g}$ decouple when taking $m \to 0$,

[16] The results of [72] are reproduced with the parametrisation $\beta_1+2\beta_2+\beta_3 \mapsto 1$, $\beta_2+\beta_3 \mapsto -\alpha$ and $\beta_3 \mapsto \beta$.
[17] This is equally true for Massive Gravity, see [72].

upon which we recover two fully independent diffeomorphism symmetries. We therefore expect $m$ to be a naturally small parameter; this is confirmed by an analysis of the quantum corrections in Ref. [76]. Note also that we obtain an effective cosmological constant in the short distance regime, even if we drop all constant terms in the linear solution. Generalising to solutions with asymptotic dS space, this is precisely the effect of degravitation of the cosmological constant. The astrophysical and cosmological phenomenology of bigravity will be discussed in the following chapters.

## 2.3 Phenomenology of Bimetric Gravity

Having reviewed the setup and consistency of its theoretical framework, we will now discuss the phenomenological implications of bigravity. It introduces several new physical effects, which we are interested in making use of in order to resolve the known gaps in our understanding of cosmology.

Firstly, we readdress the cosmological constant problem. As discussed in the previous section, the short and long distance regimes include different effective vacuum energies. Indeed, by including the contributions of all constant terms, one finds that the large scale solution has a cosmological constant which can be arbitrarily suppressed by taking $\cos\theta \to 0$ [74]. One can therefore bring into agreement that vacuum contributions due to loops and phase transitions do indeed gravitate, and that on the other hand, cosmological surveys require a much smaller vacuum energy. However, the same does not apply within the Vainshtein radius – i.e. the cosmological constant problem can only be solved at large scales. For example, gravity is very well tested within the solar system, which we can fit inside of $r_V$ if we require $m_g < 5 \times 10^{-25}$ eV. But there are also tests of $\Lambda_{\text{eff}}$ within the solar system, which limit $\rho_{\text{vac}} < (13.2 \text{ eV})$ [77]. We conclude that if vacuum energy gravitates, there must be an additional or entirely different mechanism at play. Bimetric gravity or dRGT theory in the form presented here cannot solve the 'old' cosmological constant problem.

Setting aside this drawback, bigravity does however achieve the goal of generating an arbitrarily small and radiatively stable contribution to the cosmological constant: it accommodates a dark energy density in the form of the graviton mass. The background cosmology will be studied in more detail in the following sections.

As the next step, and recalling that at the present time, all evidence for DM is purely gravitational, one is motivated to examine the different ranges of the bigravity parameter space for a suitable DM candidate. We briefly summarise these efforts here.

Let us first discuss the scenario where DM consists of the heavy graviton itself. For the case of a very heavy spin-2 particle, this has been studied in Refs. [78, 79], where a graviton with $m_g$ of order 1 – 66 TeV is found to allow for a suitable CDM candidate. The massive graviton decays into all known particles with the exception of the massless graviton. The usual bounds on $m_g$ do not apply for such high masses, as no long range force is mediated; due to the size of $m_g$, all Vainshtein radii are extremely small, and corrections to GR are far suppressed.

On the lower end of the DM mass range, theories have been constructed where DM halos consist of a condensate of a large number of light particles. For scalar fields, this class of models is known as Fuzzy cold DM, which has been successfully extended to condensates of massive gravitons within bigravity [80, 81]. Finally, there is also the possibility of a separate matter sector that couples to the reference metric via $\sqrt{-\tilde{g}}\,\mathcal{L}_{\text{DM}}$. Interactions with SM particles occur through the mixing of the metrics through the dRGT potential. This has been studied in Refs. [82, 83].

Unfortunately, there is one unifying factor among these DM proposals: due to their purely gravitational interactions with the SM, they are unanimously hard to detect. However, future developments in astrophysical observations may shed more light on these scenarios.

**Outline of the following chapters**

In the previous discussion, we have assumed that dark energy and DM are problems which still need to be addressed in bigravity – i.e. that the cosmology of bigravity does not deviate too much from ΛCDM. In the following Chapters 3 to 5, we will see how this is the case (in particular, see Sec. 5.3.2 for a discussion of the cosmological history). We will focus on the aspects of bigravity which are testable today.

Chapter 3 focusses on the propagation of linear perturbations of both metrics. To this end, Sec. 3.3.2 discusses a stable cosmological background solution, which is evaluated at late times. On the level of linear perturbations, we encounter an oscillation phenomenon similar to two-flavour neutrino oscillations. These gravitational wave oscillations are then used to set competitive bounds on the bigravity parameter space $(\theta, m_g)$ using data from the first observations of the binary black hole (BBH) mergers.

In Chapter 4, we extend our analysis to a mass range where the spin-2 modes decohere during propagation. This leads to the possibility of echo events, a striking experimental signature which could be observed in current and future GW detectors.

We refer to Chapter 5 for an analysis of the cosmology at early and late times. This section includes an analysis of the concordance model of cosmology and several of its (minor) alternations, which are compared to bigravity cosmology and conformal gravity, a model which will be introduced and discussed in detail. We will compare the predictions of these models to several data sets, and evaluate whether the modified cosmologies improve on the fit of the Hubble function.

# 3 Gravitational wave oscillations in Bigravity

*This chapter is based on Phys. Rev. Lett. 119, 111101 [1], with Moritz Platscher and Juri Smirnov.*

## 3.1 Synopsis

In this chapter, we derive consistent equations for gravitational wave oscillations in bigravity. We review how the propagating modes arise as one massless and one massive linear combination of spin-2 modes. Due to the asymmetric coupling of the two tensors, only one of the two tensors is the physical metric coupling to matter, and thus the basis in which gravitational waves propagate is different from the basis where the wave is produced and detected. Therefore, one should expect – in analogy to neutrino oscillations – to observe an oscillatory behaviour. We show how this behaviour arises explicitly, discuss phenomenological implications and present limits on the graviton parameter space in bigravity.

## 3.2 Introduction

We have introduced the bigravity action in Sec. 2.3 as the non-linear theory of two interacting metrics. Linearising this theory and rotating to the mass basis (see below) shows that the gravitational interactions are mediated by two gravitons, one massless and one massive. Since the two are superposition of the physical and the reference metric, their effective coupling to matter is different and depends on the mixing angle between the metrics. This leads to an oscillation phenomenon, first mentioned in [84] in a theory of massive gravity and [67] in bigravity. In this chapter we will study the propagation of gravitational waves (GW) in this bimetric theory which are produced in the 'flavour basis' at the source, namely only as perturbations of the physical metric. Analysing the wave propagation, we find a close analogy to neutrino oscillations in the wave-packet formalism.

This phenomenon was presented in our study [1] for the first in a consistent approach. Attempts have been previously made in [85, 86], however only in a specific setting, and leading to an unphysical result, in particular it was concluded that one tensor mode exhibits super luminal propagation. We show that in the parameter space we consider physical no such behaviour is found, as one should expect in a healthy theory. The novelty of our work in the bigravity setup is that we consider graviton masses corresponding to length scales which can be probed by astrophysical tests, while the majority of prior works have focused on much smaller graviton masses, i.e. of the order of the Hubble scale today. This approach makes it possible to confront direct detection data of GW signals as seen by the LIGO experiment [87] with the oscillation hypothesis for the first time. The corresponding parameter space of $m_g = 10^{-22} - 10^{-20}$ eV and comparably large mixing angle $\theta$ is studied, in close resemblance to the effects of pure massive gravity.

This chapter is structured as follows. In Sec. 3.3, we discuss the background Friedmann-Lemaître-Robertson-Walker (FLRW)-like cosmology (3.3.2) at late times, a prerequisite to describe the e.o.m. of the linearised perturbations.[18] Next, we present the phenomenon of GW oscillations (3.3.3), and finally study the phenomenological implications (3.3.4). We summarize our findings in Sec. 3.4.

[18] This is necessary, as it is not a priori established that the background solution must appear locally flat for both metric objects.

## 3.3 Gravitational Wave Oscillations

### 3.3.1 Production of GWs

Before moving on to describe the cosmological background and its perturbations, we discuss how the generation of gravitational waves through BBH mergers occurs in this theory. In the allowed graviton mass range, all astrophysical processes such as solar system observations, binary coalescence, and others take place *inside* the Vainshtein sphere; e.g. for the masses involved in the binary black hole (BBH) merger event GW150914, the Vainshtein radius [72] is $r_V \approx 8 \times 10^{11}$ m for $m_g = 10^{-22}\,\mathrm{eV}$, much larger than the interaction distance of the merging BHs ($\sim 100 - 1000\,\mathrm{km}$) and their Schwarzschild radii ($\sim 10 - 100\,\mathrm{km}$). In this sphere the longitudinal graviton mode is strongly coupled and the system behaves as in pure GR. This implies that in a merger event, GWs are produced exactly as in GR, but in bigravity only the linear combination which couples to matter is produced. As in neutrino physics this linear combination is a superposition of two mass eigenstates, which is coherent owing to the Vainshtein mechanism at production.

### 3.3.2 Background cosmology

We proceed to calculate the cosmological implications on a static background, following the approach of [85]. For both $g$ and $\tilde{g}$, we assume as background the FLRW metric with conformal time $\eta$,[19]

$$\begin{aligned} \mathrm{d}s^2 &= a(\eta)^2(-\mathrm{d}\eta^2 + \mathrm{d}\vec{x}^2)\,, \\ \mathrm{d}\tilde{s}^2 &= b(\eta)^2(-\tilde{c}(\eta)^2\,\mathrm{d}\eta^2 + \mathrm{d}\vec{x}^2)\,, \end{aligned} \tag{3.3.1}$$

where $\mathrm{d}\vec{x} = \frac{\mathrm{d}r^2}{1-kr^2} + r^2(\mathrm{d}\vartheta^2 + \sin^2\vartheta\mathrm{d}\phi^2)$. The function $\tilde{c}(\eta)$ determines the light cone for the second metric and will play a role for the propagation speed of the massive gravitational wave excitations.

Plugging this ansatz into Eqs. (5.3.10) and omitting explicit dependencies yields the cosmic evolution equations,

$$\frac{3}{a^2}\left(H^2 + k\right) = \Lambda(y) + \frac{\rho(\eta)}{M_g^2}, \tag{3.3.2a}$$

$$\frac{3}{b^2}\left(J^2/\tilde{c}^2 + k\right) = \frac{\tilde{\rho}(y)}{M_{\tilde{g}}^2}, \tag{3.3.2b}$$

where

$$\Lambda(y) \equiv m^2 \sin^2\theta\left[\beta_0 + 3\beta_1 y + 3\beta_2 y^2 + \beta_3 y^3\right], \tag{3.3.3}$$

$$\tilde{\rho}(y) \equiv M_{\tilde{g}}^2 m^2 \cos^2\theta\left[\beta_1 y^{-3} + 3\beta_2 y^{-2} + 3\beta_3 y^{-1} + \beta_4\right]. \tag{3.3.4}$$

Here, a prime denotes a derivative by $\eta$, $y = b/a$, and $H = a'/a$ as well as $J = b'/b$ are the Hubble parameters for both metrics in conformal time.

Moreover, Eqs. (2.2.82) imply that $\rho'(\eta) = -3H(1+\omega)\rho(\eta)$ and

$$(\tilde{c}H - J)\underbrace{\left[\beta_1 y + 2\beta_2 y^2 + \beta_3 y^3\right]}_{\equiv\Gamma(y)} = 0, \tag{3.3.5}$$

for a perfect fluid with equation of state $P = \omega\rho$. It has been shown that only the vanishing of the round brackets yields a physically meaningful solution, as in the other case the graviton mass turns out to be zero. Thus, the missing degree of freedom will re-enter only at the non-perturbative level in the form of a ghost [65]. Thus, we find $J(\eta) = \tilde{c}(\eta)H(\eta)$.

[19] The reference metric $\tilde{g}$ could, in principle, contain an off-diagonal term $D(\eta)\,\mathrm{d}r\,\mathrm{d}\eta$; however, explicit calculations show that physically meaningful solutions always imply $D = 0$. [66] Thus, we disregard such a term altogether.

Using this result, we can derive an algebraic equation for $y$, by subtracting Eq. (3.3.2a) from Eq. (3.3.2b),

$$\begin{aligned}\beta_1 \cos^2\theta y^{-1} + (3\beta_2\cos^2\theta - \beta_0\sin^2\theta) + \\ +(3\beta_3\cos^2\theta - 3\beta_1\sin^2\theta)y + \\ +(\beta_4\cos^2\theta - 3\beta_2\sin^2\theta)y^2 - \beta_3\sin^2\theta y^3 = \frac{\rho}{M_g^2 m^2}.\end{aligned} \tag{3.3.6}$$

By assumption, $\rho$ is the density of a perfect fluid with $\omega \geq -1$, which behaves as [65]

$$\rho(\eta) = \rho_0 \begin{cases} 1 & \text{if } \omega = -1, \\ \left(\frac{a(\eta)}{a(\eta_0)}\right)^{-3(1+\omega)} & \text{if } \omega > -1, \end{cases} \tag{3.3.7}$$

such that any fluid of type $\omega > -1$ is diluted, i.e. $\rho \to 0$ for $\eta \to \infty$. It is in fact sufficient to consider such densities, since any CC type of energy density may be included in the interaction terms of the bigravity theory.

In this limit, we denote the solution of Eq. (3.3.6) as $y_*$. An exact expression is in principle feasible, however not very enlightening. Therefore, and since we are interested in late times, we linearise Eq. (3.3.6) around $y_*$ and obtain for $y = y_* + \delta y$,

$$\delta y(\eta) = -\frac{\rho(\eta)}{3m^2M_g^2}\frac{y_*^3}{\Gamma_*(\cos^2\theta + y_*^2\sin^2\theta) - 2\frac{\tilde{\rho}_* y_*^4}{3m^2M_g^2}}, \tag{3.3.8}$$

with the short-hand notation $\Gamma_* = \Gamma(y_*)$ and $\tilde{\rho}_* = \tilde{\rho}(y_*)$.

This manipulation allows us to rewrite Eq. (3.3.2a) as

$$a(\eta)^{-2}(H(\eta)^2 + k) = \frac{1}{3}\Lambda_* + \frac{\rho(\eta)}{3M_{\rm Pl}^2} \tag{3.3.9}$$

with the physical CC $\Lambda_* = \Lambda(y_*)$ and Planck mass,

$$M_{\rm Pl}^2 = M_g^2\frac{\cos^2\theta + y_*^2\sin^2\theta - \frac{2\tilde{\rho}_* y_*^4}{3m^2M_g^2\Gamma_*}}{\cos^2\theta - \frac{2\tilde{\rho}_* y_*^4}{3m^2M_g^2\Gamma_*}}, \tag{3.3.10}$$

which approaches $M_g^2\left(1 + y_*^2\tan^2\theta\right)$, as $\tilde{\rho}_* \to 0$, in agreement with [85, 86].

Finally, we may use that $y' = \left(\frac{b}{a}\right)' = y(J - H)$ and $J = \tilde{c}\,H$ to find that,

$$\begin{aligned}\tilde{c}(\eta) =& 1 + \frac{y'}{yH} \simeq 1 + \frac{\delta y'}{y_* H} \\ \simeq& 1 - (1+\omega)\frac{\rho(\eta)}{m^2\Gamma_* M_{\rm Pl}^2}\frac{y_*^2}{\frac{2\tilde{\rho}_* y_*^4}{3m^2M_g^2\Gamma_*} - \cos^2\theta}.\end{aligned} \tag{3.3.11}$$

Note that $\tilde{c}$ can be both larger or less than 1, depending on the choice of the parameters $\beta_i$. However, $\tilde{c} > 1$ would introduce GWs propagating with a speed larger than the speed of light and thus we disregard the parameter region leading to this behaviour.

As evident from Eq. (3.3.11), we can take $\tilde{c} = 1$ to a good approximation. This motivates the limit where $y$ takes the constant value $y_*$, which we apply in the following.

### 3.3.3 Linear perturbations

We perturb both metrics about an FLRW-like background with conformal time $\eta$, [65, 66]

$$\begin{aligned} \mathrm{d}s^2 &\equiv g_{\mu\nu}\mathrm{d}x^\mu \mathrm{d}x^\nu = a(\eta)^2(-\mathrm{d}\eta^2 + \mathrm{d}\vec{x}^2)\,, \\ \mathrm{d}\tilde{s}^2 &\equiv \tilde{g}_{\mu\nu}\mathrm{d}x^\mu \mathrm{d}x^\nu = b(\eta)^2(-\tilde{c}(\eta)^2\,\mathrm{d}\eta^2 + \mathrm{d}\vec{x}^2)\,, \end{aligned} \tag{3.3.12}$$

by splitting the tensors into the background and a (small) perturbation, [88]

$$\begin{aligned} g_{\mu\nu} &= a^2(\eta)\left(\eta_{\mu\nu} + \frac{h_{\mu\nu}(x,\eta)}{M_g}\right), \\ \tilde{g}_{\mu\nu} &= b^2(\eta)\left(\eta_{\mu\nu} + \frac{\tilde{h}_{\mu\nu}(x,\eta)}{M_{\tilde{g}}}\right). \end{aligned} \tag{3.3.13}$$

We now choose a transverse traceless gauge for both metrics,[20] which leaves two helicity-2 excitations for each metric.[21] The calculation is furthermore simplified by noting that $a(\eta) = \frac{1}{1+z} = 1 + \mathcal{O}(.1) \approx$ const for the distances of interest, e.g. of the event GW150914 with $z \approx 0.09$. The potential in (2.2.78), to quadratic order, reads

$$S^{(2)}_{\mathrm{Bi}} \supset \int d^4x \frac{m^2 M_{\mathrm{eff}}^2}{8} a^4\, y_* \Gamma_* \Big(\frac{\tilde{h}_{\mu\nu}}{M_{\tilde{g}}} - \frac{h_{\mu\nu}}{M_g}\Big)^2 \tag{3.3.14}$$

where we have defined $\Gamma_* \equiv (\beta_1 + 2y_*\beta_2 + y_*^2\beta_3)$, which is exactly the combination of parameters which arises in the cosmological solution within bigravity [1, 65, 66]. By recalling that we define $\sin\theta \equiv \frac{M_{\mathrm{eff}}}{M_g}$, we are able to absorb the constant value of $y_*$ into a redefinition of $\theta$.

The equations of motion of linearised bigravity in transverse traceless gauge are derived from Eq. (3.3.14) [88],

$$h'' + k^2 h + \frac{m^2}{2}\Gamma_* a^4 \sin\theta\Big(\sin\theta\, h - \cos\theta\, \tilde{h}\Big) = 0\,, \tag{3.3.15a}$$

$$\tilde{h}'' + k^2 \tilde{h} + \frac{m^2}{2}\Gamma_* a^4 \cos\theta\Big(\cos\theta\, \tilde{h} - \sin\theta\, h\Big) = 0\,, \tag{3.3.15b}$$

where the polarisation index $h_{\times,+}$ has been omitted, and $k = |\vec{k}|$ denotes the three-momentum. We diagonalise the equations of motion with the field redefinition[22]

$$\begin{pmatrix} h_1 \\ h_2 \end{pmatrix} \equiv \begin{pmatrix} \cos\theta & \sin\theta \\ -\sin\theta & \cos\theta \end{pmatrix} \begin{pmatrix} h \\ \tilde{h} \end{pmatrix} \tag{3.3.16}$$

which yields the equations of motion in the mass basis,

$$h_1'' + k^2 h_1 = 0\,, \tag{3.3.17a}$$

$$h_2'' + k^2 h_2 + a^4 \frac{m_g^2}{2} h_2 = 0\,, \tag{3.3.17b}$$

where we have defined the physical graviton mass $m_g^2 = m^2\,\Gamma_*$. By inverting (3.3.16), we obtain the composition of eigenstates of matter basis gravitons in terms of the mass eigenstates,

$$h(k,t) = \cos\theta\, h_1 - \sin\theta\, h_2\,, \tag{3.3.18a}$$

$$\tilde{h}(k,t) = \sin\theta\, h_1 + \cos\theta\, h_2\,. \tag{3.3.18b}$$

[20] In fact, the transverse traceless condition is always satisfied for the purely massive mode, since it is a gauge invariant quantity. [89]

[21] We can ignore the helicity-1 modes (as they do not couple to the energy-momentum tensor) and scalar modes (which are screened due to the Vainshtein effect [32]).

[22] Note that the redefinition is a simple rotation because the fields $h, \tilde{h}$ have been normalised canonically, different to Refs. [1, 66].

We observe that Eqs. (3.3.17) correctly comprise one massless and one massive propagating tensor perturbation. Approximating the scale factor by $a = 1$, we can solve these equations and rotate back to the physical basis,

$$h(t,k) = \cos^2\theta\, \exp\left(ikt\right) + \sin^2\theta\, \exp\left(i\sqrt{k^2+m_g^2}\, t\right), \tag{3.3.19a}$$

$$\tilde{h}(t,k) = \sin\theta\, \cos\theta \left[\exp\left(ikt\right) - \exp\left(i\sqrt{k^2+m_g^2}\, t\right)\right], \tag{3.3.19b}$$

where he have normalised s.t. $h(0,k) = 1$ and $\tilde{h}(0,k) = 0$, and $\eta$ has been replaced by cosmic time $t$ as per $a = 1$.

Since the graviton mass is restricted to be much smaller than the typical wave number $k$, we may expand $\sqrt{k^2+m_g^2} \simeq k\left[1 + m_g^2/(2k^2)\right] \equiv \omega_0 + \delta\omega$. We see that the function in Eq. (3.3.19a) is minimized when the second cosine acquires a total phase shift of $\delta\omega\, T_*\, \pi$, and thus,

$$T_*(\omega_0) = \frac{2\pi\,\omega_0}{m_g^2}\,, \tag{3.3.20}$$

which coincides with the expression for the oscillation length for neutrinos, confirming our naïve expectation.

In order to make a quantitative statement about the modulation of the strain observed in GW observations, we average this expression over a timescale $T$, which is bigger than the period of one massless mode's inverse frequency, $T_0 = \frac{2\pi}{\omega_0}$, but much smaller than the period of the modulation induced by the mass term, $T_* = \frac{\pi}{\delta\omega}$. Squaring the strain, we find the envelope function

$$\left\langle h^2(t,k)\right\rangle_{T_0 \ll T \ll T_*} = \cos^4\theta\left[1 + 2\,\tan^2\theta\,\cos(\delta\omega\, T) + \tan^4\theta\right], \tag{3.3.21}$$

where the normalization is determined by the condition $\left\langle h^2(t,k)\right\rangle\big|_{T=0} = 1$, i.e. initially a pure perturbation of the physical metric has been excited.

Finally, we aim to express the strain in terms of the cosmic redshift $z$, which is defined as $1 + z = a(t_0)/a(t)$. For a universe dominated by a CC, we find that $H = \text{const.}$ and $a(t) = e^{Ht}$. We therefore express the time as,[23]

$$t = -\frac{1}{H}\log(1+z). \tag{3.3.22}$$

In summary, the squared amplitude of the GW signal in bigravity is modulated as

$$\left\langle h^2(t,k)\right\rangle_{T_0 \ll T \ll T_*} = \cos^4\theta\left[1 + \tan^4\theta + 2\tan^2\theta\,\cos\left(\frac{\delta\omega}{H}\,\log(1+z)\right)\right]. \tag{3.3.23}$$

At this point, we would like to point out that the phenomenon has previously been studied in [85, 86], where the authors find a modulation that is proportional to $\tilde{c}-1$. As we will outline in the following, this is not the leading effect in our analysis, where oscillations occur also in flat space. Furthermore, we find that the phenomenon leads to a reduction of the amplitude compared to GR, as expected from neutrino oscillations. Both are physically sensible outcomes.

[23] Note that we have reinstated $a(t) \neq \text{const.}$ in conflict with the condition $a = 1$ used in the analytic derivation of Eq. (3.3.21). Thus Eq. (3.3.23) is only a valid approximation for small $z$.

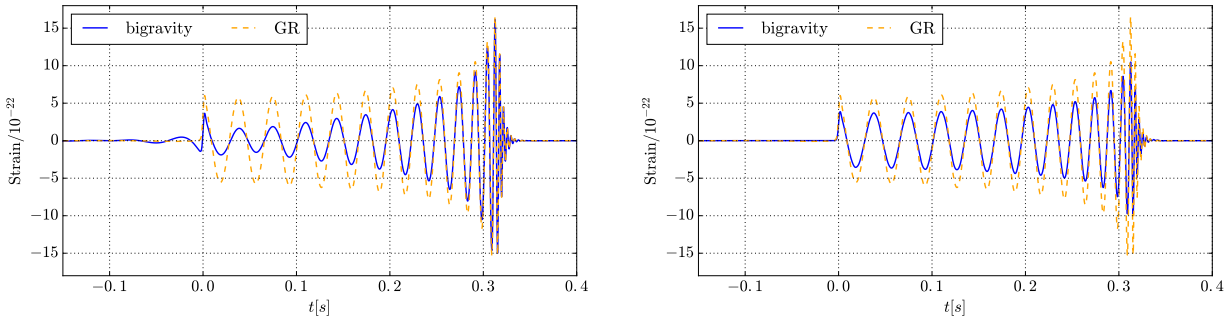


**(a)** $m_g = 10^{-22}\,\mathrm{eV}$ **(b)** $m_g = 10^{-19}\,\mathrm{eV}$

**Figure 3.1:** Bigravity vs. GR: simulated strain in the detector due to gravitational waves as emitted by the black hole merger event GW150914, as observed by LIGO. The dashed orange curve shows the results in GR, while the solid blue curve is obtained by multiplying with the frequency-dependent modulation due to bigravity. Note the constant suppression in panel (b).

### 3.3.4 Phenomenology

Given that we have reached a quantitative understanding of GW oscillations in terms of the modulation (3.3.23), we now ask whether this effect is visible in realistic scenarios. To this end, we have made use of the available data for the events GW150914 [90] and GW151226 [91] obtained by means of numerical simulations [92–103]. This yields the strain as it would be observed in a detector on Earth. We then modulate the strain according to Eq. (3.3.23). Two such examples for GW150914 are shown in Fig. 3.1, where the parameters are chosen such that one obtains a maximally visible effect, i.e. $\theta = \pi/4$. One observes that a graviton mass of $m_g = 10^{-22}\,\mathrm{eV}$ strongly changes the shape of the signal, where the modulation is at first strongly suppressing the amplitude and then gradually approaching the GR amplitude towards the typical merger peak, commonly referred to as *chirp*. On the other hand, a larger graviton mass $m_g = 10^{-19}\,\mathrm{eV}$ leads to a global suppression of the amplitude by a constant factor. This effect is similar to the decoherence of oscillating neutrino wave packets and we will now briefly discuss this effect.

The massive and the massless modes propagate in wave packets with different group velocities $v_g = \frac{\partial\omega}{\partial k}$. As for very light, relativistic neutrinos, the difference of group velocities is approximately given by $\Delta v_g \simeq \frac{m_g^2}{2E^2}$. The wave packets will de-cohere, i.e. interference will be absent and the frequency dependence of the suppression is lost in favour of a constant reduction, once the time of propagation exceeds $T_{\mathrm{coh}} = L_{\mathrm{coh}}/c$, given by [104]

$$T_{\mathrm{coh}}\,\Delta v_g \sim \sigma_x\,, \tag{3.3.24}$$

where $\sigma_x$ is the spatial/temporal width of the wave packet. Since its determination would involve an exact solution of the full set of Einstein equations for the system, it will be practically impossible to obtain $\sigma_x$. However, from the shape of the signal, we estimate that $\sigma_x \sim 0.1\,\mathrm{s}$. Therefore, we find that for $E/\hbar \sim 100\,\mathrm{Hz}$,

$$L_{\mathrm{coh}} \sim 0.1\,\mathrm{s}\,\frac{2E^2}{m_g^2} = \left(\frac{10^{-21}\,\mathrm{eV}}{m_g}\right)^2 \mathrm{Gpc}\,. \tag{3.3.25}$$

This rather heuristic argument is nevertheless in good agreement with Fig. 3.2, where for $m_g = 10^{-22}\,\mathrm{eV}$ no averaging is observable at distances of the order 100 Mpc, while for $m_g = 5\cdot 10^{-22}\,\mathrm{eV}$, or even $m_g = 10^{-19}\,\mathrm{eV}$, the amplitude levels out for distances below the Gpc scale.

Once the distance increases beyond the scale set by $L_{\mathrm{coh}}$, the strain suppression relative to the

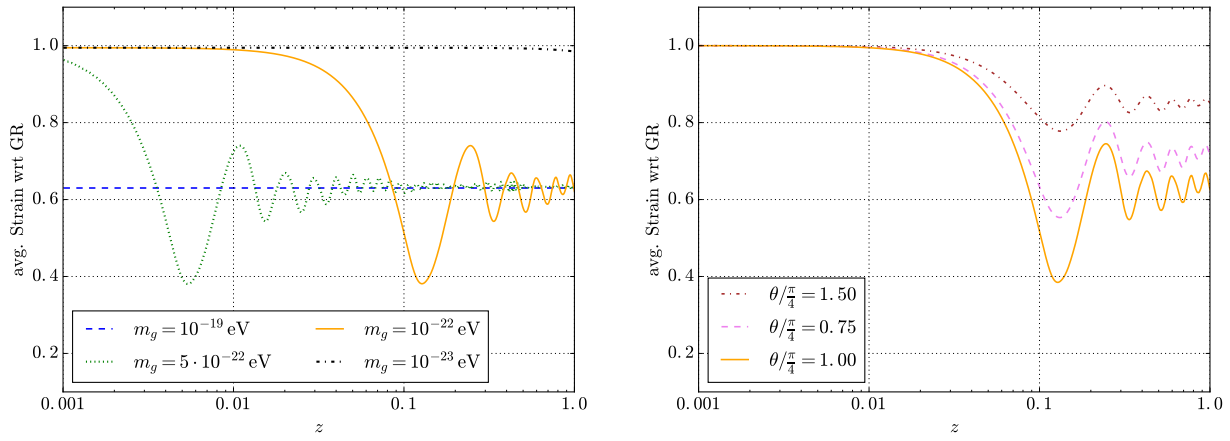


**(a)** Variable $m_g$ for $\theta = \frac{\pi}{4}$.

**(b)** Variable $\theta$ for $m_g = 10^{-22}$ eV.

**Figure 3.2:** Average suppression of a GW150914-like strain as a function of the redshift for different sets of the parameters $m_g$ and $\theta$. Note that, in the left panel, for large $m_g$ and redshift the suppression levels out at $\sim 64\%$ as discussed in the main text. The right panel illustrates that the mixing angle $\theta$ determines the average level of reduction of the strain relative to GR at large distances.

prediction of General Relativity caused by oscillations levels out. E.g. for $\theta = \pi/4$ we find

$$\langle h(t,k)\rangle_{T\gg T_{\rm coh}} = \left\langle \sqrt{\frac{1}{2}\left[1+\cos\left(\delta\omega\, t\right)\right]} \right\rangle_{T\gg T_{\rm coh}} = \frac{2}{\pi}, \tag{3.3.26}$$

which predicts a suppression factor constant in frequency and distance of about 64 % at large redshifts, which is clearly confirmed in Fig. 3.2.

Note that higher graviton masses lead to shorter length scales before the amplitude averages out, in complete analogy to neutrino oscillations. In practice, such a frequency-independent suppression is indistinguishable from ordinary GW of General Relativity and would be interpreted as a larger redshift, i.e. one would generally *overestimate* the redshift on such BBH merger events. If a larger set of events becomes available, this can be used to constrain the larger-graviton mass regime by comparing expected distribution of BBH systems with the observed event rates.

For the low-mass regime, we can constrain the parameters of the model by demanding that the waveform be in agreement with the error bars of the observed events. We have used a simple $\chi^2$-analysis to obtain Fig. 3.3. This categorizes the effect of bigravity into three classes. For very small $m_g$, or $\theta \approx 0$ or $\pi/2$, the suppression vanishes. Alternatively, if the distance lies beyond the scale of coherence, $L_{\rm coh}$, the suppression is constant in frequency and any event is indistinguishable from an equivalent event within pure GR at larger $z$. From the remaining events, where the waveform of the bigravity-suppressed strain is clearly distinguishable from the GR strain, we draw our conclusions on the excluded parameter space. From Fig. 3.3 we find that, first of all, the event GW150914 gives stronger constraints than the second event GW151226. But even with only one observation, we find that for large enough mixing angles we may exclude values of $m_g \gtrsim 10^{-22}$ eV, comparable to the bounds set by GW150914 via a modified dispersion relation [87]. Note that the bounds from the dispersion relation are derived in pure massive gravity and have to be compared to our framework setting $\theta = \pi/2$. We have adopted this bound, which reads $7.2 \cdot 10^{-23}$ eV [105], to the present case by multiplying the mass with a factor $\sin\theta$ to account for the bigravity modification of the classical Newtonian potential, see e.g. [74]. We find that GW oscillations give stronger constraints for smaller mixing angles, where the bound from local gravity tests quickly becomes weaker.[24] We conclude

[24]The bound is derived from the modified Newtonian potential and only applies up to $m_g \approx 10^{-3}$ eV, as for larger

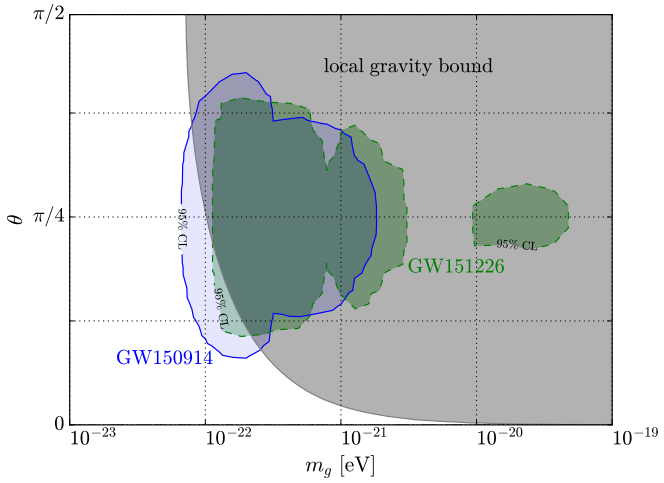


**Figure 3.3:** Excluded parameter space due to a simplified wave form analysis as discussed in the main text. Note that massive gravity is recovered for $\theta = \pi/2$, from which we apply model independent mass bounds.

that with more events available and higher precision, GW oscillations offer excellent prospects to probe the bigravity parameter space.

## 3.4 Conclusions

We have studied the oscillatory behaviour of gravitational waves in the framework of bigravity, where one massive and one massless mode propagate. In full analogy to neutrino oscillations, we have seen that a non-diagonal coupling of the two modes to matter gives rise to potentially significant modulations of the strain that would be observable e.g. in the LIGO or LISA detectors. Using the first ever detected gravitational wave signals GW150914 and GW151226, we illustrated that the bigravity modification of General Relativity can lead to drastic modulations of the strain compared to the predictions of Einstein gravity. Using this, we have constrained the parameter space of the model in the low-mass regime, and pointed out that, once more events are available, the high-mass regime can be constrained, too.

In the derivation presented here, we have made several approximations and assumptions in order to be able to give compact analytic expressions that allow the reader to understand the mechanisms behind gravitational wave oscillations. Nevertheless, the fully general results are straightforwardly obtained by following our approach such that future analyses may directly use the results of this work.

masses the graviton can be integrated out and comprises just a new spin two field weakly coupled to matter.

# 4 Decoherence of Gravitational Wave Oscillations in Bigravity

*This chapter is based on Phys. Rev. D97 (2018) no. 6, 064009 [2], with Moritz Platscher and Juri Smirnov.*

## 4.1 Synopsis

Following up on the study presented in Chapter 3, we consider the regime of graviton masses and gravitational wave propagation distances at which decoherence of the wave packets plays a major role for phenomenology. This regime is of particular interest, as it can lead to very striking phenomena of echo events in the gravitational waves coming from coalescence events. The power of the experimental search in this case lies in the fact that it becomes sensitive to a large range of graviton masses, while not relying on a specific production mechanism. We are thus able to place new relevant limits on the parameter space of the graviton mixing angle.

## 4.2 Introduction

When a GW propagates through space, the effect discussed in Chapter 3 takes place while the waves are still coherent: as long as the condition $d_L \approx L_{\rm coh}$ is satisfied [where $d_L$ is the luminosity distance and the coherence length $L_{\rm coh}$ is defined in Eq. (4.3.1)], the oscillation can have a detectable effect on the GW signal shape and thus is distinguishable from GR. For the details of the modified shape analysis, we refer to Chapter 3. If, however, $d_L > L_{\rm coh}$, the wave packets decohere, i.e. the spatial distance between the propagating mass eigenstates is larger than the sizes of the corresponding wave packets. Consequently, a GW detector sees only an overall reduction of the strain compared to GR, and a second signal may appear. This effect is the main purpose of this work: We discuss how it can be used to falsify or verify the existence of GW oscillations on the basis of a (large) number of BBH merger observations.

With current observations, we show that we are able to probe the parameter range $m_g \gtrsim 10^{-22}\,\text{eV}$ and small mixing angle. For a comprehensive reference of graviton mass studies, see [105]. Therein, the most stringent model-independent bound is $m_{\rm bound} \leq 7.2 \times 10^{-23}\,\text{eV}$, found from solar system tests. Note however that this probes only the pure massive gravity case, i.e. bigravity with $\theta = \pi/2$.

This chapter is structured as follows. In Sec. 4.3, we give a summary of the decoherence regime of propagating GWs in bigravity. A detailed discussion of the observable effects is given in Sec. 4.4, where we analyse the modified BBH merger rate and possible echo signals. We summarise our results in Sec. 4.5 and put them into perspective with complementary studies.

## 4.3 Decoherence of Gravitational waves

Assuming the GW waveform can be modelled as a wave packet, it is sufficient to know the plane wave solution to the equations of motion; the travelling wave packets are then superpositions of plane waves. The GWs are generated via the coupling of $h$ to matter, and subsequently propagate as the mass eigenstates $h_1$ and $h_2$. These will decohere if the flight length exceeds the coherence

length

$$L_{\rm coh} \approx 0.1\,{\rm s}\,\frac{2E^2}{m_g^2} = \left(\frac{10^{-21}\,{\rm eV}}{m_g}\right)^2 {\rm Gpc}\,, \tag{4.3.1}$$

e.g. for a plane wave of $E = 25$ hz and distance 100 Mpc, if the mass exceeds $m_g \gtrsim 6 \times 10^{-22}$ eV. We recall the plane wave solutions of (3.3.19),

$$h_1(k,t) \propto \exp(k\,t)\,, \tag{4.3.2a}$$

$$h_2(k,t) \propto \exp\left(\sqrt{k^2+m_g^2}\,t\right) \approx \exp\left(\left[k+\frac{m_g^2}{2k}\right]t\right), \tag{4.3.2b}$$

where the massive mode propagates as two superimposed oscillations, the plane wave frequency $\omega_0 \equiv k$ and the modulation frequency $\delta\omega \equiv \frac{m_g^2}{2k}$, valid if $\omega_0 \gg \delta\omega$. By means of Eq. (3.3.18), we can now go back to the matter coupling basis and study oscillations, as was done in Sec. 3.3.4. However, we now pursue a different path: we are now interested in the regime where $L \gg L_{\rm coh}$.

In the decoherent regime, these two waves propagate completely independently. The detector response is determined by their overlap with the physical metric, given by (3.3.18):

$$h_a(k,t) = \cos^2\theta\,\cos(kt)\,, \tag{4.3.3a}$$

$$h_b(k,t) = \sin^2\theta\,\cos\left((k+\frac{m_g^2}{2k})\,t\right), \tag{4.3.3b}$$

where we have normalised such that $h(k,0) = 1$ ($h'(k,0) = 0$) and $\tilde{h}(k,0) = 0$. We stress that $h_a$ and $h_b$ are two independent perturbations of the physical metric $g_{\mu\nu}$. We average out the fast oscillations by integrating over their period $T_0 = 2\pi/k$ and obtain the suppression factors of the decohered graviton wave packets:

$$\langle h_a\rangle = \cos^2\theta\,, \qquad \langle h_b\rangle = \sin^2\theta\,. \tag{4.3.4}$$

Note that this is different to the case discussed in Chapter 3, where the interference between $h_1$ and $h_2$ causes a time-dependent modulation of the amplitude.

The results of this section are the suppression factors Eq. (4.3.4) of a GW wave packet. This is only valid in the parameter region where the GWs decohere, i.e., when the luminosity distance of the event exceeds the coherence length Eq. (4.3.1) for all frequency modes. If the mixing angle $\theta$ is non-zero (which recovers GR) and not equal to $\pi/2$ (corresponding to pure massive gravity), a detector of GWs will see two events of approximately the same waveform separated in time, but with their amplitudes rescaled according to Eq. (4.3.4). Note that the waveform corresponding to the massive mode obeys a frequency dependent dispersion in time.

This allows us to probe the parameter space of bigravity where one has a larger mass $m_g$ than relevant for GW oscillations, and small angle $\theta$. This is the subject of the following section.

## 4.4 Phenomenology and results

In current GW detection measurements (such as those of the LIGO/Virgo network), the luminosity distance,

$$d_L(z) = c\,(1+z)\int H(z')^{-1}{\rm d}z'\,, \tag{4.4.1}$$

of a BBH merger event is inferred solely from the amplitude of the strain, as it scales as $h \propto 1/d_L$ [106]. In the decoherence regime of bigravity, the strain will suffer a frequency-independent suppression with respect to GR. Without any other means to measure the distance, an event at actual redshift $z$ will therefore be misinterpreted (assuming GR as the base model) to stem from

an observed redshift $z_{\rm obs}$, with $z_{\rm obs} > z$. Additionally, the secondary gravitational wave with rescaled amplitude could be seen. We assume in the following the physical graviton to be composed mostly of the massless mode, i.e. small $\theta$; this means that the wave corresponding to the massless graviton arrives with $z_{\rm obs}^{m=0} \gtrsim z$; the subsequent strain of the massive graviton will be interpreted as $z_{\rm obs}^{m\neq 0} > z_{\rm obs}^{m=0}$. If measurements are sensitive to both signals, one can look for echoed signals arriving shortly after the primary GW signal. Otherwise, a reduction and/or enhancement of the merger rates is expected, i.e. when one signal isn't seen or both are seen but interpreted as independent events. We will now discuss the two possible interpretations of decoherence in more detail.

**Interpretation as independent events** Let us first take the point of view that the second event is not identified to originate from the same source, or is not seen at all. In this case we will observe a different merger rate than expected in pure GR. Our procedure to quantify this statement is as follows.

First, we must express the number of events per year expected at a given redshift. Following Ref. [107], we define the differential BBH merger rate

$$\frac{dN}{dz} = 4\pi\, R\, \chi(z)^2 (1+z)^{(R_b-1)} \frac{c}{H(z)}\,, \tag{4.4.2}$$

where $\chi(z)$ is the comoving distance, $R_b$ parametrises the redshift-dependence of the merger rate, apart from the expansion of the Universe, and $R$ is the (constant) BBH merger rate density. The above reference finds a best-fit point near $R_b = 2$, which we will assume in the following. Note that the fit cannot accommodate redshifts $z \gtrsim 10$. [107]

The rate density of BBH mergers can be estimated from the events observed by LIGO/Virgo during the O1 run [108] to be $R = 55^{+103}_{-41}\,(\mathrm{Gpc}^3\ \mathrm{yr})^{-1}$. We expect the rather large errors of this number to decrease significantly in the near future, as LIGO/Virgo collect more data; in [107], it is shown that the merger rate may improve up to $< 10\%$ accuracy within a few years of advanced LIGO measurements at design sensitivity.

Using Eq. (4.4.2) we estimate the rate of observable events. Recent GW detections have reached distances about $z \approx 0.1$. Taking this as the current experimental sensitivity translates to $20^{+37}_{-15}$ observable events per year. This may increase by a factor $10^3$ once advanced LIGO reaches its design sensitivity up to $z \approx 1$ [109].

Requiring that the luminosity distance exceeds the coherence length Eq. (4.3.1) leads to a lower bound on $m_g$. On the other hand, graviton mass bounds from other observations impose the condition $m_g \sin\theta \leq m_{\rm bound}$, where $m_{\rm bound}$ is obtained e.g. from tests of a modified dispersion relation or modified Newtonian potential of gravity. Combining these bounds, we obtain a minimum distance between BBH merger and observer for decoherence,

$$\begin{aligned} d_L &\gtrsim \frac{2\,\sigma_x\, c\, E^2}{m_{\rm bound}^2} \sin^2\theta \\ &= 1.62\ \mathrm{Gpc} \left(\frac{E}{100\ \mathrm{hz}}\right)^2 \frac{\sigma_x}{0.1\ \mathrm{s}} \left(\frac{7.2\times 10^{-23}\ \mathrm{eV}}{m_{\rm bound}}\right)^2 \sin^2\theta\,. \end{aligned} \tag{4.4.3}$$

Note that this condition is necessary but not sufficient for decoherence to occur. We employ the bound $m_{\rm bound} = 7.2 \times 10^{-23}\,\mathrm{eV}$ from solar system tests [105], which is the most stringent, model-independent bound available.

We now consider a BBH merger event at true redshift $z$. Given the suppression factor for the physical metric $g$, we determine the interpreted redshift $z_{\rm obs}$ by solving the equation

$$\cos^2\theta / d_L(z) = 1/d_L(z_{\rm obs})\,, \tag{4.4.4}$$

which is found from the fact that $h \propto 1/d_L(z)$. In the next step, we calculate the observed merger rate $\frac{\mathrm{d}N}{\mathrm{d}z}\big|_{z=z_{\rm obs}}$ for a given redshift. The results are summarised in Fig. 4.1. Note two important

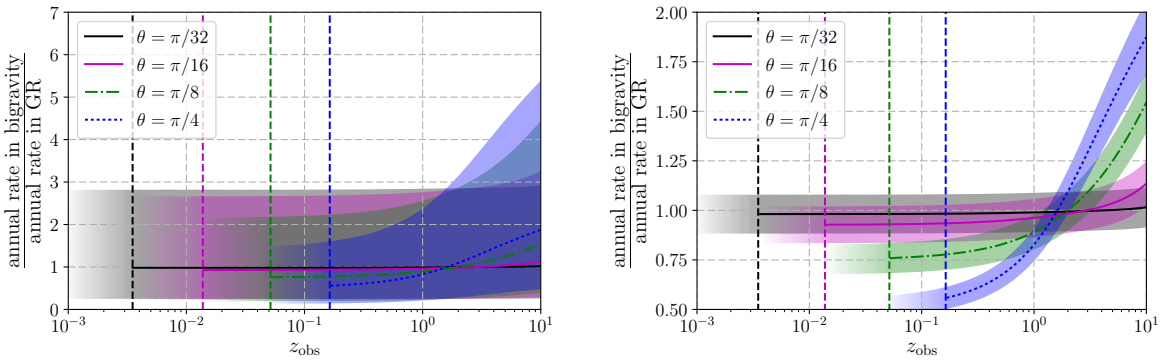


**(a)** Merger rate with current uncertainty

**(b)** Merger rate with projected uncertainty

**Figure 4.1:** *Independent events.* Annual rates of BBH merger events for different observed redshifts $z_{\rm obs}$. Bigravity in the decohered regime shifts the number of events towards higher $z_{\rm obs}$. Rates are normalised to the GR expectation for different mixing angles, based on the BBH merger rate measured to be $R = 55^{+103}_{-41}\,(\mathrm{Gpc}^3\ \mathrm{yr})^{-1}$ and the projected rate with 10% accuracy. [107, 108] The rates are calculated using $m_g = m_{\rm bound} \sin\theta$ with the upper bound $m_{\rm bound} = 7.2 \times 10^{-23}\,\mathrm{eV}$. Coloured regions indicate the errors and the fading the crossing from the coherent regime to decoherence. At present, all values of the mixing angles are consistent with 1, i.e. the GR prediction.

features: first, we have also included the (current and projected) errors on the merger rate density as estimated by LIGO/Virgo. This is indicated by the coloured bands in Fig. 4.1. Secondly, we have included the effect that decoherence requires events to occur at a certain distance/redshift $z_{\rm min}$ which is a function of the mixing angle, cf. Eq. (4.4.3). This is represented by the dashed vertical lines. As it is an order-of-magnitude criterion, the bands fade out below $z_{\rm min}$.

Normalised to the rate predicted in GR, we find that small redshift events are more scarce than in GR (ratio $< 1$), while large redshift events appear to be more abundant (ratio $> 1$). Clearly, the observation of an echoed waveform would be a striking signature for observations, and one would naturally assume the two consecutive detections to be correlated. However, the current analysis equally applies to the low-$z$ range: if the echoed signal is lost in detector noise, one may still observe *too few* events compared to the prediction at lower $z$. In other words, the echo event's observed redshift is simply beyond the detector reach. This is the power of the present approach: we do not require a correlation of two events and/or a measured time difference between them (which would depend on the parameters of the binary system). For a desired sensitivity, a sufficiently large number of events at different redshifts has to be observed, in order to draw conclusions on the merger rate density and thereby on the bigravity parameter space.

In conclusion, no restrictions arise from this analysis at present, since all mixing angles are consistent with the annual merger rate predicted in GR (ratios consistent with 1). However, Fig. 4.1b shows that in the future, with a 10% uncertainty on the merger rate, one can clearly distinguish the cases with large mixing angles $\theta \gtrsim \pi/16$ from the GR predicted merger rate.

**Interpretation as echoed events** If the parameters of bigravity lie in the decoherence regime for astrophysical distances, an initial wave packet of a GW event will split into two waveforms. The waveform corresponding to the massless modes arrives first and is simply the GR waveform rescaled by $\cos^2\theta$. The waveform composed of massive modes is distorted due to the frequency-dependence of the time delay $\Delta t \propto 1/E^2$. The LIGO-Virgo detector network should then see a distinctive signal of two separated events with a time separation of the order of seconds.

The rescaling of the separated wave packets is given by Eq. (4.3.4). Requiring that the secondary

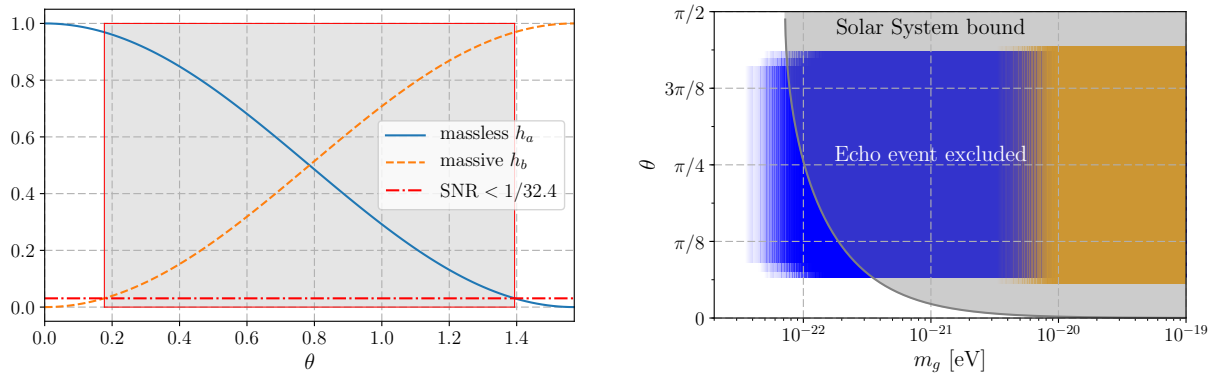


**(a)** Suppression factor and bound from GW170817

**(b)** Summary of echo event constraints

**Figure 4.2:** *Echoed Events. Left*: Suppression factor Eq. (4.3.4) of a travelling GW for varying mixing angle $\theta$ in the decohered parameter regime. Requiring the secondary waveform to be lost in detector noise excludes a large parameter range (shaded area). *Right*: Excluded parameter range for all available GW events published by LIGO/Virgo (blue: black hole mergers, orange: neutron star merger). [106, 110–114] The fading indicates the onset of the decoherence regime ($L_{\text{coh}} < d_L < 10 \times L_{\text{coh}}$). Also shown is the bound $m_g \leq \sin\theta \times 7.2 \times 10^{-23}\,\text{eV}$ from solar system tests [105].

signal (due to the massive mode, if bigravity is mostly massless, or vice versa) is not observed due to the finite signal-to-noise ratio (SNR) of the detectors, we can set a limit on the bigravity mixing angle $\theta$, assuming that $m_g$ is such that the wave packets are fully separated. The highest SNR so far achieved stems from the neutron star merger observation GW170817, with a combined SNR of 32.4. [115] For the mostly-massless scenario, this restricts $\theta \lesssim 0.18 \approx \frac{\pi}{16}$, while for a mostly-massive graviton $\theta \gtrsim 1.39 \approx \frac{7\pi}{16}$ is required, see Fig. 4.2a.

Recall however that the bound only applies if $d_L > L_{\text{coh}}$ is satisfied. Under this constraint, the bounds on the parameter space $(\theta, m_g)$ are summarised in Fig. 4.2b for all GW events observed so far. Once more, the fading indicates the transition into the decoherence regime. We find that even though the most stringent bound on $\theta$ is obtained from the high SNR of GW170817 (orange), the large temporal width $\mathcal{O}(60\,\text{s})$ of this signal requires a large $m_g$ in order for the wave packets to separate sufficiently; the bound is thus overlapped by the local gravity bound. Better results are achieved from the BBH merger observations, which are of shorter durations $\mathcal{O}(1\,\text{s})$ (blue).

Finally, we comment on the search for said echoed signals with LIGO/Virgo. The time separation of the two events is given by (4.3.1), requiring the event separation $\Delta t$ to be of order of the signal width $\sigma_x$. For currently probed distances and graviton masses in the decohered regime which are not excluded by observations, this translates into $\Delta t = \mathcal{O}(0.1 - 1\,\text{s})$.

We thus propose a template search: for every detected GW event, one should investigate the region of a few seconds about the triggering signal and look for an echoed event. The waveform of the secondary strain is fully determined by the triggering waveform and the dispersion relation of massive gravitons. A complete analysis of the modified observational signature is however beyond the reach of this study.

Finally, we wish to point out that such echo signals have recently been proposed in the context of exotic compact objects, which mimic black holes at large distances, but modify the near-horizon physics, see e.g. [116, 117] and references therein for realisations. In these cases the horizon of the black hole is replaced with a reflective surface, such that part of the GW signal is reflected. In contrast to our proposal, these echo signals would not only entail one (or $N-1$ in the case of $N$-metric gravity [54]), but infinitely many echoes, with decreasing amplitude. Furthermore, if

an echo is created due to decoherence, the time difference to the initial signal must grow with the distance of the merger.

However, a recent claim that such echoes are in fact seen by LIGO/Virgo [118–120] is under debate [121, 122] in the literature. It is therefore too early to make any claims in this direction. We may tentatively note, however, that the $\Delta t$ obtained in [120] fits the above scenario for $m_g = 10^{-22} - 10^{-23}\,\mathrm{eV}$.

## 4.5 Conclusions

We have discussed the decoherence regime of gravitational wave oscillations in the framework of our previous analysis in Ref. [1]. In short, the two propagating wave packets, massive and massless, will no longer overlap spatially in this regime, and two signals can in principle be seen in the GW detector. We find that two possible interpretations are feasible. One, where the second event is interpreted as an independent event, and another, where the second event is treated as an echo of the first event.

In the former case, we find no further constraints on the parameter space of bigravity, assuming otherwise only solar system tests. With more events and better precision, this will significantly improve over the forthcoming years when more events are available and the uncertainty on the annual merger rate decreases. In the latter interpretation, on the other hand, we find a phenomenological bound $\theta \lesssim \pi/16$ for the mostly-massless and $\theta \gtrsim 7\pi/16$ for the mostly-massive scenario, assuming a large enough $m_g$, such that the corresponding wave packets are non-overlapping.

Finally, we comment on the possibility of having both GW and optical signals, as was the case for the neutron star binary merger GW170817. [115] Such an event is in principal very appealing because it could allows a direct comparison of the speed of the GW and the optical signal. However, at present, no reliable estimate for the different emission times is available, and thus only model dependent constraints arise: It is commonly assumed that the optical signal in the form of a gamma-ray burst (GRB) is emitted within a few 100 ms of the GW chirp. Albeit, for GW170817, the GRB was observed 1.7 *s after* the GW chirp. Instead of a modified dispersion relation, this could simply indicate that the optical signal was delayed by ejected material, see [123] for a mechanism that delays the GRB by more than $\mathcal{O}(10^3\,s)$. The present analysis stays agnostic to such model-dependent production/emission mechanisms and thus puts more general bounds on the parameter space of bigravity based on the propagation of the GWs only.

We conclude with the proposal of a template search, where one searches the observational data for a secondary waveform of a detected GW event, separated by up to a few seconds. The triggering event can be searched for with the current analysis methods, as it is only a rescaled version of the strain predicted by GR. This provides a clear signature for bigravity in the decoherent regime, and, while current claims of observations are under debate, the search method has been proposed in the literature and is readily applied to our scenario.

# 5 Probing Alternative Cosmologies Through the Inverse Distance Ladder

*This chapter is based on JCAP 10 (2020) 040 [3], with Manfred Lindner, Moritz Platscher, and Jonas Rezacek.*

## 5.1 Synopsis

In this chapter, we study the implications of a combined analysis of cosmic standard candles and standard rulers on the viability of cosmological models beyond the cosmological concordance model ΛCDM. To this end, we employ well-established data in the form of the joint light-curve analysis supernova compilation, baryon acoustic oscillations, and cosmic microwave background data on the one hand, and a recently proposed set of quasars as objects of known brightness on the other hand. The advantage of including the latter is that they extend the local distance measures to redshifts which have previously been out of reach and we investigate how this allows one to test cosmologies beyond ΛCDM. While there exist various studies on parametric extensions of ΛCDM, we present here a comparative study of both parametric and fundamental extensions of the standard cosmology. In order to keep the scope of this work contained, we focus on two particular modifications: One is the consistent theory of two interacting spin-2 objects, bigravity, as introduced in Chapter 2. The other is conformal gravity, a theory of gravity that has no knowledge of fundamental length scales. The former of the two constitutes a veritable extension of General Relativity, given that it adds to the metric tensor of gravity a second dynamical tensor field. As advertised in Sec. 2.3, we will see how the resulting dynamics can incorporate self-accelerating cosmologies. Conformal gravity on the other hand is a much more drastic change of the underlying gravitational theory. Its ignorance towards fundamental length scales offers a completely different approach to the origin of late time acceleration. In this sense, both models offer – in one way or another – an explanation for the dark energy problem. We perform a combined cosmological fit which provides strong constraints on these extensions. We also briefly comment on the implications of the long-standing $H_0$-tension.

## 5.2 Introduction

As we have argued in Chapter 1, given the prevailing absence of (pure) *particle* physics beyond the SM, it is a timely question to ask if and how well BSM theories at the intersection of particle and gravitational physics can address the open questions of Dark Matter and Dark Energy. In this chapter, we approach this topical divide from the gravitational viewpoint. We wish to help bridge the gap between parametrised physics beyond standard cosmology and fundamental models, building upon some previous analyses that have studied such modifications in isolation, such as $f(R)$ [124–128] and $f(T)$ gravity [129–131], Brans-Dicke gravity [132, 133], Galileons and Horndeski gravity [134–137], Quintessence [138], some combinations of these [139], and even non-local gravity [140–142] to name only a few recent examples. Our aim is to deliver a blueprint to study fundamental modifications of the gravitational sector, and choose among the theories the one that best explains the data. In this we rely on statistical methods and available cosmological and astrophysical data sets, which we apply to ΛCDM and some of its parametrised extensions, as well as two fundamental cosmologies.

The data sets under consideration include the well-known Supernovae (SNe) type-I data that first hinted at the accelerated expansion of the universe at late times and thus manifested the dark energy problem in the late 1990s [27, 28]. We also include data from quasar surveys which have only recently been shown to serve as standard candles, however, tracing the expansion of the universe to much larger redshift than SNe [143, 144]. Very recently, these were used to obtain new constraints on the standard cosmological model in Ref. [145]. Furthermore, we use data from galaxy and Lyman-$\alpha$ (Ly$\alpha$) surveys that extract from the clustering of matter the scale of baryon acoustic oscillations (BAO) in the early universe. Finally, this sample is enhanced by the measurement of the acoustic scale from the CMB by the Planck Collaboration [29]. In using these data sets we employ the so-called inverse distance ladder method, meaning that we calibrate the (unknown) absolute magnitude of the standard candles via cosmic standard rulers, see e.g. Refs. [146–148] for similar studies.

As for the models, we compare parametric extensions of the concordance model to models which are constructed from a symmetry or particle content point-of-view; i.e. we study bigravitational cosmologies, and moreover conformal gravity (CG) cosmology. For this analysis, we have chosen these two models because they are sufficiently complementary in their construction and phenomenology and will allow us to exemplify the usefulness of cosmological data applied to microscopic models. At the same time, both models are apt to address the problem associated with late-time acceleration, i.e. the identity of DE.

The theory of bimetric gravity has been introduced and amply discussed in the previous chapters. In this chapter, we will complement the previous analyses with a detailed description of its cosmological history. As opposed to Chapters 3 and 4, where the oscillation phenomena allowed us to probe graviton masses of order $m_g \sim 10^{-22}$ eV, we will now focus on parameter ranges which enable self late-time acceleration. If the mass is of order of the Hubble rate today, not only can this parametrise the late-time acceleration, but also stabilize it against radiative corrections. In this case, the CC problem is reduced to the question why the vacuum energy of the matter Lagrangian does not yield large corrections to the CC (even if degravitation plays a role – see Sec. 2.3).

CG, on the other hand, is an attempt to abolish all scales in nature on a fundamental level by means of a symmetry principle: A conformally invariant action cannot contain any dimensionful parameters or couplings in four dimensions. Thus, the issue of small mass scales in nature (often termed a hierarchy problem with respect to the large Planck mass in General Relativity (GR)) is diverted to the problem of generating such scales dynamically, for which several mechanisms are well-known. In such conformal models of gravity, like e.g. [149, 150], it is often argued that GR is recovered as an effective theory at low energies, so no significant deviations from the standard $\Lambda$CDM scenario are to be expected. In other realizations, e.g. Ref. [151], different predictions for cosmic expansion arise than in the $\Lambda$CDM model. At the same time these predictions are well testable with the aforementioned data sets and this therefore constitutes an interesting model to study in this work. The absence of scales on a fundamental level has the amusing consequence that the theory and its cosmological solution are sensitive to systems of very different length scales, such as the scale of BAO on the far end of scales, but also to galaxy dynamics. In fact, it has been prominently argued in the past that CG can address the missing mass problem – at least at the galactic level manifesting as the rise in rotation curves [152].

The work presented here extends the existing literature in several directions. First, it includes the recent distance measurements of quasars are used in conjunction with SN data, BAO data and $H(z)$ measurements. Moreover, we do not only consider parametrised extensions of $\Lambda$CDM, but take a close look at two microscopic generalizations of GR that give rise to modified cosmologies. One of them, CG, is a theory devoid of any fundamental length scale. We feel that the literature lacks a statistically sound and, as far as cosmology is concerned, comprehensive study of this model exploiting available cosmological data. The strong claims about CG, i.e. being able to reconcile late time acceleration and the dark matter puzzle, call for such a comprehensive survey.

On the other hand we have bigravity, which is studied within the only known, fully analytical regime. Previous work performing a statistical analysis of various cosmological observations within bigravity can be found in [153]; our analysis improves on this by assuming a less restrictive parameter set (non-zero curvature and radiation density). We furthermore present a completely new approach to solving the non-linear dynamical equations and identify the relevant physical branches. This combined effort allows us to draw some important conclusions on the model parameters and on the models themselves.

Note that in performing this cosmological fit, we do not address the current $H_0$-tension, i.e. the discrepancy at the level of $4.4\,\sigma$ between the measurement of $H_0$ inferred from the Planck CMB ($H_0 = 67.4 \pm 0.5\,\frac{\mathrm{km}}{\mathrm{s\,Mpc}}$ [29]) and Supernova ($H_0 = 73.24 \pm 1.74\,\frac{\mathrm{km}}{\mathrm{s\,Mpc}}$ [154]) observations at $z = \mathcal{O}(0.01 - 0.1)$. SNe on their own do not constrain $H_0$; the tension arises only when the data is calibrated, for example using nearby Cepheids in the same host galaxy [155] (see also App. 5.4.3); a high value of $H_0$ in agreement with this is also found via time delays in gravitational lensing [156]. Reproducing the calibrated SN + Cepheid measurement of $H_0$ is beyond the scope of this work and a solution of the tension is not hinted at by the best fits of our modified cosmologies. This is in agreement with a recent study [157], which finds that the locally measured value of $H_0$ remains largely unaffected by the choice of exotic background cosmologies; in particular, a variant of bimetric gravity is tested, and no alleviation of the $H_0$-tension is found.

We also point out the recent discussion which revolves around a possible discrepancy between ΛCDM and the high-redshift quasar data set. The authors of [144] fit a concordance model to the SN + quasar data up to $z < 1.4$. They then extrapolate the model to the whole redshift region of the quasar data and, perhaps unsurprisingly, find that model and data are in $\approx 4\,\sigma$-tension at high-$z$. Finally, the authors perform an expansion of the Hubble function at low-$z$ and fit the Taylor coefficients to the data ('*cosmographic expansion*'), and reach the conclusion that this can alleviate the tension. Several other works have appeared in the meantime, re-analysing these claims. In particular, if the quasar data is calibrated by the distance modulus of the SNe, as in the original study, the tension is reproduced [158, 159]. However, if the fit is performed including all parameters required to calculate the distance modulus from the raw quasar data (i.e. including nuisance parameters), no such tension arises. In this work, we adopt the latter viewpoint. As we will see, comparing the SN and joint SN + quasar fits then does not lead to a discrepancy for ΛCDM.

Before moving on, we point out further data sets which we do not consider in our analysis:
While we incorporate the acoustic scale measurement from CMB, a full analysis including the matter fluctuation amplitude $\sigma_8$ is not performed. Planck has measured $\sigma_8$ to very high accuracy, which can be used to improve constraints of scenarios beyond SM plus GR, see for example [160]. However a moderate tension arises when compared to observations of large scale structures, see DES lensing results [29, 161] for the current status. The tension has called for various theoretical models which modify the late-time universe compared to ΛCDM; a feature which may be provided by bigravity as well as CG, and in the case of $\omega$ΛCDM has shown to slightly alleviate the tension [162]. However a full analysis of the CMB spectrum is beyond the scope of this work. In particular, the analysis of perturbations to the cosmological background solution within bigravity has proven a difficult task, as linear perturbations show unstable scalar and/or tensor modes [163]. See Sec. 5.3.2 for a discussion of the branches and stability requirements in bigravity.

Another promising avenue is that of velocity-induced acoustic oscillations (VAO) due to relative velocity between baryons and DM. Using data from the upcoming HERA interferometer, the Hubble function could be probed up to redshift $z = 15 - 20$ [164]; however, data is not yet available. While the recent discovery of gravitational waves has opened a new window on the cosmological history of the universe, current observations are not yet precise enough to improve constraints on cosmological parameters. We also do not make use of extragalactic background light data measured by Fermi-LAT [165] or gamma-ray bursts, which can be observed up to redshift $z \approx 6$ [166]. In both cases,

inclusion of the data sets does not promise to increase the precision, nor does it extend the redshift-range of the test.

This chapter is structured as follows: in Sec. 5.3, we review the basics of the models we analyse, and construct the Hubble function which enters the cosmological fit. In the case of CG, this entails a discussion whether the galactic rotation curves may be explained without DM. In Sec. 5.4, we discuss the different data sets we include and lay out the details of the Bayesian analysis as well as any other physical constraints. In Sec. 5.5, we discuss the results of the cosmological fits, and present the Hubble diagrams as well as the posterior probability distributions for the relevant parameters. We furthermore compare the competing theories and explain which model is favoured by statistical evidence. We draw our conclusions in Sec. 5.6.

## 5.3 Cosmological models

In this chapter we study a number of cosmological models and compare their predictions for a range of complementary cosmological data sets. While the choice of these models is highly biased, they each represent a larger class of cosmological models which attempt to solve or at least address some of the mentioned issues associated with the late-time acceleration of the universe. Before moving on to the specifics of implementing bigravity and conformal gravity cosmologies, we briefly review the quantities needed to analyse GR-based cosmologies.

### 5.3.1 GR-based cosmologies

The first cases we study are based on the standard cosmological model, as it is obtained from the field equations of General Relativity with the Friedmann-Lemaître-Robertson-Walker (FLRW) metric ansatz, which implements the assumption that the universe is homogeneous and isotropic,

$$\mathrm{d}s^2 = -\mathrm{d}t^2 + a(t)^2 \left[\frac{\mathrm{d}r^2}{1-k\,r^2} + r^2 \mathrm{d}\Omega^2\right], \tag{5.3.1}$$

where $k = 0, \pm 1$ represents a flat, or positive/negative curvature universe.[25] Plugging this ansatz into Einstein's field equations yields two dynamical equations for the scale factor,

$$\frac{\dot{a}(t)^2 + k}{a(t)^2} = \frac{8\pi\, G_N\, \rho(t) + \Lambda}{3} \quad \text{and} \tag{5.3.2}$$

$$\frac{\ddot{a}}{a} = \frac{4\pi G_N}{3}\left[\rho(t) + 3p(t)\right] + \Lambda \xrightarrow{\text{Eq. (5.3.2)}} \dot{\rho} = -3H(\rho + p)\,. \tag{5.3.3}$$

The latter of these is nothing but a continuity equation for an ideal fluid with energy density $\rho$ and pressure $p$, and $H = \frac{\dot{a}}{a}$ is the Hubble rate. Defining the critical energy density $\rho_c = \frac{3H_0^2}{8\pi G_N}$, we can put this into the familiar form

$$H(z)^2 = H_0^2\left[\Omega_r(1+z)^4 + \Omega_m(1+z)^3 + \Omega_k(1+z)^2 + \Omega_\Lambda\right], \tag{5.3.4}$$

where we have introduced the cosmic redshift $z = a^{-1} - 1$, and the density parameters today

$$\Omega_{(m/r)} = \frac{\rho_{(m/r)}(t=t_0)}{\rho_c}, \quad \Omega_k = -\frac{k}{H_0^2}, \quad \Omega_\Lambda = \frac{\Lambda}{3H_0^2}\,. \tag{5.3.5}$$

In these equations the label $(m)$ refers to non-relativistic matter with an equation of state $p = 0$, and $(r)$ refers to relativistic degrees of freedom, i.e. radiation with $p = 1/3\rho$.

We now specify the models of interest based on GR:

**Flat ΛCDM cosmology** The simplest model we study is the concordance cosmology, i.e. the FLRW metric with vanishing spatial curvature, $k = 0$, and a (positive) cosmological constant. This is described by the equation

$$H(z)^2 = H_0^2\left[\Omega_r(1+z)^4 + \Omega_m(1+z)^3 + \Omega_\Lambda\right], \tag{5.3.6}$$

which today ($z = 0$ and $H(0) = H_0$) implies that $\Omega_\Lambda = 1 - \Omega_r - \Omega_m$ must hold.

[25] In the case of $k \neq 0$, $r$ should be thought of as a dimensionless radial coordinate, $r/r_0$, rescaled by the radius of curvature.

**ΛCDM with curvature** A less minimal version of ΛCDM is obtained by allowing for spatial curvature, cf. Eq.(5.3.4), which we will refer to as $k\Lambda$CDM. It is described by the Friedmann equation (5.3.4) together with the more general constraint

$$\Omega_k = 1 - \Omega_\Lambda - \Omega_r - \Omega_m \,. \tag{5.3.7}$$

**Dynamical dark energy, $w\Lambda$CDM** Finally, we can be even more general by both dropping the requirement of spatial flatness and modifying the equation of state of the dark energy component, $p = w\rho$ which allows for an accelerated expansion as long as $w < -1/3$, thus representing a larger class of cosmological models of dynamical dark energy. One finds that

$$H(z)^2 = H_0^2 \left[\Omega_r(1+z)^4 + \Omega_m(1+z)^3 + \Omega_k(1+z)^2 + \Omega_\Lambda(1+z)^{3(w+1)}\right], \tag{5.3.8}$$

and Eq. (5.3.7) must be satisfied, too.

### 5.3.2 Bigravity cosmology

We have discussed the construction of bigravity as the generalisation of the de Rham-Gabadadze-Tolley theory of ghost-free massive gravity in Sec. 2.2.8. Based on this, the following section will go into detail on how to construct measurable quantities for astrophysics, and what kind of cosmological history to expect in bigravity.

Recall the bimetric action, Eq. (2.2.78), which in the parametrisation of our choice reads[26]

$$\begin{aligned} S_{\rm bi} = &\frac{M_g^2}{2}\int d^4x\sqrt{-g}\; R(g) + m^2 M_g^2 \int d^4x\sqrt{-g}\sum_{n=0}^{4}\beta_n e_n(\sqrt{g^{-1}\tilde{g}}) \\ &+ \frac{M_{\tilde{g}}^2}{2}\int d^4x\sqrt{-\tilde{g}}\;\tilde{R}(\tilde{g}) + \int d^4x\sqrt{-g}\;\mathcal{L}_{\rm matter}, \end{aligned} \tag{5.3.9}$$

where the bigravity potential is built from elementary symmetric polynomials [63], and the corresponding equations of motion are

$$R_{\mu\nu} - \frac{1}{2}g_{\mu\nu}R + B_{\mu\nu}(g,\tilde{g}) = \frac{8\pi}{M_g^2}T_{\mu\nu}\,, \tag{5.3.10a}$$

$$\tilde{R}_{\mu\nu} - \frac{1}{2}\tilde{g}_{\mu\nu}\tilde{R} + \tilde{B}_{\mu\nu}(g,\tilde{g}) = 0\,, \tag{5.3.10b}$$

where $R_{\mu\nu}$ ($\tilde{R}_{\mu\nu}$) is the Ricci tensor constructed from $g$ ($\tilde{g}$), while the $B_{\mu\nu}$ and $\tilde{B}_{\mu\nu}$ are derived from the potential $V(g,\tilde{g})$ (see [65] for explicit expressions). Here, $M_g$ is the Planck mass corresponding to the physical metric $g$, while the auxiliary metric comes with the mass scale $M_{\tilde{g}}$.

[26] As opposed to Sec. 2.2.8, we here normalise the potential of metric with the prefactor $m^2M_g^2$ (instead of $m^2M_{\rm eff}^2$). While this somewhat obscures the symmetric nature of the bimetric action, it is a convention more commonly employed in the literature of cosmological evolution of bigravity [65, 167], which will be useful when putting the results of this chapter into context with other studies.

Making $\tilde{g}$ a dynamical field has a number of advantages, foremost it removes the arbitrariness of the reference metric, which instead obeys a dynamical field equation.[27] In the setup of bigravity which we investigate here, where matter couples exclusively to the physical metric $g$, while the other tensor $\tilde{g}$ is regarded as an additional degree of freedom rather than a geometrical object. Under these assumptions and a bi-FLRW ansatz [85], the equations governing the dynamics of the universe read

$$\frac{3}{a^2}\left(H^2+k\right) - m^2\left[\beta_0 + 3\beta_1 y + 3\beta_2 y^2 + \beta_3 y^3\right] = 8\pi\, G_N \rho, \tag{5.3.11a}$$

$$\frac{3}{b^2}\left(J^2/\tilde{c}^2+k\right) - m^2\frac{1}{\alpha^2}\left[\beta_1 y^{-3} + 3\beta_2 y^{-2} + 3\beta_3 y^{-1} + \beta_4\right] = 0. \tag{5.3.11b}$$

with $\alpha \equiv \frac{M_{\tilde{g}}}{M_g}$. Here $a$ is the scale factor of the physical metric and $b$ that of the auxiliary metric, while $\tilde{c}$ is the lapse of the auxiliary metric. We have also defined $J \equiv \frac{\dot{b}}{b}$ and $y \equiv b/a$. The parameters $\beta_i$ are constants of a priori unknown magnitude, while $m$ is a mass scale related to the physical graviton mass (see below). It is evident from Eqs. (5.3.11) that the parameters $\beta_i$ and the mass scale $m$ are not independent parameters; however, the latter is conventionally factored out by introducing a new set of parameters,

$$B_i \equiv \beta_i \frac{m^2}{H_0^2} \qquad i = 0,1,2,3,4 \tag{5.3.12}$$

for reasons that will become apparent momentarily. Moreover, it can be shown from the action that a rescaling of the hidden sector Planck mass, $M_f$, can always be compensated by an appropriate rescaling of the $B_i$. Thus, the ratio $\alpha$ is also not an independent parameter [167]. For our statistical analysis, we will set $\alpha = 1$ and choose an appropriate range for the sampling of the $B_i$; for details on our choice of priors on the bigravity parameters, we refer to Sec. 5.5.4. We stress that a rescaling invariance remains for all cosmological solutions which we will present, under which $B_i \mapsto \alpha^{-i} B_i$ [167].

As a related note, we briefly discuss the role of perturbations on the cosmological background. A number of analyses on the topic exist for bigravity [68, 169–177]; however, it is generally found that the models suffer from gradient or ghost instabilities at the linear level of perturbations [163, 178], which can either be avoided by fine tuning the initial conditions [179], or by considering more exotic matter couplings [88]. It has also been argued by some authors that these instabilities could actually serve as seeds for structure formation by virtue of the Vainshtein mechanism that is expected to set in when these instabilities lead to large overdensities [180].

Finally, there is also the viewpoint that it could be sufficient to shift the instabilities of the cosmological solution to the very early universe. In the conventional parametrisation with $\alpha$ as a free parameter, taking $\alpha = \mathcal{O}(10^{-17})$ and choosing all $B_i$ within the same order can push the age of the onset of instabilities up to the time of Big Bang nucleosynthesis (BBN) [181]. This parameter space is therefore a region of particular interest, and is also the limit which recovers GR from bigravity. However, this feature is obscured in our minimal choice of parametrisation: as we pick $\alpha = 1$, the $B_i$ need to be tuned finely over several different orders of magnitude in order to reproduce the same type of background cosmology.

Notice that (5.3.11a) is identical to the standard Friedmann equation augmented by a dynamical CC,

$$\Lambda(z) = H_0^2\left[B_0 + 3B_1 y(z) + 3B_2 y^2(z) + B_3 y^3(z)\right], \tag{5.3.13}$$

which is now a function of redshift $z$ and thus time.

[27] While we focus on bigravity, note that there are viable cosmological solutions in massive gravity for an appropriate, non-flat reference metric [88, 168].

**Determination of the ratio of scale factors.** The specific form of coupling the two tensor fields implies that several branches of solutions of Eq. (5.3.11) exist. We choose the dynamic/finite branch [65], for which $J^2/\tilde{c}^2 = H^2$. This allows us to rewrite the two Friedmann equations into one *master equation* for the ratio of the two scale factors,

$$y^4 + a_3 y^3 + a_2 y^2 + a_1(z) y + a_0 = 0 \tag{5.3.14}$$

with

$$a_3 = \frac{B_4 - 3B_2\,\alpha^2}{-B_3\,\alpha^2} \qquad a_2 = \frac{3B_3 - 3B_1\,\alpha^2}{-B_3\,\alpha^2}$$
$$a_1(z) = \frac{(3B_2 - B_0\,\alpha^2) - 3\left(\Omega_m\,(1+z)^3 + \Omega_r\,(1+z)^4 + \Omega_\Lambda\right)\alpha^2}{-B_3\,\alpha^2} \qquad a_0 = -\frac{B_1}{B_3}\frac{1}{\alpha^2}$$

where we have replaced the energy density $\rho$ with the matter density parameter $\Omega_m$ and radiation component $\Omega_r$ as well as a constant dark energy component $\Omega_\Lambda$.[28] Note that $a_1$ brings in a redshift-dependence. In particular, for $z \to \infty$, it scales as $a_1 \to \pm\infty$.

In order for our chosen background solution to be viable, we enforce the model to lie on the *finite branch* of solutions, i.e. that $y$ vanishes at $z \to \infty$ and evolves to a finite value in the distant future, $z = -1$. While it is possible to have a solution that yields $y \to \infty$ in the early universe, such *infinite branch* solutions are unphysical [65, 182]. This can be seen by taking a derivative w.r.t. $\log a$ of Eq. (5.3.14) and recasting it into [167]

$$\frac{\mathrm{d}y}{\mathrm{d}\log a} = y\frac{(1+w_m)\rho_m/M_g^2}{m_{\rm eff}^2 - 2H^2}, \tag{5.3.15}$$

where

$$m_{\rm eff}^2 \equiv \left(1 + \frac{1}{\alpha^2\,y^2}\right) H_0^2 (y\,B_1 + 2y^2 B_2 + y^3 B_3) \tag{5.3.16}$$

is the time-dependent, effective spin-2 mass. This quantity must satisfy the Higuchi bound $m_{\rm eff}^2 \geq 2H^2$ at all times, as otherwise the ghost d.o.f. re-appears [183]. Thus, in the infinite branch, where for $z \to \infty$, $y \to \infty$, we have $y' < 0$ in order to end the evolution at a finite value for $y$ today. Thus, we must either violate the Higuchi bound, which renders the theory inconsistent, or we must introduce exotic forms of matter with $\rho_m < 0$, which dominate the universe.

Conversely, Eq. (5.3.16) highlights that, when considering the finite branch and a regime where $\rho_m > 0$, $m_{\rm eff}^2 \geq 2H^2$, $y'$ cannot change signs, i.e. the asymptotic value $y_* = y(z \to \infty)$ fixes the sign of $y$ for all redshifts. Since we must have $H(z)^2 \geq 0$ for all $z$, this equation further implies that $m_{\rm eff}^2 \geq 0$, and thus [167]

$$B_1 > 0 \tag{5.3.17}$$

in the finite branch.

We now continue our approach to solving Eq. (5.3.14). The solutions to this fourth order equation read

$$y_{1,2} = -\frac{a_3}{4} + \frac{R}{2} \pm \frac{D}{2} \qquad y_{3,4} = -\frac{a_3}{4} - \frac{R}{2} \pm \frac{E}{2}$$

[28] Note that $\Omega_\Lambda$ and $B_0$ are degenerate; therefore, in our numerical analysis we have chosen $B_0$ such that Eq. (5.3.13) yields no additional constant dark energy component at $z = 0$. Hence, $\Omega_\Lambda$ has the expected physical interpretation.

with

$$R \equiv \sqrt{\frac{1}{4}a_3^2 - a_2 + x_1(z)}\,, \tag{5.3.18a}$$

$$D \equiv \sqrt{\frac{3}{4}a_3 - R^2 - 2\,a_2 + \frac{1}{4}(4\,a_3\,a_2 - 8a_1 - a_3^3)R^{-1}}\,, \tag{5.3.18b}$$

$$E \equiv \sqrt{\frac{3}{4}a_3 - R^2 - 2\,a_2 - \frac{1}{4}(4\,a_3\,a_2 - 8a_1 - a_3^3)R^{-1}}\,, \tag{5.3.18c}$$

and where $x_1$ is a real root of

$$x(z)^3 - a_2 x(z)^2 + [a_1(z)a_3 - 4a_0]x(z) + [4a_2a_0 - a_1^2(z) - a_3^2 a_0] = 0. \tag{5.3.19}$$

Recall that we require that $y \to 0$ for $z \to \infty$, which is enforced by the infinite energy density limit in the early universe [65]. Let us therefore have a look at the asymptotic behaviour of Eq. (5.3.19), where by assumption $|a_1(z)| \gg |a_{0,2,3}|$, and keeping all orders in $x(z)$:

$$x(z)^3 - a_2 x(z)^2 + a_1(z)a_3\,x(z) - a_1^2(z) = 0\,, \tag{5.3.20}$$

which has only one real solution, which scales as

$$x(z \to \infty) \equiv x_\infty = \frac{a_2}{3} + a_1(z)^{\frac{2}{3}} - \frac{a_3}{3}\,a_1(z)^{\frac{1}{3}} \tag{5.3.21}$$

if $B_3 > 0$ and

$$x(z \to \infty) \equiv x_\infty = \frac{a_2}{3} + |a_1(z)|^{\frac{2}{3}} + \frac{a_3}{3}\,|a_1(z)|^{\frac{1}{3}} \tag{5.3.22}$$

in the case $B_3 < 0$. Thus, we always have that asymptotically $R_\infty = \sqrt{x_\infty}$ and in the limit of large redshift,

$$D_\infty = \sqrt{-x_\infty - \frac{2\,a_1(z)}{\sqrt{x_\infty}}},\ E_\infty = \sqrt{-x_\infty + \frac{2\,a_1(z)}{\sqrt{x_\infty}}}\,. \tag{5.3.23}$$

It is clear from this equation that only one solution can be asymptotically real, either involving $D$ ($a_1 < 0$) or $E$ ($a_1 > 0$), where the sign of $a_1$ is fixed by $B_3$. For a parametric scan, we pick a sample of the parameters $B_i$ and use the asymptotically real branch. In summary, we have identified the unique solution branch only by demanding that GR be restored at sufficiently early times.

In order to comply with our assumption that $y \to 0$ for $z \to \infty$, we must then also demand that $a_3 = 0$. This is consistent with the requirement $d\rho/dy < 0$, a condition sufficient to avoid the Higuchi ghost instability [163, 182, 184].

Finally, we determine the physical graviton mass by taking the future limit, where $z = -1$ and $y$ goes to a constant value $y_*$. The graviton mass is then [2]

$$m_g^2 = y_* H_0^2\, G_* \qquad \text{with} \quad G_* \equiv (B_1 + 2y_* B_2 + y_*^2 B_3) = \text{const.} \tag{5.3.24}$$

The future fixed point of the scale factor $y_*$ is determined from the master equation (5.3.14) for $\rho \to 0$.

By having chosen the finite branch, we obtain a stable cosmology at the background level. However, linear perturbations on this background solution are known to develop a scalar instability at early times [68, 88, 163, 177]. While this instability occurs at the perturbative level, it is currently unclear whether this issue is resolved due to strong coupling effects; the on-set of the instability may also be pushed to unobservable early times, which can be achieved by a large hierarchy of the Planck masses [181].

We conclude this section with a sketch of the cosmic history in bigravity: In the early universe, dominated by matter and radiation, the modifications of bigravity are irrelevant, as we have chosen a finite branch solution with $y \to 0$ for $z \to \infty$; this is identical to a ΛCDM cosmology without any CC contribution (which is irrelevant at large $z$). At a certain redshift, $y$ will develop dynamics and modify the expansion history of the universe, effectively through a dynamical CC, cf. Eq. (5.3.11). Finally, the scale factors reach a constant ratio, $y_*$, which is the value assumed in the far future, $z = -1$. If we live in a bigravity universe, where we are sufficiently far away from this equilibrium point, we may hope to identify the characteristic features of the dynamical CC in this model, or constrain it otherwise.

Notice the similarity between this behaviour and the behaviour found in spherically symmetric solutions in bigravity [74]. In this metric space, the potential looks Newtonian far away from the source; however, at a certain distance from the source $r_c = m_g^{-1}$, the solution begins to deviate from GR and develops a Yukawa-type potential. Finally, and even closer to the source at a distance $r_V$, the longitudinal polarisation modes of the massive spin-2 field will become strongly coupled and non-linearities conspire to restore the GR predictions by rendering any longitudinal polarisation state non-dynamical [185]. This so-called Vainshtein screening is indeed also incorporated in the cosmological solution we employ, which was obtained without any assumptions about linearity. See also Ref. [186] for a recent study of this effect in cosmology.

### 5.3.3 Conformal gravity cosmology

CG is a generalization of GR which demands conformal symmetry in addition to general covariance. The CG action,

$$S_{\mathrm{CG}} = -\alpha_g \int \mathrm{d}^4x\sqrt{-g}\, C_{\lambda\mu\nu\kappa}C^{\lambda\mu\nu\kappa}\,, \tag{5.3.25}$$

is constructed from the Weyl tensor $C^{\lambda}{}_{\mu\nu\kappa}$, which is the complete traceless part of the Riemann tensor[29] and is conformally invariant. By construction, the coupling constant $\alpha_g$ is dimensionless and the action is invariant under conformal transformations where the metric is locally rescaled by

$$g_{\mu\nu}(x) \to \Omega(x)^2 g_{\mu\nu}(x)\,. \tag{5.3.26}$$

Due to quadratic dependence on curvature invariants in Eq. (5.3.25), the actions depends on up to fourth-order derivatives of the metric, a fact which can be seen as a virtue and as a disadvantage. On the one hand, the inclusion of these higher-order terms renders these theories renormalizable by naive power-counting arguments [187]. On the other hand, these terms give rise to new degrees of freedom containing a spin-2 ghost state [188, 189]. Such a degree of freedom is in general considered unphysical since it suffers from the so-called Ostrogradski instability at the classical level[30] [190], and consequently unitarity is violated in the quantum theory [191]. However, proposals exist to deal with the ghost state (see e.g. Refs. [192–199]). In this work, we intend to study a particular cosmological model following the ideas of Refs. [151, 200] and references therein. In addition, this model offers a possible solution to the missing mass problem of galaxies which we discuss in Sec. 5.3.3. In the past, attempts have been made to explain galactic rotation curve data without the addition of a dark matter halo in this model [201], and furthermore, Refs. [202, 203] also address observed galaxy cluster motion with no dark matter. Furthermore, if CG is to account for all dark matter in the universe, it is so far unclear if it can pass gravitational lensing tests [204–210], and inconsistencies with gravitational wave observation of binaries have been found [211]. Also, tensions between predictions of primordial nucleosynthesis in a CG cosmology and observation of light element abundances have been found in Refs. [212, 213]. In the remainder of this section we discard all these concerns for now and review the derivation of the modified Friedmann equations in CG following closely Ref. [151]. The field equations obtained from Eq. (5.3.25), also known as Bach equations [214], read

$$4\alpha_g W_{\mu\nu} \equiv 4\alpha_g\Big(2\nabla^\alpha\nabla^\beta C_{\alpha\mu\nu\beta} + C_{\alpha\mu\nu\beta}R^{\alpha\beta}\Big) = T_{\mu\nu}\,, \tag{5.3.27}$$

where the Bach tensor $W_{\mu\nu}$ can be understood as the generalization of the Einstein tensor and the energy-momentum tensor $T_{\mu\nu}$ can be derived from a conformally invariant matter action, e.g. containing a complex scalar $\phi$ and a fermion $\psi$,

$$S_{\mathrm{M}} = -\int \mathrm{d}^4x\sqrt{-g}\,\left[\left(\frac{1}{2}(\nabla^\mu\phi)^\dagger\nabla_\mu\phi + \frac{R}{6}\phi^\dagger\phi\right) + \lambda(\phi^\dagger\phi)^2 + i\overline{\psi}\not{D}\psi + y\phi\overline{\psi}\psi\right]\,. \tag{5.3.28}$$

Due to conformal invariance, the non-minimal coupling term, $R\,\phi^\dagger\phi$, is required and it introduces a piece proportional to the Einstein tensor $G_{\mu\nu}$ in the energy-momentum-tensor (EMT)

$$T_{\mu\nu} = T^{\mathrm{GR}}_{\mu\nu} + \frac{1}{6}\phi^\dagger\phi\, G_{\mu\nu}\,, \tag{5.3.29}$$

where $T^{\mathrm{GR}}_{\mu\nu}$ is the usual matter EMT.

[29] The Weyl tensor is defined by $C_{\lambda\mu\nu\kappa} = R_{\lambda\mu\nu\kappa} - (g_{\lambda[\nu}R_{\kappa]\mu} - g_{\mu[\nu}R_{\kappa]\lambda}) + \frac{1}{3}g_{\lambda[\nu}g_{\kappa]\mu}R$.

[30] We have encountered the Ostrogradski instability in Sec. 2.2.2, where avoiding the ghost modes has served as a guiding principle in the consistent construction of bigravity. Here, we take the an orthogonal approach, and assume that the instability is cured by a yet unspecified mechanism.

Amusingly, the FLRW ansatz for the metric [cf. Eq. (5.3.1)] is conformally indistinguishable from a flat solution which satisfies the vacuum equation $W_{\mu\nu} = 0$, and thus the Bach equation reduces to Einstein's field equations with a flipped sign $\langle \phi^\dagger \phi \rangle G_{\mu\nu} = -6\, T^{\rm GR}_{\mu\nu}$ and an effective gravitational coupling constant set by the vacuum expectation value (vev) of the field $\phi$. Independently of whether we wish to view the field $\phi$ as the Higgs field, once $\phi$ takes a constant field value, it will break the conformal symmetry and set the scale of gravitational interactions. Plugging the FLRW metric ansatz (5.3.1) into the field Eq. (5.3.27) and assuming that $T^{\rm GR}_{\mu\nu}$ constitutes a perfect fluid leads to the modified Friedmann equation of CG,

$$H(z)^2 = -\epsilon\, H_0^2 \left[\Omega_r (1+z)^4 + \Omega_m (1+z)^3 + \Omega_\Lambda\right] + H_0^2 \Omega_k (1+z)^2, \tag{5.3.30}$$

where the densities $\Omega_{m,r,k}$ are defined as in Eqs. (5.3.5) but the dark energy density is set by the vev of the scalar $\Omega_\Lambda = \lambda \langle \phi^4 \rangle / H_0^2$. In Eq. (5.3.30) we have introduced the dimensionless quantity $\epsilon \equiv \frac{3}{4\pi G_N \langle \phi^2 \rangle}$. This allows us to define *modified* energy densities $\overline{\Omega}_i = -\epsilon\, \Omega_i$[31] and bring the Friedmann equation into the familiar form

$$\frac{H(z)^2}{H_0^2} = \left[\overline{\Omega}_r (1+z)^4 + \overline{\Omega}_m (1+z)^3 + \overline{\Omega}_\Lambda\right] + \Omega_k (1+z)^2\,, \tag{5.3.31}$$

where matter and radiation contribute negatively to the Friedmann equation, as $\overline{\Omega}_{(m)r} < 0$, and the cosmological constant is assumed to contribute positively as demanded by observations.[32] It should be stressed that the physical densities of matter $\rho_m$ and $\rho_r$ are still positive, but their gravitational interactions are repulsive on cosmological scales.

Due to the negative energy density parameters entering Eq. (5.3.31), there is a *maximal* redshift $z_{\rm max}$, which is reached once the squared Hubble rate has a root, $H(z^2_{\rm max}) = 0$. For a flat universe with only matter (radiation) and a cosmological constant, the maximal redshift is

$$z_{\rm max} \approx \left(\frac{\overline{\Omega}_\Lambda}{-\overline{\Omega}_{m(r)}}\right)^{\frac{1}{3}\left(\frac{1}{4}\right)}\,, \tag{5.3.32}$$

which translates to a minimal scale factor $a_{\rm min} = 1/(1+z_{\rm max})$.

For the present analysis we adapt the following assumptions, which allow us to put conservative bounds on CG. Processes in the early universe such as recombination and nucleosynthesis are well established via the CMB and the abundance of nuclei in the universe, respectively. Therefore, we demand that $z_{\rm max} > 10^{15}$, for BBN to be safely inside the expanding phase when these processes take place. Thus, $\overline{\Omega}_{m(r)}$ must be tiny if we assume $\overline{\Omega}_\Lambda \sim 1$, which can only be achieved if $\epsilon < 10^{-15}$.

We also take into account the vacuum energy due to the scale of the electroweak phase transition. To this end, we must bring into agreement the observed vacuum energy density $\rho^{\rm obs}_{\rm vac} \sim (10^{-2}\,{\rm eV})^4$ with the expected contribution $\rho^{\rm EW}_{\rm vac} \sim (100\,{\rm GeV})^4$. For that contribution we have $\overline{\Omega}_\Lambda = \epsilon \rho^{\rm EW}_{\rm vac}/\rho_c \sim 10^{54}\epsilon$, so the appropriate order of magnitude suppression demands that $\epsilon \sim 10^{-54}$. Furthermore, we have to consider the contribution coming from the vev of the scalar $\phi$ to the cosmological constant $\rho_\Lambda = \lambda \langle \phi^4 \rangle$. The vev $\langle \phi \rangle$ is set by $\epsilon \sim 10^{-54}$ to $\langle \phi \rangle \sim 10^{26} M_{\rm Pl}$. This huge vacuum expectation value requires to fine-tune the scalar self-coupling to $\lambda \sim 10^{-176}$ in order to maintain $\overline{\Omega}_\Lambda \sim 1$. This vast amount of fine-tuning indicates that the cosmological constant problem persists in CG. However, we find that $\epsilon$ is constrained even stronger due to vacuum energy contributions to $\overline{\Omega}_\Lambda$ so that the BBN constraint is easily satisfied.

From the above considerations we conclude that $\epsilon \ll 1$, and that only the vacuum energy and curvature (the latter of which is not multiplied by $\epsilon$) contribute to the cosmology of CG in the range of redshifts we are interested in,

$$H(z)^2 = H_0^2 \left[\overline{\Omega}_\Lambda + \Omega_k (1+z)^2\right]\,. \tag{5.3.33}$$

[31] If we wish to achieve $\overline{\Omega}_\Lambda > 0$, we must accept that $\lambda < 0$ in the action, since $\rho_\Lambda = \lambda \langle \phi^4 \rangle$.

[32] For $\Omega_k > 0$, which is demanded by galactic rotation curves (see Sec. 5.3.3), the universe is in an accelerated phase at all times.

### Galactic Rotation Curves without Dark Matter

As mentioned above, the modified gravitational potential of CG has been used to address the missing mass problem of galaxies in the past [152, 215–217]. Here, we briefly review the potential generated by a spherical symmetric source and novel effects that arise only in CG following closely Ref. [201]. The potential generated outside the source of radius $R$ reads

$$V^*(r > R) = -\frac{\beta^*}{r} + \frac{\gamma^* r}{2}\,. \tag{5.3.34}$$

For small radius $r$ the Newtonian limit is recovered if $\beta^* = G_N M$, and the linear term in $r$ marks a departure from the known behaviour on larger scales. Due to the fourth-order derivatives inherent to CG, Newton's shell theorem is no longer valid. The global contribution can be divided into two components: the homogeneous cosmological background and the inhomogeneities on this background. First, we consider the homogeneous and isotropic background described by the FLRW metric (5.3.1). To compute the gravitational potential due to the ambient FLRW background which an observer in the Schwarzschild rest frame experiences, one can use general coordinate invariance. By a suitable coordinate transformation for the time and radial coordinates, Eq. (5.3.1) is transformed into a Schwarzschild-type metric

$$\mathrm{d}s^2 = \Omega^2(\tau,\rho)\left[-(1+\gamma_0 r)\mathrm{d}t^2 + \frac{\mathrm{d}r^2}{(1+\gamma_0 r)} + r^2\mathrm{d}\Omega^2\right]. \tag{5.3.35}$$

This reveals that the FLRW background generates the linear term in the potential for non-zero curvature, and this term is related to the spatial curvature $k$ through the relation[33]

$$\gamma_0 = 2\sqrt{-k}. \tag{5.3.36}$$

This allows us to test the parameter $\gamma_0$ on two distinct scales. On the one hand, it appears as a global term in the potential below, where it can be determined by local data such as galactic rotation curves. On the other hand, $k$ will enter the Friedmann Eq. (5.3.33) through the curvature density $\Omega_k$ and its value can be constrained by a cosmological fit. We discuss this particular feature in Sec. 5.5.5.

The second, global contribution to the potential is due to inhomogeneities on the FLRW background, which introduce a quadratic term in the potential (see Ref. [201] for details). To sum up, we obtain for the full potential outside the source

$$V(r > R) = V^*(r > R) + \frac{\gamma_0 r}{2} - \kappa\, r^2, \tag{5.3.37}$$

from which galactic rotation curves are predicted in Refs. [201, 218–222].

[33] For a well-behaved potential we demand that $k < 0$ which corresponds to an open universe with $\Omega_k > 0$.

## 5.4 Data sets and analysis methods

In this section we describe the data samples we have used in this and document our data analysis methods. The contents of this section will enable the inclined reader to reproduce all of our results. Furthermore, we provide the code to reproduce our results at [223].

### 5.4.1 Distance measures

Having specified a given model in terms of its Hubble rate's dependence on redshift, testable observables can be derived. To this end, objects of known brightness (standard candles) and known size (standard rulers) are identified at a certain redshift in order to infer the corresponding cosmic distance measures. We define the co-moving distance as a function of redshift

$$d_C(z) = \int_0^z \frac{\mathrm{d}z'}{H(z')}, \tag{5.4.1}$$

from which a number of useful distance measures can be derived.
**Standard candles** are objects of known brightness and their *luminosity distance* is given by

$$d_L(z) = (1+z)\Phi_k\left(d_C(z)\right) , \tag{5.4.2}$$

with

$$\Phi_k(x) = \begin{cases} \sqrt{\Omega_k H_0^2}^{-1} \sinh\left(\sqrt{\Omega_k H_0^2}\, x\right), & k < 0, \\ x, & k = 0, \\ \sqrt{|\Omega_k|\, H_0^2}^{-1} \sin\left(\sqrt{|\Omega_k|\, H_0^2}\, x\right), & k > 0. \end{cases} \tag{5.4.3}$$

**Standard rulers** are objects of known size, such as the BAO scale, and one measure their *angular diameter distance*,

$$d_A(z) = \frac{\Phi_k\left(d_C(z)\right)}{1+z} = \frac{d_L(z)}{(1+z)^2} . \tag{5.4.4}$$

### 5.4.2 Big bang nucleosynthesis

Our analysis assumes that BBN proceeds in the standard manner. In order to be in agreement with measurements of the primordial deuterium abundance, we combine *all* likelihoods with a Gaussian prior on $100\,\Omega_b h^2 = 2.22 \pm 0.05$. This is the 'conservative BBN prior' of Planck 2018 [29] on the basis of the deuterium abundance measurement by Cooke et al. [224].

### 5.4.3 Supernova data

In order to employ the power of SN standard candles, we make use of the Joint Light Curve Analysis (JLA) data [225], a combined analysis of the available SDSS and SNLS data including very low ($z < 0.1$) and high redshift data points ($z \gtrsim 1$). The resulting set of 740 SN events, available from [226], have previously been used to discriminate cosmological models, see e.g. Ref. [227] for recent work. The distance modulus of a generic SN event is defined as $\mu = 5\,\log_{10}\left(\frac{d_L(z)}{1\,\mathrm{Mpc}}\right) + 25$, and can be related to the absolute and apparent bolometric magnitude of the given SN as,

$$\mu = m_B + \alpha'\, X_1 - \beta\, C - M_B\,, \tag{5.4.5}$$

where $m_B$ and $M_B$ are apparent and absolute B-band magnitudes, respectively; $X_1$ characterises the shape of the SN light curve; and $C$ its deviation from the standard type Ia SN color. While $m_B$, $X_1$ and $C$ are measured, $\alpha'$, $\beta$ and $M_B$ need to be extracted from a *joint fit* of the data to a given

cosmological background model.[34] As proposed by the JLA analysis, we include an 'adjustment parameter' $\Delta M_B$ for SNe in host galaxies with a masses $> 10^{10} M_\odot$, i.e.

$$M_B = \begin{cases} M_B^0 & \text{if } M_{\text{host}} \leq 10^{10} M_\odot, \\ M_B^0 + \Delta M_B & \text{if } M_{\text{host}} > 10^{10} M_\odot. \end{cases} \tag{5.4.6}$$

This, together with a given model prediction for $d_L(z)$, allows us set up our log-likelihood for the SN data, most compactly written in matrix notation,

$$-2 \log \mathcal{L}_{\text{SN}} = [\vec{\mu} - \vec{\mu}_{\text{model}}]^T \, \mathbf{C}^{-1} \, [\vec{\mu} - \vec{\mu}_{\text{model}}] + \log[\det(\mathbf{C})], \text{[35]} \tag{5.4.7}$$

with the covariance matrix $\mathbf{C}$ decomposed into

$$\mathbf{C} = \mathbf{D}_{\text{stat}} + \mathbf{C}_{\text{stat}} + \mathbf{C}_{\text{sys}} \,, \tag{5.4.8}$$

and the diagonal matrix $\mathbf{D}_{\text{stat}}$ given as

$$\mathbf{D}_{\text{stat},\, ii} = \sigma^2_{m_B,\, i} + \alpha'^2 \, \sigma^2_{X_1,\, i} + \beta^2 \, \sigma^2_{C,\, i} + C_{m_B\, X_1\, C,\, i} + \sigma^2_{\text{pec}\, i} + \sigma^2_{\text{lens},\, i} + \sigma^2_{\text{coh},\, i} \,. \tag{5.4.9}$$

The matrices $\mathbf{C}_{\text{stat}}$ and $\mathbf{C}_{\text{sys}}$ can be obtained from [226], which also includes the standard deviations due to the peculiar velocities $\sigma^2_{\text{pec}\, i}$, lensing $\sigma^2_{\text{lens},\, i}$, the dispersion $\sigma^2_{\text{coh},\, i}$, and the covariance among $m_B$, $X_1$ and $C$, $C_{m_B\, X_1\, C,\, i}$. Notice that $\mathbf{C}$ depends (quadratically) on the auxiliary parameters, and thereby minimising Eq. (5.4.7) is not fully equivalent to a least squares fitting – even for uniform priors.

### 5.4.4 Quasar data

In order to use quasars as cosmological standard candles, we follow the program outlined in Refs. [143, 144], and which is founded on an empirical log-linear relation among the UV and X-ray luminosities,

$$\log_{10}(L_{\text{X}}) = \gamma \, \log_{10}(L_{\text{UV}}) + \text{const} \,. \tag{5.4.10}$$

This translates into observable fluxes $F = L / \left[4\pi d_L(z)^2\right]$ as

$$\log_{10}(F_{\text{X}}) = \gamma \, \log_{10}(F_{\text{UV}}) + \beta' + 2(\gamma - 1) \underbrace{\log_{10}\left(\frac{d_L(z)}{1\,\text{Mpc}}\right)}_{=\mu/5 - 5} \,. \tag{5.4.11}$$

Here, $\beta'$ can in principle be related to the constant in Eq. (5.4.10), but an overall normalisation of $\mu$ remains undetermined [143]. Therefore, we treat $\beta'$ as another auxiliary parameter to be fitted with the cosmology. The parameter $\gamma$ in turn can be determined from a linear fit of the flux data. In order for the redshift-dependence to be negligible, this must be carried out in narrow redshift bins, $\Delta[\log z] < 0.1$, or assuming a standard cosmology [143]. This yields a mean of $\gamma = 0.634$ that we use throughout our statistical analysis. The data set we employ is described in Ref. [144] and has already undergone a number of pre-selection steps, which leave a total of $N = 1598$ quasar samples with redshifts $0.036 < z < 5.1$. Our likelihood function is

$$-2 \log \mathcal{L}_{\text{quasar}} = \sum_{i=1}^{N} \left\{ \frac{[\mu_i - \mu_{\text{model}}(z_i)]^2}{\sigma_i^2} + \log(\sigma_i) \right\} , \tag{5.4.12}$$

with the observed $\mu$ obtained via Eq. (5.4.11) and the standard deviation $\sigma^2 = \left[\frac{5}{2\,(1-\gamma)} \, \Delta F_{\text{X}}\right]^2 + \delta^2$ is augmented by a dispersion parameter $\delta$, which is included in the cosmological fit as a nuisance parameter.

[34] Taking $M_B$ as a fit parameter is the result of our ignorance about the absolute magnitude of the SN luminosity. Because this introduces an arbitrary rescaling of $d_L$, we are not able to infer $H_0$ from the SN fit alone. This is only possible if one includes a local calibrator (see [155]).

[35] For practical reasons, the last term needs to be implemented as $\log[\det(\mathbf{C})] = \text{tr}[\log(\mathbf{C})]$ as otherwise the determinant is below machine precision and this term evaluates to $-\infty$.

### 5.4.5 BAO data

In the early universe, the interaction of the relativistic photon plasma with the cooling baryons leads to density oscillations which imprint a characteristic length scale onto the CMB and also the large scale structure (LSS) of the universe. This scale can be measured as a characteristic angular scale, a *standard ruler*. The rather recent measurements of the BAO scale provide an independent and complementary probe of the base cosmological model and in promise more precision and reach with upcoming surveys, such as EUCLID. Recent BAO analyses [137, 146, 228, 229] have shown that measuring the BAO scale is a powerful tool for probing cosmological models.

The relevant length scale for BAO is the sound horizon at the end of the so-called drag epoch $z_d$, which is the time when the photon and baryon components of the primordial plasma decouple,

$$r_d \equiv r_s(z_d) = \int_{z_d}^{\infty} \mathrm{d}z \, \frac{c_s(z)}{H(z)} = z_d \int_0^1 \mathrm{d}x \, x^{-2} \, \frac{c_s(z_d/x)}{H(z_d/x)}, \tag{5.4.13}$$

where the integral expressed in terms of the variable $x = \frac{z_d}{z}$ is more suitable for numerical integration, and the sound speed given by

$$c_s(z) = \frac{1}{\sqrt{3}} \left[ 1 + \frac{3}{4} \frac{\rho_b(z)}{\rho_\gamma(z)} \right]^{-\frac{1}{2}}. \tag{5.4.14}$$

$\rho_b$ is the physical baryon density and $\rho_\gamma$ the energy density of the photon plasma. The photon density is determined from the CMB temperature $T_{\mathrm{CMB}} = 2.7255\,\mathrm{K}$ [230],

$$\frac{3}{4\,\Omega_\gamma h^2} = 31500 \times (T_{\mathrm{CMB}}/2.7\,\mathrm{K})^{-4}. \tag{5.4.15}$$

Notice also that at the end of the drag epoch $z_d$ the energy density of radiation in $H(z)$ cannot be ignored.

| Name | $z_{\mathrm{eff}}$ | $d_V/r_d$ | $\frac{d_M}{\mathrm{Mpc}} \frac{r_{d,\mathrm{fid}}}{r_d}$ | $\frac{d_A}{\mathrm{Mpc}} \frac{r_{d,\mathrm{fid}}}{r_d}$ | $\frac{H(z)\,r_d/r_{d,\,\mathrm{fid}}}{\mathrm{km\,s^{-1}Mpc^{-1}}}$ | $d_H/r_d$ | $\frac{r_{d,\,\mathrm{fid}}}{\mathrm{Mpc}}$ | $r_{\mathrm{corr}}$ |
|---|---|---|---|---|---|---|---|---|
| 6dFGS [231] | 0.106 | $2.976 \pm 0.133$ | – | – | – | – | – | – |
| SDSS MGS [232] | 0.15 | $4.466 \pm 0.168$ | – | – | – | – | 148.69 | – |
| BOSS DR12 [233] | 0.38 | – | $1518 \pm 22$ | – | $81.5 \pm 1.9$ | – | 147.78 | cov. matrix |
| | 0.51 | – | $1977 \pm 27$ | – | $90.4 \pm 1.9$ | – | 147.78 | |
| | 0.61 | – | $2283 \pm 32$ | – | $97.3 \pm 2.1$ | – | 147.78 | |
| BOSS DR14 [234] | 0.72 | $16.08 \pm 0.41$ | – | – | – | – | 147.78 | – |
| eBOSS QSO [235] | 0.978 | – | – | $1586 \pm 284$ | $113.72 \pm 14.63$ | – | 147.78 | cov. matrix |
| | 1.23 | – | – | $1769 \pm 160$ | $131.44 \pm 12.42$ | – | 147.78 | |
| | 1.526 | – | – | $1768.8 \pm 96.6$ | $148.11 \pm 12.75$ | – | 147.78 | |
| | 1.944 | – | – | $1808 \pm 146$ | $172.63 \pm 14.79$ | – | 147.78 | |
| eBOSS Ly$\alpha$ [236] | 2.34 | – | $(37.41 \pm 1.86)\, r_{d,\mathrm{fid}}$ | – | – | $8.86 \pm 0.29$ | 147.33 | $-0.34$ |
| eBOSS Ly$\alpha$-QSO [237] | 2.35 | – | $(36.3 \pm 1.8)\, r_{d,\mathrm{fid}}$ | – | – | $9.20 \pm 0.36$ | 147.33 | $-0.44$ |
| eBOSS Ly$\alpha$ combined [237] | 2.34 | – | $(37.1 \pm 1.2)\, r_{d,\mathrm{fid}}$ | – | – | $9.00 \pm 0.22$ | 147.33 | $-0.40$ |

**Table 5.1:** BAO measurements used in our analysis. This table is adapted from Ref. [146] with updated data sets as found in Ref. [228]. The correlation matrices can be found in the references.

The dynamics of the drag epoch have been thoroughly analysed in [238], where a numerical fitting

formula for $z_d$ is given,

$$\begin{aligned} z_d &= 1345\,\frac{(\Omega_m h^2)^{0.251}}{1+0.659\,(\Omega_m h^2)^{0.828}}\,[1+b_1(\Omega_b h^2)^{b_2}],\\ b_1 &= 0.313\,(\Omega_m h^2)^{-0.419}\,[1+0.607(\Omega_m h^2)^{0.674}],\\ b_2 &= 0.238\,(\Omega_m h^2)^{0.223}. \end{aligned} \tag{5.4.16}$$

The relevant cosmological distance measure for an object of known size is the redshift-weighted comoving distance $d_M$,

$$d_M(z) = (1+z)d_A(z) = \frac{d_L(z)}{1+z}. \tag{5.4.17}$$

In order to measure the BAO scale, a fiducial cosmology is employed that allows to translate the power spectrum to a distance measure, while allowing the BAO scale to shift relative to the fiducial cosmology's prediction. The measurements are then typically quantified by one or two numbers, that quantify the discrepancy between the measured BAO angle and the fiducial BAO angle. In the case of an anisotropic survey, this yields a measurement perpendicular to the line of sight and one parallel to it:

$$\frac{d_M(z)}{r_d} = \alpha_\perp \frac{d_{M,\,\mathrm{fid}}(z)}{r_{d,\,\mathrm{fid}}}, \qquad \text{and} \qquad \frac{d_H(z)}{r_d} = \alpha_\parallel \frac{d_{H,\,\mathrm{fid}}(z)}{r_{d,\,\mathrm{fid}}}, \tag{5.4.18}$$

with $d_H(z) = c/H(z)$, while isotropic surveys constrain a single quantity defined as

$$\frac{d_V(z)}{r_d} = \alpha \frac{d_{V,\,\mathrm{fid}}(z)}{r_{d,\,\mathrm{fid}}}, \tag{5.4.19}$$

with $d_V(z) = [z\,d_H(z)\,d_M^2(z)]^{\frac{1}{3}}$ a volume averaged distance measure. In Tab. 5.1 we present all measurements that have been taken into account in our study.

In summary, the BAO likelihood piece is

$$-2\log\mathcal{L}_{\mathrm{BAO}} = \left[\vec{Y} - \vec{Y}_{\mathrm{model}}\right]^T \mathbf{C}_{\mathrm{BAO}}^{-1} \left[\vec{Y} - \vec{Y}_{\mathrm{model}}\right], \tag{5.4.20}$$

where $\vec{Y}$ is a vector containing the measured quantities in Tab. 5.1 and $\mathbf{C}_{\mathrm{BAO}}$ is a matrix of correlations assembled also from it.

**CMB anisotropies as BAO measurement.** Finally, we treat the measurement of the first peak in the CMB spectrum as a BAO experiment at redshift $z_*$. This is a well-established procedure, which was also used in the analysis of SN data in Ref. [226], BAO data in Ref. [146]. For our purposes, we use the Planck 2018 results.

The redshift of last scattering is approximated as in [238] by

$$\begin{aligned} z_* &= 1048\,[1+0.00124(\Omega_b h^2)^{-0.738}]\,[1+g_1\,(\Omega_m h^2)^{g_2}],\\ g_1 &= 0.0783\,(\Omega_b h^2)^{-0.238}\,[1+39.5\,(\Omega_b h^2)^{0.763}]^{-1},\\ g_2 &= 0.560\,[1+21.1\,(\Omega_b h^2)^{1.81}]^{-1}. \end{aligned} \tag{5.4.21}$$

Crucially, the redshift $z_d$ which sets the end of the drag epoch and that of last scattering $z_*$ are not exactly equal, with $z_* \gtrsim z_d$. For example, we find $z_* = 1092$ and $z_d = 1063$ for the best fit $\Lambda$CDM cosmology. This affects the comoving sound horizon at the percent level.

The CMB data is implemented in the form of distance priors, which compress the information of the full parameter chains inferred from the final Planck 2018 data. They have been calculated

in Ref. [239] for the cross correlation of TT, EE, TE + lowE power spectra. For the base model ΛCDM, this is

$$\vec{X}^T \equiv \left(R, l_A, \Omega_b h^2\right) = (1.7502, 301.471, 0.02236)\,, \tag{5.4.22}$$

and a marginalised covariance matrix is obtained

$$\mathbf{C}_{\text{Planck}} = 10^{-5} \cdot \begin{pmatrix} 2.1 & 19 & -0.045 \\ 19 & 789 & -0.43, \\ -0.045 & -0.43 & 0.0022 \end{pmatrix}. \tag{5.4.23}$$

See [239] for the distance priors for cosmologies including curvature and dynamical dark energy, which we have implemented as well. The parameters $R$ and $l_A$ are determined by the cosmology as

$$\begin{aligned} R &= \frac{H_0}{c}\sqrt{\Omega_m}\,(1+z_*)\,D_A(z_*) \\ l_A &= (1+z_*)\frac{\pi D_A(z_*)}{r_s(z_*)}. \end{aligned} \tag{5.4.24}$$

Thus, for all analyses labelled '+CMB', we include in the likelihood function a factor

$$-\,2\log\mathcal{L}_{\text{CMB}} = \left[\vec{X} - \vec{X}_{\text{model}}\right]^T \mathbf{C}^{-1}_{\text{Planck}} \left[\vec{X} - \vec{X}_{\text{model}}\right] \tag{5.4.25}$$

### 5.4.6 Joint analysis of cosmological data

To combine the SN and quasar likelihoods, we assume the data to be independent and thus multiply the probabilities, or equivalently add the log-likelihoods,

$$\log\mathcal{L}_{\text{tot}} = \log\mathcal{L}_{\text{SN}} + \log\mathcal{L}_{\text{quasar}} + \log\mathcal{L}_{\text{BAO}} + \log\mathcal{L}_{\text{CMB}}\,. \tag{5.4.26}$$

We sample the posterior probability distribution,

$$p(\theta|\vec{x}) \propto p(\theta)\,\mathcal{L}(\vec{x}|\theta) \tag{5.4.27}$$

assuming uniform prior distributions $p(\theta)$ for the auxiliary as well as the cosmological parameters $\theta = (\alpha', \beta, M_B^0, \Delta M_B, \beta', \delta, \Omega_m, \Omega_\Lambda, w, \ldots)^T$. To this end, we make use of the python package `emcee`, which implements an affine invariant MCMC ensemble sampler [240], a technique particularly well suited for our purposes [241].

In order to quantitatively compare models, we employ the so-called 'Bayes information criterion' (BIC), which takes into account not only how well a model fits a data but also its simplicity in terms of the number of parameters it introduces:

$$\text{BIC} \equiv |\theta|\log(|\vec{x}|) - 2\,\log\left(\hat{\mathcal{L}}\right), \tag{5.4.28}$$

where $\hat{\mathcal{L}}$ is the maximised value of the posterior probability distribution and $|\cdot|$ denotes the length of a vector. In order to select among two models the preferred one, we compare the *evidence* of the data occurring within a given model,

$$p(\vec{x}|M) \equiv \int \mathrm{d}\theta\, p(\theta_M)\, p(\vec{x}|\theta_M)\,, \tag{5.4.29}$$

where $\theta_M$ represents the vector of parameters in a given model $M$. It is in general not possible to directly evaluate this integral, so either this has to done via another MCMC approach, or an

approximate method. It can be shown that the BIC, as defined in Eq. (5.4.29), serves as an estimator of the evidence

$$p(\vec{x}|M) \propto \exp(-\mathrm{BIC}/2)\,. \tag{5.4.30}$$

To see this, we expand the posterior into a Taylor series to second order about the point of maximal likelihood, i.e.

$$\log p(\theta|\vec{x}) \propto \log\left[p(\theta)\,\mathcal{L}(\vec{x}|\theta)\right] \approx \log p(\hat{\theta})\,\mathcal{L}(\vec{x}|\hat{\theta}) - \frac{1}{2}(\theta-\hat{\theta})_i\,\tilde{H}_{ij}\,(\theta-\hat{\theta})_i\,, \tag{5.4.31}$$

with $\tilde{H}$ the negative Hessian of the posterior $p(\theta|\vec{x})$ evaluated at the parameter value $\theta = \hat{\theta}$ that maximises it.[36] The integral in Eq. (5.4.29) is now a multidimensional Gaussian and yields

$$\log p(\vec{x}|M) = \log p(\hat{\theta}) + \log \mathcal{L}(\vec{x}|\hat{\theta}) + \frac{1}{2}\log\left(\frac{2\,\pi^{|\hat{\theta}|}}{\det \tilde{H}}\right). \tag{5.4.32}$$

Note that $\tilde{H}$ is the Fisher information matrix, which one can show factorizes as $\tilde{H} = n\tilde{I}$, where $\tilde{I}$ is the Fisher information matrix for a single data point [242]. Thus, in the limit of large $n$,

$$\log p(\vec{x}|M) = \log p(\hat{\theta}) + \log \mathcal{L}(\vec{x}|\hat{\theta}) + \frac{1}{2}\log\left(\frac{2\,\pi^{|\hat{\theta}|}}{n^{|\hat{\theta}|}\det \tilde{I}}\right). \tag{5.4.33}$$

Taking the asymptotic limit $n \to \infty$ and ignoring all terms that do not scale with $n$, one finds,

$$-\,2\,\log p(\vec{x}|M) = |\hat{\theta}|\log(n) - 2\,\log \mathcal{L}(\vec{x}|\hat{\theta})\,, \tag{5.4.34}$$

from which Eq. (5.4.30) emerges. Therefore, the probability of erroneously choosing Model $M$ over model $M'$ can be estimated as

$$P(M) = \frac{e^{-\mathrm{BIC}(M)/2}}{e^{-\mathrm{BIC}(M)/2} + e^{-\mathrm{BIC}(M')/2}} = \frac{1}{1+e^{\Delta/2}}\,, \quad \text{with } \Delta = \mathrm{BIC}(M) - \mathrm{BIC}(M'). \tag{5.4.35}$$

Thus, if $\Delta = 1.5/5.9/11.6$ there is mild/strong/very strong evidence to reject model $M$ in favour of model $M'$, corresponding to $1 - P(M) = 68\%/95\%/99.7\%$ CL, respectively.

[36] The first order term vanishes due to the maximum condition, and we define $\tilde{H} = -H$, such that it is positive definite.

## 5.5 Cosmological fits

Having defined all model quantities and data sets, we now present the results of the numerical data analyses in the various cosmological models. For each model, the full list of sampling parameters consists of the model-specific parameters introduced in Sec. 5.3, plus a number of universal nuisance parameters, which we have defined in Sec. 5.4. First off, we study the flat concordance cosmology, ΛCDM. We then turn to two parametrised extensions of ΛCDM, adding curvature ($k$ΛCDM) and finally a free DE equation of state ($w$ΛCDM) in Secs. 5.5.2 and 5.5.3. Here, we will validate our findings in the context of existing surveys, and we will present for the first time results of a combined analysis using SNe, BAO, CMB data in conjunction with the advertised quasar standard candles. In order to compare the validity of the models, we evaluate the Bayes information criterion (BIC), which has been defined in Eq. (5.4.29).

Subsequently, we turn to non-parametric extensions of ΛCDM, the first of which is bigravity – with and without curvature. Finally, we discuss the phenomenological implications within CG, where we will conclude that this framework is not apt to explain the current data, and can essentially be ruled out in its basic formulation. Nevertheless, we also show that an intriguing feature of the model is that certain parameters appear both in the cosmological solution as well as local geometries, and therefore both galactic and cosmological data can constrain the same set of parameters. However, it turns out that the two data sets yield incompatible results for the model parameters. We hope that these results can point towards a phenomenologically viable theory in the future. We summarize our results in Table 5.2.

### 5.5.1 Flat ΛCDM model

In a first step, we apply the techniques introduced in Sec. 5.4 to a standard ΛCDM model to cross validate our findings with the literature. Setting up a total of 512 uniformly sampled parameter points and evolving the Markov Chain Monte Carlo (MCMC) sampler for 1000 iterations, we find for different data sets the posterior distributions shown in the rightmost panels of Fig. 5.1. Note that we have chosen flat priors whose allowed ranges encode some physical expectation, i.e. $60\,\frac{\mathrm{km/s}}{\mathrm{Mpc}} < H_0 < 80\,\frac{\mathrm{km/s}}{\mathrm{Mpc}}$ and $0 < \Omega_m < 1$, and a Gaussian prior for $\Omega_b\,h^2$ (see App. 5.4), which implements independent information from nucleosynthesis (which we thereby implicitly assume to proceed in a standard manner).[37] From Fig. 5.1 we can draw a number of important conclusions: First, there is no significant correlation between model and nuisance parameters. Second, SN nuisance parameters are only affected by SN data and do not respond significantly to the inclusion of quasar data and vice versa. Thus, the calibration can – in principle – be done independently, and we see that the combined data sets (which also include BAO and CMB data) yield confidence intervals that are compatible with the individual analyses. Third, the $M_B$–$H_0$ panel of Fig. 5.1 shows that SN data (and also quasar data) alone cannot constrain $H_0$ as their absolute magnitudes are degenerate with $H_0$ – even if only weakly. In order to calibrate the SN data, we need to break this degeneracy, e.g. by measurements involving standard rulers, or $H(z)$ measurements as given by the BAO data, cf. App. 5.4. And finally, our findings are in agreement with those in the literature for the JLA SNe sample, cf. Ref. [226], and the quasar sample [143, 243].

Marginalising over the nuisance parameters yields the compressed results displayed in Fig. 5.2 and summarised in Tab. 5.2. Here, we would like to note that our results agree well with the findings by the Planck collaboration, which find a slightly lower value for $H_0 = (67.4 \pm 0.5)\,\frac{\mathrm{km/s}}{\mathrm{Mpc}}$ [29] (we find $H_0 = 68.4 \pm 0.4\,\frac{\mathrm{km/s}}{\mathrm{Mpc}}$). The inclusion of more data sets does not affect the value of $H_0$ significantly and thus does not alleviate or worsen the long-standing tension between local calibrations of SNe (see e.g. Refs. [155] for the most recent analysis) and the results from CMB measurements. In conclusion,

[37] The radiation density is negligible at low redshifts, hence $\Omega_\Lambda + \Omega_m = 1$. We are then left with $\Omega_m$, $\Omega_b$ and $H_0$ as the cosmological parameters.

we find that SNe and quasars yield compatible, tight constraints on $\Omega_m$, which is found to be $\Omega_m = 0.31 \pm 0.03$. Notice that neither SNe nor quasars can constrain $H_0$ alone because their absolute magnitudes are unknown [cf. Eq. (5.4.5)]. Via the inverse distance ladder approach, we break the degeneracy between $H_0$ and the magnitudes by including measurements of acoustic oscillation scale standard rulers. Combined, these allow us to constrain tightly the absolute magnitudes and $H_0$, as Fig. 5.2b reveals. In combination with the accurate determination of the location and height of the first CMB anisotropy peak, the parameters converge to $\Omega_m = 0.308 \pm 0.006$ and $H_0 = (68.0 \pm 0.4)\,\frac{\mathrm{km/s}}{\mathrm{Mpc}}$, which is in good agreement with analyses of the CMB [29] with the results $H_0 = (67.4 \pm 0.5)\,\frac{\mathrm{km/s}}{\mathrm{Mpc}}$ and $\Omega_m = 0.315 \pm 0.007$, BAO [146] with the results $H_0 = (67.3 \pm 1.1)\,\frac{\mathrm{km/s}}{\mathrm{Mpc}}$ and $\Omega_m = 0.302 \pm 0.008$, and the JLA SN sample [225] with result $\Omega_m = 0.295 \pm 0.034$, establishing the robustness of our methodology.

### 5.5.2 ΛCDM with curvature

Next, we modify the analysis carried out in the previous section by relaxing the condition $\Omega_m + \Omega_\Lambda = 1$ to include finite spatial curvature by introducing a new model parameter $\Omega_k = 1 - \Omega_m - \Omega_\Lambda$. A glance at the posterior distribution in Fig. 5.3 and the results summarised in Tab. 5.2 allows us to draw a number of interesting conclusions.

It is conspicuous that the expected values for $\Omega_m$ and $\Omega_\Lambda$ are shifted to larger values once the quasar data is taken into account on top of the SN data, while in the previous case they were reasonably in accordance. This can be understood by recalling that quasars can be tested to much higher redshift so the effect of spatial curvature becomes relevant, effectively shifting $\Omega_m$ and $\Omega_\Lambda$ to much larger values compared to what is found for the SN data alone.

One further interesting observation is that the inclusion of BAO and CMB data stabilises the values of the matter and dark energy densities at values close to the flat ΛCDM case, $\Omega_m = 0.302 \pm 0.006$, $\Omega_\Lambda = 0.698 \pm 0.006$ and $H_0 = 68.6 \pm 0.6\,\frac{\mathrm{km/s}}{\mathrm{Mpc}}$.

The curvature density is obtained from Eq. (5.3.7) and the results in Tab. 5.2,

$$\Omega_k = 0.000 \pm 0.008\,,$$

which hints at a flat universe. In fact, the statistical evidence shows that $k$ΛCDM is disfavoured with respect to ΛCDM for any data sets considered in Tab. 5.2. Our results show that relaxing the flatness condition of ΛCDM is not beneficial in terms of statistical evidence and the cosmological parameters converge nevertheless to a flat ΛCDM universe, while adding another free parameter is penalised by the BIC.

### 5.5.3 $w$ΛCDM

We find similar results if we parametrically extend the standard cosmology ΛCDM to leave the equation of state parameter $w$ of dark energy an undetermined parameter. In this case, $w$ΛCDM is strongly disfavoured compared to ΛCDM for SN, SN+Q and SN+Q+BAO+CMB, and disfavoured for SN+Q+BAO. The curvature density here is found to be $\Omega_k = -0.001 \pm 0.013$ and the equation of state parameter turns out to be $w = -1.011 \pm 0.05$, values which are again very close to those of ΛCDM.

From Fig. 5.4 we conclude that the additional parameters open up new regions of parameter space and intricate degeneracies arise, see e.g. in the $w$–$\Omega_m$ marginalised posterior. Consequently, we see that certain data sets, e.g. the BAO-only posterior, favour a much lower Hubble rate around $H_0 = 67.6\,\frac{\mathrm{km/s}}{\mathrm{Mpc}}$ compared to the combined fit. The reason lies in the fact that the CMB data do not allow an equation of state parameters much larger than $w = -1$ (as preferred by the BAO data), and the two parameters share precisely such a degeneracy, cf. bottom left panel of Fig. 5.4b.

### 5.5.4 Bigravity cosmology

We now discuss the bigravity model fits for our setup.[38] As shown in Sec. 5.3.2, the parameters $m$ and $\alpha$ have been absorbed into the definition of the $B_i$, which leaves us with three bigravity fit parameters (on top of the usual number of parameters for ΛCDM and $k$ΛCDM). This is the correct number of independent, physical bigravity parameters [167]. Previous works on cosmological fits of bigravity include Refs. [153, 171, 246]. We improve on these results by the inclusion of the new quasar data set, and by performing the full Bayesian analysis over all bigravity parameters. Previous analyses have often restricted their attention to subsets of models, in which only one or two of the $B_i$ are non-zero (for a counterexample, see Ref. [153]). The main reason for restricting only to subsets of the parameter space in some previous work has been the fact that increasing the number of free parameters enlarges the volume of the parameter space, which then results in a larger Bayes factor. At the present time, we see no a priori physical motif to restrict the bigravity parameter space, and have therefore only analysed the unrestricted model, i.e. we fit *all* bigravity parameters ($B_{1,2,3}$) as well as a free parameter to describe curvature. The analysis in [153] has shown that the quality of the fit does not improve significantly when using a restricted model; however, due to the large number of possible correlations between the full set of bigravity parameters, a fit using a constrained model offers more insight into the structure of the bimetric model.

Nevertheless, the bigravity parameters are *a priori* allowed to take on any value in $\mathbb{R}$, and with the restriction on $B_1$ presented in Sec. 5.3.2, the allowed ranges are $B_1 > 0$ and $B_2, B_3 \in \mathbb{R}$.

This parameter space could be sensibly scanned by a logarithmic sampling over a large range. However, it is reasonable to assume that the best fit cosmology closely resembles ΛCDM. We therefore anticipate that the dynamical CC takes the current value $\Lambda(z=0) \sim (H_0^{\Lambda\mathrm{CDM}})^2$. Under the constraint of the master equation Eq. (5.3.14), this implies that all $B_i$ are of the same order, barring any fine tuning. For the analysis, we therefore sample the bigravity parameters in the ranges $B_1 = [0, +100]$ and $B_{2,3} = [-100, +100]$ using flat priors. The chosen range ensures that the dynamical effects of bigravity are small, yet non-negligible: as Eq. (5.3.14) shows, choosing a larger value for any of the $B_i$ decreases the redshift-dependence of the ratio of scale factors $y$, as the time-varying energy densities are suppressed in this case. However, with a constant $y$ the model's dynamics reproduce ΛCDM.

Fig. 5.5 shows the results in bigravity with zero curvature, where we find that the best fit values of $\Omega_m$, $\Omega_b$ and $H_0$ for the combined analysis depart only slightly from their counterparts in concordance cosmology and its related theories. For the bigravity parameters $B_{1,2,3}$, we find neither a clear sign of convergence, nor a simply visualised correlation between any pair of parameters.[39] This can be understood by inspecting Fig. 5.7: due to our choice of priors, the bigravity models which are probed by our setup deviate from ΛCDM, however only at the percent level and in a redshift interval where the data is less constraining. In consequence, the standard cosmological parameters $(\Omega_m, \Omega_b, H_0)$ are well constrained, which also holds for the parameter which characterises the onset of the deviation from ΛCDM, the graviton mass [Eq. (5.3.24)]. Using the best fit cosmology, we obtain $m_g = (142 \pm 1)\, H_0$, which complies with our expectation: it is a value close enough to $H_0$ so that the physical interpretation is that the graviton mass provides the dark energy component, but also satisfies the Higuchi ghost bound. It is also compatible with local tests of gravity and massive spin-2 states [1, 247, 248].

While these results show that a consistent bigravity cosmology can be formulated, and that it is compatible with our range of observational tests, the pressing question is whether bigravity improves the fit compared to ΛCDM. The value $\Delta\mathrm{BIC} = 32$ reveals that this model is not preferred

[38] Note that there are several possible modifications to our standard bigravity setup, which may considerably alter the cosmology. One such case is the choice of the matter coupling; e.g., see the analyses in Refs. [244, 245] for bigravity with doubly coupled matter.

[39] As a check, we have also performed the fit using the logarithmic sampling variables $\log_{10} \pm B_i$, the results of which support these conclusions.

w.r.t. simpler modifications of ΛCDM. This is explained as this model mimics ΛCDM with zero curvature at large $z$, and thus is unable to improve the fit of the precisely known data sets BAO and CMB; but at the same time, the model brings with it an increased number of model parameters, which increases the BIC.

With flat bigravity being strongly disfavoured, we thus turn to bigravity with a free curvature parameter in Fig. 5.6. Again, we find all bigravity parameters to be $\mathcal{O}(100)$, while the mass density parameters and $H_0$ are similar to those found with $(k)\Lambda$CDM. The physical graviton mass is of the same order, $m_g = (169 \pm 2)\, H_0$. The curvature density is compatible with a flat universe. With these results it is not a surprise that we find $\Delta\text{BIC} = 29$, indicating that bigravity with curvature is also strongly disfavoured, as it does not provide a significant improvement on the cosmological fit. However, one must keep in mind that these results do not rule out the possibility of a bimetric cosmology compatible with observations; the BIC is merely a statement about the improvement of the fit, while penalising the introduction of additional variables. From a model building point of view, bigravity still retains its desired features.

Furthermore, we comment on the fate of bimetric cosmologies at high $z$: as discussed in Sec. 5.3.2, our chosen branch of bigravity must reduce to ΛCDM in this limit, as the second metric is effectively turned off when $y \to 0$. We have verified this behaviour numerically for the best fit parameters, see Fig. 5.7. This shows that the best fit bigravity cosmologies match $(k)\Lambda$CDM at early times, i.e. at redshifts upwards of $z = 10 - 100$. Therefore, a fit involving only BAO and CMB measurements must yield the same result for $(k)$bigravity or $(k)\Lambda$CDM; we have verified this as well. Following the argumentation of Ref. [186], one can interpret this as the Vainshtein screening kicking in for large densities (large redshifts).

Finally, we discuss our choice of sampling the parameters $B_{1,2,3}$, fixing the redundant parameter $\alpha$. As we have seen, the results do not converge on the interval we are probing. However, we will now recall the discussion of perturbative stability at early times. In this light, our results should be interpreted as implementing the choice $\alpha = 1$. As shown in Ref. [181], for $\alpha \ll 1$ and the $B_i$ within the same order, the instability of linear perturbations can be shifted to very early times. By the rescaling invariance of the combination of parameters $\alpha^{-i} B_i$, an equivalent cosmology is given by the choice $\alpha = 1$ while $B_1 \ll B_2 \ll B_3$. Clearly, for e.g. $\alpha = 10^{-17}$, this is not accommodated by our choice of priors. However, we have also implemented a search for solutions of this type through logarithmic sampling; we do not find a statistically relevant cosmological fit for such a choice of parameters. This is easily understood when looking at the master equation Eq. (5.3.14): for a large hierarchy between the $B_i$, these parameters need to be tuned to a high degree in order to allow for a dynamical solution of the master equation.

### 5.5.5 Conformal Gravity

Previous works on cosmological fits in CG can be found in Refs. [151, 249–251]. The first of these references uses SN data as standard candles; Ref. [249] uses SNe and GRBs as standard candles; Ref. [250] uses supernovae as standard candles and $H(z)$ measurements. In Ref. [251] the model parameters are fixed to the best fit values of Ref. [151] and extrapolated to GRB and quasar data to account for the statistical evidence of these model parameters.

In the present work, we utilise the SNe and quasars data sets for an up-to-date assessment of the viability of CG cosmology compared to the base ΛCDM model. Note that we do not include the CMB measurements in this section, since the Planck analysis is based on a flat ΛCDM cosmology, and CG cosmology does not reduce to the concordance model at high redshift. For similar reasons, we exclude also the BAO data set. In this case, a careful treatment of the calculations of the drag epoch $z_d$ and the comoving sound horizon $c_s(z)$ (cf. Tab. 5.1 in Sec. 5.4) are required, a task which is beyond the scope of this work. Note that in this fit, the Hubble parameter remains unconstrained, as our SN and quasar samples are not calibrated in absolute magnitude.

As explained in Sec. 5.3.3, we use Eq. (5.3.33) as the Friedmann equation valid for low redshifts. Hence, we choose $\Omega_k = 1 - \overline{\Omega}_\Lambda$ as free model parameter which can be tested by the SN+Q data set. The results are presented in Fig. 5.8 (see also Table 5.2). Under consideration of only SN data, CG is disfavoured with respect to ΛCDM and becomes strongly disfavoured if quasars are included in the analysis. The best fit value for the joint analysis of SNe and quasar data is $\Omega_k = 0.850^{+0.070}_{-0.081}$. This value for $\Omega_k$ agrees well with the results of Ref. [249] which find $\Omega_k = 0.836^{+0.015}_{-0.022}$. However, Refs. [151, 250] find smaller values, $\Omega_k \approx 0.63$ and $\Omega_k = 0.67 \pm 0.06$, respectively. These deviations may be caused by the difference in the data sets which are considered. In particular, the observational data considered in Ref. [249] and in this work reaches out to higher redshifts $z \sim 6$ compared to the data considered in Refs. [151, 250].

Under the above considerations we are led to the conclusion that the cosmological model obtained from CG as outlined in Sec. 5.3.3 is strongly disfavoured with respect to the baseline ΛCDM cosmology.

As we have outlined in Sec. 5.3.3, CG has the unique feature that $\Omega_k$ can also be tested by galactic dynamics and we find that this impairs the viability of CG further. To be more precise, the relation in Eq. (5.3.36) enables us to independently infer the value of $\Omega_k$ from galactic rotation curves. For instance, the result of Ref. [222] is

$$\gamma_0 = 3.06 \cdot 10^{-30}\mathrm{cm}^{-1} \quad \Rightarrow \quad \Omega_k = 4.12 \cdot 10^{-4}\,,$$

if it is assumed that CG addresses the missing mass problem of galaxies without invoking a dark matter component. This result was obtained from a fit of galactic rotation curves of 207 galaxies. A severe tension of the above value for $\Omega_k$ with our results obtained from cosmological data is manifest, cf. Tab. 5.2. It is clear that the observed galactic dynamics demand a significant smaller value of $\Omega_k$ (or equivalently $\gamma_0$) than the observations on cosmological scales which we consider in this work. Hence, if it is assumed that CG explains galactic rotation curves without dark matter, a consistent reconciliation of both phenomena seems unlikely. In fact, we have performed a joint analysis of cosmological and galactic data which is based on the relation in Eq. (5.3.36) and we did not find sensible results. Furthermore, we can confirm that we find a similar value of $\gamma_0$ as in Ref. [201] from our own analysis of the SPARC rotation curve data set. These considerations allow us to make the statement that CG is not able to address the missing mass problem without invoking dark matter and to account for a viable cosmological evolution simultaneously. However, with a dark matter component present as in ΛCDM one has to take only the constraints imposed by cosmology into account.

| model | parameter | SN | SN+Q | SN+Q+BAO | SN+Q+BAO+CMB |
|---|---|---|---|---|---|
| ΛCDM | $\Omega_m$ | $0.296^{+0.030}_{-0.028}$ | $0.311^{+0.028}_{-0.027}$ | $0.292^{+0.013}_{-0.012}$ | $0.3081^{+0.0063}_{-0.0057}$ |
| | $100\,\Omega_b$ | $4.71^{+0.93}_{-0.87}$ | $4.74^{+0.96}_{-0.87}$ | $4.82^{+0.13}_{-0.13}$ | $4.85^{+0.05}_{-0.05}$ |
| | $H_0$ $[\frac{\text{km/s}}{\text{Mpc}}]$ | $68.6^{+7.4}_{-6.0}$ | $68.4^{+7.3}_{-6.0}$ | $67.86^{+0.94}_{-0.93}$ | $68.04^{+0.43}_{-0.44}$ |
| | BIC | −447 | 2722 | 2850 | 2825 |
| $k$ΛCDM | $\Omega_m$ | $0.21^{+0.10}_{-0.10}$ | $0.36^{+0.049}_{-0.050}$ | $0.307^{+0.017}_{-0.017}$ | $0.302^{+0.006}_{-0.006}$ |
| | $\Omega_\Lambda$ | $0.55^{+0.19}_{-0.19}$ | $0.80^{+0.10}_{-0.10}$ | $0.775^{+0.051}_{-0.054}$ | $0.698^{+0.006}_{-0.006}$ |
| | $100\,\Omega_b$ | $4.77^{+0.93}_{-0.89}$ | $4.68^{+0.94}_{-0.84}$ | $4.39^{+0.36}_{-0.34}$ | $4.80^{+0.09}_{-0.09}$ |
| | $H_0$ $[\frac{\text{km/s}}{\text{Mpc}}]$ | $68.2^{+7.5}_{-5.8}$ | $68.9^{+7.2}_{-6.1}$ | $71.1^{+2.9}_{-2.8}$ | $68.60^{+0.63}_{-0.63}$ |
| | ΔBIC | +6 | +6 | +6 | +6 |
| $w$ΛCDM | $\Omega_m$ | $0.173^{+0.110}_{-0.096}$ | $0.335^{+0.064}_{-0.073}$ | $0.312^{+0.018}_{-0.018}$ | $0.304^{+0.009}_{-0.008}$ |
| | $\Omega_\Lambda$ | $0.45^{+0.35}_{-0.21}$ | $0.82^{+0.24}_{-0.23}$ | $0.899^{+0.069}_{-0.072}$ | $0.695^{+0.009}_{-0.009}$ |
| | $100\,\Omega_b$ | $4.68^{+0.94}_{-0.85}$ | $4.76^{+0.91}_{-0.91}$ | $4.61^{+0.42}_{-0.35}$ | $4.74^{+0.14}_{-0.14}$ |
| | $H_0$ $[\frac{\text{km/s}}{\text{Mpc}}]$ | $68.8^{+7.3}_{-6.0}$ | $68.3^{+7.6}_{-5.7}$ | $69.3^{+2.8}_{-2.9}$ | $68.73^{+0.97}_{-0.96}$ |
| | $w$ | $-1.09^{+0.32}_{-0.68}$ | $-0.96^{+0.20}_{-0.35}$ | $-0.821^{+0.054}_{-0.062}$ | $-1.011^{+0.045}_{-0.045}$ |
| | ΔBIC | +13 | +14 | +7 | +13 |
| Bigravity | $\Omega_m$ | $0.319^{+0.059}_{-0.035}$ | $0.330^{+0.049}_{-0.034}$ | $0.305^{+0.025}_{-0.015}$ | $0.3016^{+0.0071}_{-0.0063}$ |
| | $100\,\Omega_b$ | $4.67^{+0.91}_{-0.82}$ | $4.7^{+0.95}_{-0.85}$ | $4.64^{+0.21}_{-0.39}$ | $4.66^{+0.11}_{-0.10}$ |
| | $H_0$ $[\frac{\text{km/s}}{\text{Mpc}}]$ | $68.9^{+7.0}_{-5.9}$ | $68.7^{+7.2}_{-6.1}$ | $69.2^{+3.1}_{-1.6}$ | $69.17^{+0.71}_{-0.78}$ |
| | $B_1$ | $53^{+32}_{-34}$ | $53^{+34}_{-33}$ | $53^{+32}_{-35}$ | $44^{+29}_{-23}$ |
| | $B_2$ | $-40^{+49}_{-40}$ | $-48^{+52}_{-35}$ | $-53^{+47}_{-32}$ | $-55^{+35}_{-30}$ |
| | $B_3$ | $-21^{+73}_{-53}$ | $-24^{+70}_{-51}$ | $-24^{+73}_{-52}$ | $-41^{+51}_{-40}$ |
| | ΔBIC | +20 | +23 | +24 | +32 |
| $k$Bigravity | $\Omega_m$ | $0.24^{+0.12}_{-0.11}$ | $0.386^{+0.069}_{-0.059}$ | $0.317^{+0.024}_{-0.020}$ | $0.2974^{+0.0068}_{-0.0071}$ |
| | $\Omega_\Lambda$ | $0.53^{+0.18}_{-0.17}$ | $0.780^{+0.092}_{-0.107}$ | $0.755^{+0.053}_{-0.058}$ | $0.7056^{+0.0079}_{-0.0076}$ |
| | $100\,\Omega_b$ | $4.84^{+0.87}_{-0.90}$ | $4.77^{+0.95}_{-0.89}$ | $4.24^{+0.39}_{-0.39}$ | $4.70^{+0.11}_{-0.11}$ |
| | $H_0$ $[\frac{\text{km/s}}{\text{Mpc}}]$ | $67.8^{+7.2}_{-5.5}$ | $68.3^{+7.3}_{-6.0}$ | $72.4^{+3.5}_{-3.2}$ | $69.23^{+0.77}_{-0.72}$ |
| | $B_1$ | $52^{+32}_{-32}$ | $53^{+34}_{-35}$ | $47^{+35}_{-33}$ | $49^{+32}_{-29}$ |
| | $B_2$ | $-43^{+50}_{-41}$ | $-46^{+53}_{-37}$ | $-58^{+45}_{-28}$ | $-41^{+29}_{-33}$ |
| | $B_3$ | $-18^{+73}_{-57}$ | $-25^{+76}_{-53}$ | $-24^{+74}_{-54}$ | $-36^{+45}_{-44}$ |
| | ΔBIC | +26 | +30 | +30 | +29 |
| CG | $\Omega_k$ | $0.772^{+0.081}_{-0.068}$ | $0.850^{+0.070}_{-0.081}$ | – | – |
| | $100\,\Omega_b$ | $4.51^{+0.83}_{-0.73}$ | $4.32^{+0.67}_{-0.57}$ | – | – |
| | $H_0$ $[\frac{\text{km/s}}{\text{Mpc}}]$ | $70.0^{+6.6}_{-5.6}$ | $71.6^{+5.4}_{-4.9}$ | – | – |
| | ΔBIC | +9 | +56 | – | – |

**Table 5.2:** Summary of the results in the different model as discussed in Sec. 5.5. The BIC in ΛCDM is given in absolute numbers, while all others are relative w.r.t the ΛCDM best fit. The color indicates the statistical significance: strong support ($\Delta\text{BIC} < -12$), favourable ($\Delta\text{BIC} < -6$), inconclusive ($\Delta\text{BIC} < 6$), disfavoured ($\Delta\text{BIC} < 12$), strongly disfavoured ($\Delta\text{BIC} \geq 12$) with respect to ΛCDM; see the Sec. 5.4.6 for details.

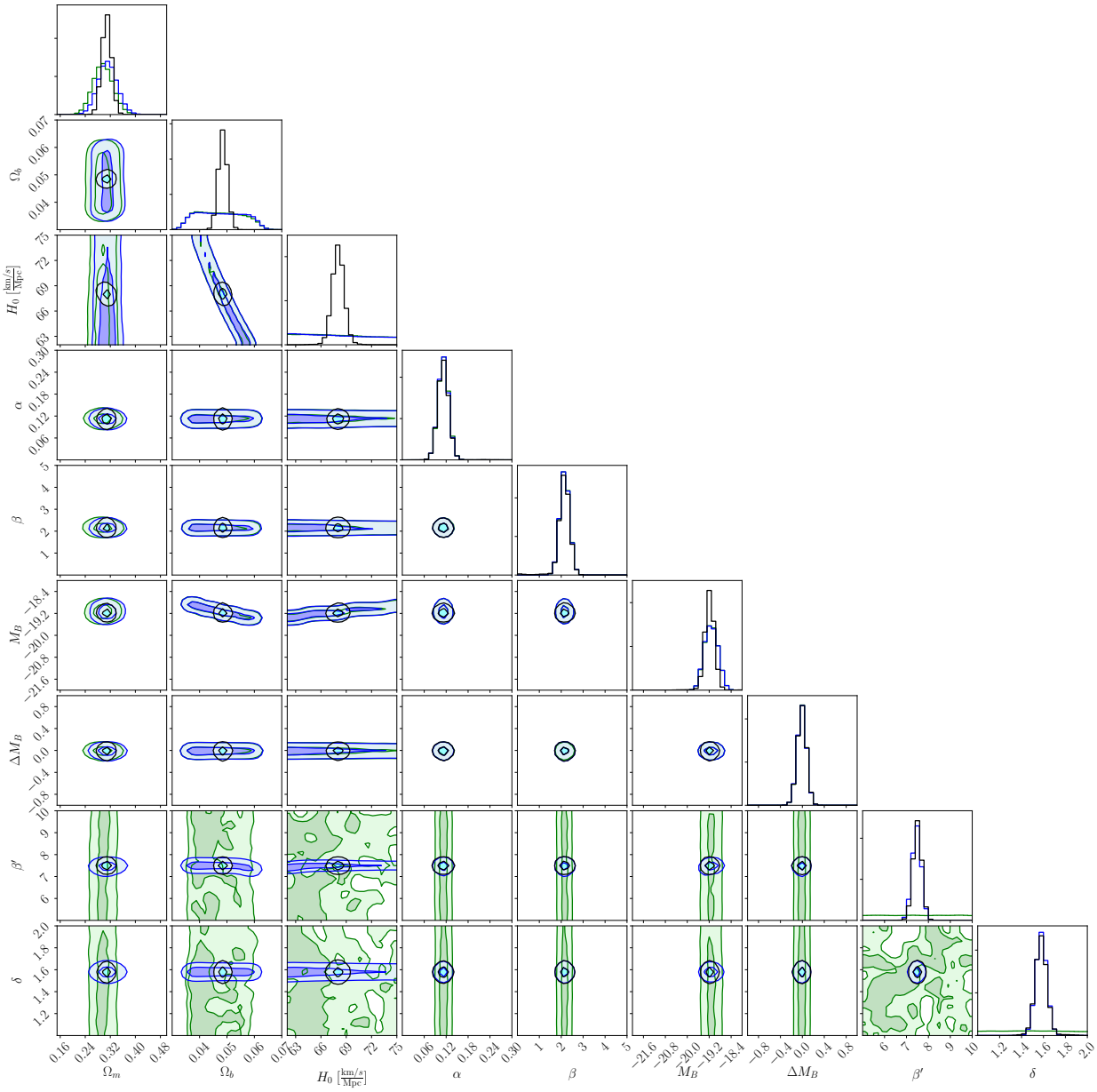


**Figure 5.1:** Marginalised 1D and 2D posterior distributions for ΛCDM for all cosmological and nuisance parameters for SNe (green), SN+quasars (blue) and combined SN+quasars+BAO+CMB (black) data sets, also including the Gaussian prior on $\Omega_b\, h^2$. The SN data alone does not constrain the quasar nuisance parameters $\beta'$ and $\delta$, while the inclusion of quasars has only little effect on the SN nuisance parameters. Notice also that there is no significant correlation between the nuisance and cosmological parameters. See Sec. 5.4 for the definitions of all nuisance parameters.

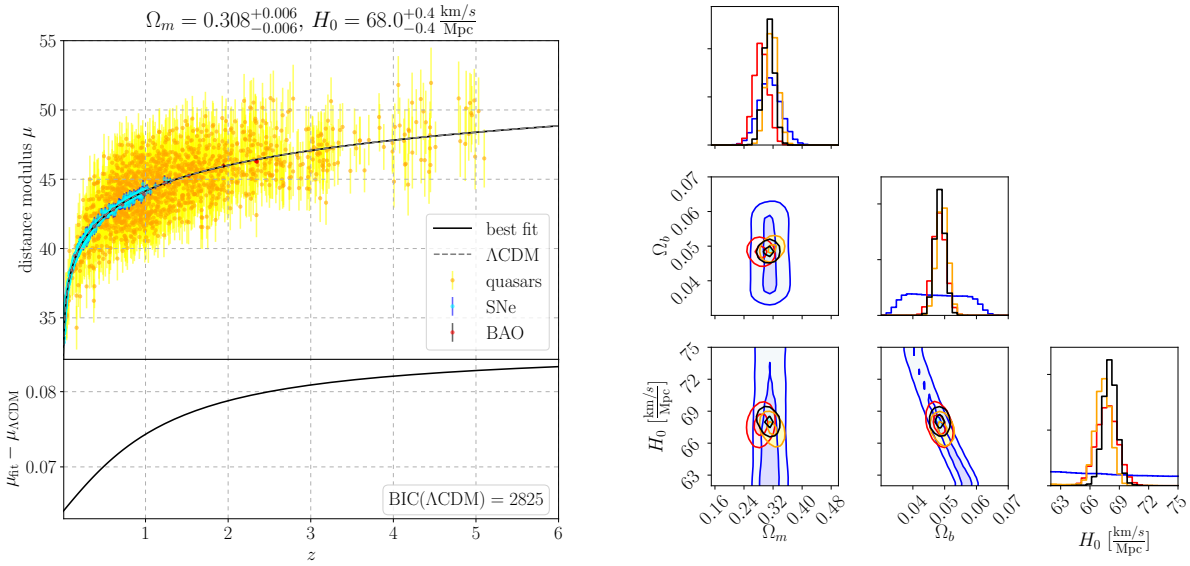


**(a)** Hubble diagram in ΛCDM

**(b)** posterior distribution in ΛCDM

**Figure 5.2:** Results in ΛCDM. *Left:* Hubble diagram of the combined fit using all available data sets. The BIC is given in absolute numbers. *Right*: Posterior distribution of model parameters with marginalised auxiliary parameters (including BBN prior). SN+Quasars (blue), BAO (red), CMB (orange), all combined (black). The contours represent $1\sigma$ and $2\sigma$ intervals.

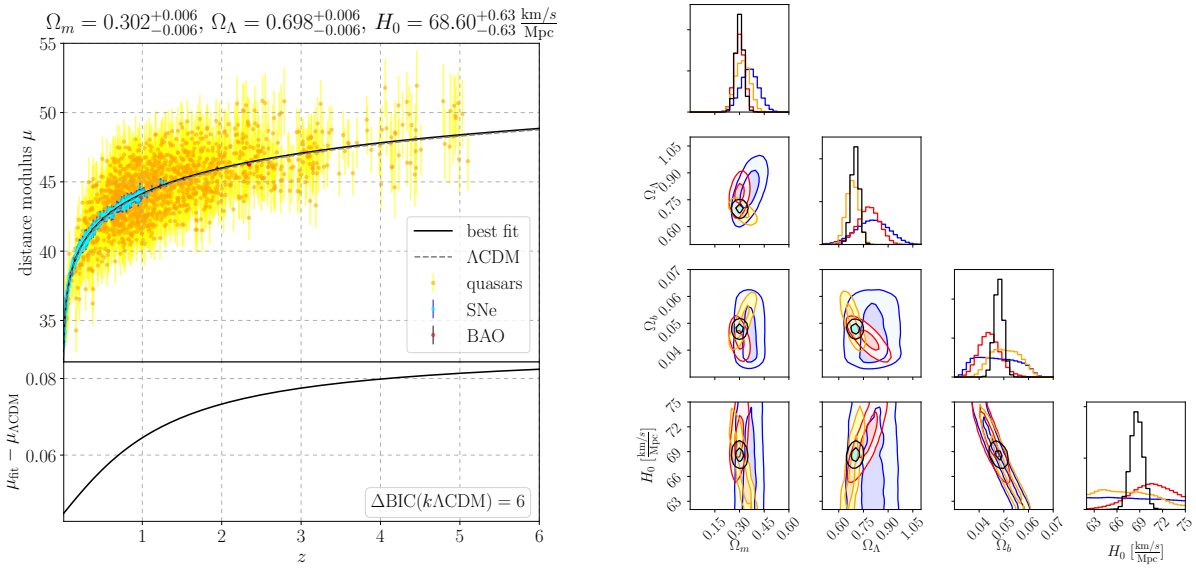


**(a)** Hubble diagram in $k\Lambda$CDM

**(b)** posterior distribution in $k\Lambda$CDM

**Figure 5.3:** Results in $k\Lambda$CDM. *Left:* Hubble diagram of the combined fit using all available data sets. *Right*: Posterior distribution of model parameters with marginalised auxiliary parameters (including BBN prior). SN+Quasars (blue), BAO (red), CMB (orange), combined (black).

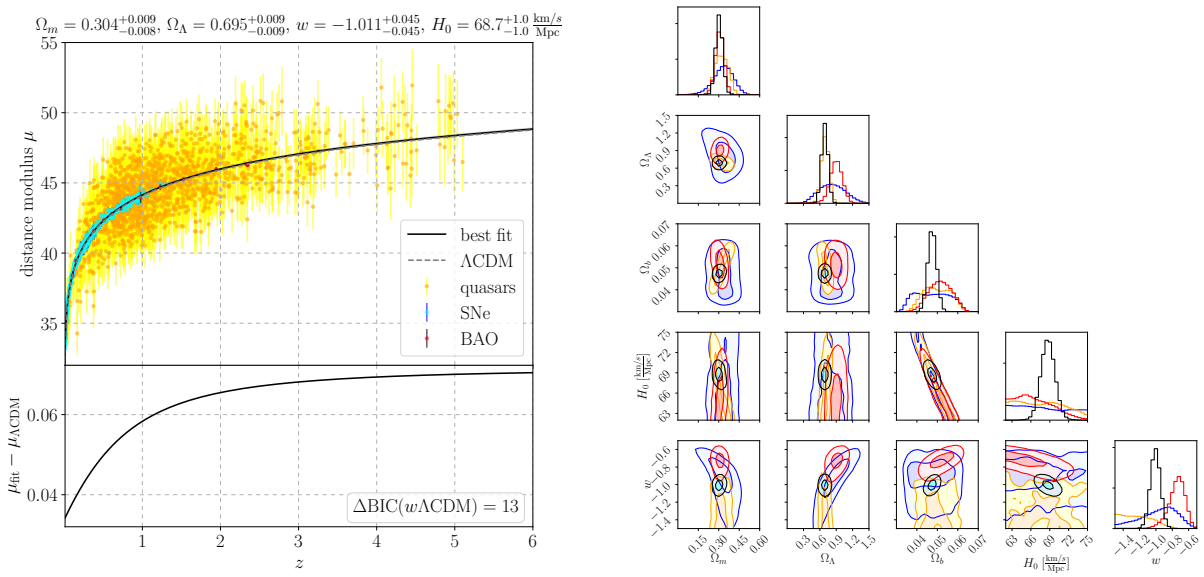


**(a)** Hubble diagram in $w\Lambda$CDM

**(b)** posterior distribution in $w\Lambda$CDM

**Figure 5.4:** Results in $w\Lambda$CDM. *Left:* Hubble diagram of the combined fit using all available data sets. *Right*: Posterior distribution of model parameters with marginalised auxiliary parameters (including BBN prior). SN+Quasars (blue), BAO (red), CMB (orange), combined (black).

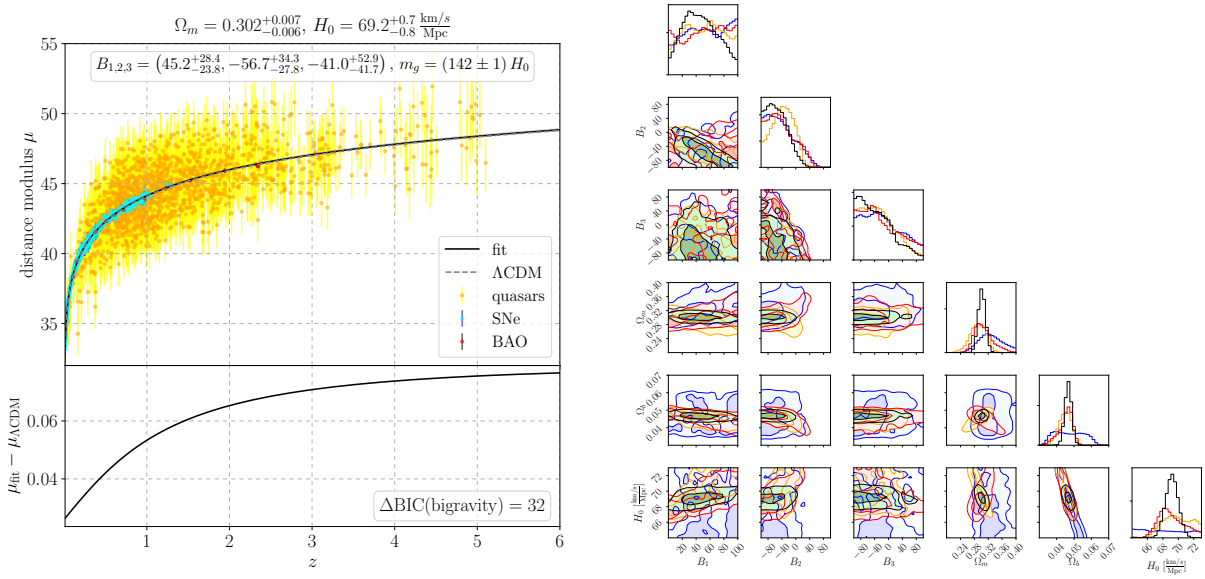


**(a)** Hubble diagram in bigravity

**(b)** posterior distribution in bigravity

**Figure 5.5:** Results in bigravity with flat geometry. *Left:* Hubble diagram of the combined fit using all available cosmological data sets. The inset shows the best fit values of $B_{1,2,3}$ and the physical graviton mass as given by Eq. (5.3.24). *Right*: Posterior distribution of model parameters with marginalised auxiliary parameters (including BBN prior). SN+quasars (blue), BAO (red), CMB (orange), combined (black).

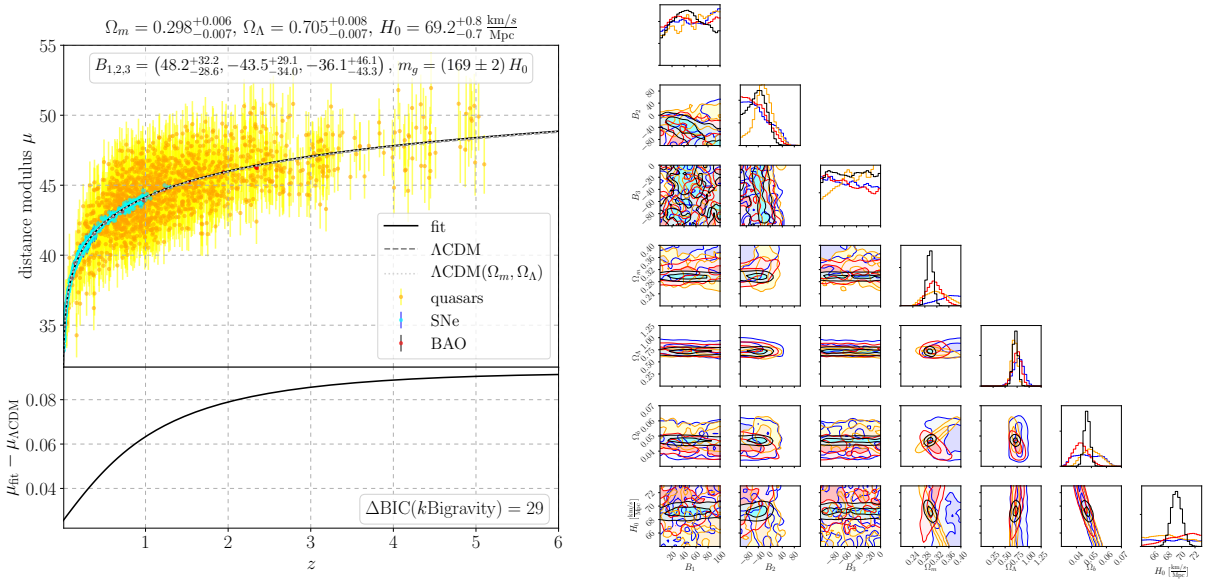


**(a)** Hubble diagram in $k$Bigravity

**(b)** posterior distribution in $k$Bigravity

**Figure 5.6:** Results in bigravity with curvature. *Left:* Hubble diagram of the combined fit using all available cosmological data sets. The best fit values of $B_{1,2,3}$ and the physical graviton mass are shown as an inset. *Right*: Posterior distribution of model parameters with marginalised auxiliary parameters (including BBN prior). SN+quasars (blue), BAO (red), CMB (orange), combined (black).

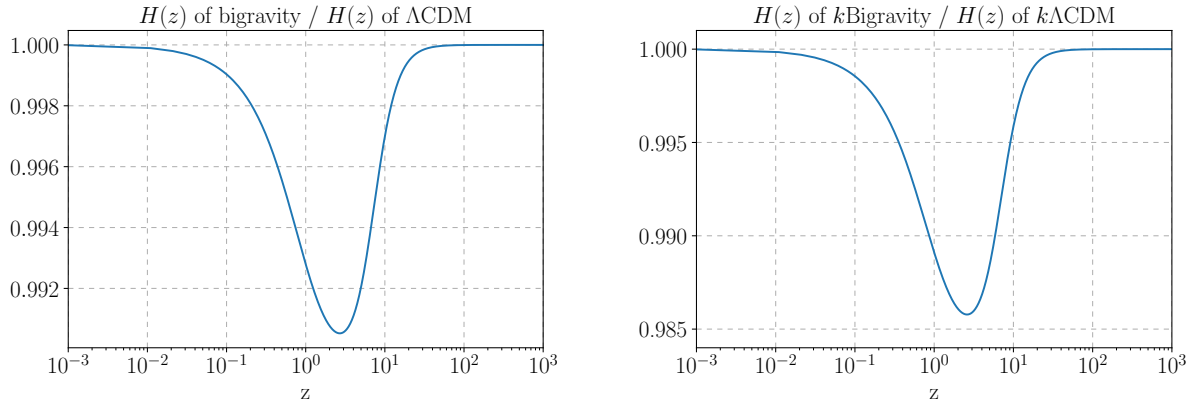


**(a)** Hubble rate in bigravity over ΛCDM

**(b)** Hubble rate in $k$Bigravity over $k$ΛCDM

**Figure 5.7:** Ratio of Hubble parameter $H(z)$ in (open) bigravity over (open) ΛCDM. The cosmological parameters have been set to the best fit (considering all data sets) of the respective bimetric theory. As expected, the bimetric theories asymptotically match ($k$)ΛCDM at high and low $z$.

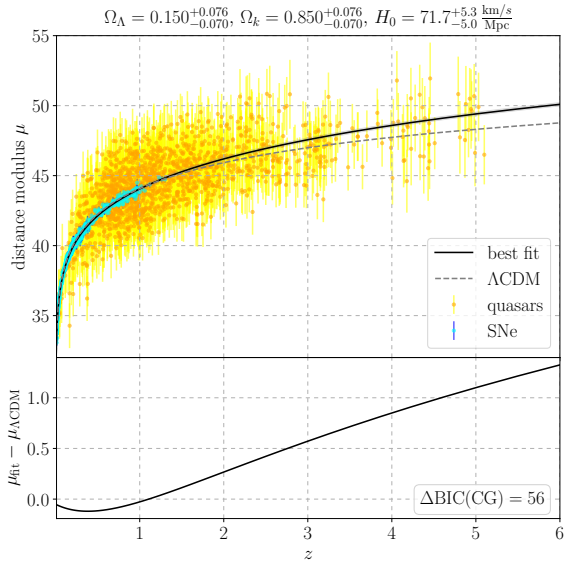


**(a)** Hubble diagram in CG

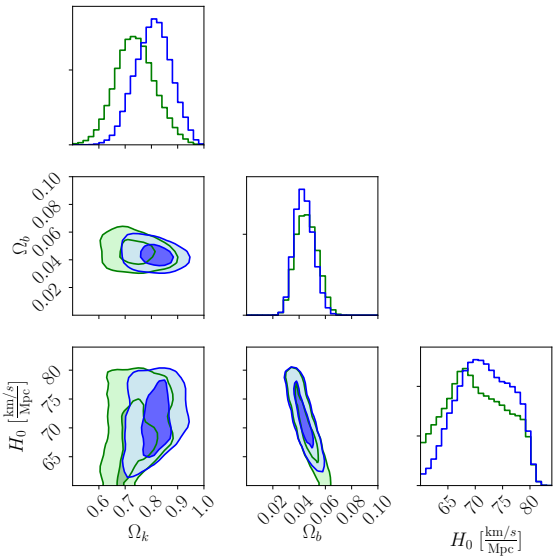


**(b)** posterior distribution in ΛCDM

**Figure 5.8:** Results in CG. *Left:* Hubble diagram of the combined fit using SN and Quasar data sets. *Right*: Posterior distribution of model parameters with marginalised auxiliary parameters (including BBN prior). SN (green), SN+Quasars (blue).

## 5.6 Conclusions and outlook

In this chapter we have studied a combined analysis of standard candles and standard rulers to account for the viability of six cosmological models: flat ΛCDM, ΛCDM with curvature, ΛCDM with curvature and dynamical dark energy, bigravity, bigravity with curvature and conformal gravity (CG) cosmology. To this end, we have employed various data sets in the form of the joint light-curve analysis SN compilation, measurements of the BAO scale in the large scale structure, and the CMB measurement of the acoustic scale. In addition, we have extended this list for the first time by quasar measurements, which only recently have been proposed to serve as standard candles [143, 144]. Although these measurements are afflicted with large uncertainties, they add many new standard candles at a previously unprobed range of high redshifts $1 \lesssim z \lesssim 6$ (complementary to the SN measurements at lower redshifts $z \lesssim 1$ and the CMB measurements at very high redshift). This enables us to test cosmological models on a wider range of scales, and thus to estimate cosmological parameters better. Recently, the same quasar data set has been utilized to test the ΛCDM model and its parametric extensions in Ref. [145], albeit not in conjunction with SN measurements. The analysis therein draws similar conclusions to the ones presented in this study.

Utilising the flat ΛCDM concordance model, we established the robustness of our methods by comparing our results to the literature. Considering our data sets, we have found in all cases that the modifications $k\Lambda$CDM and $w\Lambda$CDM are not favoured with respect to the concordance cosmology, with the latter even being strongly disfavoured. In both cases the deviation from a flat ΛCDM universe is small, i.e. close to flat and the equation of state is $w \approx -1$, if the complete data set is considered. Furthermore, the remaining cosmological parameters converge to values close to those found in ΛCDM and no alleviation to the $H_0$ tension is present in these models.

Moving on to bigravity, our results show that the best fit cosmologies in this framework closely approximate ΛCDM. The differentiation between bimetric theory and concordance cosmology is irrelevant at the time when CMB and BAO are set. At smaller redshift, where deviations from ΛCDM are expected, bigravity is not able to improve the fit, and is strongly disfavoured from a statistical point of view – irrespective of the geometry which is assumed (flat or with curvature).

Similarly, definitive conclusions can be drawn for CG cosmology. While the SN data alone already suggests that CG is disfavoured with respect to ΛCDM, testing the model at higher redshifts with quasar measurements impairs the viability further. In addition, the curvature parameter we deduce from our results is in considerable tension with results from galactic surveys, if CG is also to account for the missing mass in galaxies without the addition of dark matter. This leaves no other conclusion than discarding this version of CG, where no dark matter in the universe is assumed, to describe both galactic and cosmic dynamics.

We hope that our results might hint to new avenues for cosmological model building based on modifications of GR. To this end, we give a transparent description of our methodology in Sec. 5.4 in conjunction with our code publicly available at [223] including the aforementioned quasar data set.

We stress that our approach is solely focused on the level of the background cosmology, and that it would be desirable to extend this study to the computation of primordial temperature fluctuations. In this way, the cosmological models could be confronted with the measurement of the full CMB spectrum.

As far as CG is concerned, such an analysis is at present not available owing to the fact that it involves higher-order equations which render the computations much more involved than the standard ΛCDM case. For the case of bigravity, we refer to the discussion in Sec. 5.3.2. In summary, also in this case a full analysis of the cosmological perturbations remains as an open question.

# 6 | Going Beyond: The Standard Model

As we have seen in Chapters 2 and 5, the discrepancies between observations and the sum of GR plus the SM can motivate theories which modify gravity. However, current analyses find that the cosmological concordance model is the best fit to observational data, a result which we have also reproduced in Chapter 5. Thus, we now set aside modified gravity models, and assume ΛCDM as the base cosmological model. In this case, the most pressing question is that of the nature of DM, which we will investigate in the following. We will briefly review various DM candidates found in the BSM literature, and set up an analysis of a wider class of DM models, which will be carried out in detail in Chapter 7. However, before moving on to extensions of the SM, let us review whether there are viable options of known physics which could comprise the DM.

## 6.1 DM from known Physics

As we have noted already in Chapter 2, the evidence in favour of DM can be grouped into two broad phenomenological categories of astrophysical (e.g. galactic rotation curves, galaxy velocity dispersion, gravitational lensing) and cosmological (CMB spectrum and structure formation) nature. In theory, the solution to the DM problem on cosmological scales may be decoupled from astrophysics, and we may first ask if the small scale structures of the universe can be explained with standard baryonic matter. The physics of stellar dynamics provides us with possible candidates in the form of massive compact halo objects (MACHOs). By definition, this is any astronomical body which emits little or no radiation, for examples faint dwarf stars, planets, and black holes. Extensive experimental searches have been conducted on the abundance of MACHOs in galactic halos using microlensing. These observations rule out MACHOs as the prime component in DM halos, as they find that faint stars only form less than 1 % of mass density of the Milky Way halo mass [252–254] and less than 8 % within the Large Magellanic Cloud [255–257]. In addition, simulation show that MACHOs as DM would produce an overabundance of heavy elements [258].

A related and still open alternative are *primordial* black holes (PBHs) as DM [259, 260]. Through gravitational collapse of density fluctuations in the early universe, clusters of PBHs with masses of order $(10^{-2} - 10^{3})\, M_{\odot}$ and broad mass distributions can be generated. However, we take note that they require a production mechanism set during inflation, and are thus not firmly set on established dynamics of base ΛCDM. Such PBH clusters may be tested in the future by microlensing, CMB, tests of large scale structures and a signature of a stochastic background of GWs.

Moving away from DM in the form of astrophysical objects, we turn towards particle DM. In this category, let us briefly review two contenders of SM physics which have been considered to comprise the DM.

The three neutrino species in the SM are electrically neutral and feebly interacting, and therefore a prime candidate. However, as pointed out already in Chapter 2, their low mass specifies them as hot DM, which leads to matter clusters of scales much larger than those observed [26]. Additionally, neutrinos are fermions, and the construction of massive halos from fermions is generally limited by the available phase-space. A simple bound can be derived from the density of states of a free degenerate fermion gas. For a spherically symmetric halo of mass $M$ and radius $R$, this is quantified

as

$$\frac{g\, m_{f\mathrm{DM}}^4}{(2\pi\hbar)^3} \geq \frac{M}{\frac{4\pi}{3}R^3}\frac{1}{\frac{4\pi}{3}v^3} \tag{6.1.1}$$

which limits the mass of any fermionic DM candidate $m_{f\mathrm{DM}}$ given its number of d.o.f. $g$ and the characteristic velocity of DM particles $v$. A slightly refined statement is given by the Tremaine-Gunn bound [261], which also takes into account the evolution of the phase-space density. In either case, analysis of the phase-space distributions in dwarf spheroidal galaxies lead to a lower bound $m_{f\mathrm{DM}} \geq 400$ eV, firmly excluding neutrinos in the SM as DM candidates [262].

As an alternative within the SM, one may consider metastable bound states of QCD. A recent example of interest is the *uuddss*-hexaquark, discussed as a cold DM candidate in Refs. [263–267]. While one is able to reproduce the DM abundance if its mass lies at about 1.2 GeV, it is not possible to bring its phenomenology in agreement with observations, e.g. of stable nuclei, stability of neutron stars and supernova timing.

## 6.2 Particle DM beyond the SM

Therefore, as the SM appears unable to provide a suitable DM candidate, it is a sensible assumption to extend it with a new particle sector. We denominate such an extension a Dark Sector (DS), as it comprises the DM particle(s). Because we haven't observed such a sector as of yet, schematically, there are two possibilities:

- the lightest states in the DS are massive enough such that the mass gap has not (yet) been overcome by terrestrial experiments and observed astrophysical phenomena.
- the mass gap of the DS is low enough, but the interactions with the SM are too feeble to produce such states.

An example in the first category are heavy, weakly interacting massive particles (WIMPs). In the minimal setup, their interactions with the SM are mediated by the massive electroweak gauge bosons or the Higgs portal, and the correct relic density is reproduced if a WIMP exists with a mass of $\mathcal{O}(\Lambda_{\mathrm{EW}})$. This renders it a very attractive and well-testable DM candidate, and the WIMP proposal has been subject to a wide range of experimental searches. Under these tests, a WIMP interaction mediated by a SM portal is substantially prohibited unless the mass exceeds currently testable ranges (for recent reviews, see Refs. [268] and [269]).

On the other hand, axions or axion-like particles (ALPs) can be placed firmly in the second category. The possible mass range of ALPs as DM spans from $10^{-22} - 10^{-2}$ eV, but their interaction with the SM is mediated by operators of dimension five and higher. Many efforts have been dedicated to probing these portal interactions, placing bounds on the suppressing scale $f_a$ in excess of $10^{10}$ GeV [270, 271].

Finally, we mention theories with a parameter space which allows them to be placed in either category. A widely studied class are composite states of DS with confining dynamics. These models are often constructed in analogy to QCD, however with a free choice for the representations of the DS states under the dark confining force. The DM may be comprised of dark mesons or baryons with masses in the vicinity of the DS confinement scale, which is allowed to be $\mathcal{O}\big(10^{-2} - 10^{4}\big)$ GeV [272–274]. A similar possibility is that the DM may consist of dark glueballs with masses in the range 100 MeV to 1 TeV [275–279]. Either of these setups can be realised s.t. the DM candidate escapes production at colliders due to its high mass, or alternatively with a low mass gap which can only be probed via higher dimensional portal interactions.

In the case that the DM is not hidden behind the energy frontier, we can use currently available searches to quantify its properties and set bounds on the mediating portal interactions. In the following, we will investigate the class of models characterised by a low mass gap and irrelevant portal interaction to the SM. Our aim is to find commonalities between these DS theories, so as to place bounds on such models in a general way. In the remainder of this chapter, we will give a brief summary of the strategy employed in Chapter 7, and define some of the nomenclature which we will make use of.

We reiterate that a DS candidate theory needs a *long-lived* DM candidate. This can be accommodated easily by a particle which is accidentally stable, i.e. protected by symmetries which are broken only by higher-dimensional operators. A feeble interaction with the SM then translates into having effective operators with sufficiently large EFT scale $\Lambda_{\rm UV}$. Complementarily, we refer to the scale of the DM candidate as $\Lambda_{\rm IR}$.[40] Collecting these conditions, we define the object of our investigation: a hidden sector external to the SM with low mass gap $\Lambda_{\rm IR}$, coupled to the SM via the EFT scale $\Lambda_{\rm UV}$, and with a large scale separation $\Lambda_{\rm UV} \gg \Lambda_{\rm IR}$. Additionally, we allow for strong coupling within the dark sector. All of these qualities are naturally provided by a hidden sector with an approximate *conformal symmetry* between $\Lambda_{\rm IR}$ and $\Lambda_{\rm UV}$, and we will make ample use of knowledge about CFTs to derive phenomenological implications.[41]

We thus define our DS theories of interest as any BSM sectors with approximate scale invariance between two scales $\Lambda_{\rm UV}$ and $\Lambda_{\rm IR}$. The only coupling to the SM occurs at the UV scale through operators which are $SU(3)_c \times SU(2)_L \times U(1)_Y$ invariant. We do not need to specify the gauge group or exact particle content of the DS, but instead work with the gauge invariant operators which can be constructed from these building blocks. By keeping the definition criteria as loose as possible, we hope to capture a large number of DS candidate theories and provide phenomenological constraints on them, whereas conventional searches are highly specialised, with only limited extendibility to related theories.

For example, without further specification, this study simultaneously produces bounds on QCD-like theories in the conformal window, pure Yang-Mills dark sectors, as well as theories of free fermions as IR degrees of freedom. They are also applicable to certain BSM theories in extra dimensions, such as Randall-Sundrum models with an IR brane. We refer to Sec. 7.3 for several explicit examples, to which our general analysis can be applied immediately.

Before proceeding to the next chapter, we point out a historic success of the $\Lambda_{\rm IR}/\Lambda_{\rm UV}$ detection scheme for DS defined above: the discovery of neutrinos. The electron neutrino was postulated by Pauli in 1930 in order salvage the concept of energy conservation in beta decays [280]. The nuclear decay is mediated through a four-fermi interaction, which expressed in our language constitutes a dimension-six portal. In this case, the role of the UV dynamics is taken by the heavy gauge bosons $W$ and $Z$. The mass hierarchy between the IR physics (the neutrinos) and the UV degrees of freedom is over ten orders of magnitude. Due to the difficulty of openly producing such massive UV states, the historic timeline follows the scheme laid out above: the neutrino was first detected in 1956 [281], while the mediating gauge $W$ boson could only be produced in 1983 [282, 283].

Today, we may find ourselves in a similar situation. The overwhelming experimental evidence in favour of the cosmological concordance model has inspired us to postulate a dark matter sector. Depending on the realisation nature has chosen, such a dark sector could be seen first through its IR degrees of freedom, while the UV states would be probed only indirectly for the time being. This is the motivation behind the study we will perform in the following chapter.

[40] In doing so, we assume that the DM mass is of order of the lightest mass in the DS.

[41] Here, we use the terms 'conformal symmetry' and 'scale invariance' interchangeably.

# 7 | Searching for Elusive Dark Sectors with Terrestrial and Celestial Observations

*This chapter is based on Ref. [4], with Roberto Contino and Rashmish Mishra.*

## 7.1 Synopsis

We consider the possible existence of a SM-neutral and light dark sector coupled to the visible sector through irrelevant portal interactions. Scenarios of this kind are motivated by dark matter and arise in various extensions of the Standard Model. We characterize the dark dynamics in terms of one ultraviolet scale $\Lambda_{\rm UV}$, at which the exchange of heavy mediator fields generates the portal operators, and by one infrared scale $\Lambda_{\rm IR}$, setting the mass gap. At energies $\Lambda_{\rm IR} \ll E \ll \Lambda_{\rm UV}$ the dark sector behaves like a conformal field theory and its phenomenology can be studied model independently. We derive the constraints set on this scenario by high- and low-energy laboratory experiments and by astrophysical observations. Our results are conservative and serve as a minimum requirement that must be fulfilled by the broad class of models satisfying our assumptions, of which we give several examples. The experimental constraints are derived in a manner consistent with the validity of the effective field theory used to define the portal interactions. We find that high-energy colliders give the strongest bounds and exclude UV scales up to a few TeVs, but only in specific ranges of the IR scale. The picture emerging from current searches can be taken as a starting point to design a future experimental strategy with broader sensitivity.

## 7.2 Introduction and Motivations

As we have argued in the previous chapters, new physics beyond the Standard Model (SM) of particle physics is well motivated from the requirement of a suitable Dark Matter (DM) candidate. It is possible that some of the new fields reside in a light and neutral 'dark' sector, coupled to the SM only through portal interactions formed by the product of one SM and one dark singlet operator. Scenarios of this kind are predicted in various extensions of the SM and have been intensively studied under the assumption that the portal operators have dimension 4 or less, see for example [284–287] and references therein. In this work we analyse the more *elusive* dark sectors where the portal operators are higher-dimensional and are generated at some ultraviolet (UV) scale $\Lambda_{\rm UV}$ by heavy mediator fields. The DM candidate might reside in the dark sector (DS) or be part of the UV dynamics. Given the constraints on new dynamics charged under the SM set by current and past experiments, we assume that the UV scale is larger than the electroweak scale, $\Lambda_{\rm UV} \gtrsim 100\,\text{GeV}$, although some of our results apply to theories with a lower UV scale as well, when allowed. The portal interactions can thus be written in terms of $SU(3)_c \times SU(2)_L \times U(1)_Y$ invariant operators.

We will adopt a broad characterization of the dark dynamics in terms of one infrared (IR) scale, $\Lambda_{\rm IR}$, setting its mass gap. We assume, for simplicity, that no other parametrically different scale exists in the theory. At energies between $\Lambda_{\rm UV}$ and $\Lambda_{\rm IR}$ the new dynamics is approximately conformal and flows slowly (i.e. logarithmically) in the vicinity of a fixed point of its renormalization group. The fixed point can be free (if the dark dynamics is asymptotically free), weakly or strongly coupled.

| Operator | Dimension |
|---|---|
| $H^\dagger H$ | 2 |
| $B_{\mu\nu}$ | 2 |
| $\ell H$ | 5/2 |
| $J_\mu^{SM} = \bar{\psi}\gamma^\mu\psi,\ H^\dagger i\overleftrightarrow{D}_\mu H$ | 3 |
| $O_{\mu\nu}^{\rm SM} = F^i_{\mu\alpha}F_\nu^{\alpha\, i},\ D_\mu H^\dagger D_\nu H,\ \bar{\psi}\gamma_\mu D_\nu\psi$ | 4 |
| $O_{SM} = \bar{\psi} i\not{D}\psi,\ D_\mu H^\dagger D^\mu H,\ F_{\mu\nu}F^{\mu\nu},\ F_{\mu\nu}\tilde{F}^{\mu\nu},\ \bar{\psi}_L H\psi_R,\ (H^\dagger H)^2$ | 4 |

**Table 7.1:** List of the SM gauge-singlet operators with (classical) dimension equal or smaller than 4. Here $\psi$ and $F_{\mu\nu}$ stand respectively for any SM fermion and any SM gauge field strength.

When probed at energies $\Lambda_{\rm IR} \ll E \ll \Lambda_{\rm UV}$ the dark dynamics can be thus described as a conformal field theory (CFT) in terms of its composite operators. Having a sufficiently large hierarchy $\Lambda_{\rm IR} \ll \Lambda_{\rm UV}$ is the working hypothesis of our analysis. Notice that it is also a prerequisite to explain the stability of the DM candidate as accidental, if the DM is part of the DS.

It is important at this point to ask what is the minimal structure that must be present in the dark sector. At energies well above $\Lambda_{\rm IR}$, this corresponds to identifying the set of lowest-dimensional gauge-invariant operators which define the CFT. Clearly, the CFT must at least contain some relevant deformation $\mathcal{L}_{\rm def} = c_{\mathcal{O}}\,\mathcal{O}/\Lambda_{\rm UV}^{\Delta_{\mathcal{O}}-4}$ to break the conformal invariance in the IR and generate the hierarchy between $\Lambda_{\rm IR}$ and $\Lambda_{\rm UV}$. A *natural* hierarchy, as we will assume in the following, implies that, in absence of a symmetry protection, the operator $\mathcal{O}$ must be slightly relevant, i.e. must have a scaling dimension $\Delta_{\mathcal{O}} = 4 - \epsilon$ with $\epsilon \ll 1$. Alternatively, one can also have $\Delta_{\mathcal{O}} \lesssim 4$ if the coefficient $c_{\mathcal{O}}$ is the (only) spurion of a global symmetry and has a value $c_{\mathcal{O}} \simeq (\Lambda_{\rm IR}/\Lambda_{\rm UV})^{4-\Delta_{\mathcal{O}}}$ at $\Lambda_{\rm UV}$. Clearly, no scalar singlet operators with dimension much smaller than 4 can exist in a natural dark sector since they would destabilize the hierarchy.

Our analysis will be restricted, for simplicity, to dark sectors that are *unitary* and *local* CFTs.[42] This implies that there must necessarily exist also a local stress-energy tensor operator, $T_{\mu\nu}^{DS}$, with scaling dimension equal to 4. Furthermore, if the dark sector has additional global symmetries, the list of CFT operators will include the corresponding conserved currents, $J_\mu^{DS}$, with dimension equal to 3. The CFT spectrum may contain other relevant operators, depending on the specific underlying dark dynamics. Their presence, however, is not a robust feature implied by our general assumptions or by symmetry arguments.

Any of the above CFT operators can appear in a portal interaction multiplied by one SM gauge-singlet operator. The lowest-lying SM operators are listed in Table 7.1. The first three have dimension smaller than 4 and can give rise to the well-studied marginal or relevant portals. The others necessarily appear in irrelevant portals. We will focus on the portals that can be constructed with the CFT operators $\mathcal{O}, J_\mu^{DS}, T_{\mu\nu}^{DS}$ and those of Table 7.1. These are:[43]

$$\mathcal{O}H^\dagger H, \quad \mathcal{O}O_{SM}, \quad J_\mu^{DS}J_{SM}^\mu, \quad T_{\mu\nu}^{DS}O_{SM}^{\mu\nu}\,. \tag{7.2.1}$$

Dimensional analysis suggests that the portal $\mathcal{O}O_{SM}$ is less important than the Higgs portal $\mathcal{O}H^\dagger H$. One can consider UV theories where $\mathcal{O}H^\dagger H$ is generated with a suppressed coefficient, though

[42] The flow near complex, non-unitary CFTs has been conjectured in Ref. [288] to correspond to the Walking Technicolor regime, see also Ref. [289]. It would be interesting to investigate how our analysis gets modified when the theory flows near one such complex CFT.

[43] The portals $J_\mu^{DS}\partial_\nu B_{\mu\nu}$ and $\partial_\mu\mathcal{O}J_{SM}^\mu$ can be rewritten in terms of respectively $J_\mu^{DS}J_{SM}^\mu$ and $\mathcal{O}O_{SM}$ by using the SM equations of motion.

notice that, in general, $\mathcal{O}H^\dagger H$ is radiatively induced from $\mathcal{O}O_{SM}$ at the 1-loop level, so the relative suppression cannot be smaller than a SM loop factor. This might be enough for $\mathcal{O}H^\dagger H$ to still give the leading effects. An important exception is when $\mathcal{O}$ is an axion field with an associated Peccei-Quinn shift symmetry and $O_{SM} = G_{\mu\nu}\tilde{G}^{\mu\nu}$. In the case of the QCD axion, neither $\mathcal{O}H^\dagger H$ nor any potential for $\mathcal{O}$ is generated above the QCD scale. A hierarchy $\Lambda_{\rm IR} \sim \Lambda_{QCD}^2/\Lambda_{\rm UV}$ is instead generated by $\mathcal{O}^2$ after QCD confinement. Depending on the UV dynamics, additional portals of the type $\mathcal{O}O_{SM}$ can be present, with $O_{SM} = F_{\mu\nu}\tilde{F}^{\mu\nu}$ or $\bar{\psi}_L H \psi_R$. Apart from the special and thoroughly studied axion case, the portal $\mathcal{O}O_{SM}$ usually plays a subleading role compared to $\mathcal{O}H^\dagger H$.[44] We will neglect it in the following and focus on the remaining three portals.

Notice that, while portals involving the Higgs boson, the $Z$ or the top quark require values of $\Lambda_{\rm UV}$ larger than the EW scale to be consistently defined, those featuring only light quarks and leptons can in principle be generated at much smaller scales provided the UV mediators do not have $O(1)$ SM charges and elude current experimental searches. This implies that some of the bounds we will derive are of interest even though they probe values of $\Lambda_{\rm UV}$ well below the EW scale.

We define our portal Lagrangian between the dark and SM sectors schematically as:

$$\mathcal{L}_{\rm portal} = \frac{\kappa_{\mathcal{O}}}{\Lambda_{\rm UV}^{\Delta_{\mathcal{O}}-2}} \mathcal{O}\, H^\dagger H + \frac{\kappa_J}{\Lambda_{\rm UV}^2} J_\mu^{DS} J_{SM}^\mu + \frac{\kappa_T}{\Lambda_{\rm UV}^4} T_{DS}^{\mu\nu} O_{\mu\nu}^{SM}\,, \tag{7.2.2}$$

where $\kappa_{\mathcal{O}}$, $\kappa_J$ and $\kappa_T$ are dimensionless coefficients. Our notation here is schematic since, as discussed later, different couplings may be introduced for different SM operators $O_{\mu\nu}^{SM}$ and $J_{SM}^\mu$.

The coefficient $\kappa_{\mathcal{O}}$ cannot be too large otherwise the hierarchy would be destabilized. Indeed, by contracting the two Higgs fields in a loop, the Higgs portal in Eq. (7.2.2) induces a radiative UV correction to the relevant deformation $\mathcal{L}_{\rm def}$. The hierarchy does not get destabilized provided that

$$\kappa_{\mathcal{O}} \lesssim 16\pi^2 \left(\frac{\Lambda_{\rm IR}}{\Lambda_{\rm UV}}\right)^{4-\Delta_{\mathcal{O}}} \qquad \text{(UV threshold)}\,. \tag{7.2.3}$$

An additional contribution to $\mathcal{L}_{\rm def}$ is generated at the electroweak scale, i.e. when $H$ acquires a vev $v$; this leads to the condition

$$\kappa_{\mathcal{O}} \lesssim \frac{\Lambda_{\rm IR}^2}{v^2} \left(\frac{\Lambda_{\rm IR}}{\Lambda_{\rm UV}}\right)^{2-\Delta_{\mathcal{O}}} \qquad \text{(EW contribution)}\,. \tag{7.2.4}$$

In most of the parameter space (i.e. for $\Lambda_{\rm UV} > 4\pi v$), this constraint is weaker than that of Eq. (7.2.3), although the latter may be avoided if some UV mechanism is at work which tunes $c_{\mathcal{O}}$ to be small at $\Lambda_{\rm UV}$. Similar considerations apply to the coefficient of $\mathcal{O}O_{SM}$, which is subject to a bound analog to Eq. (7.2.3). Furthermore, if $O_{SM} = \bar{q}_L H q_R$, the portal $\mathcal{O}O_{SM}$ gives an additional contribution to $\mathcal{L}_{\rm def}$ at the QCD scale from the quark condensate. One can also envisage a scenario, as done in Ref. [290], where $\kappa_{\mathcal{O}}$ (or the coefficient of $\mathcal{O}O_{SM}$) saturates its upper bound, and the hierarchy is generated by the portal interactions themselves.[45]

In this study we focus on elusive dark sectors that feature the portals of Eq. (7.2.2). These are minimal scenarios as, in general, additional portals may be present. We derive general constraints on these theories from laboratory experiments and astrophysical data by making use only of the general features of the dark dynamics, without relying on its specific details. More explicitly, our analysis will exploit the high-energy conformal regime and the fact that the lightest dark state has mass of order $\Lambda_{\rm IR}$ (as implied by the absence of other infrared scales in the dark sector). Our results

[44] One exception arises if $\mathcal{O}$ can singly excite a CP-odd resonance, whose decay will proceed through the $\mathcal{O}F_{\mu\nu}\tilde{F}^{\mu\nu}$ portal and not through $\mathcal{O}H^\dagger H$. This is the case of CP-odd glueballs in a pure-YM dark sector; we thank Alessandro Podo for pointing this out. Notice that if, as in the previous example, $\mathcal{O}$ has dimension 4, then the constraints on $\mathcal{O}O_{SM}$ are expected to be similar to those on $T_{\mu\nu}^{DS} O_{SM}^{\mu\nu}$ discussed in this work.

[45] Ref. [290] studied the cosmology of dark sectors where the hierarchy is generated by $\mathcal{O}H^\dagger H$ or $\mathcal{O}\bar{q}_L H q_R$. The 1-loop UV corrections to $\Delta\mathcal{L}$ was neglected.

will be conservative and can be improved if a full theory is defined explicitly. Indeed, knowing the IR behaviour of the dark dynamics allows one to perform complete rather than just approximate calculations of rates and cross sections, and thus to derive stronger constraints. Furthermore, as discussed in section 7.4, effective operators generated by the exchange of UV degrees of freedom and made of SM fields alone can lead to constraints on $\Lambda_{\rm UV}$ that are stronger than those obtained from our analysis (but are opaque about the details of the underlying DS). These effects have been thoroughly studied in the literature and several systematic analyses have been performed. In this work we will provide a conservative characterization of these constraints by estimating the smallest value of the effective coefficients compatible with the existence of our portal interactions.

Our approach is not entirely new and in fact has some overlap with previous studies on Hidden Valleys and on the phenomenology of conformal field theories. The scenarios that are referred to as Hidden Valleys are similar to those we consider in this study: new confining dynamics with low mass scale is assumed to couple to the SM through some irrelevant portal, generated for example by heavy mediators [291]. This possibility was envisaged before the beginning of the LHC operation, pointing out that the energy increase provided by the LHC could have been enough to climb over the barrier separating us from the Hidden Valley if the mediators have mass of order a few TeVs. In that case, the mediators can be produced on shell and decay copiously to the hidden hadrons with spectacular experimental signatures. The LHC data collected at Run1 and Run2 have discovered no new particles and suggest that, if realized at all in nature, these scenarios must be hidden from us through a higher barrier. In this work we thus assume that the mediators are sufficiently heavy to be out of the direct reach of the LHC, and ask if we can test the existence of the dark sector, i.e. the hidden sector with low mass scale. Hence, while the theories studied in this chapter have a large overlap with Hidden Valleys (though, notice, we do not assume the dark sector to be necessarily strongly coupled and confining), our approach and assumptions are different.

On the front of the phenomenology of conformal field theories, there is a vast literature on 'unparticle' physics where similar experimental data were used to set constraints on the theoretical parameter space. The question originally motivating the study of unparticles is whether new dynamics can first manifest itself and be discovered at colliders in its conformal regime [292]. We differ from those works for the choice of the portals in Eq. (7.2.2), our thorough inclusion of experimental bounds, and for our self-consistent use of effective field theory techniques. Furthermore, while unparticle studies assume that the CFT degrees of freedom are stable on distances relevant for the analysis, we have also considered the constraints that arise when these CFT excitations decay inside the detector with displaced vertices.

Previous studies of the phenomenology of dark sectors coupled to the SM through irrelevant portals include Refs. [275, 276, 293–304]. While these papers have some aspects in common with our work and some of their assumptions are similar to ours, we believe that our approach is original and our analysis extends previous results. We will focus on laboratory experiments and astrophysical observations that can test and set limits on elusive dark sectors. An additional important probe comes from cosmology, and a study in this direction has been performed in Ref. [290].

The outline of this chapter is as follows. In Section 7.3 we illustrate some examples of elusive dark sectors, exhibiting their UV completion. Sec. 7.4 explains our strategy and estimates the effects from DS virtual effects and DS production. Three possible experimental manifestations of the DS excitations, in the form of missing energy, displaced decays and prompt decays, are discussed, and the validity of the effective field theory is analysed. The bounds from terrestrial experiments and celestial observations are derived in Sec. 7.5. We analyse: resonant and non-resonant DS production at high-energy colliders; high-intensity experiments; stellar evolution and supernova energy loss; positronium decays; fifth-force experiments; and electroweak precision tests. We draw our summary and conclusions in Sec. 7.6. The appendix includes useful formulas on two-point correlators (B), additional details on a 5D Randall-Sundrum dark sector (C), and formulas for the probabilities used to compute the rate of displaced decays (D).

## 7.3 Examples of Elusive Dark Sectors

Although our analysis will be model independent and will not make reference to the underlying dark dynamics, it is useful to discuss a few specific models that can serve as benchmark examples. In this section we will thus consider four different kinds of dark sectors and specify the mediator fields that generate their portal interactions.

### 7.3.1 Pure Yang-Mills dark sector

One of the simplest and most motivated example of dark sectors is pure Yang-Mills (YM) dynamics. Models of this kind have been considered in the context of glueball DM [278], and can arise as the low-energy limit of theories of accidental DM with dark fermions heavier than the dynamical scale [274]. Their mass gap is generated dynamically at dark confinement and the lightest states in the spectrum are the dark glueballs. Consider as an example the $L \oplus N$ model of Ref. [274], defined in terms of one Dirac fermion $L$ and one Majorana fermion $N$ transforming as fundamental representations of an $SO(N_{DC})$ dark color group. Under the SM gauge symmetry, $N$ is a singlet while $L$ transforms as a $2_{-1/2}$ of $SU(2)_{EW} \times U(1)_Y$. The Lagrangian (in 4-component notation) is:

$$\begin{aligned} \Delta\mathcal{L} = &- \frac{1}{4g_{DC}^2}\mathcal{G}_{\mu\nu}\mathcal{G}^{\mu\nu} + \bar{L}(i\not{D} - m_L)L + \frac{1}{2}\bar{N}(i\not{\partial} - m_N)N \\ &- \left(y_L\, \bar{N} P_L L H + y_R\, \bar{N} P_R L H + h.c.\right), \end{aligned} \tag{7.3.1}$$

where $\mathcal{G}$ is the dark gluon field and $P_{L,R}$ are left and right projectors. The theory has an accidental dark baryon parity that makes the lightest baryon cosmologically stable and a potential DM candidate [274]. If both $m_L$ and $m_N$ are larger than the dark dynamical scale $\Lambda_{DC}$, then the low-energy dark sector consists of a pure YM dynamics, while the DM candidate resides in the UV sector.[46] Integrating out the heavy fermions at 1-loop generates the dim-6 and dim-8 operators

$$\mathcal{G}_{\mu\nu}\mathcal{G}^{\mu\nu}H^\dagger H \qquad\qquad \kappa_{\mathcal{O}} \sim \frac{\alpha_{DC}(\Lambda_{\rm UV})}{4\pi}(|y_L|^2 + |y_R|^2) \tag{7.3.2}$$

$$\mathcal{G}_{\mu\nu}\mathcal{G}^{\mu\nu}W_{\alpha\beta}W^{\alpha\beta},\ \mathcal{G}_{\mu\alpha}\mathcal{G}^{\alpha}_{\nu}W^{\mu}_{\beta}W^{\beta\nu} \qquad\qquad \kappa_T \sim \alpha_{DC}(\Lambda_{\rm UV})\alpha_2(\Lambda_{\rm UV}) \tag{7.3.3}$$

where $\Lambda_{\rm UV} \sim m_L, m_N$. There are two kinds of light states in this model: CP-odd and CP-even glueballs. While the latter can decay through the dim-6 portal, CP-odd glueballs can only decay through the dim-8 one and their lifetime is longer.

As another example of a theory that leads to a pure YM dark sector, consider an $SU(N_{DC})$ theory with massive fermions $\psi$ transforming as the adjoint representation of dark color and as a $3_0$ of $SU(2)_{EW} \times U(1)_Y$ [305]. Since $\psi$ does not have Yukawa couplings to the Higgs, integrating it out does not lead to any dim-6 operator at 1-loop. Therefore, this theory has only the dim-8 portal of Eq. (7.3.3). The DM candidate in this case is the gluequark, a bound state made of one dark quark and dark glue. It is cosmologically stable due to an accidental dark parity, has mass of order $m_\psi \gg \Lambda_{DC}$ and thus resides in the UV sector.

### 7.3.2 Strongly coupled dark sector

Another interesting limit of the theory defined by Eq. (7.3.1) is when the doublet is heavy, $m_L \gg \Lambda_{DC}$, while the singlet is light with mass of order of the dynamical scale, $m_N \lesssim \Lambda_{DC}$. In this case the dark sector is a strongly coupled $SO(N_{DC})$ theory with one Majorana fermion in the fundamental representation. The spectrum of lowest-lying states contains dark baryons (the lightest of which is

[46] For example, if $m_L > m_N > \Lambda_{DC}$ then the lightest dark baryon, i.e. the DM candidate, is a bound state of $N$ with spin $N_{DC}/2$ and mass $\sim N_{DC} m_N$ [274].

accidentally stable and thus a DM candidate) and mesons. Integrating out the heavy doublet at tree level generates dim-5 and dim-6 portals ($\Lambda_{\rm UV} \sim m_L$):

$$\bar{N} P_L N H^\dagger H + h.c. \qquad \kappa_{\mathcal{O}} \sim y_L y_R^* \tag{7.3.4}$$

$$\bar{N} \gamma^\mu \gamma^5 N H^\dagger i \overleftrightarrow{D}_\mu H \qquad \kappa_J \sim (|y_L|^2 - |y_R|^2)\,. \tag{7.3.5}$$

The dark current appearing in the dim-6 portal is purely axial, as a consequence of $N$ being a Majorana fermion. Equation (7.3.5) thus gives $N$ an axial coupling to the $Z$ boson. A similar model with $SU(N_{DC})$ dark color group and a vectorlike (complex) representation for $N$ would give an additional portal with a vectorial current, hence a vectorial coupling to the $Z$. Such vectorial coupling is strongly constrained by direct detection experiments if dark baryons made of $N$ are the DM (see for example Ref. [274]). In the model of Eq. (7.3.1), the scattering of DM off nuclei via $Z$ exchange has a spin-dependent cross section, as a consequence of the axial coupling. The corresponding bounds are weaker, though not negligible (see [306]). The strongest constraint holds for DM masses in the range $10-100\,$GeV and requires $m_L$ to be larger than a few TeV for Yukawas of order 1. For lower DM masses, the bound becomes much weaker and sizable Yukawas are allowed for $m_L$ above the weak scale. The DM can scatter also via a Higgs exchange, with a spin-independent cross section. The corresponding bounds are slightly stronger than those from the $Z$ exchange, but also disappear for DM masses smaller than $\sim 10\,$GeV (see [307]). They can be evaded for any value of the DM mass if one of the Yukawa couplings vanishes or is very small. This would still allow for a large $\kappa_J$ in Eq. (7.3.5).

### 7.3.3 Dark sector with free fermions

Another interesting example of dark sector is a theory of free fermions. As a first UV completion, consider a theory where $(B-L)$ is gauged by $X_\mu$ and spontaneously broken at high scale by a scalar field $\phi$ with $(B-L)$ charge $-2$. To make $(B-L)$ anomaly free we introduce three left-handed neutrinos $N_i$ with $(B-L)$ charge $-1$. We impose a $Z_2$ symmetry under which the $N_i$ are odd in order to forbid their Yukawa couplings to the Higgs field and make them stable. In two-component notation, the Lagrangian for the new fields reads

$$\begin{aligned}\Delta\mathcal{L} = &-\frac{1}{4g_X^2} X_{\mu\nu} X^{\mu\nu} + \sum_{i=1}^{3} N_i^\dagger i(\partial_\mu - i X_\mu)\bar{\sigma}^\mu N_i + |D_\mu \phi|^2 \\ &+ \sum_{\psi_{SM}} q_{B-L}^{[\psi_{SM}]} \psi_{SM}^\dagger X_\mu \bar{\sigma}^\mu \psi_{SM} - \sum_{i=1}^{3} (y_i N_i N_i \phi + h.c.) - \lambda_\phi (\phi^\dagger \phi - v_\phi^2)^2\,,\end{aligned} \tag{7.3.6}$$

where $\psi_{SM}$ are the SM fields and $q_{B-L}^{[\psi_{SM}]}$ is their charge under $(B-L)$. When $(B-L)$ gets spontaneously broken, all new fields acquire mass ($m_{N_i} = y_i v_\phi$, $m_\phi = 4\sqrt{\lambda_\phi} v_\phi$, $m_X = 2\sqrt{2} g_X v_\phi$). We assume that the $N_i$ are much lighter than $X_\mu$ and $\phi$, and thus take $y_i \ll g_X, \sqrt{\lambda_\phi}$. Integrating out $X_\mu$ at tree level generates the dim-6 portal ($\Lambda_{\rm UV} \sim m_X$)

$$\bar{\psi}_{SM} \gamma_\mu \psi_{SM} \sum_i \bar{\psi}_{N_i}^\dagger \gamma^\mu \gamma^5 \psi_{N_i} \qquad \kappa_J \sim q_{B-L}^{[\psi_{SM}]} g_X^2\,, \tag{7.3.7}$$

where $\psi_{N_i}$ are Majorana fermions in 4-component notation. Searches performed at the LHC for a $Z'$ decaying into leptons and jets set rather stringent lower bounds on the mass of the mediator $X_\mu$, of order $1-5\,$TeV for $O(1)$ couplings $g_X$ [308–311].

As another example, consider a theory with one SM-neutral Majorana fermion $\chi$ and one scalar $\phi$ with hypercharge $-1$. If $\chi$ and $\phi$ are odd under an exact dark parity, the Lagrangian is

$$\Delta\mathcal{L} = (D_\mu \phi)^\dagger (D^\mu \phi) + \frac{1}{2}\bar{\chi}(i\partial\!\!\!/ - m_\chi)\chi + (y\, \bar{e}_R \phi \chi + h.c.) - m_\phi^2 \phi^\dagger \phi - \lambda_\phi (\phi^\dagger \phi)^2\,. \tag{7.3.8}$$

We take $m_\phi \gg m_\chi$, so that integrating out $\phi$ at tree level generates the dim-6 portal

$$\bar{e}_R \gamma^\mu e_R \, \bar{\chi} \gamma_\mu \gamma^5 \chi \qquad \kappa_J \sim y^2 \,. \tag{7.3.9}$$

Thanks to dark parity, $\chi$ is absolutely stable, while $\phi$ decays to $e_R \bar{\chi}$ through its Yukawa coupling. This theory is similar to a simplified supersymmetric model with neutralino and selectron, where $\chi$ plays the role of the neutralino and $\phi$ of the selectron. This suggests that searches for supersymmetry at LEP can set limits on the mass of the mediator $\phi$, in particular those looking for slepton pair production followed by the decay to electron plus neutralino (see [312] and references therein). The lower bound on $m_\phi$ is expected to be of order 100 GeV or smaller, depending on the mass of $\chi$.

A final example of UV completion is a theory with a single Dirac fermion $\psi$ coupled to a real scalar field $S$, both neutral under the SM gauge group.[47] The Lagrangian is assumed to be invariant under a chiral parity $\psi \to \gamma^5 \psi$, $S \to -S$, and it reads

$$\mathcal{L} = \bar{\psi} i \partial\!\!\!/ \psi + \frac{1}{2}(\partial_\mu S)^2 - y \, \bar{\psi}\psi S - \lambda_S (S^2 - v_S^2)^2 - \lambda_{SH} \, S^2 H^\dagger H \,. \tag{7.3.10}$$

The scalar potential gives $S$ a vev and breaks the chiral parity spontaneously. Assuming $m_S = 4\sqrt{\lambda_S} v_S \gg m_\psi = y v_S$ implies at low energy a dark sector with one free Dirac fermion. Integrating out $S$ at tree level generates a dim-5 Higgs portal

$$\bar{\psi}\psi H^\dagger H \qquad \kappa_{\mathcal{O}} \sim \frac{\lambda_{SH} y v_s}{m_S} = \lambda_{SH} \frac{m_\psi}{m_S} \,, \tag{7.3.11}$$

as well as the operator $O_H = [\partial_\mu (H^\dagger H)]^2$ with coefficient $c_H \sim \lambda_{SH}^2 v_s^2 / m_S^4$. The value of $\kappa_{\mathcal{O}}$ satisfies the naturalness bounds (7.2.3),(7.2.4) as long as $\lambda_{SH} < \min(16\pi^2, m_S^2/v^2)$. Differently from the strongly-coupled dark sector discussed above, in this theory there is only one spurion (i.e. $m_\psi$) breaking the chiral parity, and $\kappa_{\mathcal{O}}$ automatically bears a suppressing factor $m_\psi/m_S \sim \Lambda_{\rm IR}/\Lambda_{\rm UV}$. The operator $O_H$ implies a universal shift in the Higgs couplings of order $\delta g/g \sim (\lambda_{SH}/\lambda_S)^2 (v/v_S)^2$, which can be sufficiently small if $\lambda_{SH} \ll \lambda_S$ and/or $v \ll v_S$.

### 7.3.4 5D Randall-Sundrum Dark sector

Finally, let us discuss a 5-dimensional example of dark sector that is dual to a strongly-coupled 4-dimensional theory. Consider a Randall-Sundrum theory [316] with the full SM sector localized on the UV brane and only gravity propagating in the bulk and on the IR brane. We add the following boundary action on the UV brane:

$$\int d^4x \sqrt{-g} \left( M_0^2 R + \frac{1}{\Lambda_{\rm UV}^2} R_{\mu 5 \nu 5} T_{SM}^{\mu\nu} \right) . \tag{7.3.12}$$

The first term, with $M_0 \sim M_{\rm Pl}$, sets the strength of the gravitational interaction at low energy, so that one can assume $\Lambda_{\rm UV} \sim M_5, k \ll M_{\rm Pl}$, where $M_5$ and $k$ are respectively the 5-dimensional Planck mass and the AdS curvature. The UV brane gives an effective description of the dynamics at energies smaller than $\Lambda_{\rm UV}$, and in fact the model can be thought of as the low-energy effective limit of a multi-brane RS theory [317]. The dynamics in the bulk and on the IR brane, dual to the 4D CFT, play the role of the dark sector. The second term of Eq. (7.3.12) induces a dim-8 portal interaction between the SM and the CFT in the dual theory,

$$\frac{\kappa_T}{\Lambda_{\rm UV}^4} T_{\mu\nu}^{DS} T_{SM}^{\mu\nu} \,, \qquad \text{with} \quad \kappa_T \sim \frac{k^3}{M_5^3} \,, \tag{7.3.13}$$

as discussed in Appendix C.

[47] See Refs. [301, 313–315] for similar, though different, models.

### 7.3.5 Summary

The models discussed above provide concrete realizations of dark sectors with portal interactions of the type considered in Eq. (7.2.2). They will serve as benchmarks in Sec. 7.4.2 and in our final discussion of Sec. 7.6, where different constraints are analysed and compared. Table 7.2 summarizes the models, indicating the DS content, its possible UV completions and the leading portals to the SM. For additional models see for example Refs. [298, 300, 301, 315].

| Dark Sector | UV completion | Portals |
|---|---|---|
| Pure $SO(N_{DC})$ Yang-Mills | L+N model | $\kappa_{\mathcal{O}}, \kappa_T$ |
| | V model | $\kappa_T$ |
| $SO(N_{DC})$ + 1 Majorana fermion | L+N model | $\kappa_{\mathcal{O}}, \kappa_J$ |
| Strongly coupled CFT with only $T^{DS}_{\mu\nu}$ | 5D RS model | $\kappa_T$ |
| Free Fermions: | | |
| 3 Majorana $N_i$ | gauged $U(1)_{B-L}$ model | $\kappa_J$ |
| 1 Majorana $\chi$ | 'slepton + neutralino' model | $\kappa_J$ |
| 1 Dirac $\psi$ | model with real scalar mediator $S$ | $\kappa_{\mathcal{O}}$ |

**Table 7.2:** Summary of benchmark models that serve as examples of dark sectors with irrelevant portals interactions.

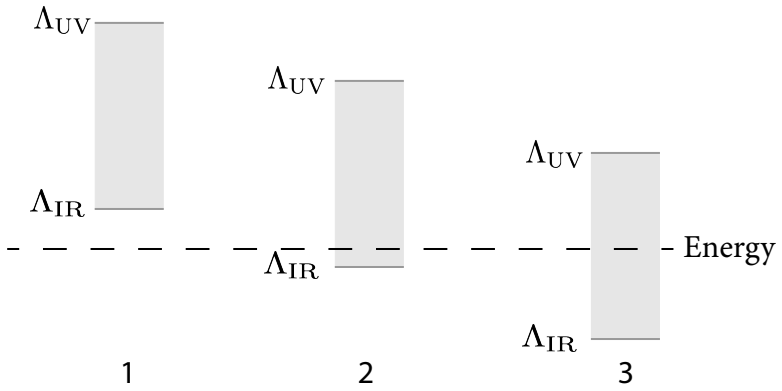


**Figure 7.1:** Cartoon of the three possible situations characterizing the energy $\sqrt{s}$, at which the dark sector is probed, compared to the scales $\Lambda_{\rm UV}, \Lambda_{\rm IR}$.

## 7.4 Strategy

In this section we discuss how the dark dynamics can be probed using processes at energies $\sqrt{s} < \Lambda_{\rm UV}$. We can envisage three different situations, sketched in Fig. 7.1, depending on the value of $\sqrt{s}$. Furthermore, one can consider two broad classes of effects:

- Indirect contributions to SM processes from virtual exchange of DS or UV states
- Production of DS states.

Indirect effects are the only ones that can occur if $\Lambda_{\rm IR} > \sqrt{s}$, as in situation 1 of Fig. 7.1. Production of DS states, on the other hand, occurs differently in situations 2 and 3. One can imagine discovering the dark sector through the production of a few new states upon crossing the IR energy threshold. This is situation 2 of Fig. 7.1. On the other hand, a dark sector with low mass gap and feeble interactions with the SM could be first observed directly in its conformal regime if one reaches a minimum luminosity. Discovery in this case is not limited by energy, and the new states can be produced well above threshold (situation 3 of Fig. 7.1). In what follows we estimate the relative importance of indirect effects and DS production, and try to highlight the best strategy to probe the dark dynamics.

### 7.4.1 Indirect (virtual) effects

The DS degrees of freedom can be exchanged virtually in processes involving SM external states. This requires (at least) two insertions of the portal interactions, either at tree-level or at loop-level, depending on the process and the portal involved. Physical amplitudes are thus written in terms of two-point correlators of the DS operators appearing in the portal interactions. These have the form

$$\langle O_{DS}(p) O_{DS}(-p)\rangle \sim \frac{c}{16\pi^2}\left(p^{2\Delta-4} + p^{2\Delta-6}\Lambda_{\rm IR}^2 + \cdots + \Lambda_{\rm IR}^{2\Delta-4}\right) + \text{divergent terms}\,, \tag{7.4.1}$$

for a generic DS operator $O_{DS}$ with dimension $\Delta$, where $c$ accounts for the multiplicity of DS states. An additional contribution to the same process comes from the exchange of UV states. This is a local effect and can be encoded by a single insertion of dim-6 operators generated at the UV scale. The different contributions are illustrated in Fig. 7.2. The dim-6 (as well as higher-dimensional) operators are in fact required as counterterms to cancel the power-law divergences

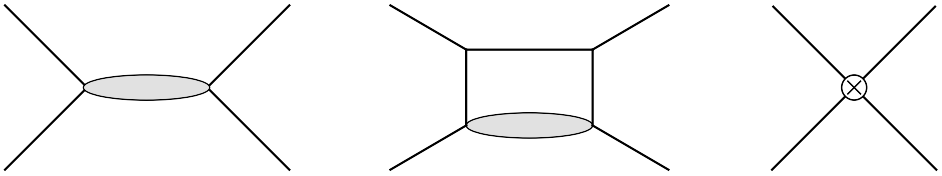

**Figure 7.2:** Contributions to processes involving SM external states: virtual exchange of DS states at tree-level and 1-loop (first two diagrams from the left), contact interaction from UV-generated dim-6 operators (diagram on the right). Solid lines denote SM particles, the gray blob stands for a DS propagator.

that arise for $D > 5$, where $D$ is the overall dimension of the portal, in the two-point correlator of Eq. (7.4.1). In the spirit of effective field theory, this is a UV threshold correction arising at the scale $\Lambda_{\rm UV}$. For example, a tree-level diagram with two insertions of $J^{DS}_\mu H^\dagger i\overleftrightarrow{D}^\mu H$ requires a counterterm $O_T = (H^\dagger i\overleftrightarrow{D}^\mu H)^2$ to remove the quadratic divergence of the two-point correlator $\langle J^{DS}_\mu J^{DS}_\nu \rangle$.[48] We can thus estimate a minimum value of the coefficient of a generic dim-6 operator made of $n$ SM fields, compatible with the existence of the portal interactions:

$$\Delta c_6(\Lambda_{\rm UV}) \sim g_{SM}^{n-4} \frac{\kappa^2}{\Lambda^2_{\rm UV}} \frac{c}{16\pi^2} \left(\frac{g^2_{SM}}{16\pi^2}\right)^\ell \qquad \text{(UV threshold)}\,. \tag{7.4.2}$$

Here $g_{SM}$ is a generic SM coupling and $\ell$ is the number of loops at which $\Delta c_6$ is generated. For $D < 5$, diagrams with two portal insertions can be made finite with counterterms already present in the SM Lagrangian, and they do not imply any UV threshold correction. While Eq. (7.4.2) corresponds to the minimum value of the dim-6 coefficients compatible with the existence of the portal interactions, an additional and possibly larger contribution can arise from the virtual exchange of just UV states. The size of such effect clearly depends on the type of UV physics and cannot be estimated on general grounds. For integer $D$, with $D \geq 5$, diagrams with two portal insertions will also have a logarithmic divergence, which implies a renormalization of the dim-6 operators and a contribution to their RG evolution below $\Lambda_{\rm UV}$. A naive estimate of such effect gives:

$$\Delta c_6(\mu) \sim g_{SM}^{n-4} \frac{\kappa^2}{\Lambda^2_{\rm UV}} \frac{c}{16\pi^2} \left(\frac{g^2_{SM}}{16\pi^2}\right)^\ell \left(\frac{\bar\Lambda^2}{\Lambda^2_{\rm UV}}\right)^{D-5} \log\frac{\mu}{\Lambda_{\rm UV}} \qquad \text{(RG running)}\,, \tag{7.4.3}$$

where $\bar\Lambda \equiv \max(\Lambda_{\rm IR}, m_H)$ and $\mu$ is an RG scale below $\Lambda_{\rm UV}$ and above $\Lambda_{\rm IR}$. The degree of divergence can be lowered to zero (corresponding to a log divergence) by making insertions of the Higgs mass term (hence $\bar\Lambda = m_H$) if the diagram features Higgs propagators, or by making use of the subleading terms in the DS correlator of Eq. (7.4.1) (hence $\bar\Lambda = \Lambda_{\rm IR}$). For example, for integer $D \geq 5$ the operator $O_H = [\partial_\mu (H^\dagger H)]^2$ will be renormalized at tree level by $\mathcal{O} H^\dagger H$.

For a given process with SM external states, the DS gives an additional contribution, not associated with divergences, that takes a different form depending on whether the energy $\sqrt{s}$ is above or below the IR scale $\Lambda_{\rm IR}$. If $\sqrt{s} < \Lambda_{\rm IR}$, then the DS dynamics can be integrated out at $\Lambda_{\rm IR}$ and generates (for any $D$) an IR threshold correction to dim-6 operators. We estimate in this case

$$\Delta c_6(\Lambda_{\rm IR}) \sim g_{SM}^{n-4} \frac{\kappa^2}{\Lambda^2_{\rm UV}} \frac{c}{16\pi^2} \left(\frac{g^2_{SM}}{16\pi^2}\right)^\ell \left(\frac{\bar\Lambda^2}{\Lambda^2_{\rm UV}}\right)^{D-5} \qquad \text{(IR threshold)}\,. \tag{7.4.4}$$

This is smaller than Eq. (7.4.3) by a log factor. If $\sqrt{s} > \Lambda_{\rm IR}$, then the exchange of DS states will

[48] Such quadratic divergence arises if the invariance associated to the conserved current $J^{DS}_\mu$ is broken by the UV dynamics. As an example, consider the $L \oplus N$ model of Sec. 7.3.2, where the axial $U(1)$ acting on the singlet $N$ is broken by the Yukawa couplings.

induce a long-distance contribution to the rate of events $R$ of order

$$\frac{\Delta R}{R} \sim \frac{\kappa^2 c}{16\pi^2 g_{SM}^2}\left(\frac{g_{SM}^2}{16\pi^2}\right)^{\ell}\left(\frac{s}{\Lambda_{\rm UV}^2}\right)^{D-4} \qquad \text{(Long-Distance)}\,, \tag{7.4.5}$$

arising through the interference with the SM amplitude. This should be compared with the correction from the interference of the SM amplitude with diagrams featuring one insertion of a dim-6 operator, $\Delta R/R \sim c_6/g_{SM}^{n-2}(s/\Lambda_{\rm UV}^2)$.

We can, at this point, establish the relative importance of the various virtual effects in Eqs. (7.4.2), (7.4.3), (7.4.4) and (7.4.5). In the case $\sqrt{s} < \Lambda_{\rm IR}$ (situation 1 of Fig. 7.1), the contributions from both DS and UV states are local and parametrized by dim-6 operators. As such, they are qualitatively indistinguishable at low energy. Furthermore, for $D \geq 5$ the UV threshold correction is always larger than the RG running, which in turn dominates (for $D$ even) over the IR thresholds. For $4 < D < 5$, instead, the DS exchange gives only an IR threshold contribution, which can (depending on the UV dynamics) be larger than the one generated by heavy mediators at $\Lambda_{\rm UV}$.

If $\sqrt{s} > \Lambda_{\rm IR}$ (situations 2 and 3 of Fig. 7.1), then for $D \geq 5$ the UV threshold corrections are larger than the long-distance effects, which in turn are larger than the RG running. In principle, one could distinguish experimentally the long-distance from local effects, since the former induce a non-analytic dependence of the cross section on the energy [318] (see also the discussion in Sec. 7.5.6). For $4 < D < 5$, the DS exchange generates only a long-distance contribution, which can win over the UV effect induced by heavy mediators.

To summarize, UV thresholds are expected to give the most important virtual effects for $D \geq 5$; portals with $4 < D < 5$, instead, generate only long-distance (for $\sqrt{s} > \Lambda_{\rm IR}$) or IR threshold (for $\sqrt{s} < \Lambda_{\rm IR}$) corrections, and can give the largest indirect contribution.

### 7.4.2 Production of DS states

The rate of production of DS states scales as $(1/\Lambda_{\rm UV}^2)^{D-4}$, and is clearly suppressed for large portal dimensions $D$. On the other hand, the experimental significance of the new physics events strongly depends on the kind of signature and on the size of the SM background. Depending on the lifetime of the lightest DS particle(s) (LDSP), one can have processes at colliders with missing energy, displaced vertices or prompt DS decays. In the rest of this subsection we will estimate the lifetime of the LDSP, explain our strategy to quantify the yield of events with respectively missing energy and displaced vertices, and discuss the validity of the effective field theory approach.

#### Lifetime of the Lightest DS Particle

At energies $\sqrt{s} \gg \Lambda_{\rm IR}$ (situation 3 of Fig. 7.1), the DS operator will excite a CFT state made of DS degrees of freedom whose evolution depends on the underlying dark dynamics. In strongly-coupled dark dynamics, there will be a phase of parton showering followed by dark hadronization, at the end of which many DS particles are produced. Weakly-coupled dark dynamics, on the other hand, will lead to few particles. In either case, these states will generally decay among themselves through fast transitions, and eventually decay to the LDSP $\psi$. Metastable or stable particles can also exist as a consequence of symmetries or kinematic suppressions. The LDSP itself might be stable if charged under some dark symmetry preserved by the portals. Generically, $\psi$ will decay to SM states through the portal interactions. The rate for this transition is expected to be much smaller than that characterizing inter-DS decays, especially in the case of strongly-coupled dynamics. Hence, the general expectation is that in a given process with dark excitations in the final state, these will promptly decay to $\psi$ and to stable particles (if present), and at later times $\psi$ decays back to the SM.

If the LDSP decays through a portal with dimension $D$ and is heavier than the EW scale, its lifetime can be naively estimated to be

$$\tau_\psi \sim \left[\Lambda_{\rm IR}\frac{\kappa^2}{8\pi}\left(\frac{f^2}{\Lambda_{\rm IR}^2}\right)\left(\frac{\Lambda_{\rm IR}^2}{\Lambda_{\rm UV}^2}\right)^{D-4}\right]^{-1}, \tag{7.4.6}$$

where $f$ is a decay constant defined by $\langle 0|\mathcal{O}|\psi\rangle = \hat{A}\, f\, \Lambda_{\rm IR}^{\Delta-2}$, and $\hat{A}$ is a dimensionless tensor that depends on the quantum numbers of $\mathcal{O}$ and $\psi$. For example, if the DS operator is a conserved current, then $\hat{A}$ is proportional to the polarization vector $\epsilon_\mu$ of $\psi$ if the latter is a massive spin-1 state, and to $p_\mu/\Lambda_{\rm IR}$ if $\psi$ has spin 0 (as for a Nambu-Goldstone boson). For strongly-coupled dark dynamics, one expects the decay constant to scale as $f \sim \sqrt{c}$ in the limit of large $c$, where $c$ is proportional to the number of degrees of freedom of the DS (see Eq. (7.4.1)). The LDSP can decay through one of the minimal portals of Eq. (7.2.2) or through operators with different quantum numbers and a larger dimension. The value of $\tau_\psi$ can differ from the estimate of Eq. (7.4.6) if $\psi$ is lighter than the EW scale and its main decay channel requires EW symmetry breaking. This occurs for example when $\psi$ mixes with the Higgs boson or the $Z$, respectively through the $\mathcal{O}H^\dagger H$ or $J_\mu^{DS} H^\dagger i\overleftrightarrow{D}^\mu H$ portal. In this case, one can compute $\tau_\psi$ (for $m_\psi < m_{Z,h}$) as

$$\tau_\psi = \left(\Gamma_i \sin^2\theta_i\right)^{-1}, \qquad \tan 2\theta_i = \frac{2\delta_i}{m_\psi^2 - m_i^2}, \qquad i = Z, h, \tag{7.4.7}$$

where $\Gamma_{Z,h}$ are the total decay widths of the $Z$ and $h$ (defined as the sum of the partial decay widths into the accessible SM final states) evaluated at $m_{Z,h} = m_\psi$. The mixing angle $\theta_{Z,h}$ is computed from the mass mixing terms

$$\delta_h = \kappa_{\mathcal{O}} v f \left(\frac{\Lambda_{\rm IR}}{\Lambda_{\rm UV}}\right)^{\Delta-2}, \qquad \delta_Z = \kappa_J\, v f\, \frac{m_Z \Lambda_{\rm IR}}{\Lambda_{\rm UV}^2}, \tag{7.4.8}$$

where we assumed that $\psi$ has spin 1 when it mixes with the $Z$. If the decay proceeds through the mixing with the Higgs boson, the value of $\tau_\psi$ from Eq. (7.4.7) is parametrically larger than the estimate (7.4.6) by a factor $m_h^2/\Lambda_{\rm IR}^2$. In the case of mixing with the $Z$, on the other hand, the lifetime is parametrically similar to that induced by a generic $D = 6$ portal.

**Missing Energy Events**

In the limit of a large hierarchy, i.e. for $\Lambda_{\rm IR}/\Lambda_{\rm UV}$ small enough, the LDSPs produced in high-energy collisions will decay outside the detector, and manifest themselves as missing energy. We will classify an event as a missing energy one if all of its LDSPs emerging from the primary collision decay outside the detector. The probability for one LDSP to decay within a distance $x$ from the primary vertex is $\exp(-x/c\tau_\psi\gamma)$, where $\gamma$ is the boost factor of the LDSP. We will thus estimate the probability for an event to be a missing-energy one as

$$\mathrm{P}[all > L_d] = \exp\left(-\frac{\langle n\rangle L_d}{c\tau_\psi\langle\gamma\rangle}\right), \tag{7.4.9}$$

where $L_d$ is the detector length, $\langle n\rangle$ is the average number of DS particles per event, and $\langle\gamma\rangle$ is the average boost factor. As already mentioned, the average number of DS particles depends on the type of dark dynamics. We will consider two benchmark values: the first, $\langle n\rangle = 2$, is representative of weakly-coupled dark sectors; in the second we set

$$\langle n\rangle = A\left(\frac{1}{\log\left(\langle E\rangle^2/\bar{\Lambda}^2\right)}\right)^B \exp\left(\frac{C}{\sqrt{\log\left(\langle E\rangle^2/\bar{\Lambda}^2\right)}}\right), \qquad \begin{array}{ll} A = 0.06 & C = 1.8 \\ B = 0.5 & \bar{\Lambda} = 0.1\,\Lambda_{\rm IR} \end{array} \tag{7.4.10}$$

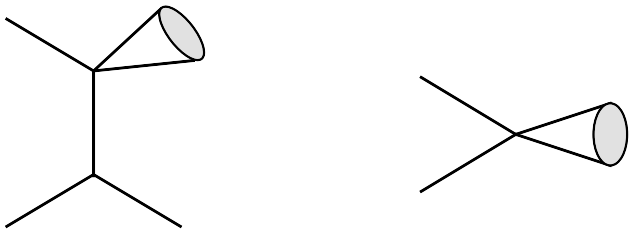

**Figure 7.3:** Prototype Feynman diagrams for DS production: associated production $SM+SM \to DS+SM$ (left), and single production $SM + SM \to DS$ (right). Solid lines denote SM particles, the gray blob stands for a DS state.

to characterize the behaviour of $\langle n \rangle$ in strongly-coupled dark sectors in terms of the energy $\langle E \rangle$ of the DS system. The functional dependence of Eq. (7.4.10) corresponds to the leading-order theoretical prediction in QCD [319, 320]. The values of the numerical coefficients well approximate those of QCD with 5 flavours, except for the overall normalization $A$ that cannot be computed perturbatively in QCD and has been fixed so that $\langle n \rangle = 2$ for $\langle E \rangle = 2\Lambda_{\rm IR}$.[49] We take Eq. (7.4.10) as representative of strongly-coupled dark sectors near a fixed point where couplings evolve (nearly) logarithmically like in QCD. Finally, we will estimate the average boost factor in Eq. (7.4.9) as

$$\langle \gamma \rangle = \frac{\langle E \rangle}{\langle n \rangle \Lambda_{\rm IR}} \,. \tag{7.4.11}$$

Triggering on missing-energy events requires (at least) one SM tagging object in the final state, and the prototype Feynman diagram for DS production in this case is that on the left of Fig. 7.3. For $\Lambda_{\rm IR} \ll \sqrt{\hat{s}} \ll \Lambda_{\rm UV}$, where $\hat{s} = p_{DS}^2$ is the squared momentum of the DS system, the inclusive cross section can be predicted independent of the low-energy details of the dark dynamics by exploiting its conformal behaviour. From the optical theorem it follows

$$\sum_n \int d\Phi_{DS} |\langle 0|O_{DS}|n\rangle|^2 = 2\,{\rm Im}\left[i\langle 0|T\{O_{DS}O_{DS}\}|0\rangle\right] \tag{7.4.12}$$

for a generic operator $O_{DS}$ that interpolates the dark state $|n\rangle$ from the vacuum, denoting the dark sector phase space with $d\Phi_{DS}$. Since conformal invariance determines the two-point function of $O_{DS}$ in terms of its dimension and up to an overall constant, the inclusive cross section well above threshold can be predicted in a model-independent way. As an analogy, consider for example the production of QCD hadrons in $e^+e^-$ collisions: near threshold the inclusive cross section exhibits a complicated pattern of resonances, but at energies $\sqrt{\hat{s}} \gg \Lambda_{QCD}$ its behaviour is determined by the asymptotic freedom of QCD, and depends only on the number of colors and the fact that the photon couples to a conserved quark current. In this regime, resumming the contributions of all the hadronic states reproduces the much simpler quark contribution (quark-hadron duality), as dictated by perturbativity. Notice, however, that the universal behaviour of the inclusive cross section stems from the fact that the theory is nearly conformal, and having a free fixed point is not crucial. Similar results, therefore, hold also for a strongly-coupled dark dynamics in its conformal regime.

In our analysis we will approximate the inclusive cross section for DS production by including only the contribution from the conformal regime and by using the optical theorem as in Eq. (7.4.12). We will thus neglect the events produced near threshold (in practice, we will impose a lower cut on $p_{DS}^2$). Including them obviously increases the total cross section and leads to more stringent constraints. Our results will be thus conservative. The importance of such threshold contribution

[49] This normalization gives a smaller average number of dark hadrons at $\langle E \rangle / \Lambda_{\rm IR}$ compared to the QCD prediction at $\langle E \rangle / \Lambda_{QCD}$. This is in fact reasonable given that the QCD spectrum includes particles (i.e. the pions and other pseudo Nambu-Goldstone bosons) that are parametrically lighter than other resonances.

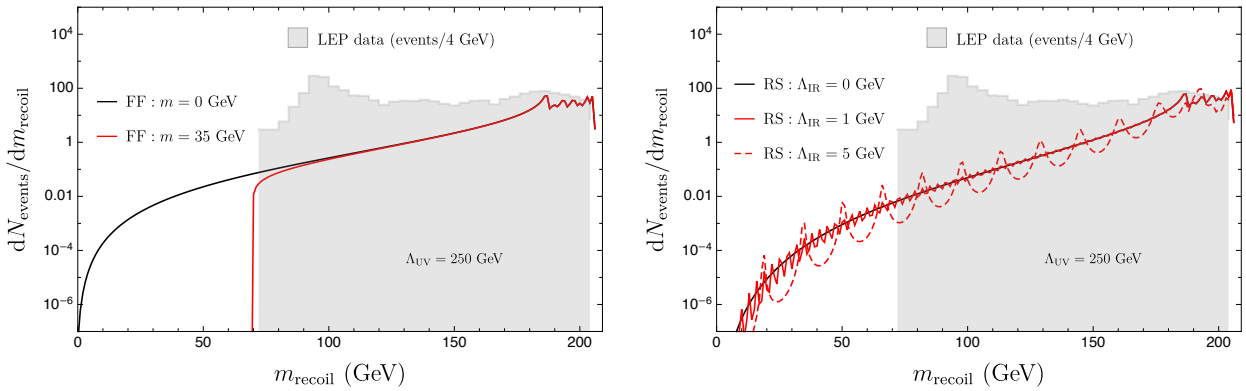


**Figure 7.4:** Differential number of events for $e^+e^- \to DS+\gamma$ as a function of the recoil mass (equal to the DS invariant mass) at LEP. The black and red curves in the left panel correspond to the prediction of the second model of Sec. 7.3.3, which leads to a DS with one Majorana fermion coupled to the SM through the $D = 6$ portal of Eq. (7.3.9). We have set $\kappa_J = 1$, $\Lambda_{\rm UV} = m_\phi = 250\,\text{GeV}$, and the fermion mass $m_\chi = m$ to the value indicated in the plot. Similarly, the curves in the right panel show the prediction of the RS model of Sec. 7.3.4, where the DS couples through the $D = 8$ portal of Eq. (7.3.13). We have set $(N_{CFT}^2 - 1) = 10$ (corresponding to $c_T = 400$, see Eq. (C.8)), $\kappa_T = 1$ and $\Lambda_{\rm UV} = 250\,\text{GeV}$. The gray region shows the number of events measured at LEP by the L3 Collaboration [321].

depends on the dimensionality of the portal responsible for the DS production and on the energy range probed by the collider. In the case of irrelevant portals, the (partonic) cross section usually grows with the energy; larger dimensions of the DS operator lead to faster growths at high energy and thus enhance the contribution away from threshold. As a consequence, the bulk of events can be produced in the deep conformal regime, where our approximation is accurate. To illustrate this point, we show in Fig. 7.4 the number of events predicted at LEP for the process $e^+e^- \to DS + \gamma$ as a function of the recoil mass (i.e. the invariant mass of the DS). This process has been measured by L3 [321] and OPAL [322] and sets constraints on elusive DS, as discussed in Sec. 7.5.2. The plots of Fig. 7.4 report the theoretical predictions for two benchmark dark sectors: the case of a free Majorana fermion coupled through the $D = 6$ portal of Eq. (7.3.9), and the 5D Randall-Sundrum theory with the $D = 8$ portal of Eq. (7.3.13). They show clearly that in those cases the bulk of the events are created away from threshold, in the regime where the DS dynamics is conformal. This situation should be contrasted with the case of relevant or marginal portals, where threshold events are more important and could first lead to discovery [323]. Notice that the $D = 8$ portal in the RS theory has the proper quantum numbers to singly excite the radion and spin-2 resonances, and that these appear as resonant peaks in the right panel of Fig. 7.4. We have used a modified expression of the two-point form factor as in Eq. (B.17), with a radion mass $m_\phi = \Lambda_{\rm IR}$. In the free-fermion case, the $D = 6$ portal excites pairs of fermions, and for this reason no resonant peak appears in the left panel of Fig. 7.4.

### Validity of the Effective Field Theory Description

An additional aspect of our calculation is the validity of the Effective Field Theory (EFT) approximation. The form of the portal interactions considered in this work, between the dark and SM sectors, arises by integrating out mediators of mass close to $\Lambda_{\rm UV}$. If the momentum at which this interaction is probed exceeds $\Lambda_{\rm UV}$, it is no longer a good approximation to describe it as a contact interaction mediated by a local operator. As we consider various experimental bounds, the validity of the EFT approximation must be enforced for internal self-consistency. The experimental data are usually presented in terms of a differential distribution of the number of events or cross section as a function of some kinematic variables (e.g. 3-momentum, transverse momentum or recoil mass)

relative to one or more of the visible particles. From momentum conservation, these kinematic variables are related to the momentum $p_{DS}$ that flows into the contact interaction. Assuming an $s$-channel exchange of the mediator field, the EFT expansion is controlled by $p_{DS}^2/\Lambda_{\rm UV}^2$; consistency requires $p_{DS}^2/\Lambda_{\rm UV}^2 \ll 1$, which translates into a condition on the kinematic variables. If the data are presented as a histogram, the condition in general varies bin by bin.

Taking this into consideration, we will adopt the approach advocated for example in Ref. [324], and use the subset of events that allows us to derive a self-consistent bound on $\Lambda_{\rm UV}$. To see how this works in practice, let us consider a scattering process with a mono-X final state plus missing momentum, as in the left diagram of Fig. 7.3. In this case

$$p_{DS}^2 = \hat{s} - 2\sqrt{\hat{s}}\,\not{p}\,, \tag{7.4.13}$$

where we take the final SM state to be massless, and $\not{p} \equiv |\vec{\not{p}}|$ is the magnitude of its 3-momentum. Requiring $p_{DS}^2/\Lambda_{\rm UV}^2 < \xi$, where $\xi$ is some value smaller than 1, translates into a condition on $\Lambda_{\rm UV}$:

$$\Lambda_{\rm UV} \gtrsim \frac{1}{\xi^{1/2}}\sqrt{\hat{s} - 2\sqrt{\hat{s}}\,\not{p}} \geq \frac{1}{\xi^{1/2}}\sqrt{\hat{s} - 2\sqrt{\hat{s}}\,\not{p}_T}\,, \tag{7.4.14}$$

where in the last step we have used $\not{p}_T \equiv \not{p}\sin\theta < \not{p}$. Here $\not{p}_T$ is the transverse missing momentum carried by the DS (equal to the transverse momentum of the SM final state). The EFT is within its validity as long as the missing momentum is sufficiently large. One can thus exclude bins with low $\not{p}_T$ to extend the validity of the analysis to smaller values of $\Lambda_{\rm UV}$. Including a given range of bins, consistency with EFT implies a lower and an upper bound in the range of $\Lambda_{\rm UV}$. Removing progressively bins of low $\not{p}_T$ and finally taking the union of the excluded regions, we obtain the overall bound. The advantage is that while taking all the data may not result in a valid exclusion region at all, discarding data in some bins gives a self-consistent, though weaker, bound. In the following, when applying this procedure, we will fix $\xi = 0.1$.

**Events with displaced decays**

Besides events with missing energy, the production of DS states can lead to displaced vertices (DV) if some of the LDSPs decay inside the detector far from the interaction region. For a fixed value of $\Lambda_{\rm UV}$, this occurs in a range of IR scales $\Lambda_{\rm IR}$ that varies with the portal dimensionality $D$. Depending on the experimental analysis, events are selected by requiring a minimum number of decays in specific regions of the detector (inner detector, calorimeters, muon spectrometer). To analyse those data we construct a probability for each event to pass the required conditions as explained in Appendix D. This probability is maximized and close to 1 for lifetimes $\tau_\psi$ in a certain interval, which in turn corresponds to an interval of $\Lambda_{\rm IR}$ values at fixed $\Lambda_{\rm UV}$. Events with displaced vertices can be triggered on and reconstructed without the need of a SM tagging object. The leading production diagram is thus the one on the right of Fig. 7.3. As for missing energy events, the rate of DV events can be computed conservatively by including only the contribution from the conformal regime $\sqrt{\hat{s}} \gg \Lambda_{\rm IR}$, but in this case the result depends on additional quantities whose value is model dependent. For example, the LDSPs from strongly-coupled dark sectors will be produced with energies and angular distributions determined by the showering and hadronization processes. This leads to an acceptance efficiency in the reconstruction of the displaced vertices that depends on the type of dark dynamics. Since the goal of our analysis is to assess the importance of DV searches in testing our theories, we will estimate the event rate by using the two benchmark values of $\langle n \rangle$ described above and by making reasonable assumptions to average out any further model dependency.

**Events with prompt decay**

Finally, for small hierarchy of scales, i.e. $\Lambda_{\rm IR}/\Lambda_{\rm UV}$ not too small, the LDSPs produced in a DS event will decay promptly. The significance of these events strongly depends on the details of the underlying DS dynamics and cannot be assessed in a model-independent way. An analysis of this kind goes beyond the scope of this work, and we will not consider the region of the parameter space where only prompt decays occur.

| Probes of DS production | Probes of DS virtual exchange |
|---|---|
| • $Z$ and Higgs boson decays | • Fifth-force experiments |
| • Non-resonant production at LEP and LHC | • EW precision tests |
| • High-intensity experiments | |
| • Supernova and stellar cooling | |
| • Positronium lifetime | |

**Table 7.3:** List of processes and experiments analysed in this work that probe the dark sector dynamics.

## 7.5 Terrestrial and Astrophysical Bounds

In this section we present our analysis of the terrestrial and astrophysical processes that can probe the dark sector dynamics. Following the strategy outlined in the previous section, we will derive constraints on the scales $\Lambda_{\rm IR}$ and $\Lambda_{\rm UV}$, for given coupling $\kappa$ and dark multiplicity $c$, by considering individually each of the portals in Eq. (7.2.2). We have analysed both processes with production of DS states and processes where these are virtually exchanged. The complete list is reported in Table 7.3. It includes searches at high-energy colliders, where DS excitations can manifest themselves as missing energy, displaced vertices or in precision observables, and fixed-target and beam dump experiments, which probe the DS-SM interaction at energies of order $10 - 100\,\text{GeV}$. Complementary to these, there is another class of experiments that probe the DS-SM interaction at much lower energies. They study the effect of the DS on long-range forces or precision observables like the ortho-positronium lifetime. Finally, there are celestial constraints coming from astrophysical observations, which probe the DS-SM interaction at MeV and keV energies.

In the following we discuss each process starting from those with DS production.

### 7.5.1 DS production from $Z$ and Higgs boson decays

When $\Lambda_{\rm IR}$ is smaller than the EW scale, one of the most efficient ways to produce DS states at colliders is through the decay of the $Z$ and Higgs bosons. Such resonant production proceeds respectively through $\mathcal{O}H^\dagger H$ (Higgs portal) and $J^\mu_{DS} H^\dagger i\overleftrightarrow{D}_\mu H$ ($Z$ portal). The rate of DS events can be computed, in the narrow width approximation, as the SM cross section for Higgs or $Z$ production times the branching ratio for their decay into DS states. No issue arises in this case with the validity of the effective field theory description, since the energy characterizing the production of DS states is that of the $Z$ or Higgs boson mass, while $\Lambda_{\rm UV}$ is required to be larger. One can extract the inclusive decay width of the Higgs or $Z$ boson into DS states from the imaginary part of the 2-point correlator of the DS operator in the portal. For example, working at leading order in the Higgs portal interaction, the pole residue and width of the Higgs boson propagator are corrected by:

$$Z_h \equiv 1 + \delta Z_h = 1 + \frac{\kappa_{\mathcal{O}}^2 v^2}{\Lambda_{\rm UV}^{2\Delta_{\mathcal{O}}-4}} \frac{d}{dp^2} \text{Re}\, i \langle \mathcal{O}(-p)\mathcal{O}(p)\rangle \,|_{p^2=m_h^2} \tag{7.5.1}$$

$$\Gamma_{h\to DS} = -\frac{1}{m_h} \frac{\kappa_{\mathcal{O}}^2 v^2}{\Lambda_{\rm UV}^{2\Delta_{\mathcal{O}}-4}} \text{Im}\, i \langle \mathcal{O}(-p)\mathcal{O}(p)\rangle \,|_{p^2=m_h^2}\,. \tag{7.5.2}$$

We approximate the imaginary part of the 2-point correlator at $m_h \gg \Lambda_{\rm IR}$ by using its conformal expression in Eq. (B.8) of Appendix B, and obtain

$$\Gamma_{h\to DS} = \frac{\kappa_{\mathcal{O}}^2\, c_{\mathcal{O}}}{\pi^{3/2}} \frac{\Gamma(\Delta_{\mathcal{O}}+1/2)}{\Gamma(\Delta_{\mathcal{O}}-1)\Gamma(2\Delta_{\mathcal{O}})} \frac{v^2\, m_h^{2\Delta_{\mathcal{O}}-5}}{\Lambda_{\rm UV}^{2\Delta_{\mathcal{O}}-4}}\,. \tag{7.5.3}$$

Similar steps in the case of the $Z$ portal, and the use of Eq. (B.9) in Appendix B, lead to the $Z \to DS$ decay width:

$$\Gamma_{Z\to DS} = -\frac{\kappa_J^2 v^2 m_Z}{3\Lambda_{\rm UV}^4} \sum_{i=1,2,3} \epsilon_\mu^i \epsilon_\nu^{*i} \ \text{Im}\ i\langle J^\mu_{\rm DS}(p) J^\nu_{\rm DS}(-p)\rangle\big|_{p^2=m_Z^2} = \frac{\kappa_J^2 v^2 m_Z^3}{\Lambda_{\rm UV}^4}\frac{c_J}{96\pi}\,. \tag{7.5.4}$$

The total width of the $Z$ boson has been measured accurately by the LEP experiments, which put an upper bound on beyond-the-SM contributions $\Delta\Gamma_Z < 2.0$ MeV at 95% confidence level [325]. Using this result and Eq. (7.5.4) leads to the constraint

$$\Lambda_{\rm UV} > 525\,{\rm GeV} \times (\kappa_J^2 c_J)^{1/4}\,. \tag{7.5.5}$$

A similarly inclusive bound can be obtained through a global fit to data from Higgs searches at the LHC. The correction to the residue of the Higgs propagator due to the DS exchange implies a universal shift of the Higgs couplings by a factor $Z_h^{n/2}$, where $n$ is the number of Higgs bosons in the vertex. Neglecting possible modifications to the couplings from the UV dynamics, the common signal strength modifier used by LHC collaborations can be expressed as

$$\mu \equiv \frac{\sigma \times BR}{\sigma_{SM} \times BR_{SM}} \simeq 1 + \delta Z_h - \frac{\Gamma_{h\to DS}}{\Gamma_h^{SM}}\,, \tag{7.5.6}$$

where $\Gamma_h^{SM}$ is the SM Higgs boson total decay width, $\Gamma_h^{SM} = 4.07\,{\rm MeV}$ [326]. From Eq. (7.5.1), (7.5.2) and Eqs. (B.4), (B.8) it follows that $\delta Z_h$ is smaller than $\Gamma_{h\to DS}/\Gamma_h^{SM}$ by a factor $\Gamma_h^{SM}/m_h \ll 1$, and can be thus neglected. Using Eq. (7.5.2) and the measurement $\mu = 1.17 \pm 0.10$ made by CMS with 13 TeV data [327] gives the constraint

$$\Lambda_{\rm UV} > m_h \times \left(1.9\times 10^5\, \kappa_{\mathcal O}^2 c_{\mathcal O}\, \frac{\Gamma(\Delta_{\mathcal O}+1/2)}{\Gamma(\Delta_{\mathcal O}-1)\Gamma(2\Delta_{\mathcal O})}\right)^{\frac{1}{2\Delta_{\mathcal O}-4}}\,, \tag{7.5.7}$$

at 95 % probability.[50]

Measuring precisely the decay rates of the $Z$ and of the Higgs boson into SM particles leads to the indirect constraints on the production of DS states discussed above. Searches at high-energy colliders, however, also look for non-standard decay modes in a variety of final states. The bound on the Higgs invisible branching ratio set by the LHC experiments, for example, constrains the region of parameter space where the LDSP decays outside the detector. We use the recent result obtained by the ATLAS collaboration, $BR_{inv} < 0.13$ at 95% CL [328], and estimate the number of missing-energy events through Eqs. (7.4.9), (7.5.3). For small values of $\Lambda_{\rm IR}$ the probability of Eq. (7.4.9) is approximatively 1 and the bound turns out to be very similar to that of Eq. (7.5.7). Conversely, for $\Lambda_{\rm IR}$ large enough the majority of LDSPs decay inside the detector and the probability of Eq. (7.4.9) goes to zero. The corresponding exclusion region is shown in Fig. 7.5 (solid contours) for three different LDSP decay portals: the same Higgs portal responsible for Higgs-resonant production, and generic $D = 6$ and $D = 8$ portals. Similar constraints come from mono-X searches sensitive to the resonant production of a $Z$ boson followed by its decay into invisible final states. We have analysed missing-energy searches performed at LEP2 by the L3 collaboration (at a centre-of-mass energy between 189 GeV and 209 GeV) in association with a photon [321] and a $Z$ boson [332], and by the OPAL collaboration (at $\sqrt{s} = 189\,{\rm GeV}$) with single photon events [322]. The corresponding bounds turn out to be weaker than the inclusive one from the $Z$ decay width and will not be discussed. From the LHC Run2 at $\sqrt{s} = 13\,{\rm TeV}$ we have analysed the ATLAS mono-jet [333], mono-photon [334] and mono-$Z$ [335] searches. From Run1 at $\sqrt{s} = 8\,{\rm TeV}$ we considered the

[50] This bound is derived by constructing a posterior probability as a function of $\delta = 1-\mu$ in terms of the likelihood $\exp\left[(1-\delta-1.17)^2/0.02\right]$ and a flat prior. We find $\delta = \Gamma_{h\to DS}/\Gamma_h^{SM} < 0.11$ with 95 % probability, which in turn implies Eq. (7.5.7).

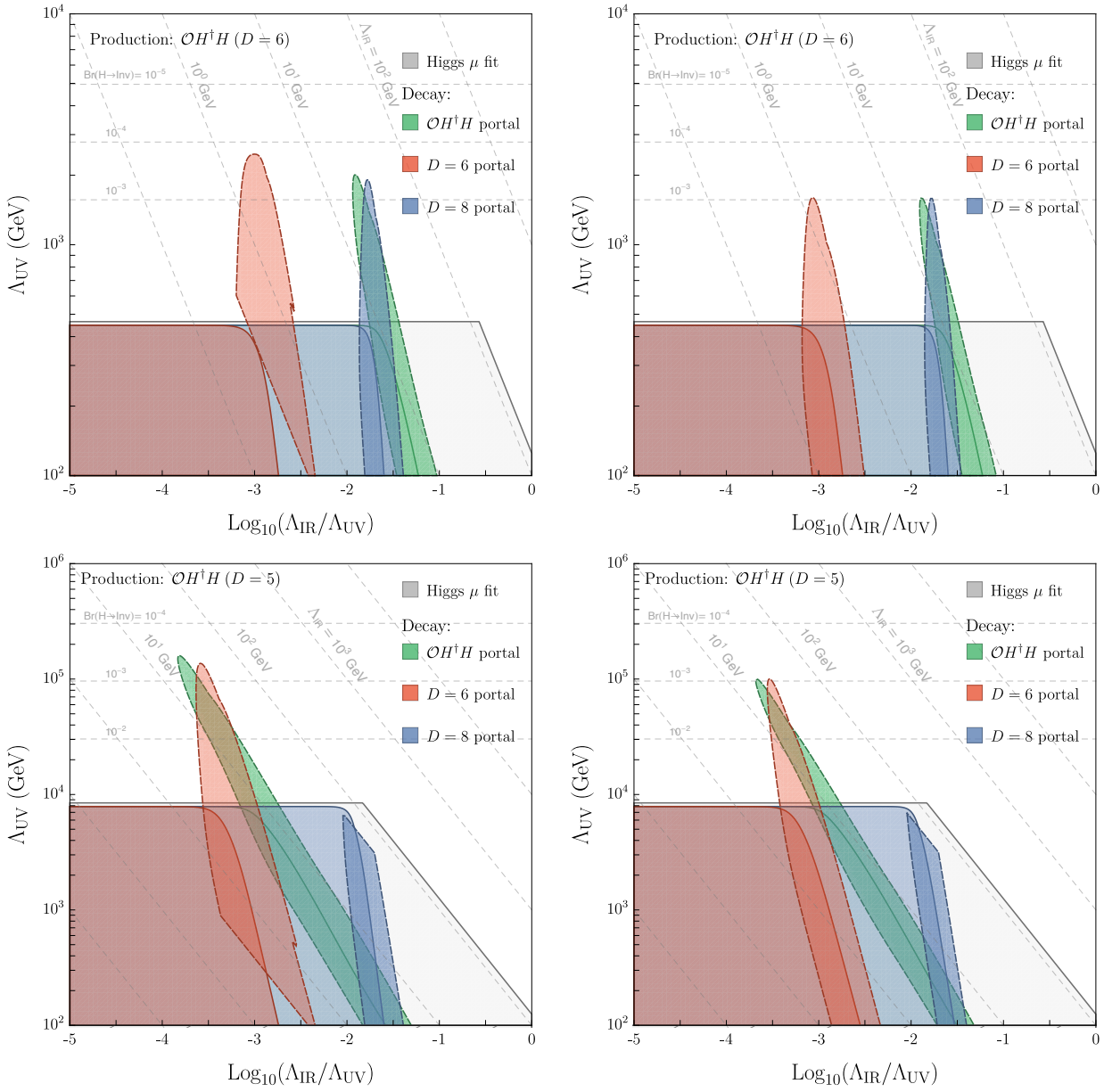


**Figure 7.5:** Constraints on resonant DS production through a $D = 6$ (upper panels) and $D = 5$ (lower panels) Higgs portal. Plots on the left (on the right) assume a strongly (weakly) coupled dark sector. Exclusion regions from the bound on the Higgs invisible width of Ref. [329] (solid contours) and the searches for displaced vertices of Refs. [330, 331] (dashed contours) are shown for three different types of LDSP decay portal: the same Higgs portal responsible for the production (green), generic $D = 6$ (red) and $D = 8$ (blue) portals. Also shown in gray is the exclusion from the LHC fit to Higgs data of Eq. (7.5.7). All the plots assume $\kappa_i^2 c_i = 1$ for the various portals.

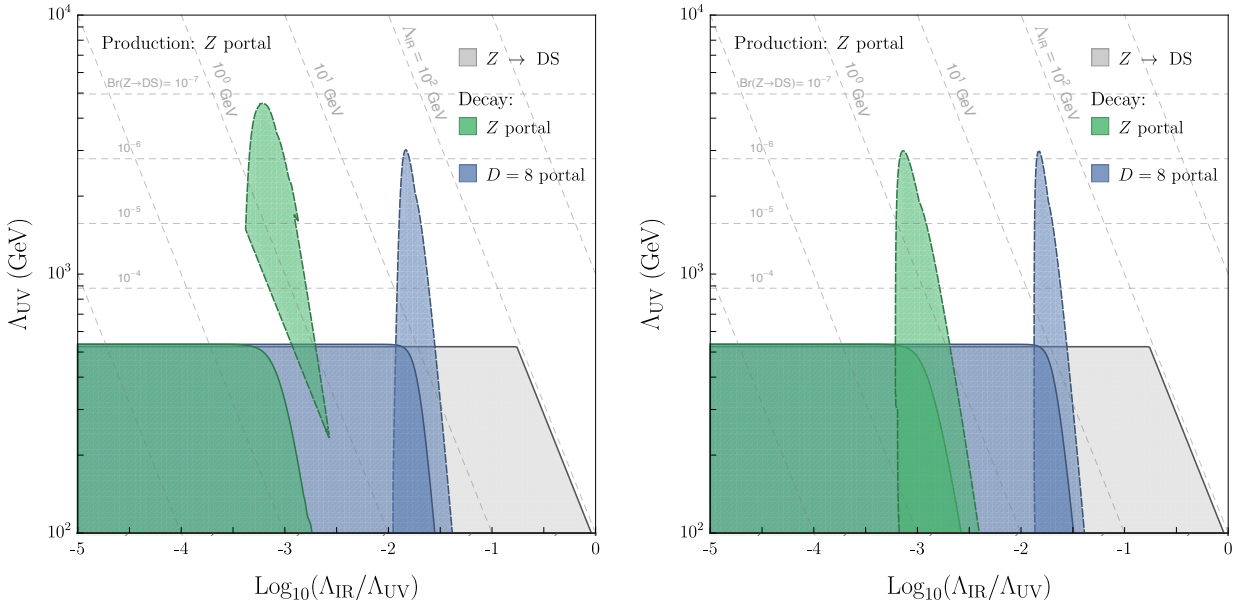


**Figure 7.6:** Constraints on resonant DS production through the $Z$ portal. The plot on the left (on the right) assumes a strongly (weakly) coupled dark sector. Exclusion regions from the mono-jet search of Ref. [333] (solid contours) and the searches for displaced vertices of Refs. [330, 331] (dashed contours) are shown for two different types of LDSP decay portal: the same $Z$ portal responsible for the production (green), and a generic $D = 8$ portal (blue). The exclusion from the invisible width measurement at LEP of Eq. (7.5.5) is shown in gray. Both plots assume $\kappa_i^2 c_i = 1$ for the various portals.

mono-jet search of Ref. [336]. All of these studies have found signals consistent with a pure SM background and set constraints on the resonant production of DS states through the $Z$ portal. The strongest bound comes from the mono-jet analysis at 13 TeV and is comparable to that from the $Z$ width at LEP. The corresponding exclusion region is shown in Fig. 7.6 (solid contours) for two choices of the LDSP decay portal: the same $Z$ portal, and a generic $D = 8$ portal.

For values of $\Lambda_{\rm IR}$ not too small, some of the LDSP produced in the event can decay inside the detector, far from the primary vertex. Signatures of this kind are searched for by the LHC collaborations in a variety of final states. A nice overview of searches for long-lived particles can be found in a recent document written by the LHC LLP Community [337]. Recasting all the existing experimental bounds into our theoretical parameter space is beyond the scope of this work. An idea of their effectiveness can be however obtained by considering the searches performed by ATLAS for displaced hadronic jets in the muon spectrometer (MS) [330] or in both the MS and the inner detector (ID) [331]. These are particularly optimized since they make use of dedicated trigger and vertex algorithms to analyse jets in the MS, with relatively low thresholds. Among the search strategies pursued in Refs. [330, 331], the simplest ones require no additional prompt decays and are inclusive of any other activity in the event. Specifically, we will make use of the analysis in Ref. [330] that searches for events with at least two displaced hadronic vertices in the MS, and the analysis of Ref. [331] where events with (at least) one decay in the MS and one in the ID are selected. We model the probability that a given event gives rise to such signatures as explained in Appendix D, and assume an overall efficiency for triggering and reconstructing an event equal to 0.01. The bounds obtained for $Z$ and Higgs resonant production are shown respectively in Figs. 7.5 and 7.6 (dashed contours). They are stronger than those set on the rate of DS events by missing-energy searches by $2-3$ orders of magnitude, and can probe branching ratios into DS states of order $10^{-6}$ for the $Z$ and a few $\times 10^{-4}$ for the Higgs boson.

Other searches for long-lived particles performed by ATLAS and CMS typically require extra

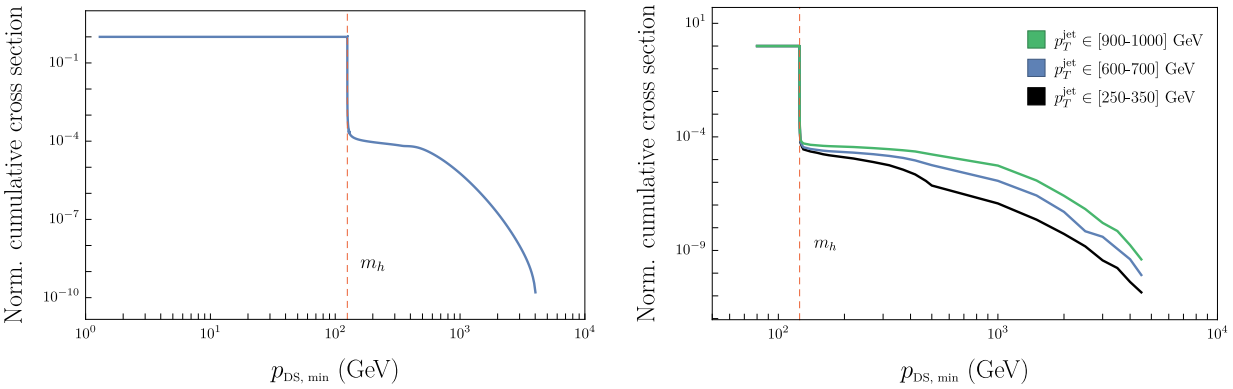


**Figure 7.7:** Normalized cumulative cross section for $pp \to DS$ (left plot) and $pp \to DS+j$ (right plot) at the 13 TeV LHC for a $D = 6$ Higgs portal, shown as a function of the lower limit of integration over the invariant mass of the DS system. In the right plot three curves are shown corresponding to events in three different bins of the jet transverse momentum.

prompt activity or missing energy in addition to the displaced vertices. Since the request of prompt and energetic SM particles reduces the production rate, these analyses are naively expected to be less effective in constraining the dark sector theories considered in this work. A possible important exception is the case where the DM is part of the DS and produced together with the LDSP. Events of this kind always contain (possibly a large amount of) missing energy, which can be used to trigger the event and reduce the background. It would be therefore interesting to assess the constraints imposed on elusive dark sectors by searches that require displaced vertices in association with large missing energy, like those on photons or jets. We leave this study to a future work. Finally, searches for long-lived particles at LHCb also make use of dedicated triggers for displaced vertices. These are however required to be inside the tracker, i.e. within a distance of 200 mm (30 mm) from the primary vertex in the beam (transverse) direction. This limits the sensitivity to short LDSP lifetimes. Considering that typically hard kinematic cuts are imposed to reduce the background and that LHCb has a smaller integrated luminosity than ATLAS and CMS, the effectiveness of these analyses is expected to be smaller than that of the searches considered above.

### 7.5.2 Non-resonant DS production at LEP and LHC

In presence of (unsuppressed) $\mathcal{O}H^\dagger H$ and $J^\mu_{DS} H^\dagger i\overleftrightarrow{D}_\mu H$ portals, and for $\Lambda_{\text{IR}}$ below the electroweak scale, the strongest constraints on the dark sector come from $Z$ and Higgs decays, as discussed in the previous subsection. Values of $\Lambda_{\text{IR}}$ larger than the electroweak scale are more difficult to probe since in that case the production of DS states is non-resonant and has a smaller rate. The relative importance of resonant vs non-resonant DS production at the LHC is illustrated in Fig. 7.7 for a $D = 6$ Higgs portal. The cumulative cross section for the processes $pp \to DS$ and $pp \to DS + j$ drops sharply when the lower limit of integration over the invariant mass of the DS system is raised above the Higgs mass threshold. Non-resonant production is thus expected to give weaker bounds than those from resonant processes. Furthermore, for $\Lambda_{\text{IR}}$ above the electroweak scale and not too large $\Lambda_{\text{UV}}$, the LDSP decays promptly. As already discussed, prompt decays at colliders give model-dependent signatures whose analysis is beyond the scope of this work. On the other hand, the DS could interact with the SM through portals different than $\mathcal{O}H^\dagger H$ and $J^\mu_{DS} H^\dagger i\overleftrightarrow{D}_\mu H$ (alternatively, these latter could be generated with a suppressed coefficient). In this case, for any value of $\Lambda_{\text{IR}}$, one needs to analyse non-resonant processes to assess the current bounds on the DS dynamics.

Assuming a non-resonant DS production, for small $\Lambda_{\text{IR}}$ the LDSP decays outside the detector and the constraints are set by missing-energy searches. We have analysed the mono-X searches performed at LEP2 [321, 322, 332] and LHC [333–336] discussed previously for $Z$ decays. Dark

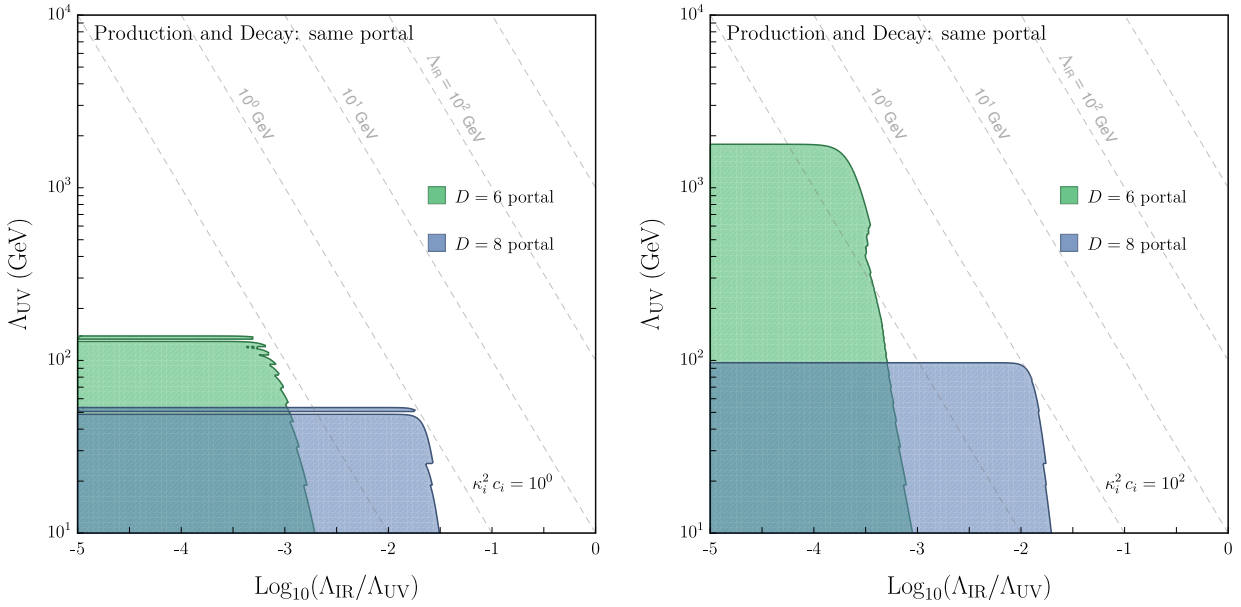


**Figure 7.8:** Constraints on non-resonant DS production from mono-photon searches at LEP. Two choices of portals are shown: $J_\mu^{DS}\bar{e}\gamma^\mu e$ $(D=6)$ and $T_{\mu\nu}^{DS}(F_\alpha^\mu F^{\alpha\nu} + \bar{e}\gamma^\mu D^\nu e)$ $(D=8)$. It is assumed that the same portal is responsible for both the DS production and the LDSP decay, and that the dark sector is strongly coupled. The value of $\kappa_i^2 c_i$ is fixed to 1 in the plot on the left and to $10^2$ in the plot on the right.

sector production proceeds through the prototype diagram on the left of Fig. 7.3, where the SM tagging particle can be an electron, photon, $Z$ boson or a jet stemming from a quark or gluon. Their yield has been computed in bins of missing momentum by assigning each event a weight given by Eq. (7.4.9).[51] For each data set, we make use of different combinations of bins in missing energy in order to increase the EFT validity, as explained in Sec. 7.4.2. We find that the strongest bounds come from mono-photon searches at LEP [321, 322], while the impact of LHC searches is limited by the request of the EFT validity, since the corresponding analyses make use of events at higher energies or invariant masses. Figure 7.8 shows the exclusion regions that we have obtained from LEP data for the following two portals involving electrons and photons: $J_\mu^{DS}\bar{e}\gamma^\mu e$ $(D=6)$ and $T_{\mu\nu}^{DS}(F_\alpha^\mu F^{\alpha\nu} + \bar{e}\gamma^\mu D^\nu e)$ $(D=8)$.

As expected, the constraints are much weaker than those from resonant DS production if the comparison is done for the same value of $\kappa_i^2 c_i$.

For large enough $\Lambda_{IR}$, the LDSP can give rise to displaced decays inside the detector. As for the case of resonant DS production, we focused on the searches for displaced jets made by ATLAS in Refs. [330, 331], and computed the signal yield by assigning each event a weight through the probabilities reported in Appendix D. We find that no bound compatible with the validity of the effective field theory can be set in this case unless $c_J\kappa_J^2$ has a very large value, $c_J\kappa_J^2 \gtrsim 10^3$.

### 7.5.3 Constraints from High-Intensity Experiments

Dark sectors with sufficiently low IR scale can be probed by high-intensity experiments operating at center-of-mass energies smaller than those reached at modern high-energy colliders. In this case the strategy is that of producing the DS particles by pushing the intensity, rather than the energy, frontier. Simple dimensional analysis suggests that this approach can probe most effectively dark sectors that couple through relevant or marginal portals [293]. As a prototype of high-intensity

[51] The Feynman rules have been generated with `FeynRules` 2.3 [338, 339], using a model file based on [340]. The squared matrix elements have been computed with `FeynArts` 3.10 [341].

experiments consider those where an intense proton or electron beam hits a fixed target or a beam dump. Dark sector particles can be produced directly in the hard scattering between the incident beam particle and the target, or originate from the decay of QCD hadrons produced in the collision. The cross section for direct DS production naively scales as $\sigma \sim (c\kappa^2/E^2)(E/\Lambda_{\rm UV})^{2(D-4)}$, where $E$ is the beam energy. Then, a very naive estimate of the ratio of the numbers of DS events produced at a collider and a fixed-target experiment is [293]

$$\frac{N_{collider}}{N_{target}} = \frac{\sigma_{collider}\,\mathcal{L}_{collider}}{\sigma_{target}\,\mathcal{L}_{target}} \sim 10^{-3} \left(\frac{E_{collider}}{E_{target}}\right)^{2D-10} \left(\frac{\mathcal{L}_{collider}}{100\,\text{fb}^{-1}}\right) \left(\frac{10^{20}}{N_{\rm POT}}\right) , \tag{7.5.8}$$

where the integrated luminosity at the fixed target experiment, $\mathcal{L}_{target} = N_{\rm POT}\ell\rho$, depends on the total number of incident particles (protons or electrons) delivered on target, $N_{\rm POT}$, the length $\ell$ of the target and its atomic density $\rho$. To derive Eq. (7.5.8) we have assumed $\ell = 10\,\text{cm}$ and $\rho = 10^{23}\,\text{cm}^{-3}$. This estimate suggests that portals with $D \leq 5$ can be effectively probed at fixed-target experiments with high luminosity, while high-energy colliders are parametrically more efficient for $D > 5$. Clearly, a quantitatively more accurate estimate should take into account the effect of the parton distribution functions at hadron colliders, the finite mass of the target nucleus in fixed-target experiments, as well as the geometric acceptance of the detector in each case. However, the qualitative conclusion that can be drawn from Eq. (7.5.8), i.e. that direct DS production through higher-dimensional portals can be best probed by pushing the energy frontier, is generally correct and in agreement with the results of our analysis reported in this section. An estimate similar to (7.5.8) can be derived to compare the rates of DS particles produced in the decay of QCD hadrons at colliders and fixed target experiments. Such rate scales naively as $\sim \sigma_{incl}(E)c\kappa^2(M/\Lambda_{\rm UV})^{2(D-4)}$, where $M$ is the mass of the decaying hadron and $\sigma_{incl}$ is an inclusive QCD cross section. The relatively mild increase of the latter with the c.o.m. energy (see for example Ref. [342]) is not sufficient to make colliders competitive with high-intensity experiments in this case. Decays of QCD hadrons to DS particles will be thus most effectively probed by dedicated low-energy experiments with large integrated luminosity.

In this section we will study the sensitivity that high-intensity experiments have on elusive dark sectors analysing both of the possible production modes. Let us consider first the production that occurs in the hard scattering between an intense proton or electron beam and a fixed target.

### Direct DS production from the hard scattering

There are two broad experimental strategies that have been adopted to detect the DS particles. A first class of experiments makes use of a shield or active detector regions to block or veto any particle emerging from the collision, with the exception of neutrinos and DS states. These can reach a detector placed downstream of the shield where they decay in flight to SM states or scatter with the detector material. Neutrino experiments, such as CHARM [343], LSND [344], NuTeV [345], MINOS [346] and MiniBooNE [347], belong to this class. They utilize very intense proton beams (with up to $10^{20}-10^{23}$ protons delivered on target) and may include a decay volume where neutrinos are produced by the in-flight decay of pions and kaons. Other experiments, such as E137 and E141 at SLAC [348, 349] and E774 at Fermilab [350], utilized an electron beam and were dedicated to the search for new long-lived neutral particles. A second class of experiments, such as NA64 at CERN [351] and the proposed LDMX [352], are designed to measure the energy (and possibly the momentum) of the electron beam before and after the collision with the target. Calorimetry is then used to veto any significant hadronic activity following the collision. Long-lived dark sector particles can either decay outside the detector and thus give rise to events with missing energy or momentum, or lead to displaced decays inside the detector.

A complete analysis of all these experiments is clearly beyond the scope of this work. We will thus focus on two of them, one in the first experimental class and one in the second class, and use

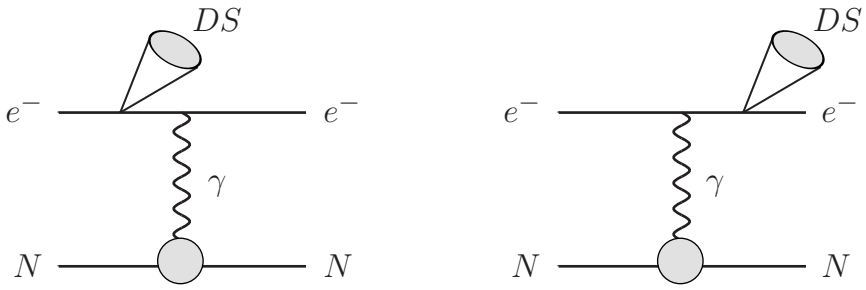


**Figure 7.9:** Feynman diagrams characterizing direct DS production at fixed target experiments with electron beams like NA64 and E137. The DS particles can be radiated off the initial or final electron line through the $D = 6$ portal $(\bar{e}\gamma^\mu e)J^\mu_{DS}$.

them to illustrate the sensitivity that fixed-target experiments have on elusive dark sectors. We will consider, in particular, theories with a $D = 6$ portal of the form $J^{em}_\mu J^\mu_{DS}$, where $J^\mu_{em} = \bar{e}\gamma^\mu e$ is the SM electron current and $J^\mu_{DS}$ is a DS current.

Among the experiments that can search for missing energy we consider NA64. It features a high-intensity electron beam with energy $E_0 = 100\,\text{GeV}$ hitting an active lead target (the ECAL). Dark sector excitations can be emitted through dark bremsstrahlung in the scattering of the incident electron with the target nucleus, see Fig. 7.9, and decay outside the detector (the HCAL) if sufficiently long lived. The HCAL itself is used to veto any hadronic activity that follows a deep inelastic scattering where the nucleus breaks apart. The analysis of Ref. [353] in particular, selects events that are characterized in their final state by one electron with energy $E'$ plus missing energy $E_{\text{miss}} \equiv E_0 - E'$, without further activity. SM backgrounds are removed by requiring $E_{\text{miss}} \geq 50\,\text{GeV}$. Using a dataset corresponding to $2.84 \times 10^{11}$ electrons on target, no event is found which passes all the cuts, with an estimated background of 0.53 events. This result is interpreted to set constraints on dark photon models where the dark photon is radiated off the electron line and decays to DM particles which escape detection. These models are particular examples of a dark sector where the invariant mass of the DS system is fixed (for a small dark photon decay width) to the dark photon mass, $p^2_{DS} = m^2_{\gamma_D}$. More in general, the DS system will consist of several particles and have arbitrary invariant mass, compatible with phase space constraints. It is convenient to reduce this general situation to the case of a dark photon with varying mass by factorizing the Lorentz invariant phase space as $d\Phi_{2+n} = (2\pi)^{-1} dp^2_{DS} d\Phi_3 d\Phi^{DS}_n$. Here $d\Phi^{DS}_n$ denotes the $n$-body phase space of the DS system with total momentum $p_{DS}$; $d\Phi_3$ is instead the 3-body phase space obtained by replacing the entire dark sector with a single particle of momentum $p_{DS}$ and mass $p^2_{DS}$. The integration over the DS phase space can be performed easily by using the optical theorem; the result is written in terms of the imaginary part of the 2-point correlator of the DS operator $J^\mu_{DS}$:

$$\begin{aligned}\sigma(eN \to eN + DS) = \frac{\kappa_J^2}{\Lambda^4_{\text{UV}}} \frac{1}{4E_0 m_N} \frac{1}{2\pi} \int dp^2_{DS} \int d\Phi_3\, \mathcal{M}_\mu \mathcal{M}^*_\nu\, G(t) \\ \times\, 2\,\text{Im}\big[i\langle 0|T(J^\mu_{DS}(p_{DS}) J^\nu_{DS}(-p_{DS}))|0\rangle\big]\ ,\end{aligned} \tag{7.5.9}$$

where $\mathcal{M}_\mu$ is the matrix element with one insertion of the portal interaction, and $G(t)$ is a form factor that parametrizes atomic and nuclear scatterings. Here $t = (p'_N - p_N)^2$ is the momentum transfer, and $p_N$, $p'_N$ are respectively the initial and final 4-momenta of the nucleus $N$, whose mass is denoted by $m_N$. We set $G(t) = G_{2,el}(t) + G_{2,in}(t)$, where $G_{2,el}(t)$ and $G_{2,in}(t)$ are respectively the elastic and inelastic contributions to the form factor, as defined by Eqs. (A18) and (A19) of Ref. [354], see also Refs. [355, 356]. The production of a dark photon of mass $m_{\gamma_D}$ is characterized by a small emission angle $\theta_{\gamma_D} \lesssim \max[(m_{\gamma_D} m_e/E_0^2)^{1/2}, (m_{\gamma_D}/E_0)^{3/2}]$ and by a spectrum of momentum transfer peaked at $t_{\min}$, where $-t_{\min} \approx m^4_{\gamma_D}/E_0^2$ if $m_{\gamma_D} \gtrsim m_e$ [354–356]. Formula (7.5.9) applies in that case as well if one replaces $(\kappa_J/\Lambda^2_{\text{UV}}) J^\mu_{DS} \to (\varepsilon e) A^\mu_D$, where $A^\mu_D$ is the dark photon field

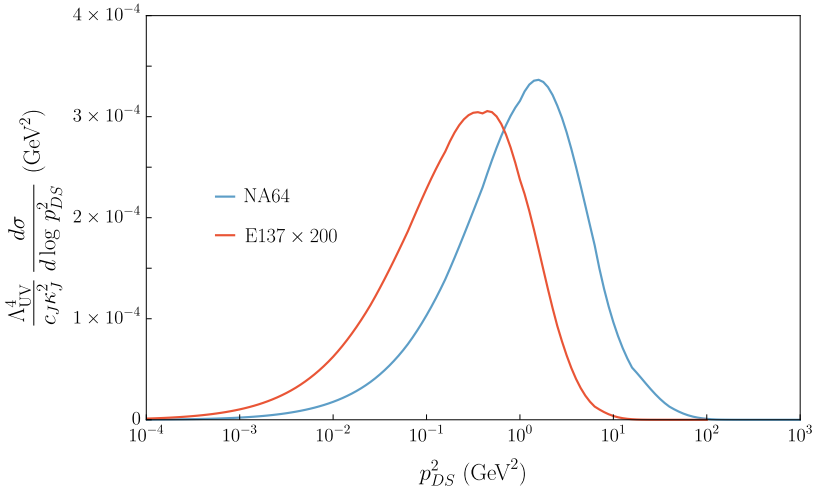


**Figure 7.10:** Differential cross section for DS production as a function of the DS invariant mass squared at NA64 and E137. The NA64 curve is obtained by imposing the cut $E_{\rm miss} \geq 50\,\text{GeV}$.

and $\varepsilon$ its kinetic mixing parameter. The imaginary part of the 2-point correlator in this case gives $\pi\delta(p_{DS}^2 - m_{\gamma_D}^2)\sum_i \epsilon_i^\mu \epsilon_i^{\nu *}$, where $\epsilon_i^\mu$ is the polarization vector of the dark photon. Using the imaginary part of the 2-point correlator given by Eq. (B.9), one can thus express the DS cross section in terms of the cross section for the production of a dark photon; we obtain

$$\frac{d\sigma}{dp_{DS}^2}(eN \to eN + DS) = \frac{\kappa_J^2 c_J}{\Lambda_{\rm UV}^4}\frac{p_{DS}^2}{96\pi^2}\frac{\sigma(eN \to eN + A_D)}{(\varepsilon e)^2}\,, \tag{7.5.10}$$

where the dark photon cross section on the right-hand side has to be evaluated for $m_{\gamma_D} = (p_{DS}^2)^{1/2}$. Using the exact tree-level calculation of Ref. [357] (see also [358]) to compute the dark photon cross section, and performing the cut $E_{\rm miss} \geq 50\,\text{GeV}$, from Eq. (7.5.10) we obtained the differential cross section shown in Fig. 7.10. The production of an elusive dark sector with a current-current portal at NA64 is thus equivalent to a convolution of dark photon theories with mass spectrum in the range $\sim 0.1 - 10\,\text{GeV}$, which corresponds to a minimum momentum transfer $-t_{\rm min} \sim 10^{-8} - 1\,\text{GeV}^2$. This suggests that most of the incident electrons at NA64 scatter off the target atom or nucleus, well above the electron screening regime and below the onset of deep inelastic scattering.[52] By integrating the differential cross section of Fig. 7.10, we obtain the total cross section at NA64:

$$\sigma(eN \to eN + DS) = 0.8 \times 10^{-41}\text{cm}^2\,\left(c_J\kappa_J^2\right)\left(\frac{500\,\text{GeV}}{\Lambda_{\rm UV}}\right)^4. \tag{7.5.11}$$

Using Fig. 7.10 and assuming a total luminosity $\mathcal{L} = 5\times10^{33}\,\text{cm}^{-2}$,[53] we derived the bound that missing-energy searches at NA64 set on elusive dark sectors. For sufficiently low $\Lambda_{\rm IR}$, all LDSPs decay outside the detector and the constraint is independent of the IR scale. In this limit we find

$$\Lambda_{\rm UV} > 4\,\text{GeV} \times (c_J\kappa_J^2)^{1/4} \quad \text{for} \quad \begin{cases} \Lambda_{\rm IR} \ll 9\,\text{MeV}\left(c_J\kappa_J^2\right)^{-1/6} & (D=6) \\ \Lambda_{\rm IR} \ll 120\,\text{MeV}\left(c_J\kappa_J^2\right)^{-1/10} & (D=8)\,, \end{cases} \tag{7.5.12}$$

[52] Processes with $d \lesssim -t \lesssim 4m_p^2$, where $m_p$ is the proton mass and $d = 0.164\,\text{GeV}^2 A^{-2/3}$ is the inverse nuclear size squared, are characterized by the scattering of the incident electron off the target nucleus. Scatterings off the target atom take place when $1/a^2 \lesssim -t \lesssim d$, where $a = 111\,Z^{-1/3}/m_e$ is the atomic radius, whereas for $-t \ll 1/a^2$ the atomic electrons screen the charge of the nucleus and the form factor dies off. In the opposite limit of very large momentum transfer, $-t \gg 4m_p^2$, the process occurs in the regime of deep inelastic scattering, where the incident electron scatters off the constituents quarks. In this case the final state is characterized by an intense hadronic activity. See Refs. [355, 356].

[53] This is obtained as $\mathcal{L} = N_{\rm EOT}\rho_{\rm Pb}\ell$, where $N_{\rm EOT} = 2.84\times10^{11}$, $\rho_{\rm Pb} = 0.3\times10^{23}\,\text{cm}^{-3}$ and we set the thickness of the detector to 1 radiation length, $\ell = 0.56\,\text{cm}$.

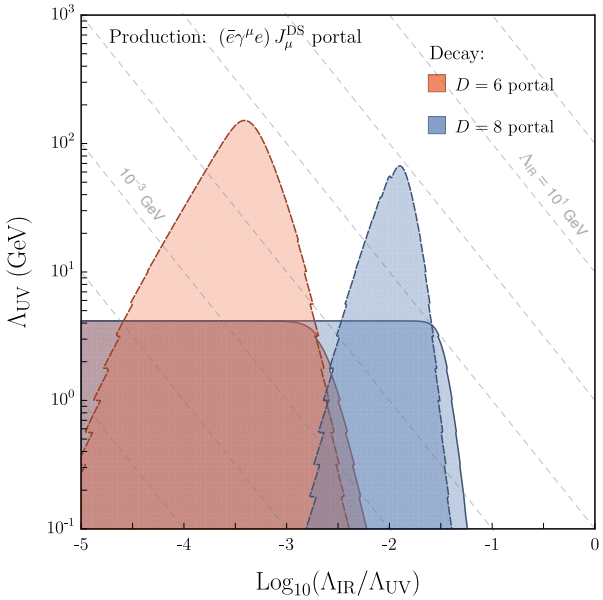


**Figure 7.11:** Constraints from NA64 (solid contours) and E137 (dashed contours) on elusive dark sectors with portal $(\bar{e}\gamma^\mu e)J_\mu^{DS}$. The plot assumes a strongly-coupled DS dynamics and two possible portals mediating the LDSP decay, respectively with dimension $D = 6$ (blue region) or $D = 8$ (red region). For both portals, $\kappa^2 c$ is set to 1.

where $D$ is the dimension of the decay portal. For larger values of $\Lambda_{\rm IR}$, fewer DS events give rise to missing energy and the constraint gets weaker. The corresponding exclusion curve is shown in Fig. 7.11 (solid contours) for a strongly-coupled DS dynamics and two possible portals mediating the LDSP decay, respectively with dimension $D = 6$ (blue region) or $D = 8$ (red region). Very similar results hold for weakly-coupled dynamics. Compared to those arising from high-energy collider searches, this bound is rather weak and does not constrain values of $\Lambda_{\rm UV}$ above the electroweak scale. To derive it, we implemented the procedure explained in Sec. 7.4.2 to enforce the EFT validity, i.e. we restricted the integration of the differential distribution of Fig. 7.10 to values below the UV scale.

A stronger bound comes from the E137 experiment performed at SLAC. The experimental setup is as follows: an incident electron beam with energy $E_0 = 20\,\text{GeV}$ hits a beam dump target made of aluminium plates interlaced with cooling water. The particles produced by the collision must traverse a hill of 179 m in thickness before reaching a 204 m-long open region followed by a detector. Bounds can be placed on long-lived dark particles that decay in the open region or rescatter with the material in the detector. No signal events were observed after two runs during which $\sim 30\,\text{C}$ of electrons (respectively 10 C in Run 1 and 20 C in Run 2, corresponding to a total of $\sim 2 \times 10^{20}$ electrons) were delivered on target. An interpretation of this result in terms of dark photon theories was given in Refs. [354, 359]. We used it to derive a bound on elusive dark sectors with portals $(\bar{e}\gamma^\mu e)J_\mu^{DS}$ as follows. First, we computed the differential cross section for atomic and nuclear scatterings of the incident electrons off the target using Eq. (7.5.10). The result is shown in Fig. 7.10. The invariant mass spectrum peaks in the range $0.03 - 3\,\text{GeV}$, which corresponds to values of the minimum momentum transfer $-t_{\rm min} \sim 10^{-11} - 10^{-3}\,\text{GeV}$. Most of the incident electrons at E137 thus scatter off the target atom. Since no veto is imposed at E137 on the hadronic activity of the final state, we have explicitly computed the contribution of deep inelastic scatterings, finding that is small (it becomes important only at very large invariant masses $p_{DS}^2 \gtrsim 25\,\text{GeV}^2$) and safely negligible to derive the bounds described below. From Fig. 7.10 we obtain the total cross section

at E137:

$$\sigma(eN \to eN + DS) = 0.4 \times 10^{-43}\text{cm}^2 \left(c_J \kappa_J^2\right) \left(\frac{500\,\text{GeV}}{\Lambda_{\text{UV}}}\right)^4 . \tag{7.5.13}$$

Using the differential cross section of Fig. 7.10, we computed the rate of LDSP decays that occur in the open region and are seen by the detector. To this aim, we estimated the geometric acceptance simply as the fraction of particles from each LDSP decay that passes through the front area of the detector. We approximated as collinear the emission of the DS excitation through bremsstrahlung (this is a reasonably good approximation for light dark photons, see for example Ref. [354]), and assumed an isotropic distribution of the decay products from the LDSP decay in its center-of-mass frame. Finally, we have used an integrated luminosity $\mathcal{L} = 3.4 \times 10^{43}\,\text{cm}^{-2}$ for Run1 and twice as much for Run2.[54] The exclusion region that we obtained is shown in Fig. 7.11 for $D = 6$ and $D = 8$ portals mediating the LDSP decay. In the relevant range of hierarchies, the exclusion on $\Lambda_{\text{UV}}$ extends up to $\sim 150\,\text{GeV}$ and is much stronger than the one set by NA64, despite the smaller cross section, thanks to the vastly larger number of electrons delivered on target.

### DS production from hadron decays

The other way to produce DS particles at high-intensity experiments is through the decay of QCD hadrons. To achieve a good sensitivity on elusive dark sectors, very large samples of hadron decays are needed. These are obtained at experiments with particularly intense proton beams and at experiments dedicated to the study of rare decays. One can broadly identify two classes of decays: those where a parent QCD hadron annihilates into DS excitations, possibly emitting an additional photon (annihilation decays), and those where it decays to a lighter hadron plus DS excitations (radiative decays). We will assume for simplicity that the portal interaction conserves baryon number and flavour. One can thus further distinguish between flavour-conserving and flavour-violating decays; these latter proceed necessarily through a flavour-violating SM loop and are correspondingly suppressed.

Annihilation decays are mediated by portals whose SM operator has the appropriate quantum numbers to excite the parent meson from the vacuum, in particular by $J_\mu^{SM} J_{DS}^\mu$ portals where $J_\mu^{SM}$ is a vector or an axial quark current. Decays of interest are for example those of light unflavoured pseudoscalar or vector mesons ($\pi^0$, $\eta$, $\eta'$, $\rho$, $\omega$, $\phi$, etc.), as well as those of flavoured mesons ($K_L$, $D$ and $B$). These processes have been considered in previous studies and used to constrain specific dark sectors whose excitations are either long lived and escape detection, see for example Refs. [303, 360–363], or promptly decay back (at least partly) to the SM, see for example Ref. [364]. See also Ref. [365] for a model-independent approach. To give an idea of how precisely one can probe elusive dark sectors through annihilation decays, we consider the decay of light vector mesons and assume that the DS excitations are sufficiently long lived to escape detection. In the case of the portal $J_\mu^{em} J_{DS}^\mu$, where $J_\mu^{em}$ is the SM electromagnetic current, we find that

$$\frac{BR(V \to DS)}{BR(V \to e^+e^-)} = \frac{c_J \kappa_J^2}{128\pi^2} \frac{1}{\alpha_{em}^2} \frac{m_V^4}{\Lambda_{\text{UV}}^4} , \tag{7.5.14}$$

where $V$ denotes a light unflavoured vector meson, and we used the optical theorem to compute the phase space integral over the DS system. The invisible decay of $V = \phi, \omega$ has been searched for by the BESSIII Collaboration [366] through $J/\psi \to V\eta$. Using a sample of $1.3 \times 10^9$ $J/\psi$ events, they obtained $BR(\phi \to \text{invisible}) < 1.7 \times 10^{-4}$ and $BR(\omega \to \text{invisible}) < 7.3 \times 10^{-5}$ at 90% confidence level. The upper limit on $BR(\phi \to \text{invisible})$ implies

$$\Lambda_{\text{UV}} > 2.3\,\text{GeV} \left(c_J \kappa_J^2\right)^{1/4} \qquad \text{for } \Lambda_{\text{IR}} \lesssim 6\,\text{MeV} \left(\kappa_J^2 c_J\right)^{-0.18} , \tag{7.5.15}$$

[54] Here we have used $\rho_{\text{Al}} = 0.6 \times 10^{23}\,\text{cm}^{-3}$ and set the thickness of the detector to 1 radiation length, $\ell = 8.9\,\text{cm}$.

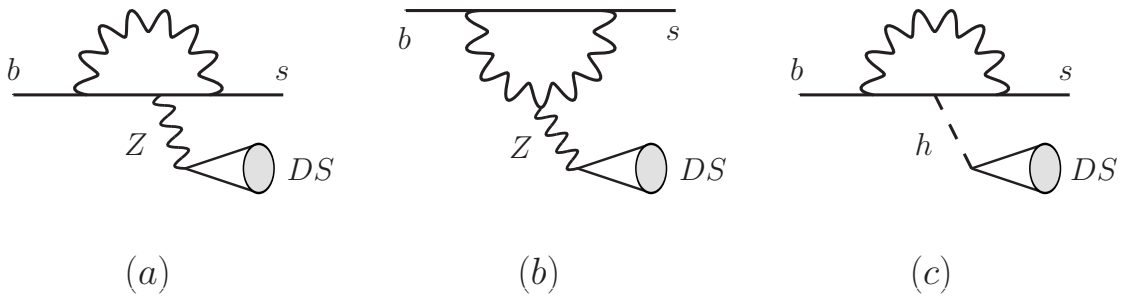


**Figure 7.12:** Feynman diagrams contributing to $B^+ \to K^+ + DS$ in theories with a $Z$-portal (diagrams $(a)$ and $(b)$) and a Higgs portal (diagram $(c)$).

where the bound on $\Lambda_{\rm IR}$ assumes a strongly-coupled dark sector and ensures that the LDSPs are long lived and escape detection. The limit on $BR(\omega \to \text{invisible})$ gives a slightly weaker constraint. The decays of pseudoscalar mesons can also be used to probe elusive dark sectors, although their rate vanishes for $J_\mu^{SM} J_{DS}^\mu$ portals where the DS current is conserved. In the case of partially conserved DS currents, the decay rate depends on the scale of explicit breaking of the associated global symmetry and receives a contribution only from values of the DS invariant mass below the onset of the conformal regime. Its estimate is thus model dependent and will not be pursued here.

Radiative decays are also interesting and are tested by various experiments. For example, experiments with very intense proton beams such as LSND and MINOS are particularly suited to probe flavour-conserving decays of light mesons and baryons, such as: $\rho \to \pi + DS$, $K^* \to K + DS$, $\Delta \to N + DS$, etc. All these decays are expected to occur, for example, through $J_\mu^{SM} J_{DS}^\mu$ portals where $J_\mu^{SM}$ is a quark vector current. This strategy has been applied for example in Refs. [293, 303] to set constraints on dark sectors. Flavour-changing meson decays can be best probed, instead, at dedicated experiments. Here we focus, in particular, on the decays $B^+ \to K^+ + DS$ and $K^+ \to \pi^+ + DS$, where the DS particles decay outside the detector and thus lead to missing energy. See for example Refs. [303, 365, 367, 368] for previous related studies of this kind of processes.

The decay $B^+ \to K^+ + DS$ can be mediated by a $J_\mu^{SM} J_{DS}^\mu$ portal where $J_{SM}^\mu = \bar{t}\gamma^\mu t$ or $iH^\dagger \overleftrightarrow{D^\mu} H$. In the case of a $Z$ portal, for example, the transition occurs via the $Z$-penguin diagrams of Fig. 7.12a-b, in analogy with the decay $B^+ \to K^+ + \nu\bar{\nu}$ in the SM. In fact, the neutrinos themselves behave as a dark sector with very low mass scale (hence conformal at energies of order of the $B$ mass), which couples to the $Z$ through a conserved current: $(g/2\cos\theta_W) Z_\mu J_{(\nu)}^\mu$, where $J_{(\nu)}^\mu$ is the neutrino current. Our elusive dark sector couples through the $Z$ portal in very much the same way: $(m_Z v \kappa_J/\Lambda_{\rm UV}^2) Z_\mu J_{DS}^\mu + \ldots$. The decay rate of $B^+ \to K^+ + DS$ can be thus computed by adapting the SM calculation of $B^+ \to K^+ + \nu\bar{\nu}$ (see [369] and references therein) by simply replacing the neutrino system with the DS one and omitting the box diagrams. From the upper limit $BR(B^+ \to K^+ + \nu\bar{\nu}) < 3.7 \times 10^{-5}$, obtained by the BABAR collaboration with a dataset of $\sim 10^8$ $B\bar{B}$ pairs [370], we find the constraint

$$\Lambda_{\rm UV} > 83\,{\rm GeV}\left(c_J\,\kappa_J^2\right)^{1/4} \quad \text{for} \quad \Lambda_{\rm IR} \ll 90\,{\rm MeV}\,(c_{\mathcal{O}}\kappa_{\mathcal{O}}^2)^{-0.17}\,. \tag{7.5.16}$$

The decay $K^+ \to \pi^+ + DS$ can be also used to constrain Higgs and current-current portals. In the case of the $Z$ portal, the transition occurs via penguin diagrams as in Fig. 7.12a-b, where both the top and charm quarks can circulate in the loop. The rate can be computed by adapting the SM calculation for $K^+ \to \pi^+ + \nu\bar{\nu}$ (see Ref. [371]), as discussed above for $B^+ \to K^+ + DS$. We then use the upper limit ${\rm BR}(K^+ \to \pi^+ + \nu\bar{\nu}) < 1.73 \times 10^{-10}$, set by the E949 collaboration [372] from a sample of $\sim 10^{12}$ $K^+$ decays, to constrain the $Z$ portal. We find:

$$\Lambda_{\rm UV} > 80\,{\rm GeV}\left(c_J\kappa_J^2\right)^{1/4} \quad \text{for} \quad \Lambda_{\rm IR} \ll 80\,{\rm MeV}\,(c_{\mathcal{O}}\kappa_{\mathcal{O}}^2)^{-0.18}\,. \tag{7.5.17}$$

The decay $B^+ \to K^+ + DS$ can also proceed through the Higgs portal, as shown in Fig. 7.12c, via a loop with the top quark. The transition $b \to hs$ has been calculated in Refs. [368, 373] and expressed in terms of an effective coupling

$$C_{bs}\, \bar{s}_L b_R h + \text{h.c.}\,, \qquad C_{bs} = \frac{3 g_2^2 m_b m_t^2 V_{ts}^* V_{tb}}{64\pi^2 m_W^2 v} \simeq 5.9 \times 10^{-6}\,. \tag{7.5.18}$$

Using this result and the optical theorem it is straightforward to compute the decay rate into DS excitations; we find:

$$\begin{aligned}\Gamma(B^+ \to K^+ + DS) = &\frac{1}{2M_B}\frac{\kappa_{\mathcal{O}}^2}{m_h^4}\frac{v^2}{\Lambda_{\rm UV}^{2\Delta_{\mathcal{O}}-4}}\int \frac{d^3p_K}{(2\pi)^3}\frac{1}{2E_K}|\mathcal{M}(B^+ \to K^+ h)|^2 \\ &\times\, 2\,\text{Im}\,\langle \mathcal{O}(p_{DS})\mathcal{O}(-p_{DS})\rangle\,,\end{aligned} \tag{7.5.19}$$

where $E_K = \sqrt{M_{K^+}^2 + |\vec{p}_K|^2}$, and $p_{DS} = p_B - p_K$. The matrix element $\mathcal{M}(B^+ \to K^+ h)$ is given by [374]

$$|\mathcal{M}(B^+ \to K^+ h)|^2 = |C_{bs}|^2 \left|f_0^K(p_{DS}^2)\right|^2 \left(\frac{M_B^2 - M_{K^+}^2}{m_b - m_s}\right)^2\,, \tag{7.5.20}$$

and we use the form factor reported in Ref. [375]: $f_0^K(q^2) = 0.33\,[1 - q^2/(37.46\,\text{GeV})]^{-1}$. We then approximate the imaginary part of the DS correlator with its conformal limit given by Eq. (B.8), and use the experimental upper limit on $BR(B^+ \to K^+ + \nu\bar{\nu})$ to set constraints on the Higgs portal. We find:

$$\begin{aligned}&\Delta_{\mathcal{O}} = 4: \quad \Lambda_{\rm UV} > 1.3\,\text{GeV}\,\left(c_{\mathcal{O}}\kappa_{\mathcal{O}}^2\right)^{1/4} \qquad \text{for} \quad \Lambda_{\rm IR} \ll 800\,\text{MeV}\,(c_{\mathcal{O}}\kappa_{\mathcal{O}}^2)^{-0.1} \\ &\Delta_{\mathcal{O}} = 3: \quad \Lambda_{\rm UV} > 2.1\,\text{GeV}\,\left(c_{\mathcal{O}}\kappa_{\mathcal{O}}^2\right)^{1/2} \qquad \text{for} \quad \Lambda_{\rm IR} \ll 750\,\text{MeV}\,(c_{\mathcal{O}}\kappa_{\mathcal{O}}^2)^{-0.05}\,.\end{aligned} \tag{7.5.21}$$

The upper limit on $\Lambda_{\rm IR}$ ensures that the LDSPs decay outside the detector and has been derived assuming a strongly-coupled dark dynamics. Notice that these results are compatible with the definition of the Higgs portal, and as such are consistent, only if the lower limit on $\Lambda_{\rm UV}$ is larger than the EW scale. This would require $c_{\mathcal{O}}\kappa_{\mathcal{O}}^2 \sim 10^8\,(10^4)$ for $\Delta_{\mathcal{O}} = 4$ ($\Delta_{\mathcal{O}} = 3$), values that are at least implausible to obtain from realistic UV completions.

### 7.5.4 Celestial constraints

The presence of a dark sector can significantly impact the dynamics of stellar objects and astronomical events. In the case of axions or axion-like particles, the two largest effects on stellar evolution were found to be an accelerated energy loss of red giants before helium ignition, and a modified lifetime of horizontal branch stars [376, 377]. Another celestial signature can be a change of the energy loss in supernovae (SNe), if the DS particles are able to escape from the core.

Ample research on these phenomena has been performed in the literature, in particular on axion emission in stellar and SNe observations. Based on this groundwork, various studies have extended the phenomenology to models of dark photons and four-fermion portal interactions [378–386]. Closely related to our case is the study performed by Freitas and Wyler in Ref. [387], where an unparticle dark sector has been probed, much akin to our $D = 6$ current portal. We will therefore be able to adapt the results found by these authors to our most relevant case, i.e. the $J_\mu^{SM} J_{DS}^\mu$ portal, where $J_\mu^{SM}$ is a current of SM fermions.[55] For this portal, we will obtain bounds from the

[55] Notice that the relative size of terms in the unparticle vector propagator proposed in [292, 318] and employed in [387] needs to be corrected by a factor which depends on the operator dimension $\Delta$ [388]. For a $J_\mu^{SM} J_{DS}^\mu$ portal, $\Delta = 3$ and the correct relative size of the terms in the propagator agrees with the one used in [387]. We are thus left with a different overall normalization factor, which we have chosen by defining $\langle J_{DS}^\mu J_{DS}^\nu\rangle$ as in Eq. (B.5). In practice, our normalization yields a multiplicative factor $16\pi^2/3$ with respect to the results of Ref. [387].

observations of SN1978A and horizontal branch stars. In the case of SN1978A, the bound will be based on the 'Raffelt criterion' of energy loss (see Eq. (7.5.28)), which states that any new particle species should not lead to an energy loss in the SN progenitor which is more efficient than that of neutrinos. We point out that recent studies have complemented this strategy by looking for DM produced in the SN cooling process through direct detection experiments [386] and gamma-ray burst observatories [385]. For simplicity, however, here we focus on the energy loss argument.

**SN1987A**

The impact of an additional conformal sector on the observation of the supernova SN1978A is a shortening of the neutrino burst.[56] Using the results derived in [387], we will make a quantitative estimate on the DS emission rate. We will then compare with the bound on the energy loss rate $Q_{\rm SN}$ derived in Refs. [376, 391].[57]

Due to the high concentration of nucleons in the supernova core, the dominant process for energy loss is the production of DS excitations through the scattering of nucleons. As argued in Refs. [387, 393], the main contribution is given by the scattering $n\,n \to n\,n + DS$, as other channels are smaller in comparison: $p\,p \to p\,p + DS$ is suppressed due to lower proton density, $e\,n \to e\,n + DS$ and $e\,e \to e\,e + DS$ are negligible due to Coulomb screening effects in the supernova core plasma [387, 393]. Therefore, we only consider DS emission in the scattering of neutrons as the leading effect.

Since the SN temperature is much smaller than the neutron mass, $T_{\rm SN} \approx 30$ MeV, the scattering occurs non-relativistically, and the DS emission is a soft one. The dominant contribution thus turns out to be DS bremsstrahlung off a neutron leg, whose rate can be factorized into that for a neutron-neutron hard scattering times the probability for soft radiation. Consider for example the diagram

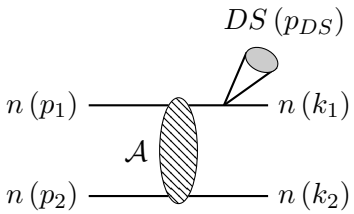


the amplitude for which can be written as

$$i\mathcal{M} = i\frac{\kappa_J}{\Lambda_{\rm UV}^2}\left[\bar{u}(k_2)\bar{u}(k_1)\gamma_\mu \frac{i(\not{q}+m_n)}{q^2-m_n^2}(-i\mathcal{A})\,u(p_1)u(p_2)\right]\langle DS|J^\mu_{DS}(p_{DS})|0\rangle\,, \tag{7.5.22}$$

where $q = p_{DS} + k_1$ and $\mathcal{A}$ is defined such that

$$\mathcal{M}_{nn\to nn} \equiv \bar{u}(q)\bar{u}(k_2)\,\mathcal{A}\,u(p_1)u(p_2) \tag{7.5.23}$$

corresponds to the amplitude for the $2 \to 2$ on-shell scattering of neutrons. Retaining only the lowest-order terms in $p_{DS}$, the matrix element acquires the factorized form

$$i\mathcal{M}(nn \to nn + DS) = i\left[\mathcal{M}_{nn\to nn}\right]\frac{\kappa_J}{\Lambda_{\rm UV}^2}\frac{(k_1)_\mu}{p_{DS}\cdot k_1}\langle DS|J^\mu_{DS}(p_{DS})|0\rangle\,. \tag{7.5.24}$$

The factor $1/(p_{DS}\cdot k_1)$ from the propagator is of order $1/T_{\rm SN}$ and brings in the enhancement due to the soft emission. A similar factorization holds from the other bremsstrahlung diagrams. The

[56] This method of constraining new physics through SN1978A relies on the modelling of the supernova by a core collapse and a neutrino-driven supernova explosion. Under other assumptions, no such bound is found [389, 390].

[57] An improved analysis takes into account the profile of the collapsing star [392].

rate of $n\,n \to n\,n + DS$ can thus be computed, at leading order in $T_{\rm SN}/m_n$, in terms of the cross section for neutron-neutron scattering, which can be extracted from nuclear data and has a value $\sigma_0(nn \to nn) \approx 25 \times 10^{-27}\,\mathrm{cm}^2$ at the relevant energy [394].

Having specified the scattering process, we define the object that will be compared to observational data: the energy loss rate [395]

$$Q_{DS} = \int d\Phi_{DS}\, p^0_{DS} \prod_{i=1,2} \int \frac{d^3p_i}{(2\pi)^3}\frac{1}{2p_i^0} \int \frac{d^3k_i}{(2\pi)^3}\frac{1}{2k_i^0} \times f_{p_1} f_{p_2}(1-f_{k_1})(1-f_{k_2})\,\langle|\mathcal{M}(nn \to nn + DS)|^2\rangle\,. \tag{7.5.25}$$

Here $f_{p_1,p_2}$ and $f_{k_1,k_2}$ are the Maxwell-Boltzmann distributions of respectively the initial and final state neutrons,

$$f_p = \frac{n_n}{2}\left(\frac{2\pi}{m_n T_{\rm SN}}\right)^{3/2} \exp\left(-\frac{|\vec{p}|^2}{2m_n T_{\rm SN}}\right)\,, \tag{7.5.26}$$

and $n_n$ denotes the neutron number density. We describe the supernova core in the non-degenerate limit, where the Pauli blocking factors are neglected, i.e. $(1 - f_{k_{1,2}}) \to 1$.

The energy loss rate of SN1978A is obtained by an integration of Eq. (7.5.25) using the parameters $T_{\rm SN} = 30\,\mathrm{MeV}$, $\sigma_0(nn \to nn) = 25 \times 10^{-27}\,\mathrm{cm}^2$ and the neutron density $\rho_n = 3 \times 10^{14}\,\mathrm{g/cm}^3$. This evaluation has been performed analytically for a vector unparticle in Ref. [387], and we adapt that result for $\Delta = 3$ as

$$Q_{DS}^{\mathrm{SN},nn} = 2.5 \times 10^8\,\mathrm{MeV}^5\left(c_J\,(\kappa_J^{nn})^2\right)\left(\frac{1\ \mathrm{MeV}}{\Lambda_{\rm UV}}\right)^4\,, \tag{7.5.27}$$

where $\kappa_J^{nn}$ is the coefficient of a neutron current portal $(\bar{n}\gamma^\mu n)\,J_\mu^{DS}$.[58] This needs to be compared to the estimated bound on the energy loss in SN1987A [376, 391],

$$Q_{\rm SN} \lesssim 3 \times 10^{33}\ \mathrm{erg\ cm^{-3}\ s^{-1}}\,, \tag{7.5.28}$$

which yields the constraint

$$\Lambda_{\rm UV} \gtrsim 400\,\mathrm{GeV}\left(c_J(\kappa_J^{nn})^2\right)^{1/4} \quad \text{for} \quad \Lambda_{\rm IR} \ll \min\left\{T_{\rm SN}, 90\,\mathrm{MeV}\left(c_J(\kappa_J^{nn})^2\right)^{-0.19}\right\}\,. \tag{7.5.29}$$

The upper limit on $\Lambda_{\rm IR}$ follows from two requirements: first, the IR scale must be much smaller than the SN temperature, $\Lambda_{\rm IR} \ll T_{\rm SN}$, in order to be able to describe the DS as an approximately conformal dynamics; second, DS excitations must escape the radius of the neutron core of the supernova, which we estimate from the SN mass $3 \times 10^{33}\,\mathrm{g}$ and neutron density to be $\mathcal{O}(10\ \mathrm{km})$.[59]. The limit due to this second requirement has been derived for a strongly-coupled DS by assuming that the LDSP decays through the neutron current portal.

### Stellar evolution

An additional bound can be obtained from a similar calculation of the energy loss in red giants before helium ignition, which would imply a decreased lifetime of horizontal branch stars. In Ref. [387], such a bound was derived by comparing the emission rate $Q_{DS}^{\rm HB}$ with the energy loss rate for axions, $Q_{\rm ax}^{\rm HB}$. This latter has been used in the literature to constrain the axion–electron coupling $g_{aee}$ through a numerical simulation of the stellar evolution [396].

As horizontal branch stars are composed of electrons, photons, $H^+$ and $He^{2+}$ nuclei, there exist multiple processes which can radiate DS excitations. Adapting the results derived in Ref. [387], we

[58] This can be related to the coefficient of the quark current portal $(\bar{q}\gamma^\mu q)\,J_\mu^{DS}$, we expect $\kappa_J^{nn} \approx \kappa_J^{qq}$.

[59] We neglect reabsorption effects of the DS particles within the SN. For marginal portals, e.g. the dark photon scenario, this effect can lead to a drastic reduction of the bounds [379, 380].

find that for a $J_\mu^{SM} J_{DS}^\mu$ portal, the dominant process is Compton scattering, $e + \gamma \to e + DS$, if $J_\mu^{SM}$ contains the electron current. The corresponding energy loss rate is

$$Q_{DS}^{\mathrm{HB},C} = 2.2 \times 10^{-24}\,\mathrm{MeV}^5 \left(c_J \kappa_J^2\right) \left(\frac{1\,\mathrm{MeV}}{\Lambda_{\mathrm{UV}}}\right)^4 . \tag{7.5.30}$$

We obtain a bound on the UV scale by comparing this with the energy loss rate for axions, $Q_{\mathrm{ax}}^{\mathrm{HB},C} = 3.8 g_{aee}^2 \times 10^{-18}$ MeV$^5$, in combination with the most stringent bound on the axion–electron coupling $g_{aee} \lesssim 2 \times 10^{-13}$ obtained for horizontal branch stars in Refs. [396, 397]. This amounts to a bound on the $(\bar{e}\gamma^\mu e) J_\mu^{DS}$ portal

$$\Lambda_{\mathrm{UV}} > 62\,\mathrm{GeV}\left(c_J (\kappa_J^{ee})^2\right)^{1/4} \qquad \text{for} \quad \Lambda_{\mathrm{IR}} \ll \min\left\{T_{\mathrm{HB}}, 10\,\mathrm{MeV}\,(c_J(\kappa_J^{ee})^2)^{-0.23}\right\} . \tag{7.5.31}$$

Similarly to the supernova case, the upper limit on $\Lambda_{\mathrm{IR}}$ follows from requiring that the IR scale be much smaller than the temperature of the star, $T_{\mathrm{HB}} \approx 8.6$ keV, and that DS excitations escape the radius of the star, $r_\odot \sim 10^5$ km. The limit due to this second requirement has been derived for a strongly-coupled DS by assuming that the LDSP decays through the electron current portal. It turns out to be always satisfied, for not too large values of $c_J(\kappa_J^{ee})^2$, as long as $\Lambda_{\mathrm{IR}} \ll T_{\mathrm{HB}}$.

### 7.5.5 Positronium lifetime

The $e^+ e^-$ bound system, positronium, comes in two spin states: orthopositronium, o-Ps ($S = 1$) and parapositronium p-Ps, ($S = 0$). Due to $C$ conservation in electromagnetic interactions, the leading decay of o-Ps is to three photons, and its relatively long lifetime offers a good opportunity to test the presence of portal interactions to the dark sector. In particular, o-Ps could annihilate into the dark sector, or decay to one photon plus DS excitations. We will focus on the case in which the LDSP is long lived and results in missing energy. The experimental bounds on the invisible decay of o-Ps and its decay to one photon plus missing energy are

$$\mathrm{Br}(\text{o-Ps} \to \text{invisible}) \leq 4.2 \times 10^{-7} \qquad [398] \tag{7.5.32}$$

$$\mathrm{Br}(\text{o-Ps} \to \gamma + \not{E}) \leq 1.1 \times 10^{-6} \qquad [399] \tag{7.5.33}$$

at 90% confidence level. The sensitivity of these constraints as probes of elusive dark sectors can be easily quantified by considering the SM rate of ortopositronium decays into neutrinos. As a matter of fact, neutrinos are a perfect prototype of dark sector coupled, at low energy, through $D = 6$ portals (i.e. the four-fermion operators generated by the exchange of weak bosons). The SM predicts

$$\mathrm{Br}(\text{o-Ps} \to \nu\bar{\nu}) = 6.2 \times 10^{-18} \qquad [400] \tag{7.5.34}$$

$$\mathrm{Br}(\text{o-Ps} \to \gamma + \nu\bar{\nu}) = 1.7 \times 10^{-21} \qquad [401]\,. \tag{7.5.35}$$

These branching fractions are much smaller than the experimental limits and this suggests that the current experimental precision is not sufficient to probe elusive dark sectors that couple through $D \geq 6$ portals generated at UV scales larger than the EW scale. Bounds on lower-dimensional portals can be stronger, depending on the portal and the nature of the dark sector. In the rest of this section we will compute the decay widths of the processes o-Ps $\to DS$, o-Ps $\to \gamma + DS$ and derive the corresponding bounds assuming $C$-conserving portals to electrons and photons. Such bounds will be relevant for dark sector theories with a UV scale much lower than the EW scale. We have checked that the limits on Higgs portals with $D < 6$ are not significantly stronger, since the virtual exchange of the Higgs boson implies an additional suppressing factor $(m_e/m_h)^4 \sim 10^{-22}$

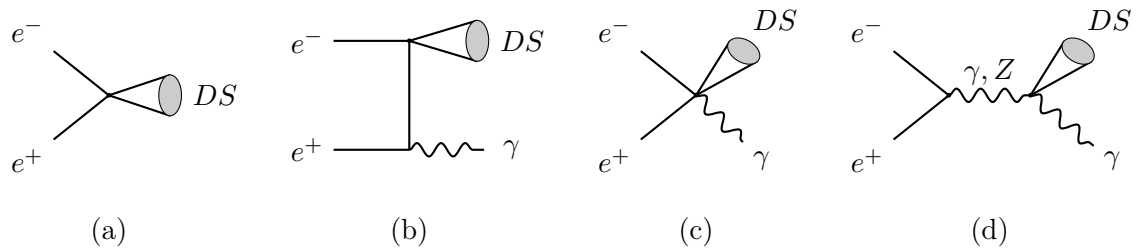


**Figure 7.13:** Feynman diagrams for o-Ps $\to DS$ (diagram (a)), mediated by the $D = 6$ portal $J_\mu^{DS}\bar{e}\gamma^\mu e$, and for o-Ps $\to \gamma + DS$, mediated by the $D = 8$ portals $T_{\mu\nu}^{DS}(\bar{e}\gamma^\mu D^\nu e)$ (diagram (b) plus its crossed and diagram (c)) and $T_{\mu\nu}^{DS}F_\alpha^\mu F^{\alpha\nu}$ (diagram (d)).

in the rate. Hence, although they can have lower dimensionality, Higgs portals are not efficiently constrained by positronium decays.

At leading order, the decay rate of positronium into a generic final state $X$ can be expressed by means of a factorized formula [402, 403] as

$$\Gamma(\text{o-Ps} \to X) = \frac{1}{3}|\psi(0)|^2 \left[4\, v_{\rm rel}\, \sigma(e^+e^- \to X)\right]_{v_{\rm rel}\to 0}\,, \tag{7.5.36}$$

where $\psi(0)$ is the o-Ps wave function at the origin, $v_{\rm rel}$ is the relative velocity of $e^-$ and $e^+$ in their center of mass frame, and the factor $1/3$ is due to the three polarisations of orthopositronium. We will use this formula and compute the cross section for $e^+e^-$ annihilation into DS and into DS plus one photon for the benchmark portals $J_\mu^{DS}\bar{e}\gamma^\mu e$ $(D = 6)$ and $T_{\mu\nu}^{DS}F_\alpha^\mu F^{\alpha\nu}$, $T_{\mu\nu}^{DS}(\bar{e}\gamma^\mu D^\nu e)$ $(D = 8)$ respectively.

### o-Ps annihilation to DS

The $D = 6$ portal $J_\mu^{DS}\bar{e}\gamma^\mu e$ can induce the annihilation of o-Ps into DS excitations through the diagram $(a)$ of Fig. 7.13. By using the optical theorem to integrate over the DS phase space, the corresponding $e^+e^-$ annihilation cross section can be easily derived to be

$$\sigma(e^+e^- \to DS) = \frac{1}{(2m_e)^2\, v_{\rm rel}} \frac{c_J\kappa_J^2}{2\pi} \frac{m_e^4}{\Lambda_{\rm UV}^4}\,. \tag{7.5.37}$$

Using Eq. (7.5.36), the leading order standard prediction for the decay rate into three photons, $\Gamma(\text{o-Ps} \to 3\gamma) = (4/3)^2(\pi^2 - 9)(\alpha^3/m_e^2)|\psi(0)|^2$, and the experimental limit (7.5.32), we obtain the bound

$$\Lambda_{\rm UV} > 346\,\text{MeV}\left(\kappa_J^2 c_J\right)^{1/4} \quad \text{for} \quad \Lambda_{\rm IR} \lesssim 3\,\text{MeV}\left(\kappa_J^2 c_J\right)^{-0.19}\,. \tag{7.5.38}$$

The upper limit on $\Lambda_{\rm IR}$ ensures that the LDSP be long lived and decay outside of the experimental apparatus, assuming a strongly-coupled DS (a very similar condition holds for weakly-coupled DS).

### o-Ps decay to one photon plus DS

The $D = 8$ portals $T_{\mu\nu}^{DS}F_\alpha^\mu F^{\alpha\nu}$ (where $F_{\mu\nu}$ is the photon field strength) and $T_{\mu\nu}^{DS}(\bar{e}\gamma^\mu D^\nu e)$ do not mediate o-Ps annihilations into the dark sector, but contribute to the decay o-Ps $\to \gamma + DS$ via the diagrams (b), (c), (d) of Fig. 7.13. The corresponding $e^+e^-$ annihilation cross section has the following form

$$\sigma(e^+e^- \to \gamma + DS) = \frac{1}{16\pi^2 v_{\rm rel}} \int_0^1 dx\, x\, \left\langle|\mathcal{M}(e^+e^- \to \gamma + DS)|^2\right\rangle \tag{7.5.39}$$

$$\left\langle|\mathcal{M}(e^+e^- \to \gamma + DS)|^2\right\rangle = \frac{\alpha}{15} c_T \left(\kappa_T^{ee} - \kappa_T^{\gamma\gamma} x\right)^2 (10 - 15x + 6x^2) \frac{m_e^6}{\Lambda_{\rm UV}^8}\,, \tag{7.5.40}$$

where $x = E_\gamma/m_e$ and $\kappa_T^{ee}$, $\kappa_T^{\gamma\gamma}$ are the coefficients of the two portals. Here $\langle|\mathcal{M}(e^+e^- \to \gamma + DS)|^2\rangle$ is the squared matrix element, summed/averaged over final/initial state polarizations and integrated over the DS phase space. Using the experimental limit (7.5.33) we obtain the bound

$$\Lambda_{\rm UV} > 3.6\,{\rm MeV} \times \left[c_T\left(\frac{3}{2}(\kappa_T^{ee})^2 - \frac{47}{30}\kappa_T^{ee}\kappa_T^{\gamma\gamma} + \frac{1}{2}(\kappa_T^{\gamma\gamma})^2\right)\right]^{1/8} \quad \text{for } \Lambda_{\rm IR} \lesssim 0.4\,{\rm MeV}\left(\kappa_T^2 c_T\right)^{-0.1} . \tag{7.5.41}$$

Here again, the upper limit on $\Lambda_{\rm IR}$ ensures that the LDSP decays outside the detector, and has been derived for a strongly-coupled DS and a $D = 8$ decay portal with coefficient $\kappa_T$. Both this bound and that of Eq. (7.5.38) probe values of $\Lambda_{\rm UV}$ well below the EW scale, but are still interesting and constrain theories where the portals $J_\mu^{DS}\bar{e}\gamma^\mu e$, $T_{\mu\nu}^{DS}F_\alpha^\mu F^{\alpha\nu}$ and $T_{\mu\nu}^{DS}(\bar{e}\gamma^\mu D^\nu e)$ are generated by very light UV mediators.

### 7.5.6 Constraints from fifth-force experiments

So far we have analysed the experimental constraints that arise from the production of DS excitations. Another way to test the dark sector is through processes involving the virtual exchange of DS degrees of freedom. As discussed in Sec. 7.4, effects from dimension-6 SM operators generated at the UV scale are naively expected to dominate over those induced by the exchange of DS states. However, there exist important exceptions of observables that are insensitive to UV contact terms and are thus a genuine probe of the dark sector.

Consider, for example, the force between two SM fermions (e.g. nucleons or leptons) measured at some finite distance. The tree-level exchange of DS states induces a potential that can be tested in a variety of precision experiments operating at different scales, such as torsion balance experiments, Casimir force experiments, neutron scattering and bouncing, and atomic and molecular spectroscopy (see for example Refs. [304, 404, 405]). The potential from the DS exchange can be computed, in the non-relativistic limit, from the Fourier transform of the scattering amplitude over the transferred three-momentum. It is thus written as an integral over the two-point DS correlator, which has a non-analytic (in momentum) part encoding the contribution from the dark-sector infrared dynamics, plus polynomial terms due to the UV dynamics whose coefficients are incalculable within the effective field theory. Upon integration, these two contributions map respectively into a long-range potential of the form $1/r^n$ (at distances $\ll 1/\Lambda_{\rm IR}$) and a contact potential given by a delta function $\delta^3(\vec{r})$ and its derivatives. Experiments operating at a finite distance, such as torsion balance and Casimir force experiments, are insensitive to the contact term and thus probe exclusively the contribution from the dark sector states. Molecular spectroscopy experiments also fall in the same class, since they are sensitive to the potential in the finite range of distances where the molecular wave function $\psi$ is non-vanishing. In practice, a potential $V(r)$ generated by the exchange of DS states induces a shift in the energy levels of the molecular system equal to

$$\Delta E = \int d^3r\; \psi^*(r)V(r)\psi(r)\,. \tag{7.5.42}$$

If the wave function vanishes sufficiently fast at the origin, the integral converges and the contribution from contact terms vanishes. For systems of this kind the energy shift is calculable and gives a genuine probe of the DS dynamics. The recent results obtained in molecular spectroscopy set the most stringent bounds on the potential from dark sectors at distances of order 1 Å or shorter [304, 404, 405]. They cannot be used, however, to directly constrain the portals of Eq. (7.2.2), as we now explain.

Let us consider, for example, the $D = 6$ portal $J_\mu^{DS}(\kappa_J^{ee}\bar{e}\gamma^\mu e + \kappa_J^{pp}\bar{p}\gamma^\mu p + \kappa_J^{nn}\bar{n}\gamma^\mu n)$ featuring a

current of electrons, protons and neutrons. It generates a potential

$$V_{ik}(r) = \frac{c_J \kappa_J^{ii} \kappa_J^{kk}}{32\pi^3} \frac{1}{\Lambda_{\rm UV}^4} \frac{1}{r^5} + \text{contact terms} \tag{7.5.43}$$

between any two (distinguishable) fermions $i$ and $k$. The corresponding energy level shift is calculable as long as the molecular wave function vanishes at the origin faster than $r$.[60] This behaviour characterizes several molecular systems whose transitional frequencies can be measured accurately with ultra stable lasers. For example, recasting the bounds on large extra dimensions set in Ref. [406] by measurements of the energy levels in molecular hydrogen ($H_2$), we obtain

$$\Lambda_{\rm UV} \gtrsim 0.2\,\text{MeV}\, \left(c_J (\kappa_J^{pp})^2\right)^{1/4} \quad \text{for } \Lambda_{\rm IR} \ll 1\,\text{keV}\,. \tag{7.5.44}$$

Other molecular systems also lead to constraints on $\Lambda_{\rm UV}$ in the MeV range [304, 405]. This value of the UV scale is below the mass of the nucleon. The effective theory obtained by integrating out the UV dynamics at $\Lambda_{\rm UV}$ is therefore a non-relativistic one, and its expansion must be performed in terms of the nucleon velocity or kinetic energy rather than in powers of 4-dimensional derivatives. The set of effective operators characterizing such non-relativistic effective theory is not in one-to-one correspondence to those, like the portals of Eq. (7.2.2), one would write at higher energies. We thus conclude that, although molecular spectroscopy and fifth-force experiments in general are interesting probes of dark sectors, the corresponding limits belong to a different category compared to those discussed in the previous sections, as they apply to operators (portals) of a different effective field theory.

### 7.5.7 EW precision tests

Another example of observables where the virtual exchange of DS states can be calculable is electroweak precision tests (EWPT). Calculability in this case requires the dimensionality of the portal to be $D \leq 5$, as already discussed in Sec. 7.4.1. Let us consider, for example, the effects of a Higgs portal on vector boson self energies, in particular we will focus on the corrections to the $\varepsilon_3$ parameter introduced by Altarelli and Barbieri [407, 408].

A $D = 5$ Higgs portal renormalizes the operator $O_H = [\partial_\mu (H^\dagger H)]^2$ via a tree-level diagram with two insertions (see Fig. 7.2), implying a coefficient

$$c_H(\mu) \sim \frac{\kappa_{\mathcal{O}}^2 c_{\mathcal{O}}}{16\pi^2} \frac{1}{\Lambda_{\rm UV}^2} \log \frac{\Lambda_{\rm UV}}{\mu}\,. \tag{7.5.45}$$

The 1-loop diagram of Fig. 7.14a with one $O_H$ insertion, in turn, renormalizes the operators $O_W = g D^\mu W^a_{\mu\nu} H^\dagger T^a i\overleftrightarrow{D}^\nu H$ and $O_B = g' \partial^\mu B_{\mu\nu} H^\dagger i\overleftrightarrow{D}^\nu H$, which give a short-distance contribution to $\varepsilon_3$. We thus estimate

$$\Delta\varepsilon_3 = \hat{S} \sim \frac{m_W^2}{\Lambda_{\rm UV}^2} \frac{\kappa_{\mathcal{O}}^2 c_{\mathcal{O}}}{(16\pi^2)^2} \log \frac{\Lambda_{\rm UV}}{\bar{\Lambda}} \log \frac{\Lambda_{\rm UV}}{m_Z}\,, \tag{7.5.46}$$

where $\bar{\Lambda} = \max(\Lambda_{\rm IR}, m_h)$. Notice that, although it is a short-distance effect due to the UV dynamics, the contributions of Eq. (7.5.46) is calculable within the effective field theory, since it stems from the RG running of dim-6 operators. Finite contributions are subleading for $D = 5$ and have been neglected.

For $4 < D < 5$, the DS exchange leads to a finite correction to $\varepsilon_3$ through the diagram of Fig. 7.14b. If $\Lambda_{\rm IR} > m_Z$, one can integrate out the DS dynamics at $\Lambda_{\rm IR}$ and match to an effective

[60] The ground state of the hydrogen atom is an example where the integral in Eq. (7.5.42) diverges, since the wave function is constant at the origin.

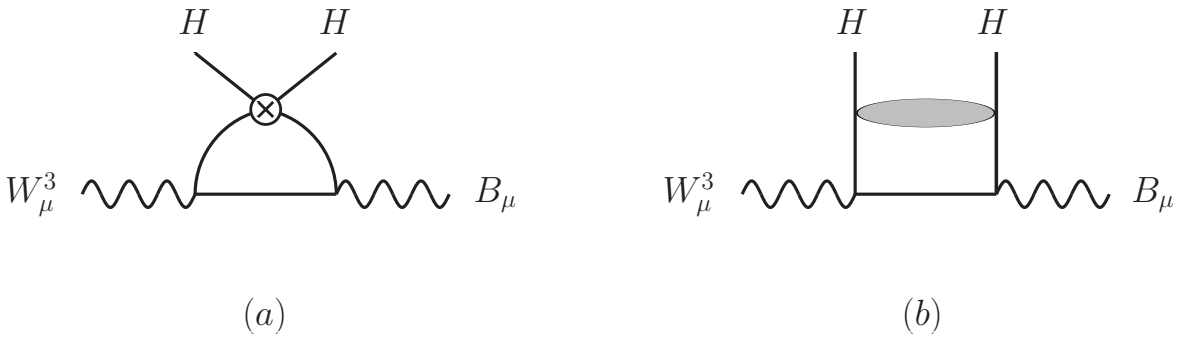


**Figure 7.14:** Diagrams contributing to $\Delta\varepsilon_3$: short-distance contribution from the insertion of $O_H$ (diagram $(a)$); long-distance contribution from the DS exchange (diagram $(b)$). Continuous internal lines correspond to Higgs propagators, the insertion of $O_H$ is denoted by a crossed vertex, and the gray blob represents the DS exchange.

theory with SM fields and higher-dimensional operators. In particular, thresholds at $\Lambda_{\rm IR}$ generate $O_H$ with a coefficient

$$c_H(\Lambda_{\rm IR}) \sim \frac{\kappa_{\mathcal{O}}^2 c_{\mathcal{O}}}{16\pi^2}\frac{1}{\Lambda_{\rm IR}^2}\left(\frac{\Lambda_{\rm IR}}{\Lambda_{\rm UV}}\right)^{2(D-4)} . \tag{7.5.47}$$

The insertion of $O_H$ into the diagram of Fig. 7.14a then gives

$$\Delta\epsilon_3 = \hat{S} \sim \frac{m_W^2}{\Lambda_{\rm IR}^2}\frac{\kappa_{\mathcal{O}}^2 c_{\mathcal{O}}}{(16\pi^2)^2}\left(\frac{\Lambda_{\rm IR}}{\Lambda_{\rm UV}}\right)^{2(D-4)} \log\frac{\Lambda_{\rm IR}}{m_Z} . \tag{7.5.48}$$

If instead $\Lambda_{\rm IR} < m_Z$, then the diagram of Fig. 7.14b gives a genuine long-distance correction of order

$$\Delta\epsilon_3 \sim \frac{m_W^2}{m_h^2}\frac{\kappa_{\mathcal{O}}^2 c_{\mathcal{O}}}{(16\pi^2)^2}\left(\frac{m_h}{\Lambda_{\rm UV}}\right)^{2(D-4)} . \tag{7.5.49}$$

For the same value of $\kappa_{\mathcal{O}}^2 c_{\mathcal{O}}$, the long-distance effect of Eq. (7.5.49) gives a less suppressed correction compared to those of Eqs. (7.5.46) and (7.5.48), although it does not have a log enhancement. By requiring $\Delta\varepsilon_3 \lesssim 10^{-3}$, Eq. (7.5.49) implies $\Lambda_{\rm UV} \gtrsim m_h \times (0.02\,\kappa_{\mathcal{O}}^2 c_{\mathcal{O}})^{1/(2D-8)}$, which is a rather weak bound. For example, if one sets $\kappa_{\mathcal{O}}$ to its largest value allowed by the naturalness bound of Eq. (7.2.4), it turns into an upper limit $\Lambda_{\rm IR} \lesssim m_h \times (10^3/c_{\mathcal{O}})^{1/(12-2D)}$, which is easily satisfied (given the initial assumption $\Lambda_{\rm IR} < m_Z$) for not too large $c_{\mathcal{O}}$. We thus conclude that EW precision tests do not set stringent constraints on the DS dynamics.

## 7.6 Summary and Discussion

The existence of neutral dark sectors with a low mass scale and irrelevant portal interactions to the visible fields is an intriguing possibility and only apparently an exotic one. Several theoretical extensions of the Standard Model, some of which address one or more of its open issues, predict scenarios of this kind. Neutrinos are an interesting historical precedent. Their existence was proposed by Pauli in 1930 as a solution to the longstanding puzzle of the $\beta$-decay spectrum, but their direct detection came only in 1958 as the culmination of the pioneering experimental efforts of Reines and Cowan. The reason why it was so difficult to detect them is because at low energy neutrinos interact feebly with charged particles through $D = 6$ portals generated at the weak scale (specifically, a portal of the form $(\bar{O}_{\rm vis}\nu + \text{h.c.})$ mediates $\beta$-decay, whereas $\mu$-decay and neutral-current scatterings proceed through $J^{\mu}_{\rm vis} J^{(\nu)}_{\mu}$ portals). Eventually, the properties of neutrinos were uncovered thanks to the possibility of obtaining intense beams from nuclear reactors, as this obviated the huge suppression of signal rates. It was only in 1983 however, more than 50 years after Pauli's original intuition, that the UV mediators responsible for the neutrino portal interactions, the $W$ and $Z$ vector bosons, were produced on shell in the UA1 and UA2 experiments at CERN, and the barrier between dark and visible sector removed forever.

The current theoretical and experimental landscapes are very different from those of the early decades of the past century, and since then the energy and intensity frontiers have been immensely pushed forward. In light of this, one may ask how a hypothetical elusive dark sector might manifest itself and be discovered at present or future facilities. We have tried to address this question by estimating the relative importance of various effects in Section 7.4. The virtual exchange of UV mediators can be parametrized in terms of $D = 6$ effective operators and gives corrections to processes with SM external states that scale as $1/\Lambda^2_{\rm UV}$. The DS contribution to the same processes necessarily involves two insertions of the portals and scales as $1/\Lambda^{2(D-4)}_{\rm UV}$, where $D$ is the dimensionality of the portal. Naively, it is subdominant compared to the UV effect except for $D < 5$ or when the experimental observable is sensible only to long-distance contributions and blind to contact ones. Electroweak tests and fifth-force experiments are interesting examples of this kind, and were analysed respectively in Sections 7.5.7 and 7.5.6. Given the current experimental precision, we find that they are not sensitive enough to test portals generated at energies above the EW scale. Direct production of DS states implies signal rates that also scale as $1/\Lambda^{2(D-4)}_{\rm UV}$ but its significance can be competitive with UV virtual effects even for $D > 5$. We have analysed an ample spectrum of processes that are summarized in Table 7.3. They include searches at high-energy colliders, high-intensity experiments, astrophysical observations (supernova cooling and stellar evolution) and low-energy precision experiments (positronium rare decays). We find that the strongest sensitivity on elusive dark sectors is currently obtained at high-energy colliders. The plots in Fig. 7.15 give a summary of our results. The most stringent constraints can be set on Higgs and $Z$ portals when the DS excitations are produced through the decay of the Higgs or $Z$ bosons, in particular when the lightest DS particles decay back to the SM with displaced vertices. In those cases, UV scales as high as several TeVs are already being probed for $\kappa^2 c$ of order 1 (see Figs. 7.5 and 7.6), where $\kappa$ is the portal coefficient and $c$ measures the multiplicity of DS states. As a matter of fact, comparable if not stronger lower bounds on $\Lambda_{\rm UV}$ are set, through their sensitivity to virtual UV effects, by the body of electroweak precision tests performed at LEP, SLC and Tevatron, and by the analysis of Higgs processes at the LHC. Searches for on-shell production of the UV mediators made at colliders, or even DM direct detection experiments (in theories where the DM candidate resides in the UV sector), can also set stringent, though model dependent, limits on $\Lambda_{\rm UV}$. This comparison suggests that, different from the historical neutrino precedent, the first signals of new physics might come this time from the heavy UV dynamics rather than from the light and elusive dark states. For example, in a likely scenario one could first observe deviations in SM precision tests induced by the virtual exchange of UV mediators, and only later on reach the experimental sensitivity to uncover

the dark sector. Hence, light and weakly-coupled new physics should not be seen as an alternative to new heavy particles: on the contrary, observing the latter could prelude the discovery of the former.

The above considerations suggest that a future physics programme at a Higgs or $Z$ factory would extend most effectively our sensitivity on Higgs and $Z$ portals thanks to the large statistics of decays. An FCC-ee running at the TeraZ option would be especially beneficial as it would increase the sensitivity on $\Lambda_{\rm UV}$ on two complementary fronts: an order-of-magnitude increase in the precision on electroweak observables [409–411] to uncover UV virtual effects, and a sample of $Z$ decays larger by two orders of magnitude compared to the LHC to produce the DS particles. In the longer run, an FCC-hh at 100 TeV would produce $\sim 10^{10}$ Higgs bosons, roughly four orders of magnitude larger than the current production at the LHC. This would allow one to probe invisible Higgs decays at the level of $\sim 10^{-4}$ [412] and extend considerably the sensitivity on exotic decays. Without looking too much ahead in the future, the approved high-luminosity phase of the LHC will already lead to a substantial increase, by a factor $\sim 30$, of the number of produced Higgs and $Z$ bosons. This corresponds naively to an increase of the lower bound on $\Lambda_{\rm UV}$ by a factor $\sim 2$ for a $D = 6$ portal. In fact, even at future Higgs and $Z$ factories the sheer increase of statistics will imply lower bounds on $\Lambda_{\rm UV}$ larger by at most factors of a few, given that rates scale as $1/\Lambda_{\rm UV}^{2(D-4)}$. For example, a naive rescaling of our results suggests that a GigaZ factory could reach a lower bound on $\Lambda_{\rm UV}$ of order 10 TeV in the case of a $Z$ portal with $\kappa_J^2 c_J \sim 1$. Similar conclusions were reached by previous studies, see for example Refs. [302, 413, 414]. Probing higher UV scales will require, for example, to improve our ability to trigger on and reconstruct displaced vertices.

While portal interactions generated at very large scales will remain elusive, future facilities will be able to extend considerably our reach on low IR scales. It is a feature of dark sectors with irrelevant portals that the strength of their interaction with the SM scales with the energy as $\sim \kappa\,(E/\Lambda_{\rm UV})^{(D-4)} \equiv \alpha_{DS}(E)$. Production rates in the conformal regime are controlled by $\alpha_{DS}(\sqrt{s})$, where $\sqrt{s}$ is the energy characterizing the process, whereas the decay length of the lightest DS particles is determined by $\alpha_{DS}(\Lambda_{\rm IR})$ and thus crucially depends on the ratio $\Lambda_{\rm IR}/\Lambda_{\rm UV}$. This has to be contrasted with the case of marginal portals, as in dark photon theories, where the same small parameter (the kinetic mixing) controls both quantities. Future experiments aimed at detecting long-lived particles, e.g. CODEX-b, FASER and MATHUSLA (see [337] and references therein), will be able to improve the reach on small $\Lambda_{\rm IR}$ by detecting the decays of the lightest DS particles far away from the interaction point. This is especially important since, as illustrated by the plots of Fig. 7.15, current searches for displaced vertices at the LHC are already sensitive enough to test benchmark models for $\Lambda_{\rm UV} \sim 1$ TeV, though only in a relatively narrow range of IR scales.

While searches for displaced vertices at high-energy colliders are able to provide the strongest constraints on Higgs and $Z$ portals, it is also important to consider different portals and discovery strategies. Fixed-target and beam-dump experiments making use of very intense beams have been found to be extremely powerful to uncover dark sectors with marginal portals. In particular, simplified dark photon models have been often taken as benchmarks in previous experimental and theoretical studies. We have shown that, at least in the conformal regime, a dark sector coupled through $J_\mu^{DS} J_{SM}^\mu$, where $J_{SM}^\mu$ is an electron or quark current, behaves like a convolution of dark photon theories with a spectrum of masses that depends on the experiment (e.g. on the incoming beam energy and composition of the target). In the case of the NA64 and E137 experiments, such mass spectrum peaks at $\sim 1$ GeV, see Fig. 7.10. In particular, diagrams with DS emission can be obtained from those with an external dark photon field $A_D^\mu$ by replacing $(\varepsilon e) A_D^\mu \to (\kappa_J/\Lambda_{\rm UV}^2) J_{DS}^\mu$. This observation led to Eq. (7.5.10) and suggests that simple quantitative estimates for the dark sector can be derived by using the known dark photon results in terms of an effective kinetic mixing parameter $\varepsilon_{\rm eff} = (p_{DS}^2/\Lambda_{\rm UV}^2)(\kappa_J^2 c_J)^{1/2}/(4\pi e)$, as a function of the DS invariant mass squared $p_{DS}^2$. Similar considerations were made previously in Ref. [302]. A quick glance to any plot showing the constraints on dark photon theories in the $(\varepsilon, m_{A_D})$ plane, like those in Fig. 6 of Ref. [284]

and Fig. 20 of Ref. [287] confirms the hierarchy of effects found by our analysis, namely that the strongest limits come from supernova cooling and beam-dump experiments with extremely intense beams like E137. It also suggests that future experiments, in particular SHiP [285], can extend the reach to UV scales of order a few TeVs [302]. Additional improvement may come if future experimental analyses will be performed so as to optimize their sensitivity to generic dark sectors and not only to benchmark dark photon models. This is especially true for searches, like those performed by BaBar and Belle II, where events are selected by assuming the resonant production of a dark photon.

While the comparison with dark photon theories can be useful for a quick recast of current searches, an experimental programme aimed at the discovery of elusive dark sectors seems justified and would require optimized strategies and analyses. For example, existing high-intensity experiments like those designed for neutrino physics where the detector is placed very far downstream of the target are not particularly effective to detect long-lived particles originating from marginal portals, since very long decay lengths also imply very small production rates. This is not the case for irrelevant portals since, as already mentioned, the decay length of the lightest DS particles can be large as a consequence of a small IR scale. Besides tailored experimental searches, more in-depth theoretical studies will also be needed to uncover new discovery strategies and thoroughly explore the theoretical landscape of possibilities. The aim of our work was that of making a first step in this direction. We attempted to study elusive dark sectors in a broad perspective and analysed current experimental results to get insight on how to design a future experimental strategy. We obtained bounds from a large array of experiments by means of a procedure where the validity of the effective field theory used to define the portals is consistently enforced at each step. Our limits are sometimes less stringent than previous ones for this reason. Clearly, much additional work is needed to get a more complete quantitative picture on elusive dark sectors. Information will come not only from laboratory experiments and astrophysical observations, but also from the analysis of the cosmological evolution of these theories.

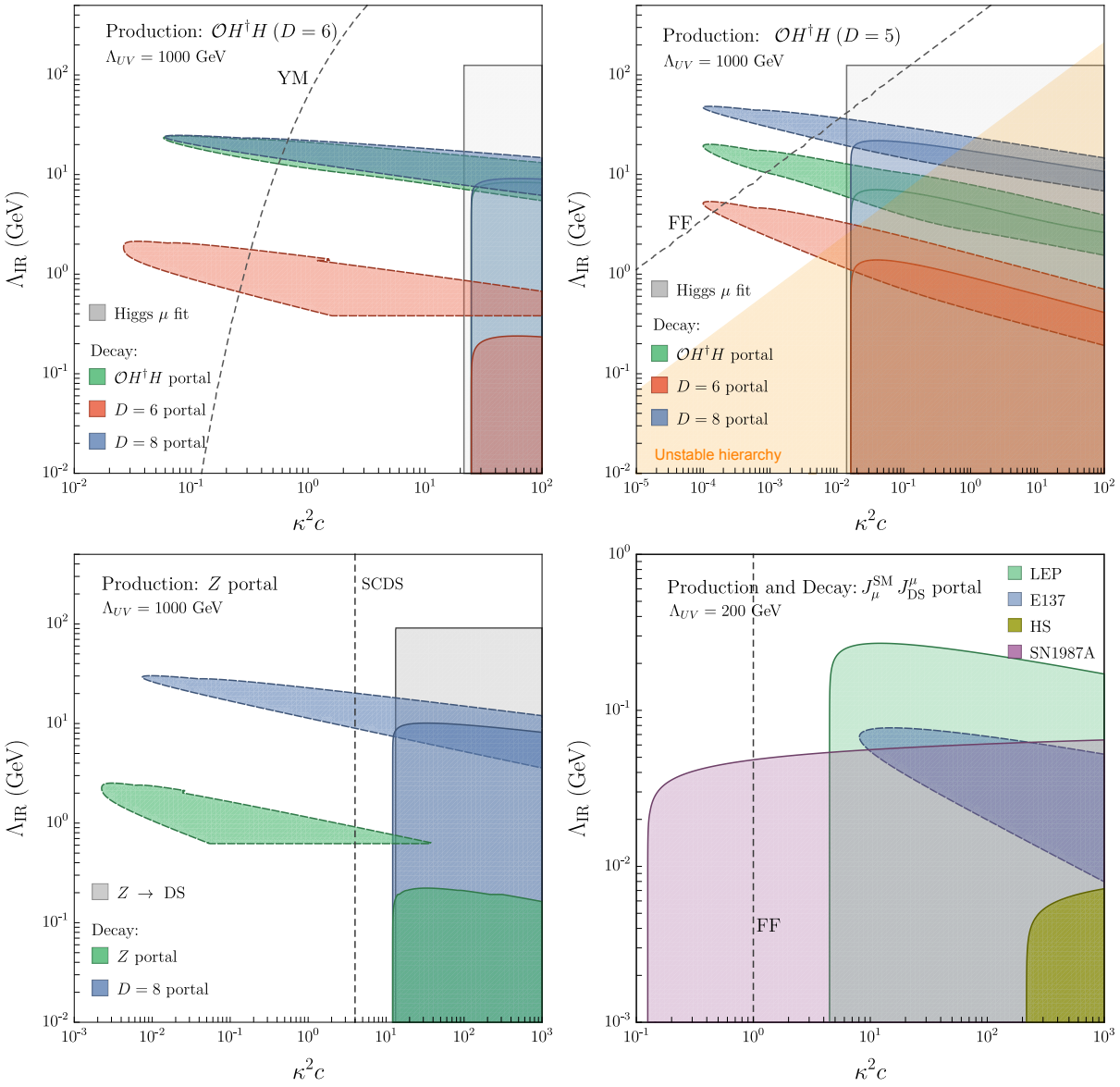


**Figure 7.15:** Exclusions at 95% probability in the plane $(\kappa^2 c, \Lambda_{\rm IR})$ for fixed $\Lambda_{\rm UV}$ and various portals. Continuous contours in the upper two panels show the exclusions from the fit to Higgs couplings and the bound on the Higgs invisible branching ratio, while those in the lower left panel arise from the invisible $Z$ decay width and mono-jet searches at the LHC. Dashed contours in these same panels show exclusions from displaced decays at the LHC. The lower right panel shows exclusions from LEP mono-photon searches, E137, SN1987A and stellar evolution. Bounds from other experiments analysed in the text are too weak to appear in the plots. The dashed curves show the predictions of the benchmark models of Sec. 7.3 for the following values of the parameters: $y_L = 1$, $y_R = 0$, $N_{DC} = 3$ for the pure Yang-Mills model of Sec. 7.3.1 (YM) and the strongly-coupled DS model of Sec. 7.3.2) (SCDS); $\lambda_{HS} = 1$ and $y = 1$ for the free fermion models of Sec. 7.3.3 (FF).

# 8 | Conclusions

Our current understanding of the fundamental constituents of nature and their interactions lies in the composition of the SM and GR. In this thesis, we have investigated several problems which arise due to the interplay of these two theories. We have argued that their resolution may require an understanding of model building both from a particle physics (BSM) point of view, and from an angle of modified gravitational models. We have explored this approach by deviating from the standard theories in several directions, by setting the focus of our discussion on the nature of dark energy and dark matter. Motivated by these open questions, we have introduced non-standard theories in the form of bimetric gravity and dark sectors of new physics. We have put these models through a wide of range of tests by deriving their phenomenology and comparing to observations.

Here we summarise the main results presented in this thesis. In Chapters 3 and 4, we have described the effect of gravitational wave oscillations in bimetric gravity. This phenomenon has been first derived in a consistent manner in the publications [1, 2] associated with this thesis. By comparing the propagation of one massive and one massless graviton mode in bigravity to observations of binary black hole mergers, we were able to place competitive bounds on its parameter space. As described in Sec. 4.4, we have made projections on these bounds based on future observations of merger events. We also expect future observations of electromagnetic signals associated with gravitational waves to serve as a valuable informant about the phenomenology of bimetric gravity.

In Chapter 5, we have presented a comprehensive analysis of the current status of the cosmological concordance model and some of its extensions. We have compared the cosmological history of these models to that of bimetric gravity and conformal gravity. By means of a comprehensive statistical analysis, we find that base ΛCDM remains the best explanation of our cosmological history. While bimetric gravity does not improve the quality of fit in our statistical analysis, the best fit model retains its attractive features, such as a dynamical dark energy component. A continued exploration of bimetric gravity is therefore appropriate, as it remains an interesting and viable proposal of a modified cosmology. This is contrary to the case of Mannheim's conformal gravity, where a severe tension arises between the curvature parameter obtained from cosmological and galactic data, as we have argued in Sec. 5.5.5. In this case, we are lead to abandon the idea that this realisation of conformal gravity can explain galactic rotation curves without the addition of dark matter.

We have explored an orthogonal ansatz in Chapter 7, where the question of the nature of dark matter has motivated us to introduce a general description of dark sector extensions to the SM. By requiring only a low mass gap and irrelevant (in the RG sense) portal couplings to the SM, we have defined a scheme by which to test an entire class of dark sectors, which obey an approximate conformal symmetry. Our ansatz exploits the well-defined properties of operator correlators in their conformal regime, which forms the key ingredient to the wide applicability of our analysis. As a proof of this concept, we have demonstrated how our results are adapted to a variety of realistic DM models, such as pure Yang-Mills dark sectors or Randall-Sundrum inspired models in 5D. After establishing this theoretical groundwork, we have derived its phenomenological implications, and have set bounds on the parameters by use of a large array of experimental data. The main effects due to the dimension-5 and -6 operators $\{\mathcal{O}|H|^2, J^{\rm DS}_\mu J^\mu_{\rm SM}\}$ are summarised in Figs. 7.15, where we note the strongest bounds come from Higgs couplings and displaced vertex searches at the LHC in the case of the Higgs portal $\mathcal{O}|H|^2$. Similarly, the strongest exclusions for a $Z$ mediated current portal to the dark sector are obtained from displaced vertex searches and the measurement

of invisible decays of the $Z$. Finally, the current portal $J_\mu^{\mathrm{DS}} J_{\mathrm{SM}}^\mu$, where $J_{\mathrm{SM}}^\mu$ is either a quark or an electron current, is probed most stringently by LEP searches for mono-photons and displaced vertex measurements at the beam dump experiment E137. The results of this work show that the description of dark sectors by their general features is a feasible programme.

As discussed in Sec. 7.4.2, in this analysis we have assumed that a dark sector can be discovered first in its conformal regime. To motivate this scenario, one needs to understand the relative importance of threshold events. We expect signatures of this kind to be observed if the energy is close to the mass gap, manifesting as spectacular new physics effects. Therefore, our programme generally assumes that the energies are much above the infrared threshold (that is, the mass gap) of the dark sector. Then, the question arises why we can expect to see significant event numbers in this high-energy tail (the conformal regime). The importance of these contributions depends on dimensionality of the portal: more irrelevant portals imply stronger scaling of the correlator with dark sector momentum $p_{DS}$, increasing the effect observed in the conformal regime. This is very much different to the case of relevant portal interactions, which do not generate cross-sections which scale with the energy. This reiterates the importance of the purely irrelevant portal interactions in our setup.

An interesting opportunity for future work is posed by the cosmological phenomenology of such a dark sector. In this case, knowledge of the portal interactions, the effective number of degrees of freedom, the infrared scale as well as the mode in which the dark sector is populated could pose a minimal information requirement on the hidden sector. We expect the limit on the number of light degrees of freedom during big bang nucleosynthesis to serve as a particularly powerful constraint.

We close this thesis by stressing that fundamental physics is at an interesting point in its development. As we have seen throughout the analyses presented in this thesis, a common theme in current theoretical physics is that new dynamics are probed mostly by placing bounds on their parameter space. While new physics in the particle and gravity sectors can easily be motivated through disagreements between current theory and observations, finding the correct description of nature in the space of possible models requires us to exclude others. It can be hoped that the advent of new tools and techniques, such as true multi-messenger astronomy, the observation of many more gravitational wave events, or the construction of more powerful particle colliders, will lead to improved versions of our standard theories of fundamental interactions.

# A | Method of statistical analysis

In Chapters 5 and 7, we have employed a Bayesian likelihood analysis to generate limits on cosmological parameters and on the suppressing mass scale of BSM interactions. Here, we describe briefly how these bounds are derived, focussing on the case of event counts at colliders. For an in-depth review of this method, see Ref. [415].

The basis of our analyses is Bayes' theorem,

$$p(\theta|x) = \frac{\mathcal{L}(x|\theta)\,\pi(\theta)}{p(x)}, \tag{A.1}$$

where $x$ represents the data vector and $\theta$ the model parameters.

We will elucidate the meaning of the different components following the application in Chapter 7: Given the number of BSM events $n^i_{\text{BSM}}$, the SM background $n^i_{\text{SM}}$ and the number of observed events $n^i_{\text{obs}}$ in $i$ bins of data, we would like to know the best fit parameters predicting SM + BSM events to the observed data. Expressed in general terms, we can write $n^i_{\text{BSM}}$ as a number times a coefficient $c$; e.g. in the case of the dimension-six portal of Chapter 7, this corresponds to $c \hat{=} \kappa_J^2 c_J\,[\text{GeV}/\Lambda_{\text{UV}}]^4$.

Summing over all bins $i$ of data, the posterior probability (A.1) now takes the form

$$p(c\,|\,n^i_{\text{obs}}) = \frac{1}{\mathcal{N}} \prod_i \mathcal{L}_i(c) \times \pi(c)\,, \tag{A.2}$$

with the normalisation

$$\mathcal{N} = \int dc \prod_i \mathcal{L}_i(c) \times \pi(c). \tag{A.3}$$

The posterior probability is constructed from the likelihood $\mathcal{L}_i$ and the prior $\pi$. The prior $\pi(c)$ is a function which describes our assumption on the range of valid $c$. For example, we may choose $c$ to follow a Gaussian distribution around a central value (see the BBN bounds in Sec. 5.4.2, where this is employed). For the cases we have investigated in Chapter 7, our assumption is simply that $c$ must be non-negative. This is accomplished by a 'flat' prior, $\pi(c) = \Theta(c)$, where $\Theta$ is the Heaviside function.

The likelihoods $\mathcal{L}_i$ is given by the conditional probability

$$\begin{aligned} \mathcal{L}_i(c) &\equiv p(n^i_{\text{obs}}|c) \\ &\overset{\text{e.g.}}{=} \text{Poisson}\big(n^i_{\text{SM}} + c\,n^i_{\text{BSM}},\, n^i_{\text{data}}\big). \end{aligned} \tag{A.4}$$

Given these ingredients, we understand that Eq. (A.2) describes the probability of the parameter $c$ under the condition that $n^i_{\text{obs}}$ events are observed. From this, we can extract a bound through the condition

$$0.95 \overset{!}{=} \int_0^{c_{95\%}} dc\, p(c\,|\,n^i_{\text{obs}})\,. \tag{A.5}$$

In words, this amount to finding the value of $c$ for which the BSM model has a probability of 95% of describing the data, given the evidence $n^i_{\text{obs}}$. This specific formula relies on the general assumption that the SM background is a good fit to the number of observed events, and that therefore, any BSM events can only decrease the goodness-of-fit. Hence, $c$ must be bounded from above.

For a counter-example where the SM prediction is not a good match for the observation, see the derivation of Eq. (7.5.7). In this case, the measured value $\mu = 1.17 \pm 0.10$ [327] does not agree

with the SM prediction $\mu = 1$. Therefore, the likelihood is constructed s.t. any deviation from the *measured* value is minimised.

In the particle physics-oriented application of Bayes' theorem, Eq. (A.4), we have assumed that the event likelihood is Poisson-distributed, and that different measurements are uncorrelated. This last assumption is justified if the data consists of several independent bins, e.g. in the energy distribution of a particle used to tag an event. In Chapter 5, we have encountered a different kind of measurement. For an example see the CMB data in Sec. 5.4.5, which comes as measurements of three correlated parameters $x = \left(R, l_A, \Omega_b h^2\right)$. We assume a Gaussian distribution and construct the likelihood

$$\mathcal{L}_{\text{CMB}} \propto \exp\left\{ -\frac{1}{2} \left[\vec{X} - \vec{X}_{\text{model}}\right]^T \mathbf{C}^{-1} \left[\vec{X} - \vec{X}_{\text{model}}\right] \right\}, \tag{A.6}$$

where $\mathbf{C}$ is the covariance matrix. For numerical applications, we use in practice the logarithm of the above likelihood, which is maximised at the same $\vec{X}_{\text{model}}$. Finally, we refer to Sec. 5.4.6 for a discussion of the Bayes information criterion, which allows us to compare different models by their goodness-of-fit and number of parameters.

# B | Two-point dark sector correlators

We report here the expression of the 2-point correlators of dark sector operators used in the analysis of Chapter 7.

For very large momenta, $|p| \gg \Lambda_{\rm IR}$, the form of the 2-point correlators is dictated by conformal invariance, up to an overall normalization constant. We define the latter as follows (in 4D Minkowski space-time):

$$\langle \mathcal{O}(x)\mathcal{O}(0)\rangle = \frac{c_{\mathcal{O}}}{8\pi^4}\frac{1}{(x^2)^{\Delta_{\mathcal{O}}}} \tag{B.1}$$

$$\left\langle J_\mu^{DS}(x)\, J_\nu^{DS}(0)\right\rangle = \frac{c_J}{8\pi^4}\frac{1}{(x^2)^3}\left(\eta_{\mu\nu} - 2\frac{x_\mu x_\nu}{x^2}\right) \tag{B.2}$$

$$\left\langle T_{\mu\nu}^{DS}(x)\, T_{\rho\sigma}^{DS}(0)\right\rangle = \frac{c_T}{8\pi^4}\frac{1}{(x^2)^4}\left[\left(I_{\mu\nu}(x)I_{\rho\sigma}(x) - \frac{1}{4}\eta_{\mu\nu}\eta_{\rho\sigma}\right) + \mu \leftrightarrow \nu\right], \tag{B.3}$$

where $I_{\mu\nu}(x) = \eta_{\mu\nu} - 2x_\mu x_\nu/x^2$. After Fourier transforming and subtracting the singular terms analytic in momenta, one obtains:

$$\langle \mathcal{O}(p)\mathcal{O}(-p)\rangle = \frac{-ic_{\mathcal{O}}}{2\pi^2}\frac{\Gamma(2-\Delta_{\mathcal{O}})}{4^{\Delta_{\mathcal{O}}-1}\Gamma(\Delta_{\mathcal{O}})}(-p^2)^{\Delta_{\mathcal{O}}-2} \tag{B.4}$$

$$\left\langle J_\mu^{DS}(p)\, J_\nu^{DS}(-p)\right\rangle = \frac{-ic_J}{\pi^2}\frac{1}{2^4 3!}\, p^2 \log\left(-p^2\right) P_{\mu\nu} \tag{B.5}$$

$$\left\langle T_{\mu\nu}^{DS}(p) T_{\rho\sigma}^{DS}(-p)\right\rangle = \frac{-ic_T}{2\pi^2}\frac{1}{2^5 5!}\, p^4 \log\left(-p^2\right) P_{\mu\nu\rho\sigma}\,, \tag{B.6}$$

for any $p^2$ in the complex plane away from the branch cut on the positive real axis, where the projectors $P_{\mu\nu\rho\sigma}$ and $P_{\mu\nu}$ are defined as

$$P_{\mu\nu\rho\sigma} = 2P_{\mu\nu}P_{\rho\sigma} - 3\left(P_{\mu\rho}P_{\nu\sigma} + P_{\mu\sigma}P_{\nu\rho}\right), \qquad P_{\mu\nu} = \eta_{\mu\nu} - \frac{p_\mu p_\nu}{p^2}\,. \tag{B.7}$$

The corresponding imaginary parts, extracted from the discontinuity across the branch cut, are:

$$\mathrm{Im}[i\,\langle \mathcal{O}(p)\,\mathcal{O}(-p)\rangle] = \frac{c_{\mathcal{O}}}{\pi^{3/2}}\,\frac{\Gamma(\Delta_{\mathcal{O}}+1/2)}{\Gamma(\Delta_{\mathcal{O}}-1)\Gamma(2\Delta_{\mathcal{O}})}\,(p^2)^{\Delta_{\mathcal{O}}-2} \tag{B.8}$$

$$\mathrm{Im}\left[i\left\langle J_\mu^{DS}(p)\, J_\nu^{DS}(-p)\right\rangle\right] = -\frac{c_J}{\pi}\frac{1}{2^4 3!}\, p^2\, P_{\mu\nu} \tag{B.9}$$

$$\mathrm{Im}\left[i\left\langle T_{\mu\nu}^{DS}(p) T_{\rho\sigma}^{DS}(-p)\right\rangle\right] = -\frac{c_T}{2\pi}\frac{1}{2^5 5!}\, p^4\, P_{\mu\nu\rho\sigma}\,. \tag{B.10}$$

The normalization in Eqs. (B.1), (B.2), (B.3) has been chosen so as to reproduce the following expressions in the case of free conformal fields (see for example [416, 417]; we denote the number of real scalars, complex scalars, Dirac fermions and real vectors respectively as $n_S^R, n_S^C, n_F^D$ and $n_V^R$):

$$\begin{aligned}
&\mathcal{O} = \frac{1}{2}\left(\partial_\mu\phi\right)^2 \quad && (\Delta_{\mathcal{O}} = 4), && c_{\mathcal{O}} = 24\, n_S^R \\
&\mathcal{O} = \bar\psi\,\gamma^\mu i\overleftrightarrow{\partial_\mu}\psi \quad && (\Delta_{\mathcal{O}} = 4), && c_{\mathcal{O}} = 0 \\
&\mathcal{O} = -\frac{1}{4}F_{\mu\nu}^2 \quad && (\Delta_{\mathcal{O}} = 4), && c_{\mathcal{O}} = 24\, n_V^R \\
&\mathcal{O} = \bar\psi\psi \quad && (\Delta_{\mathcal{O}} = 3), && c_{\mathcal{O}} = 8\, n_F^D
\end{aligned} \tag{B.11}$$

for scalar operators $\mathcal{O}$;

$$\begin{aligned} J_\mu^{DS} &= \phi^\dagger i\overleftrightarrow{\partial_\mu}\phi, & c_J &= 2\, n_S^C \\ J_\mu^{DS} &= \bar\psi\gamma^\mu\psi \text{ or } \bar\psi\gamma^\mu\gamma^5\psi & c_J &= 8\, n_F^D \end{aligned} \tag{B.12}$$

for conserved currents $J_\mu^{DS}$;

$$\begin{aligned} T_{\mu\nu}^{DS} &= \partial_\mu\phi\,\partial_\nu\phi - \frac{1}{12}\left(2\partial_\mu\partial_\nu + \eta_{\mu\nu}\,\partial^2\right)\phi^2, & c_T &= \frac{4}{3}\, n_S^R \\ T_{\mu\nu}^{DS} &= i\left[\frac{1}{2}\bar\psi\gamma_\mu\partial_\nu\psi - \frac{1}{4}\partial_\mu(\bar\psi\gamma_\nu\psi) + (\mu\to\nu)\right] - i\,\eta_{\mu\nu}\,\bar\psi\partial\!\!\!/\,\psi, & c_T &= 8\, n_F^D \\ T_{\mu\nu}^{DS} &= F_{\mu\alpha}F_\nu^\alpha - \frac{1}{4}\eta_{\mu\nu}F_{\alpha\beta}^2, & c_T &= 16\, n_V^R \end{aligned} \tag{B.13}$$

for energy momentum tensors $T_{\mu\nu}^{DS}$.

An extensive discussion and calculation of the RG flow of the central charge $c_T$ can be found in Ref. [418], together with the examples of free scalars and fermions, and a summary of results for QED with one fermion, pure Yang-Mills gauge theory and QCD-like theories up to first loop order. Massless QCD has been studied in depth also in Refs. [419–422], which provide the expression of $c_T$ and $c_{\mathcal{O}}$ (for $\mathcal{O} = -\frac{1}{4}F_{\mu\nu}^2$) up to 3-loop order. In the case of dark sectors equivalent to QED with massless fermions, the coefficients $c_J$ and $c_T$ are calculated in a large $n_F$ expansion in Refs. [423, 424]. Similarly, Refs. [425, 426] provide $c_J$ and $c_T$ in a large-$N$ expansion of the $O(N)$ vector model (scalars with $O(N)$ global symmetry and $\phi^4$-interaction) and the Gross-Neveu model (fermions with $U(N)$ global symmetry) in $d = 4-\epsilon$ space-time dimensions. Finally, the central charge $c_T$ has been calculated for explicit examples of SUSY QCD, see e.g. Ref. [427]. In some cases, lower bounds on $c_J$ and $c_T$ can be derived [427–431].

We end this section by reporting the expression of the 2-point correlators predicted in the benchmark models with a free fermion DS and in the RS model of Sec. 7.3. In these models a calculation of the 2-point correlator is possible for values of the momenta down to threshold, i.e. outside of the conformal regime.

In the $B-L$ model of Sec. 7.3.3 the DS consists of three Majorana fermions $\psi_{N_i}$ coupled through the portal (7.3.7). Using dimensional regularization with minimal subtraction and a 4-component notation, we find

$$\begin{aligned} \langle J_\mu^{DS}(p)J_\nu^{DS}(-p)\rangle = &-\frac{1}{24\pi^2}\left(\eta_{\mu\nu}p^2 - p_\mu p_\nu\right) \\ &\times\sum_{i=1}^{3}\left\{\left(1+\frac{2m_{N_i}^2}{p^2}\right)\sqrt{1-\frac{4m_{N_i}^2}{p^2}}\,\log\frac{2m_{N_i}^2 - p^2 + \sqrt{p^4 - 4m_{N_i}^2p^2}}{2m_{N_i}^2}\right. \\ &\left. + \frac{4m_{N_i}^2}{p^2} + \left(\frac{5}{3} - \gamma_E\right) + \log\frac{\mu^2}{m_{N_i}^2} + \log 4\pi\right\}, \end{aligned} \tag{B.14}$$

where $J_{DS}^\mu = (1/2)\sum_i \bar\psi_{N_i}^\dagger\gamma^\mu\gamma^5\psi_{N_i}$ and $\mu$ is the subtraction scale. In the limit $p^2 \gg m_{N_i}^2$ this expression tends to the CFT correlator of Eq. (B.5) with $c_J = (1/2)\times 3\times 8$, where the factor $1/2$ appears because the $\psi_{N_i}$ are Majorana fermions (cf. Eq. (B.12)). In the second model of Sec. 7.3.3 the DS consists of a single Majorana fermion $\chi$ coupled through the portal (7.3.9). The two-point correlator of the current $J_{DS}^\mu = \bar\chi\gamma^\mu\gamma^5\chi$ can be obtained by simply keeping the contribution of a single fermion species in Eq. (B.14) and replacing $m_{N_i}$ with $m_\chi$. Hence, the conformal limit of Eq. (B.5) in this case is recovered with $c_J = (1/2)\times 8$.

In the third model of Sec. 7.3.3 the DS consists of one Dirac fermion $\psi$, coupled to the SM through

the portal of Eq. (7.3.11). We find

$$\langle\bar{\psi}\psi(p)\bar{\psi}\psi(-p)\rangle = -\frac{p^2}{8\pi^2}\left\{\sqrt{1-\frac{4m_\psi^2}{p^2}}\,\log\frac{2m_\psi^2-p^2+\sqrt{p^4-4p^2m_\psi^2}}{2m_\psi^2}\right.$$
$$\left.+\log\frac{\mu^2}{m_\psi^2}+\log 4\pi-\gamma_E+2\right\}+\dots\,, \tag{B.15}$$

where the dots stand for terms independent of $p^2$. In the limit $p^2 \gg m_\psi^2$ this expression tends to the CFT correlator of Eq. (B.4) with $\Delta_\mathcal{O}=3$ and $c_\mathcal{O}=8$ (cf. Eq. (B.11)).

Finally, let us consider the RS model of Sec. 7.3.4. In that case the DS consists of the dynamics in the bulk and on the IR brane, coupled to the elementary SM sector through the portal (7.3.13). Despite the DS is strongly coupled in the infrared (and up to the $\Lambda_{\rm UV}$ scale), the 2-point correlator of $T^{DS}_{\mu\nu}$ can be computed thanks to holography. Indeed, it can be extracted from the UV brane-to-brane graviton propagator by sending the UV brane to the AdS boundary; in Minkowski space-time one finds [432]:

$$\langle T^{DS}_{\mu\nu}(p)T^{DS}_{\rho\sigma}(-p)\rangle = \frac{(M_5/k)^3}{12}p^4F(p^2)P_{\mu\nu\rho\sigma}\,,$$
$$F(p^2)\equiv\log\frac{p^2}{4k^2}-\pi\frac{Y_1(\sqrt{p^2}/\Lambda_{\rm IR})}{J_1(\sqrt{p^2}/\Lambda_{\rm IR})}\,, \tag{B.16}$$

where $\Lambda_{\rm IR}\equiv ke^{-\pi Rk}$ and the transverse and traceless projector $P_{\mu\nu\rho\sigma}$ is defined in Eq. (B.7). In absence of an explicit breaking of conformal symmetry, the 2-point correlator has a massless pole corresponding to the dilaton (i.e. the radion of the 5D theory): $F(p^2)\simeq -4\Lambda_{\rm IR}^2/p^2$ for $\sqrt{p^2}\ll\Lambda_{\rm IR}$. The radion acquires a mass through the mechanism that stabilizes the extra dimension, like for example the Goldberger-Wise mechanism [433]. In using the expression of $\langle T^{DS}_{\mu\nu}T^{DS}_{\rho\sigma}\rangle$ in Sec. 7.4.2, we have captured this effect by modifying the IR behaviour of the form factor as follows:

$$F(p^2)\to\hat{F}(p^2)=F(p^2)+\frac{4\Lambda_{\rm IR}^2}{p^2}-\frac{4\Lambda_{\rm IR}^2}{(p^2-m_\phi^2)} \tag{B.17}$$

where $m_\phi$ is the dilaton (radion) mass. Notice that upon breaking explicitly the conformal invariance, the 2-point correlator acquires an additional Lorentz structure that is not traceless (see for example Ref. [432]). We neglect this effect for simplicity. For $\sqrt{p^2}\gg\Lambda_{\rm IR}$, the expression of $\langle T^{DS}_{\mu\nu}T^{DS}_{\rho\sigma}\rangle$ tends to the pure CFT result provided the limit is taken in the correct way, see the discussion in the next Appendix.

# C | Details of 5D Randall-Sundrum Dark Sector

In this Appendix we analyse a few additional aspects of the 5D Randall-Sundrum dark sector theory (presented in Sec. 7.3.4) that are worth discussing. Let us first set our notation and derive some useful formulas. We take the bulk metric to be

$$ds^2 = e^{-2ky} g_{\mu\nu}(x,y) dx^\mu dx^\nu + dy^2 \,, \tag{C.1}$$

and locate the UV and IR branes respectively at $y = 0$ and $y = \pi R$. The value of the 4D Planck mass can be computed by taking the low-energy limit of the 5D action, including the localized kinetic term of Eq. (7.3.12). One has:[61]

$$M_{\rm Pl}^2 = \frac{M_5^3}{k}\left(1 - e^{-2\pi Rk}\right) + M_0^2 \,. \tag{C.2}$$

This equation can be used to express the value of $M_0$ in terms of the other parameters. Performing a Kaluza-Klein (KK) decomposition of the graviton field and neglecting at first order the effect of the second term of Eq. (7.3.12), the wave function of the $n$-th KK mode has the standard expression

$$f_n(y) = N_n\, e^{2ky}\left[J_2\big(x_n e^{ky}\big) + b_n\, Y_2\big(x_n e^{ky}\big)\right] \,, \tag{C.3}$$

where $x_n = m_n/k$, $m_n$ is the KK mass, $N_n$ is a normalization factor and

$$b_n = -\frac{J_1(x_n) - r_0\, x_n J_2(x_n)}{Y_1(x_n) - r_0\, x_n Y_2(x_n)} \,, \qquad r_0 = \frac{kM_0^2}{M_5^3} \,. \tag{C.4}$$

We are thus ready to make our considerations about this model. First of all, we would like to justify our claim that the UV-localized interaction of Eq. (7.3.12) corresponds, in the 4-dimensional holographic theory, to the dim-8 portal (7.3.13). We do so by considering the interaction between the SM energy-momentum tensor and the $n$-th KK mode; from the 5D Lagrangian, after the KK decomposition, one has

$$\frac{1}{M_5^{3/2}}\left(f_n(0) + \frac{1}{\Lambda_{\rm UV}^2}\tilde{f}_n(0)\right) h_{\mu\nu}^{(n)}(x)\, T_{SM}^{\mu\nu}(x) \,, \tag{C.5}$$

where $\tilde{f}_n(0) \equiv (-2k\,\partial_y + \partial_y^2)\, f_n(y)\big|_{y=0}$. The first term in parenthesis originates from the minimal coupling between gravity and matter, while the second term is due to the non-minimal interaction of Eq. (7.3.12). By using the solution (C.3) and expanding for $1 \ll r_0 x_n^2 \sim M_{\rm Pl}^2 \Lambda_{\rm IR}^2/\Lambda_{\rm UV}^4$, we find:

$$\frac{\pi}{2\sqrt{2}} \bar{x}_n |Y_1(\bar{x}_n)| \Lambda_{\rm IR} \left(\frac{M_5^{3/2}}{k^{3/2}}\frac{1}{M_{\rm Pl}^2} - \bar{x}_n^2 \frac{k^{3/2}}{M_5^{3/2}}\frac{1}{k^2\Lambda_{\rm UV}^2}\right) h_{\mu\nu}^{(n)}(x)\, T_{SM}^{\mu\nu}(x) \,, \tag{C.6}$$

where, we recall, $\Lambda_{\rm IR} \equiv k e^{-\pi Rk}$, and we have defined $\bar{x}_n \equiv x_n e^{\pi Rk}$, so that $\bar{x}_n \sim O(1)$. Notice that $(k/M_5)^{3/2}$ has $\hbar$ dimension of a coupling. The form of Eq. (C.6) matches the behaviour expected from the 4D holographic theory where

$$\mathcal{L}_{holo} \supset \frac{1}{M_{\rm Pl}} h_{\mu\nu} T_{SM}^{\mu\nu} + \frac{1}{M_{\rm Pl}} h_{\mu\nu} T_{DS}^{\mu\nu} + \frac{\kappa_T}{\Lambda_{\rm UV}^4} T_{SM}^{\mu\nu} T_{\mu\nu}^{DS} \,. \tag{C.7}$$

[61] We define $M_5$ and $M_{\rm Pl}$ as in Ref. [432].

Indeed, as a consequence of the second term above, the elementary graviton mixes with the tower of composites spin-2 states once conformal invariance is broken in the infrared. This implies that $h_{\mu\nu}$ in the first term in Eq. (C.7) will have some component of the spin-2 massive eigenstate. This leads to the Planck-suppressed contribution in Eq. (C.6) (first term in parenthesis). The non-minimal interaction of the holographic theory, on the other hand, is expected to give a contribution that is not suppressed by the Planck scale. That is exactly the second term in parenthesis in Eq. (C.6), from which we infer $\kappa_T \sim (k/M_5)^3$. The exact expression of $\kappa_T$ could in fact be extracted from Eq. (C.6) if one knows the matrix element between the spin-2 bound states and the energy-momentum tensor in the holographic theory. Such matrix element, in turn, can be derived from the residues of the poles in the $\langle T^{DS}_{\mu\nu} T^{DS}_{\rho\sigma} \rangle$ correlator.

The other aspect that we would like to discuss about the RS dark sector model concerns the high-energy limit of Eq. (B.16). We expect that for $|p| \gg \Lambda_{\rm IR}$ the expression of $\langle T^{DS}_{\mu\nu} T^{DS}_{\rho\sigma} \rangle$ tends to the result valid for a CFT dynamics, see Eq. (B.6). However, Eq. (B.16) has been obtained from a tree-level calculation in the 5D theory, which, on the 4D holographic side, corresponds to the leading order in $1/N_{CFT}$, where $N_{CFT}$ is the number of colors of the CFT dynamics. Correspondingly, the form factor $F(p^2)$ has an infinite series of poles on the real axis, interpreted as due to the exchange of non-interacting, stable bound states in 4D. The corresponding spectral function, computed by taking the imaginary part of $F(p^2)$, is an infinite sum of delta functions. It is thus clear that when taking the limit $|p| \gg \Lambda_{\rm IR}$, $F(p^2)$ does not lead to the logarithm predicted by a CFT. The solution to this apparent paradox comes by noticing that after including 1-loop corrections in the UV brane-to-brane calculation, the poles of $F(p^2)$ acquire an imaginary part and move above the real axis. This fact has a simple interpretation in the 4D holographic theory: the finite width of the resonances comes in only at next order in $1/N_{CFT}$. Including such subleading effect is crucial to recover the correct conformal limit. Doing so, indeed, corresponds to first evaluate the form factor at $p^2 \to p^2(1 + i\epsilon)$, where $\epsilon = \Gamma_n/m_n$ and $\Gamma_n$ is the resonance's width. Taking the limit $|p| \gg \Lambda_{\rm IR}$ then gives the correct result for Eq. (B.16), since $\lim_{x\to\infty} Y_1(x(1 + i\zeta)/J_1(x(1 + i\zeta)) = i$, for real and finite $\zeta$. The reason why a finite width of the resonances is crucial to recover the CFT result is also clear from the 'quark-hadron' duality viewpoint: the 'quark' behaviour is obtained only by resumming over the contribution of an infinite number of 'hadrons'. Increasing $\epsilon$ implies that the tails of a larger number of resonances will enter a given interval in $p^2$. Conversely, for fixed and finite $\epsilon$, the number of resonances effectively contributing into a $p^2$ interval of given length increases as $p^2 \to \infty$.

Comparing the high-energy limit of Eq. (B.16) with the CFT result of Eq. (B.6) we find the value of $c_T$ in the RS model:

$$c_T = 640\pi^2 \frac{M_5^3}{k^3} = 40(N_{CFT}^2 - 1)\,. \tag{C.8}$$

The last equality follows by using the standard holographic dictionary where $16\pi^2(M_5/k)^3 = N_{CFT}^2 - 1$.

# D | Probabilities for displaced decays

In this Appendix we describe how we modelled the probability for a signal event to pass the selections made by ATLAS in the searches for displaced jets of Refs. [330, 331]. The simplest search of Ref. [330] selects events with at least two displaced hadronic vertices in the MS, while Ref. [331] considers events with one decay in the MS and one in the ID. Let

$$P_{ij} = \exp\left(-\frac{L_i}{c\tau_\psi\gamma}\right) - \exp\left(-\frac{L_j}{c\tau_\psi\gamma}\right) \tag{D.1}$$

be the probability for a single LDSP with boost $\gamma$ to decay within distances $L_i$ and $L_j$ from the primary vertex (we assume for simplicity that the LDSP is produced promptly after the hard collision). Then, for a signal event with $n$ LDSPs, the probability to have at least two decays within distances $L_1$ and $L_2$ is:

$$P_{\geq 2 \text{ in } [L_1,L_2]} = 1 - (1-P_{12})^n - n\,P_{12}\,(1-P_{12})^{n-1}\ . \tag{D.2}$$

The probability to have at least one decay in $[L_1, L_2]$ and at least one in $[L_3, L_4]$ is instead:

$$P_{\substack{\geq 1 \text{ in } [L_1,L_2] \\ \geq 1 \text{ in } [L_3,L_4]}} = 1 - \{(1-P_{12})^n + (1-P_{34})^n - (1-P_{12}-P_{34})^n\}\ . \tag{D.3}$$

We assess the signal yield by setting $n$ to equal the average values $\langle n\rangle = 2$ and that in Eq. (7.4.10) to characterize the behaviour of respectively weakly-coupled and strongly-coupled dark dynamics. The boost factor $\gamma$ is set to its average value of Eq. (7.4.11). We then recast the results of Ref. [330] by assigning each event a weight given by Eq. (D.2) with $L_1 = 4\,\text{m}$ and $L_2 = 13\,\text{m}$, where these distances correspond to the region where the efficiency of the Muon RoI Cluster trigger of ATLAS is largest (see Fig. 2 of Ref [330]). Similarly, we recast the results of Ref. [331] by assigning each event a weight given by Eq. (D.3), with $L_1$, $L_2$ as above and $L_3 = 4\,\text{mm}$ and $L_4 = 300\,\text{mm}$. The values chosen for $L_3$, $L_4$ correspond to the region where the efficiency to select the hadronic vertex in the ID is largest (see Tab. 4 and Fig. 3 of Ref. [331]).

# Bibliography


[1] K. Max, M. Platscher, and J. Smirnov, "Gravitational Wave Oscillations in Bigravity," *Phys. Rev. Lett.* **119** no. 11, (2017) 111101, arXiv:1703.07785 [gr-qc].

[2] K. Max, M. Platscher, and J. Smirnov, "Decoherence of Gravitational Wave Oscillations in Bigravity," *Phys. Rev.* **D97** no. 6, (2018) 064009, arXiv:1712.06601 [gr-qc].

[3] M. Lindner, K. Max, M. Platscher, and J. Rezacek, "Probing alternative cosmologies through the inverse distance ladder," *JCAP* **10** (2020) 040, arXiv:2002.01487 [astro-ph.CO].

[4] R. Contino, K. Max, and R. K. Mishra, "Searching for Elusive Dark Sectors with Terrestrial and Celestial Observations," arXiv:2012.08537 [hep-ph].

[5] P. A. Dirac, "The quantum theory of the electron," *Proc. Roy. Soc. Lond. A* **A117** (1928) 610–624.

[6] C. D. Anderson, "The apparent existence of easily deflectable positives," *Science* **76** no. 1967, (1932) 238–239, https://science.sciencemag.org/content/76/1967/238.full.pdf. https://science.sciencemag.org/content/76/1967/238.

[7] S. H. Neddermeyer and C. D. Anderson, "Note on the nature of cosmic-ray particles," *Phys. Rev.* **51** (May, 1937) 884–886. https://link.aps.org/doi/10.1103/PhysRev.51.884.

[8] W. E. Lamb and R. C. Retherford, "Fine Structure of the Hydrogen Atom by a Microwave Method," *Physical Review* **72** no. 3, (Aug., 1947) 241–243.

[9] M. Gell-Mann, "The eightfold way: A theory of strong interaction symmetry,".

[10] Y. Ne'eman, "Derivation of strong interactions from a gauge invariance," *Nuclear Physics* **26** no. 2, (1961) 222 – 229. http://www.sciencedirect.com/science/article/pii/0029558261901341.

[11] A. Einstein and M. Grossmann, "Kovarianzeigenschaften der Feldgleichungen der auf die verallgemeinerte Relativitätstheorie gegründeten Gravitationstheorie," *Zeitschrift für Mathematik und Physik* **63** (Jan., 1914) 215–225.

[12] A. Einstein, *Die Grundlage der allgemeinen Relativitätstheorie*, vol. 354, pp. 769–822. 1916.

[13] A. Einstein, *Die Feldgleichungen der Gravitation*, pp. 88–92. 1915.

[14] A. A. Penzias and R. W. Wilson, "A measurement of excess antenna temperature at 4080 mc/s.,".

[15] K. Schwarzschild, "On the gravitational field of a mass point according to Einstein's theory," *Sitzungsber. Preuss. Akad. Wiss. Berlin (Math. Phys. )* **1916** (1916) 189–196, arXiv:physics/9905030.

[16] M. Persic, P. Salucci, and F. Stel, "The universal rotation curve of spiral galaxies — I. The dark matter connection," *Monthly Notices of the Royal Astronomical Society* **281** no. 1, (07, 1996) 27–47,

https://academic.oup.com/mnras/article-pdf/281/1/27/30383982/281-1-27.pdf. https://doi.org/10.1093/mnras/278.1.27.

[17] J. F. Navarro, C. S. Frenk, and S. D. M. White, "The Structure of Cold Dark Matter Halos," *Apj* **462** (1996) 563, arXiv:astro-ph/9508025 [astro-ph].

[18] G. Gentile, P. Salucci, U. Klein, D. Vergani, and P. Kalberla, "The Cored distribution of dark matter in spiral galaxies," *Mon. Not. Roy. Astron. Soc.* **351** (2004) 903, arXiv:astro-ph/0403154 [astro-ph].

[19] T. P. K. Martinsson, M. A. W. Verheijen, K. B. Westfall, M. A. Bershady, D. R. Andersen, and R. A. Swaters, "The DiskMass Survey. VII. The distribution of luminous and dark matter in spiral galaxies," *Astron. Astrophys.* **557** (2013) A131, arXiv:1308.0336 [astro-ph.CO].

[20] D. Clowe, S. W. Randall, and M. Markevitch, "Catching a bullet: Direct evidence for the existence of dark matter," *Nucl. Phys. Proc. Suppl.* **173** (2007) 28–31, arXiv:astro-ph/0611496 [astro-ph].

[21] M. Bradac, D. Clowe, A. H. Gonzalez, P. Marshall, W. Forman, C. Jones, M. Markevitch, S. Randall, T. Schrabback, and D. Zaritsky, "Strong and weak lensing united. 3. Measuring the mass distribution of the merging galaxy cluster 1E0657-56," *Astrophys. J.* **652** (2006) 937–947, arXiv:astro-ph/0608408 [astro-ph].

[22] R. Blandford and R. Narayan, "Cosmological applications of gravitational lensing," *Annual review of astronomy and astrophysics* **30** no. 1, (1992) 311–358.

[23] P. Schneider, C. Kochanek, and J. Wambsganss, *Gravitational lensing: strong, weak and micro: Saas-Fee advanced course 33*, vol. 33. Springer Science & Business Media, 2006.

[24] D. Clowe, M. Bradac, A. H. Gonzalez, M. Markevitch, S. W. Randall, C. Jones, and D. Zaritsky, "A direct empirical proof of the existence of dark matter," *Astrophys. J.* **648** (2006) L109–L113, arXiv:astro-ph/0608407 [astro-ph].

[25] M. Davis, J. Huchra, D. W. Latham, and J. Tonry, "A survey of galaxy redshifts. II. The large scale space distribution.," *The Astrophysical Journal* **253** (Feb, 1982) 423–445.

[26] S. D. M. White, C. S. Frenk, and M. Davis, "Clustering in a neutrino-dominated universe," *The Astrophysical Journal* **274** (Nov, 1983) L1–L5.

[27] **Supernova Search Team** Collaboration, A. G. Riess *et al.*, "Observational evidence from supernovae for an accelerating universe and a cosmological constant," *Astron. J.* **116** (1998) 1009–1038, arXiv:astro-ph/9805201 [astro-ph].

[28] **Supernova Cosmology Project** Collaboration, S. Perlmutter *et al.*, "Measurements of $\Omega$ and $\Lambda$ from 42 high redshift supernovae," *Astrophys. J.* **517** (1999) 565–586, arXiv:astro-ph/9812133 [astro-ph].

[29] **Planck** Collaboration, N. Aghanim *et al.*, "Planck 2018 results. VI. Cosmological parameters," arXiv:1807.06209 [astro-ph.CO].

[30] E. P. Wigner, "On Unitary Representations of the Inhomogeneous Lorentz Group," *Annals Math.* **40** (1939) 149–204.

[31] K. Hinterbichler, "Theoretical Aspects of Massive Gravity," *Rev. Mod. Phys.* **84** (2012) 671–710, arXiv:1105.3735 [hep-th].

[32] C. de Rham, "Massive Gravity," *Living Rev. Rel.* **17** (2014) 7, arXiv:1401.4173 [hep-th].

[33] M. Fierz and W. Pauli, "On relativistic wave equations for particles of arbitrary spin in an electromagnetic field," *Proc. Roy. Soc. Lond.* **A173** (1939) 211–232.

[34] M. Fierz, "Force-free particles with any spin," *Helv. Phys. Acta* **12** (1939) 3–37.

[35] E. Babichev and C. Deffayet, "An introduction to the Vainshtein mechanism," *Class. Quant. Grav.* **30** (2013) 184001, arXiv:1304.7240 [gr-qc].

[36] H. van Dam and M. J. G. Veltman, "Massive and massless Yang-Mills and gravitational fields," *Nucl. Phys.* **B22** (1970) 397–411.

[37] V. I. Zakharov, "Linearized gravitation theory and the graviton mass," *JETP Lett.* **12** (1970) 312. [Pisma Zh. Eksp. Teor. Fiz.12,447(1970)].

[38] C. J. Isham, A. Salam, and J. Strathdee, "$f$-dominance of gravity," *Phys. Rev. D* **3** (Feb, 1971) 867–873. https://link.aps.org/doi/10.1103/PhysRevD.3.867.

[39] M. B. Green and C. B. Thorn, "Continuing between closed and open strings," *Nuclear Physics B* **367** no. 2, (Dec, 1991) 462–484.

[40] W. Siegel, "Hidden gravity in open string field theory," *Phys. Rev.* **D49** (1994) 4144–4153, arXiv:hep-th/9312117 [hep-th].

[41] N. Arkani-Hamed, H. Georgi, and M. D. Schwartz, "Effective field theory for massive gravitons and gravity in theory space," *Annals Phys.* **305** (2003) 96–118, arXiv:hep-th/0210184 [hep-th].

[42] D. G. Boulware and S. Deser, "Can gravitation have a finite range?," *Phys. Rev.* **D6** (1972) 3368–3382.

[43] C. de Rham and G. Gabadadze, "Generalization of the Fierz-Pauli Action," *Phys. Rev.* **D82** (2010) 044020, arXiv:1007.0443 [hep-th].

[44] C. de Rham, G. Gabadadze, and A. J. Tolley, "Resummation of Massive Gravity," *Phys. Rev. Lett.* **106** (2011) 231101, arXiv:1011.1232 [hep-th].

[45] C. de Rham, G. Gabadadze, and A. J. Tolley, "Ghost free Massive Gravity in the Stúckelberg language," *Phys. Lett.* **B711** (2012) 190–195, arXiv:1107.3820 [hep-th].

[46] C. Deffayet and J.-W. Rombouts, "Ghosts, strong coupling and accidental symmetries in massive gravity," *Phys. Rev. D* **72** (2005) 044003, arXiv:gr-qc/0505134.

[47] S. F. Hassan and R. A. Rosen, "Resolving the Ghost Problem in non-Linear Massive Gravity," *Phys. Rev. Lett.* **108** (2012) 041101, arXiv:1106.3344 [hep-th].

[48] S. F. Hassan and R. A. Rosen, "Confirmation of the Secondary Constraint and Absence of Ghost in Massive Gravity and Bimetric Gravity," *JHEP* **04** (2012) 123, arXiv:1111.2070 [hep-th].

[49] C. de Rham, G. Gabadadze, and A. J. Tolley, "Helicity decomposition of ghost-free massive gravity," *JHEP* **11** (2011) 093, arXiv:1108.4521 [hep-th].

[50] M. Mirbabayi, "A Proof Of Ghost Freedom In de Rham-Gabadadze-Tolley Massive Gravity," *Phys. Rev.* **D86** (2012) 084006, arXiv:1112.1435 [hep-th].

[51] S. F. Hassan, A. Schmidt-May, and M. von Strauss, "Proof of Consistency of Nonlinear Massive Gravity in the Stúckelberg Formulation," *Phys. Lett.* **B715** (2012) 335–339, arXiv:1203.5283 [hep-th].

[52] H. Nicolai and H. J. Matschull, "Aspects of canonical gravity and supergravity," *J. Geom. Phys.* **11** (1993) 15–62.

[53] P. Peldan, "Actions for gravity, with generalizations: A Review," *Class. Quant. Grav.* **11** (1994) 1087–1132, arXiv:gr-qc/9305011 [gr-qc].

[54] K. Hinterbichler and R. A. Rosen, "Interacting Spin-2 Fields," *JHEP* **07** (2012) 047, arXiv:1203.5783 [hep-th].

[55] S. Deser and C. J. Isham, "Canonical vierbein form of general relativity," *Phys. Rev. D* **14** (Nov, 1976) 2505–2510. https://link.aps.org/doi/10.1103/PhysRevD.14.2505.

[56] R. L. Arnowitt, S. Deser, and C. W. Misner, "The Dynamics of general relativity," *Gen. Rel. Grav.* **40** (2008) 1997–2027, arXiv:gr-qc/0405109 [gr-qc].

[57] T. Ortin, *Gravity and Strings*. Cambridge Monographs on Mathematical Physics. Cambridge University Press, 2015. http://www.cambridge.org/mw/academic/subjects/physics/theoretical-physics-and-mathematical-physics/gravity-and-strings-2nd-edition.

[58] S. Alexandrov, "Canonical structure of Tetrad Bimetric Gravity," *Gen. Rel. Grav.* **46** (2014) 1639, arXiv:1308.6586 [hep-th].

[59] M. Bañados, "A Note on the Uniqueness of the dRGT Massive Gravity Theory. The $D = 3$ Case," *Grav. Cosmol.* **24** no. 4, (2018) 321–330, arXiv:1709.08738 [gr-qc].

[60] N. Arkani-Hamed and M. D. Schwartz, "Discrete gravitational dimensions," *Phys. Rev.* **D69** (2004) 104001, arXiv:hep-th/0302110 [hep-th].

[61] M. D. Schwartz, "Constructing gravitational dimensions," *Phys. Rev.* **D68** (2003) 024029, arXiv:hep-th/0303114 [hep-th].

[62] C. de Rham, A. Matas, and A. J. Tolley, "Deconstructing Dimensions and Massive Gravity," *Class. Quant. Grav.* **31** (2014) 025004, arXiv:1308.4136 [hep-th].

[63] S. F. Hassan and R. A. Rosen, "On Non-Linear Actions for Massive Gravity," *JHEP* **07** (2011) 009, arXiv:1103.6055 [hep-th].

[64] C. de Rham, L. Heisenberg, and R. H. Ribeiro, "Ghosts and matter couplings in massive gravity, bigravity and multigravity," *Phys. Rev.* **D90** (2014) 124042, arXiv:1409.3834 [hep-th].

[65] M. von Strauss, A. Schmidt-May, J. Enander, E. Mortsell, and S. F. Hassan, "Cosmological Solutions in Bimetric Gravity and their Observational Tests," *JCAP* **1203** (2012) 042, arXiv:1111.1655 [gr-qc].

[66] D. Comelli, M. Crisostomi, F. Nesti, and L. Pilo, "FRW Cosmology in Ghost Free Massive Gravity," *JHEP* **03** (2012) 067, arXiv:1111.1983 [hep-th]. [Erratum: JHEP06,020(2012)].

[67] S. F. Hassan, A. Schmidt-May, and M. von Strauss, "On Consistent Theories of Massive Spin-2 Fields Coupled to Gravity," *JHEP* **05** (2013) 086, arXiv:1208.1515 [hep-th].

[68] F. Koennig, Y. Akrami, L. Amendola, M. Motta, and A. R. Solomon, "Stable and unstable cosmological models in bimetric massive gravity," *Phys. Rev. D* **90** (2014) 124014, arXiv:1407.4331 [astro-ph.CO].

[69] K. Koyama, G. Niz, and G. Tasinato, "Strong interactions and exact solutions in non-linear massive gravity," *Phys. Rev. D* **84** (2011) 064033, arXiv:1104.2143 [hep-th].

[70] G. Chkareuli and D. Pirtskhalava, "Vainshtein Mechanism In $\Lambda_3$ - Theories," *Phys. Lett. B* **713** (2012) 99–103, arXiv:1105.1783 [hep-th].

[71] F. Sbisa, G. Niz, K. Koyama, and G. Tasinato, "Characterising Vainshtein Solutions in Massive Gravity," *Phys. Rev. D* **86** (2012) 024033, arXiv:1204.1193 [hep-th].

[72] E. Babichev and M. Crisostomi, "Restoring general relativity in massive bigravity theory," *Phys. Rev.* **D88** no. 8, (2013) 084002, arXiv:1307.3640 [gr-qc].

[73] E. Babichev, C. Deffayet, and R. Ziour, "The Recovery of General Relativity in massive gravity via the Vainshtein mechanism," *Phys. Rev. D* **82** (2010) 104008, arXiv:1007.4506 [gr-qc].

[74] M. Platscher and J. Smirnov, "Degravitation of the Cosmological Constant in Bigravity," *JCAP* **1703** no. 03, (2017) 051, arXiv:1611.09385 [gr-qc].

[75] C. Deffayet and T. Jacobson, "On horizon structure of bimetric spacetimes," *Class. Quant. Grav.* **29** (2012) 065009, arXiv:1107.4978 [gr-qc].

[76] C. de Rham, L. Heisenberg, and R. H. Ribeiro, "Quantum Corrections in Massive Gravity," *Phys. Rev. D* **88** (2013) 084058, arXiv:1307.7169 [hep-th].

[77] J. Martin, "Everything You Always Wanted To Know About The Cosmological Constant Problem (But Were Afraid To Ask)," *Comptes Rendus Physique* **13** (2012) 566–665, arXiv:1205.3365 [astro-ph.CO].

[78] E. Babichev, L. Marzola, M. Raidal, A. Schmidt-May, F. Urban, H. Veermäe, and M. von Strauss, "Heavy spin-2 Dark Matter," *JCAP* **1609** no. 09, (2016) 016, arXiv:1607.03497 [hep-th].

[79] E. Babichev, L. Marzola, M. Raidal, A. Schmidt-May, F. Urban, H. Veermäe, and M. von Strauss, "Bigravitational origin of dark matter," *Phys. Rev. D* **94** no. 8, (2016) 084055, arXiv:1604.08564 [hep-ph].

[80] K. Aoki and K.-i. Maeda, "Condensate of Massive Graviton and Dark Matter," *Phys. Rev. D* **97** no. 4, (2018) 044002, arXiv:1707.05003 [hep-th].

[81] K. Aoki, K.-i. Maeda, Y. Misonoh, and H. Okawa, "Massive Graviton Geons," *Phys. Rev. D* **97** no. 4, (2018) 044005, arXiv:1710.05606 [gr-qc].

[82] K. Aoki and K.-i. Maeda, "Cosmology in ghost-free bigravity theory with twin matter fluids: The origin of dark matter," *Phys. Rev. D* **89** no. 6, (2014) 064051, arXiv:1312.7040 [gr-qc].

[83] K. Aoki and K.-i. Maeda, "Dark matter in ghost-free bigravity theory: From a galaxy scale to the universe," *Phys. Rev. D* **90** (2014) 124089, arXiv:1409.0202 [gr-qc].

[84] Z. Berezhiani, D. Comelli, F. Nesti, and L. Pilo, "Spontaneous Lorentz Breaking and Massive Gravity," *Phys. Rev. Lett.* **99** (2007) 131101, arXiv:hep-th/0703264 [HEP-TH].

[85] A. De Felice, T. Nakamura, and T. Tanaka, "Possible existence of viable models of bi-gravity with detectable graviton oscillations by gravitational wave detectors," *Progress of Theoretical and Experimental Physics* **2014** no. 4, (2014) 1–5.

[86] T. Narikawa, K. Ueno, H. Tagoshi, T. Tanaka, N. Kanda, and T. Nakamura, "Detectability of bigravity with graviton oscillations using gravitational wave observations," *Phys. Rev.* **D91** (2015) 062007, arXiv:1412.8074 [gr-qc].

[87] **Virgo, LIGO Scientific** Collaboration, B. P. Abbott *et al.*, "Observation of Gravitational Waves from a Binary Black Hole Merger," *Phys. Rev. Lett.* **116** no. 6, (2016) 061102, arXiv:1602.03837 [gr-qc].

[88] D. Comelli, M. Crisostomi, and L. Pilo, "Perturbations in Massive Gravity Cosmology," *JHEP* **06** (2012) 085, arXiv:1202.1986 [hep-th].

[89] A. Schmidt-May and M. von Strauss, "Recent developments in bimetric theory," *J. Phys.* **A49** no. 18, (2016) 183001, arXiv:1512.00021 [hep-th].

[90] **Virgo, LIGO Scientific** Collaboration, B. Abbott *et al.*, "Improved analysis of GW150914 using a fully spin-precessing waveform Model," *Phys. Rev.* **X6** no. 4, (2016) 041014, arXiv:1606.01210 [gr-qc].

[91] **Virgo, LIGO Scientific** Collaboration, B. P. Abbott *et al.*, "GW151226: Observation of Gravitational Waves from a 22-Solar-Mass Binary Black Hole Coalescence," *Phys. Rev. Lett.* **116** no. 24, (2016) 241103, arXiv:1606.04855 [gr-qc].

[92] B. Wardell, I. Hinder, and E. Bentivegna, "Simulation of GW150914 binary black hole merger using the Einstein Toolkit," Sept., 2016. https://doi.org/10.5281/zenodo.155394.

[93] F. Loffler *et al.*, "The Einstein Toolkit: A Community Computational Infrastructure for Relativistic Astrophysics," *Class. Quant. Grav.* **29** (2012) 115001, arXiv:1111.3344 [gr-qc].

[94] D. Pollney, C. Reisswig, E. Schnetter, N. Dorband, and P. Diener, "High accuracy binary black hole simulations with an extended wave zone," *Phys. Rev.* **D83** (2011) 044045, arXiv:0910.3803 [gr-qc].

[95] E. Schnetter, S. H. Hawley, and I. Hawke, "Evolutions in 3-D numerical relativity using fixed mesh refinement," *Class. Quant. Grav.* **21** (2004) 1465–1488, arXiv:gr-qc/0310042 [gr-qc].

[96] J. Thornburg, "A Fast apparent horizon finder for three-dimensional Cartesian grids in numerical relativity," *Class. Quant. Grav.* **21** (2004) 743–766, arXiv:gr-qc/0306056 [gr-qc].

[97] M. Ansorg, B. Bruegmann, and W. Tichy, "A Single-domain spectral method for black hole puncture data," *Phys. Rev.* **D70** (2004) 064011, arXiv:gr-qc/0404056 [gr-qc].

[98] O. Dreyer, B. Krishnan, D. Shoemaker, and E. Schnetter, "Introduction to isolated horizons in numerical relativity," *Phys. Rev.* **D67** (2003) 024018, arXiv:gr-qc/0206008 [gr-qc].

[99] T. Goodale, G. Allen, G. Lanfermann, J. Massó, T. Radke, E. Seidel, and J. Shalf, "The Cactus framework and toolkit: Design and applications," in *Vector and Parallel Processing – VECPAR'2002, 5th International Conference, Lecture Notes in Computer Science*. Springer, Berlin, 2003. http://edoc.mpg.de/3341.

[100] J. D. Brown, P. Diener, O. Sarbach, E. Schnetter, and M. Tiglio, "Turduckening black holes: An Analytical and computational study," *Phys. Rev.* **D79** (2009) 044023, arXiv:0809.3533 [gr-qc].

[101] S. Husa, I. Hinder, and C. Lechner, "Kranc: a Mathematica application to generate numerical codes for tensorial evolution equations," *Comput. Phys. Commun.* **174** (2006) 983–1004, arXiv:gr-qc/0404023.

[102] M. Thomas and E. Schnetter, "Simulation factory: Taming application configuration and workflow on high-end resources," in *Grid Computing (GRID), 2010 11th IEEE/ACM International Conference on*, pp. 369 –378. Oct., 2010. arXiv:1008.4571 [cs.DC].

[103] http://www.black-holes.org/waveforms, catalog entry sxs:bbh:0317 for gw151226.

[104] M. Beuthe, "Oscillations of neutrinos and mesons in quantum field theory," *Phys. Rept.* **375** (2003) 105–218, arXiv:hep-ph/0109119 [hep-ph].

[105] C. de Rham, J. T. Deskins, A. J. Tolley, and S.-Y. Zhou, "Graviton Mass Bounds," arXiv:1606.08462 [astro-ph.CO].

[106] **LIGO Scientific Collaboration and Virgo Collaboration** Collaboration, B. P. Abbott *et al.*, "Properties of the binary black hole merger gw150914," *Phys. Rev. Lett.* **116** (Jun, 2016) 241102. https://link.aps.org/doi/10.1103/PhysRevLett.116.241102.

[107] E. D. Kovetz, I. Cholis, P. C. Breysse, and M. Kamionkowski, "Black hole mass function from gravitational wave measurements," *Phys. Rev. D* **95** (May, 2017) 103010. https://link.aps.org/doi/10.1103/PhysRevD.95.103010.

[108] **LIGO Scientific Collaboration and Virgo Collaboration** Collaboration, B. P. Abbott *et al.*, "Binary black hole mergers in the first advanced ligo observing run," *Phys. Rev. X* **6** (Oct, 2016) 041015. https://link.aps.org/doi/10.1103/PhysRevX.6.041015.

[109] D. V. Martynov *et al.*, "Sensitivity of the advanced ligo detectors at the beginning of gravitational wave astronomy," *Phys. Rev. D* **93** (Jun, 2016) 112004. https://link.aps.org/doi/10.1103/PhysRevD.93.112004.

[110] **VIRGO, LIGO Scientific** Collaboration, B. P. Abbott *et al.*, "GW170104: Observation of a 50-Solar-Mass Binary Black Hole Coalescence at Redshift 0.2," *Phys. Rev. Lett.* **118** no. 22, (2017) 221101, arXiv:1706.01812 [gr-qc].

[111] **Virgo, LIGO Scientific** Collaboration, B. P. Abbott *et al.*, "GW170608: Observation of a 19-solar-mass Binary Black Hole Coalescence," arXiv:1711.05578 [astro-ph.HE].

[112] **Virgo, LIGO Scientific** Collaboration, B. P. Abbott *et al.*, "GW170814: A Three-Detector Observation of Gravitational Waves from a Binary Black Hole Coalescence," *Phys. Rev. Lett.* **119** no. 14, (2017) 141101, arXiv:1709.09660 [gr-qc].

[113] **LIGO Scientific Collaboration and Virgo Collaboration** Collaboration, B. P. Abbott *et al.*, "Gw170817: Observation of gravitational waves from a binary neutron star inspiral," *Phys. Rev. Lett.* **119** (Oct, 2017) 161101. https://link.aps.org/doi/10.1103/PhysRevLett.119.161101.

[114] B. P. Abbott, R. Abbott, T. D. Abbott, M. R. Abernathy, F. Acernese, K. Ackley, C. Adams, T. Adams, P. Addesso, R. X. Adhikari, and et al., "GW151226: Observation of Gravitational Waves from a 22-Solar-Mass Binary Black Hole Coalescence," *Physical Review Letters* **116** no. 24, (June, 2016) 241103, arXiv:1606.04855 [gr-qc].

[115] **Virgo, LIGO Scientific** Collaboration, B. Abbott *et al.*, "GW170817: Observation of Gravitational Waves from a Binary Neutron Star Inspiral," *Phys. Rev. Lett.* **119** no. 16, (2017) 161101, arXiv:1710.05832 [gr-qc].

[116] Z. Mark, A. Zimmerman, S. M. Du, and Y. Chen, "A recipe for echoes from exotic compact objects," *Phys. Rev.* **D96** no. 8, (2017) 084002, arXiv:1706.06155 [gr-qc].

[117] V. Cardoso, S. Hopper, C. F. B. Macedo, C. Palenzuela, and P. Pani, "Gravitational-wave signatures of exotic compact objects and of quantum corrections at the horizon scale," *Phys. Rev.* **D94** no. 8, (2016) 084031, arXiv:1608.08637 [gr-qc].

[118] J. Abedi, H. Dykaar, and N. Afshordi, "Echoes from the Abyss: Tentative evidence for Planck-scale structure at black hole horizons," *Phys. Rev.* **D96** no. 8, (2017) 082004, arXiv:1612.00266 [gr-qc].

[119] J. Abedi, H. Dykaar, and N. Afshordi, "Echoes from the Abyss: The Holiday Edition!," arXiv:1701.03485 [gr-qc].

[120] R. S. Conklin, B. Holdom, and J. Ren, "Gravitational wave echoes through new windows," arXiv:1712.06517 [gr-qc].

[121] G. Ashton, O. Birnholtz, M. Cabero, C. Capano, T. Dent, B. Krishnan, G. D. Meadors, A. B. Nielsen, A. Nitz, and J. Westerweck, "Comments on: "Echoes from the abyss: Evidence for Planck-scale structure at black hole horizons"," arXiv:1612.05625 [gr-qc].

[122] J. Westerweck, A. Nielsen, O. Fischer-Birnholtz, M. Cabero, C. Capano, T. Dent, B. Krishnan, G. Meadors, and A. H. Nitz, "Low significance of evidence for black hole echoes in gravitational wave data," arXiv:1712.09966 [gr-qc].

[123] R. Ciolfi and D. M. Siegel, "Short gamma-ray bursts in the "time-reversal" scenario," *Astrophys. J.* **798** no. 2, (2015) L36, arXiv:1411.2015 [astro-ph.HE].

[124] I. Leanizbarrutia, F. S. N. Lobo, and D. Saez-Gomez, "Crossing SNe Ia and BAO observational constraints with local ones in hybrid metric-Palatini gravity," *Phys. Rev.* **D95** no. 8, (2017) 084046, arXiv:1701.08980 [gr-qc].

[125] R. C. Nunes, S. Pan, E. N. Saridakis, and E. M. C. Abreu, "New observational constraints on $f(R)$ gravity from cosmic chronometers," *JCAP* **1701** no. 01, (2017) 005, arXiv:1610.07518 [astro-ph.CO].

[126] S. D. Odintsov, D. Sáez-Chillón Gómez, and G. S. Sharov, "Is exponential gravity a viable description for the whole cosmological history?," *Eur. Phys. J.* **C77** no. 12, (2017) 862, arXiv:1709.06800 [gr-qc].

[127] S. Hagstotz, M. Costanzi, M. Baldi, and J. Weller, "Joint halo-mass function for modified gravity and massive neutrinos – I. Simulations and cosmological forecasts," *Mon. Not. Roy. Astron. Soc.* **486** no. 3, (2019) 3927–3941, arXiv:1806.07400 [astro-ph.CO].

[128] Y.-C. Chen, C.-Q. Geng, C.-C. Lee, and H. Yu, "Matter Power Spectra in Viable $f(R)$ Gravity Models with Dynamical Background," *Eur. Phys. J.* **C79** no. 2, (2019) 93, arXiv:1901.06747 [gr-qc].

[129] E. Bellini, A. J. Cuesta, R. Jimenez, and L. Verde, "Constraints on deviations from ΛCDM within Horndeski gravity," *JCAP* **1602** no. 02, (2016) 053, arXiv:1509.07816 [astro-ph.CO]. [Erratum: JCAP1606,no.06,E01(2016)].

[130] R. C. Nunes, "Structure formation in $f(T)$ gravity and a solution for $H_0$ tension," *JCAP* **1805** no. 05, (2018) 052, arXiv:1802.02281 [gr-qc].

[131] O. Akarsu, J. D. Barrow, C. V. R. Board, N. M. Uzun, and J. A. Vazquez, "Screening $\Lambda$ in a new modified gravity model," arXiv:1903.11519 [gr-qc].

[132] J. de Cruz Pérez and J. Solà Peracaula, "Brans–Dicke cosmology mimicking running vacuum," *Mod. Phys. Lett.* **A33** no. 38, (2018) 1850228, arXiv:1809.03329 [gr-qc].

[133] J. Sola, A. Gomez-Valent, J. d. C. Perez, and C. Moreno-Pulido, "Brans-Dicke gravity with a cosmological constant smoothes out $\Lambda$CDM tensions," arXiv:1909.02554 [astro-ph.CO].

[134] C. D. Kreisch and E. Komatsu, "Cosmological Constraints on Horndeski Gravity in Light of GW170817," *JCAP* **1812** no. 12, (2018) 030, arXiv:1712.02710 [astro-ph.CO].

[135] J. Renk, M. Zumalacárregui, F. Montanari, and A. Barreira, "Galileon gravity in light of ISW, CMB, BAO and $H_0$ data," *JCAP* **1710** no. 10, (2017) 020, arXiv:1707.02263 [astro-ph.CO].

[136] J. Noller and A. Nicola, "Cosmological parameter constraints for Horndeski scalar-tensor gravity," *Phys. Rev.* **D99** no. 10, (2019) 103502, arXiv:1811.12928 [astro-ph.CO].

[137] C. Leloup, V. Ruhlmann-Kleider, J. Neveu, and A. De Mattia, "Observational status of the Galileon model general solution from cosmological data and gravitational waves," *JCAP* **1905** no. 05, (2019) 011, arXiv:1902.07065 [astro-ph.CO].

[138] W. Yang, M. Shahalam, B. Pal, S. Pan, and A. Wang, "Constraints on quintessence scalar field models using cosmological observations," *Phys. Rev.* **D100** no. 2, (2019) 023522, arXiv:1810.08586 [gr-qc].

[139] M. Raveri, "Reconstructing Gravity on Cosmological Scales," arXiv:1902.01366 [astro-ph.CO].

[140] Y. Dirian, S. Foffa, M. Kunz, M. Maggiore, and V. Pettorino, "Non-local gravity and comparison with observational datasets. II. Updated results and Bayesian model comparison with $\Lambda$CDM," *JCAP* **1605** no. 05, (2016) 068, arXiv:1602.03558 [astro-ph.CO].

[141] E. Belgacem, Y. Dirian, S. Foffa, and M. Maggiore, "Nonlocal gravity. Conceptual aspects and cosmological predictions," *JCAP* **1803** no. 03, (2018) 002, arXiv:1712.07066 [hep-th].

[142] L. Amendola, Y. Dirian, H. Nersisyan, and S. Park, "Observational Constraints in Nonlocal Gravity: the Deser-Woodard Case," *JCAP* **1903** no. 03, (2019) 045, arXiv:1901.07832 [astro-ph.CO].

[143] G. Risaliti and E. Lusso, "A Hubble Diagram for Quasars," *Astrophys. J.* **815** (2015) 33, arXiv:1505.07118 [astro-ph.CO].

[144] G. Risaliti and E. Lusso, "Cosmological constraints from the Hubble diagram of quasars at high redshifts," *Nat. Astron.* **3** no. 3, (2019) 272–277, arXiv:1811.02590 [astro-ph.CO].

[145] N. Khadka and B. Ratra, "Quasar X-ray and UV flux, baryon acoustic oscillation, and Hubble parameter measurement constraints on cosmological model parameters," arXiv:1909.01400 [astro-ph.CO].

[146] E. Aubourg *et al.*, "Cosmological implications of baryon acoustic oscillation measurements," *Phys. Rev.* **D92** no. 12, (2015) 123516, arXiv:1411.1074 [astro-ph.CO].

[147] S. M. Feeney, H. V. Peiris, A. R. Williamson, S. M. Nissanke, D. J. Mortlock, J. Alsing, and D. Scolnic, "Prospects for resolving the Hubble constant tension with standard sirens," *Phys. Rev. Lett.* **122** no. 6, (2019) 061105, arXiv:1802.03404 [astro-ph.CO].

[148] **DES** Collaboration, E. Macaulay *et al.*, "First Cosmological Results using Type Ia Supernovae from the Dark Energy Survey: Measurement of the Hubble Constant," *Mon. Not. Roy. Astron. Soc.* **486** no. 2, (2019) 2184–2196, arXiv:1811.02376 [astro-ph.CO].

[149] A. Zee, "A Broken Symmetric Theory of Gravity," *Phys. Rev. Lett.* **42** (1979) 417.

[150] S. L. Adler, "Einstein Gravity as a Symmetry-Breaking Effect in Quantum Field Theory," *Rev. Mod. Phys.* **54** (1982) 729. [,539(1982)].

[151] P. D. Mannheim, "Alternatives to dark matter and dark energy," *Prog. Part. Nucl. Phys.* **56** (2006) 340–445, arXiv:astro-ph/0505266 [astro-ph].

[152] P. D. Mannheim and D. Kazanas, "Exact Vacuum Solution to Conformal Weyl Gravity and Galactic Rotation Curves," *Astrophys. J.* **342** (1989) 635–638.

[153] Y. Akrami, T. S. Koivisto, and M. Sandstad, "Accelerated expansion from ghost-free bigravity: a statistical analysis with improved generality," *JHEP* **03** (2013) 099, arXiv:1209.0457 [astro-ph.CO].

[154] A. G. Riess *et al.*, "A 2.4% Determination of the Local Value of the Hubble Constant," *Astrophys. J.* **826** no. 1, (2016) 56, arXiv:1604.01424 [astro-ph.CO].

[155] A. G. Riess, S. Casertano, W. Yuan, L. M. Macri, and D. Scolnic, "Large Magellanic Cloud Cepheid Standards Provide a 1% Foundation for the Determination of the Hubble Constant and Stronger Evidence for Physics beyond ΛCDM," *Astrophys. J.* **876** no. 1, (2019) 85, arXiv:1903.07603 [astro-ph.CO].

[156] K. C. Wong *et al.*, "H0LiCOW XIII. A 2.4% measurement of $H_0$ from lensed quasars: $5.3\sigma$ tension between early and late-Universe probes," arXiv:1907.04869 [astro-ph.CO].

[157] S. Dhawan, D. Brout, D. Scolnic, A. Goobar, A. G. Riess, and V. Miranda, "Cosmological model insensitivity of local $H_0$ from the Cepheid distance ladder," arXiv:2001.09260 [astro-ph.CO].

[158] T. Yang, A. Banerjee, and E. O. Colgain, "On cosmography and flat ΛCDM tensions at high redshift," arXiv:1911.01681 [astro-ph.CO].

[159] H. Velten and S. Gomes, "Is the Hubble diagram of quasars in tension with concordance cosmology?," *Phys. Rev.* **D101** no. 4, (2020) 043502, arXiv:1911.11848 [astro-ph.CO].

[160] E. Di Valentino, E. Giusarma, M. Lattanzi, O. Mena, A. Melchiorri, and J. Silk, "Cosmological Axion and neutrino mass constraints from Planck 2015 temperature and polarization data," *Phys. Lett.* **B752** (2016) 182–185, arXiv:1507.08665 [astro-ph.CO].

[161] **DES** Collaboration, T. M. C. Abbott *et al.*, "Dark Energy Survey year 1 results: Cosmological constraints from galaxy clustering and weak lensing," *Phys. Rev.* **D98** no. 4, (2018) 043526, arXiv:1708.01530 [astro-ph.CO].

[162] G. Lambiase, S. Mohanty, A. Narang, and P. Parashari, "Testing dark energy models in the light of $\sigma_8$ tension," *Eur. Phys. J.* **C79** no. 2, (2019) 141, arXiv:1804.07154 [astro-ph.CO].

[163] F. Könnig, "Higuchi Ghosts and Gradient Instabilities in Bimetric Gravity," *Phys. Rev. D* **91** (2015) 104019, arXiv:1503.07436 [astro-ph.CO].

[164] J. B. Muñoz, "A Standard Ruler at Cosmic Dawn," arXiv:1904.07868 [astro-ph.CO].

[165] A. Domínguez, R. Wojtak, J. Finke, M. Ajello, K. Helgason, F. Prada, A. Desai, V. Paliya, L. Marcotulli, and D. Hartmann, "A new measurement of the Hubble constant and matter content of the Universe using extragalactic background light $\gamma$-ray attenuation," arXiv:1903.12097 [astro-ph.CO].

[166] J.-J. Wei, X.-F. Wu, and F. Melia, "The Gamma-Ray Burst Hubble Diagram and Its Implications for Cosmology," *Astrophys. J.* **772** (2013) 43, arXiv:1301.0894 [astro-ph.HE].

[167] M. Lüben, A. Schmidt-May, and J. Weller, "Physical parameter space of bimetric theory and SN1a constraints," arXiv:2003.03382 [gr-qc].

[168] A. De Felice, A. E. Gumrukcuoglu, and S. Mukohyama, "Massive gravity: nonlinear instability of the homogeneous and isotropic universe," *Phys. Rev. Lett.* **109** (2012) 171101, arXiv:1206.2080 [hep-th].

[169] M. Berg, I. Buchberger, J. Enander, E. Mortsell, and S. Sjors, "Growth Histories in Bimetric Massive Gravity," *JCAP* **1212** (2012) 021, arXiv:1206.3496 [gr-qc].

[170] F. Könnig and L. Amendola, "Instability in a minimal bimetric gravity model," *Phys. Rev.* **D90** (2014) 044030, arXiv:1402.1988 [astro-ph.CO].

[171] A. R. Solomon, Y. Akrami, and T. S. Koivisto, "Linear growth of structure in massive bigravity," *JCAP* **1410** (2014) 066, arXiv:1404.4061 [astro-ph.CO].

[172] M. Lagos and P. G. Ferreira, "Cosmological perturbations in massive bigravity," *JCAP* **1412** (2014) 026, arXiv:1410.0207 [gr-qc].

[173] G. Cusin, R. Durrer, P. Guarato, and M. Motta, "Gravitational waves in bigravity cosmology," *JCAP* **1505** no. 05, (2015) 030, arXiv:1412.5979 [astro-ph.CO].

[174] J. Enander, Y. Akrami, E. Mörtsell, M. Renneby, and A. R. Solomon, "Integrated Sachs-Wolfe effect in massive bigravity," *Phys. Rev.* **D91** (2015) 084046, arXiv:1501.02140 [astro-ph.CO].

[175] G. Cusin, R. Durrer, P. Guarato, and M. Motta, "Inflationary perturbations in bimetric gravity," *JCAP* **1509** no. 09, (2015) 043, arXiv:1505.01091 [astro-ph.CO].

[176] T. Kobayashi, M. Siino, M. Yamaguchi, and D. Yoshida, "Perturbations of Cosmological and Black Hole Solutions in Massive gravity and Bi-gravity," *PTEP* **2016** no. 10, (2016) 103E02, arXiv:1509.02096 [gr-qc].

[177] M. Lagos and P. G. Ferreira, "A general theory of linear cosmological perturbations: bimetric theories," *JCAP* **1701** no. 01, (2017) 047, arXiv:1610.00553 [gr-qc].

[178] L. Amendola, F. Könnig, M. Martinelli, V. Pettorino, and M. Zumalacarregui, "Surfing gravitational waves: can bigravity survive growing tensor modes?," *JCAP* **1505** (2015) 052, arXiv:1503.02490 [astro-ph.CO].

[179] M. Johnson and A. Terrana, "Tensor Modes in Bigravity: Primordial to Present," *Phys. Rev.* **D92** no. 4, (2015) 044001, arXiv:1503.05560 [astro-ph.CO].

[180] E. Mortsell and J. Enander, "Scalar instabilities in bimetric gravity: The Vainshtein mechanism and structure formation," *JCAP* **1510** no. 10, (2015) 044, arXiv:1506.04977 [astro-ph.CO].

[181] Y. Akrami, S. F. Hassan, F. Könnig, A. Schmidt-May, and A. R. Solomon, "Bimetric gravity is cosmologically viable," *Phys. Lett.* **B748** (2015) 37–44, arXiv:1503.07521 [gr-qc].

[182] A. De Felice, A. E. Gümrükçüoğlu, S. Mukohyama, N. Tanahashi, and T. Tanaka, "Viable cosmology in bimetric theory," *JCAP* **1406** (2014) 037, arXiv:1404.0008 [hep-th].

[183] A. Higuchi, "Forbidden Mass Range for Spin-2 Field Theory in De Sitter Space-time," *Nucl. Phys.* **B282** (1987) 397–436.

[184] Y. Yamashita and T. Tanaka, "Mapping the ghost free bigravity into braneworld setup," *JCAP* **1406** (2014) 004, arXiv:1401.4336 [hep-th].

[185] A. I. Vainshtein, "To the problem of nonvanishing gravitation mass," *Phys. Lett.* **B39** (1972) 393–394.

[186] M. Lüben, A. Schmidt-May, and J. Smirnov, "Vainshtein Screening in Bimetric Cosmology," arXiv:1912.09449 [gr-qc].

[187] K. S. Stelle, "Renormalization of higher-derivative quantum gravity," *Phys. Rev. D* **16** (Aug, 1977) 953–969. https://link.aps.org/doi/10.1103/PhysRevD.16.953.

[188] K. S. Stelle, "Classical Gravity with Higher Derivatives," *Gen. Rel. Grav.* **9** (1978) 353–371.

[189] R. J. Riegert, "THE PARTICLE CONTENT OF LINEARIZED CONFORMAL GRAVITY," *Phys. Lett.* **A105** (1984) 110–112.

[190] M. Ostrogradsky, "Mémoires sur les équations différentielles, relatives au problème des isopérimètres," *Mem. Acad. St. Petersbourg* **6** no. 4, (1850) 385–517.

[191] R. P. Woodard, "Ostrogradsky's theorem on Hamiltonian instability," *Scholarpedia* **10** no. 8, (2015) 32243, arXiv:1506.02210 [hep-th].

[192] C. M. Bender and P. D. Mannheim, "No-ghost theorem for the fourth-order derivative Pais-Uhlenbeck oscillator model," *Phys. Rev. Lett.* **100** (2008) 110402, arXiv:0706.0207 [hep-th].

[193] P. D. Mannheim, "Unitarity of loop diagrams for the ghostlike $1/(k^2 - M_1^2) - 1/(k^2 - M_2^2)$ propagator," *Phys. Rev.* **D98** no. 4, (2018) 045014, arXiv:1801.03220 [hep-th].

[194] A. Salvio, "Metastability in Quadratic Gravity," arXiv:1902.09557 [gr-qc].

[195] I. L. Shapiro, A. M. Pelinson, and F. de O. Salles, "Gravitational Waves and Perspectives for Quantum Gravity," *Mod. Phys. Lett.* **A29** (2014) 1430034, arXiv:1410.2581 [gr-qc].

[196] J. F. Donoghue and G. Menezes, "Unitarity, stability and loops of unstable ghosts," arXiv:1908.02416 [hep-th].

[197] A. Salvio and A. Strumia, "Quantum mechanics of 4-derivative theories," *Eur. Phys. J.* **C76** no. 4, (2016) 227, arXiv:1512.01237 [hep-th].

[198] M. Raidal and H. Veermäe, "On the Quantisation of Complex Higher Derivative Theories and Avoiding the Ostrogradsky Ghost," *Nucl. Phys.* **B916** (2017) 607–626, arXiv:1611.03498 [hep-th].

[199] S. W. Hawking and T. Hertog, "Living with ghosts," *Phys. Rev.* **D65** (2002) 103515, arXiv:hep-th/0107088 [hep-th].

[200] P. D. Mannheim, "Conformal Cosmology With No Cosmological Constant," *Gen. Rel. Grav.* **22** (1990) 289–298.

[201] P. D. Mannheim and J. G. O'Brien, "Galactic rotation curves in conformal gravity," *J. Phys. Conf. Ser.* **437** (2013) 012002, arXiv:1211.0188 [astro-ph.CO].

[202] J. G. O'Brien, S. S. Chaykov, J. Dentico, M. Stulge, B. Stefanski, and R. J. Moss, "Recent advancements in conformal gravity," *J. Phys. Conf. Ser.* **845** no. 1, (2017) 012004.

[203] J. G. O'Brien, S. Chaykov, T. L. Chiarelli, T. Saintable, and J. Harrington, "Conformal Gravity Solutions to Standard Gravity Problems," *Int. J. Mod. Phys. Conf. Ser.* **45** (2017) 1760003.

[204] D. Cutajar and K. Z. Adami, "Strong lensing as a test for Conformal Weyl Gravity," *Mon. Not. Roy. Astron. Soc.* **441** no. 2, (2014) 1291–1296, arXiv:1403.7930 [gr-qc].

[205] O. Kasikci and C. Deliduman, "Gravitational Lensing in Weyl Gravity," arXiv:1812.01076 [gr-qc].

[206] J. Sultana and D. Kazanas, "Bending of light in conformal Weyl gravity," *Phys. Rev.* **D81** (2010) 127502.

[207] A. Edery and M. B. Paranjape, "Classical tests for weyl gravity: Deflection of light and time delay," *Phys. Rev. D* **58** (Jun, 1998) 024011. https://link.aps.org/doi/10.1103/PhysRevD.58.024011.

[208] C. Cattani, M. Scalia, E. Laserra, I. Bochicchio, and K. K. Nandi, "Correct light deflection in Weyl conformal gravity," *Phys. Rev.* **D87** no. 4, (2013) 047503, arXiv:1303.7438 [gr-qc].

[209] Y.-K. Lim and Q.-h. Wang, "Exact gravitational lensing in conformal gravity and Schwarzschild–de Sitter spacetime," *Phys. Rev.* **D95** no. 2, (2017) 024004, arXiv:1609.07633 [gr-qc].

[210] M. C. Campigotto, A. Diaferio, and L. Fatibene, "Conformal gravity: light deflection revisited and the galactic rotation curve failure," arXiv:1712.03969 [astro-ph.CO].

[211] C. Caprini, P. Hölscher, and D. J. Schwarz, "Astrophysical Gravitational Waves in Conformal Gravity," *Phys. Rev.* **D98** no. 8, (2018) 084002, arXiv:1804.01876 [gr-qc].

[212] L. Knox and A. Kosowsky, "Primordial nucleosynthesis in conformal Weyl gravity," arXiv:astro-ph/9311006 [astro-ph].

[213] D. Elizondo and G. Yepes, "Can conformal Weyl gravity be considered a viable cosmological theory?," *Astrophys. J.* **428** (1994) 17–20, arXiv:astro-ph/9312064 [astro-ph].

[214] R. Bach, "Zur weylschen relativitätstheorie und der weylschen erweiterung des krümmungstensorbegriffs," *Mathematische Zeitschrift* **9** no. 1, (Mar, 1921) 110–135. https://doi.org/10.1007/BF01378338.

[215] P. D. Mannheim and D. Kazanas, "Newtonian limit of conformal gravity and the lack of necessity of the second order Poisson equation," *Gen. Rel. Grav.* **26** (1994) 337–361.

[216] P. D. Mannheim, "Linear potentials and galactic rotation curves," *Astrophys. J.* **419** (1993) 150–154, arXiv:hep-ph/9212304 [hep-ph].

[217] D. Kazanas and P. D. Mannheim, "General Structure of the Gravitational Equations of Motion in Conformal Weyl Gravity," *Astrophys. J. Suppl.* **76** (1991) 431–453.

[218] P. D. Mannheim, "Is dark matter fact or fantasy? – clues from the data," arXiv:1903.11217 [astro-ph.GA].

[219] P. D. Mannheim and J. G. O'Brien, "Impact of a global quadratic potential on galactic rotation curves," *Phys. Rev. Lett.* **106** (2011) 121101, arXiv:1007.0970 [astro-ph.CO].

[220] P. D. Mannheim and J. G. O'Brien, "Fitting galactic rotation curves with conformal gravity and a global quadratic potential," *Phys. Rev.* **D85** (2012) 124020, arXiv:1011.3495 [astro-ph.CO].

[221] J. G. O'Brien and P. D. Mannheim, "Fitting dwarf galaxy rotation curves with conformal gravity," *Mon. Not. Roy. Astron. Soc.* **421** (2012) 1273, arXiv:1107.5229 [astro-ph.CO].

[222] J. G. O'Brien, T. L. Chiarelli, and P. D. Mannheim, "Universal properties of galactic rotation curves and a first principles derivation of the Tully–Fisher relation," *Phys. Lett.* **B782** (2018) 433–439, arXiv:1704.03921 [astro-ph.GA].

[223] https://github.com/kma-code/cosmological_tests-1.

[224] R. J. Cooke, M. Pettini, and C. C. Steidel, "One Percent Determination of the Primordial Deuterium Abundance," *Astrophys. J.* **855** no. 2, (2018) 102, arXiv:1710.11129 [astro-ph.CO].

[225] **SDSS** Collaboration, M. Betoule *et al.*, "Improved cosmological constraints from a joint analysis of the SDSS-II and SNLS supernova samples," *Astron. Astrophys.* **568** (2014) A22, arXiv:1401.4064 [astro-ph.CO].

[226] http://supernovae.in2p3.fr/sdss_snls_jla/ReadMe.html.

[227] F. Melia, J.-J. Wei, R. Maier, and X. Wu, "Cosmological Tests with the Joint Lightcurve Analysis," *EPL* **123** no. 5, (2018) 59002, arXiv:1809.05094 [astro-ph.CO].

[228] A. Cuceu, J. Farr, P. Lemos, and A. Font-Ribera, "Baryon Acoustic Oscillations and the Hubble Constant: Past, Present and Future," arXiv:1906.11628 [astro-ph.CO].

[229] N. Schöneberg, J. Lesgourgues, and D. C. Hooper, "The BAO+BBN take on the Hubble tension," arXiv:1907.11594 [astro-ph.CO].

[230] D. J. Fixsen, "THE TEMPERATURE OF THE COSMIC MICROWAVE BACKGROUND," *The Astrophysical Journal* **707** no. 2, (Nov, 2009) 916–920. https://doi.org/10.1088%2F0004-637x%2F707%2F2%2F916.

[231] F. Beutler, C. Blake, M. Colless, D. H. Jones, L. Staveley-Smith, L. Campbell, Q. Parker, W. Saunders, and F. Watson, "The 6dF Galaxy Survey: Baryon Acoustic Oscillations and the Local Hubble Constant," *Mon. Not. Roy. Astron. Soc.* **416** (2011) 3017–3032, arXiv:1106.3366 [astro-ph.CO].

[232] A. J. Ross, L. Samushia, C. Howlett, W. J. Percival, A. Burden, and M. Manera, "The clustering of the SDSS DR7 main Galaxy sample – I. A 4 per cent distance measure at $z = 0.15$," *Mon. Not. Roy. Astron. Soc.* **449** no. 1, (2015) 835–847, arXiv:1409.3242 [astro-ph.CO].

[233] **BOSS** Collaboration, S. Alam *et al.*, "The clustering of galaxies in the completed SDSS-III Baryon Oscillation Spectroscopic Survey: cosmological analysis of the DR12 galaxy sample," *Mon. Not. Roy. Astron. Soc.* **470** no. 3, (2017) 2617–2652, arXiv:1607.03155 [astro-ph.CO].

[234] J. E. Bautista *et al.*, "The SDSS-IV extended Baryon Oscillation Spectroscopic Survey: Baryon Acoustic Oscillations at redshift of 0.72 with the DR14 Luminous Red Galaxy Sample," *Astrophys. J.* **863** (2018) 110, arXiv:1712.08064 [astro-ph.CO].

[235] G.-B. Zhao *et al.*, "The clustering of the SDSS-IV extended Baryon Oscillation Spectroscopic Survey DR14 quasar sample: a tomographic measurement of cosmic structure growth and expansion rate based on optimal redshift weights," *Mon. Not. Roy. Astron. Soc.* **482** no. 3, (2019) 3497–3513, arXiv:1801.03043 [astro-ph.CO].

[236] M. Blomqvist *et al.*, "Baryon acoustic oscillations from the cross-correlation of Ly$\alpha$ absorption and quasars in eBOSS DR14," arXiv:1904.03430 [astro-ph.CO].

[237] V. de Sainte Agathe *et al.*, "Baryon acoustic oscillations at z = 2.34 from the correlations of Ly$\alpha$ absorption in eBOSS DR14," arXiv:1904.03400 [astro-ph.CO].

[238] W. Hu and N. Sugiyama, "Small scale cosmological perturbations: An Analytic approach," *Astrophys. J.* **471** (1996) 542–570, arXiv:astro-ph/9510117 [astro-ph].

[239] L. Chen, Q.-G. Huang, and K. Wang, "Distance Priors from Planck Final Release," *JCAP* **1902** (2019) 028, arXiv:1808.05724 [astro-ph.CO].

[240] D. Foreman-Mackey, D. W. Hogg, D. Lang, and J. Goodman, "emcee: The MCMC Hammer," *Publ. Astron. Soc. Pac.* **125** (2013) 306–312, arXiv:1202.3665 [astro-ph.IM].

[241] J. Goodman and J. Weare, "Ensemble samplers with affine invariance," *Communications in Applied Mathematics and Computational Science, Vol. 5, No. 1, p. 65-80, 2010* **5** (2010) 65–80.

[242] H. S. Bhat and N. Kumar, "On the derivation of the bayesian information criterion," 2010. https://web.archive.org/web/20120328065032/http://nscs00.ucmerced.edu/~nkumar4/BhatKumarBIC.pdf.

[243] F. Melia, "Cosmological test using the Hubble diagram of high-z quasars," *Mon. Not. Roy. Astron. Soc.* **489** no. 1, (2019) 517–523, arXiv:1907.13127 [astro-ph.CO].

[244] J. Enander, A. R. Solomon, Y. Akrami, and E. Mortsell, "Cosmic expansion histories in massive bigravity with symmetric matter coupling," *JCAP* **01** (2015) 006, arXiv:1409.2860 [astro-ph.CO].

[245] Y. Akrami, P. Brax, A.-C. Davis, and V. Vardanyan, "Neutron star merger GW170817 strongly constrains doubly coupled bigravity," *Phys. Rev. D* **97** no. 12, (2018) 124010, arXiv:1803.09726 [astro-ph.CO].

[246] E. Mörtsell and S. Dhawan, "Does the Hubble constant tension call for new physics?," *JCAP* **1809** no. 09, (2018) 025, arXiv:1801.07260 [astro-ph.CO].

[247] M. Platscher, J. Smirnov, S. Meyer, and M. Bartelmann, "Long Range Effects in Gravity Theories with Vainshtein Screening," *JCAP* **1812** no. 12, (2018) 009, arXiv:1809.05318 [astro-ph.CO].

[248] M. Lüben, E. Mörtsell, and A. Schmidt-May, "Bimetric cosmology is compatible with local tests of gravity," arXiv:1812.08686 [gr-qc].

[249] A. Diaferio, L. Ostorero, and V. F. Cardone, "Gamma-ray bursts as cosmological probes: LambdaCDM vs. conformal gravity," *JCAP* **1110** (2011) 008, arXiv:1103.5501 [astro-ph.CO].

[250] R. Yang, B. Chen, H. Zhao, J. Li, and Y. Liu, "Test of conformal gravity with astrophysical observations," *Phys. Lett.* **B727** (2013) 43–47, arXiv:1311.2800 [gr-qc].

[251] C. Roberts, K. Horne, A. O. Hodson, and A. D. Leggat, "Tests of ΛCDM and Conformal Gravity using GRB and Quasars as Standard Candles out to $z \sim 8$," arXiv:1711.10369 [astro-ph.CO].

[252] K. Freese, B. Fields, and D. Graff, "Limits on stellar objects as the dark matter of our halo: nonbaryonic dark matter seems to be required," *Nucl. Phys. B Proc. Suppl.* **80** (2000) 0305, arXiv:astro-ph/9904401.

[253] D. S. Graff and K. Freese, "Analysis of a hubble space telescope search for red dwarfs: limits on baryonic matter in the galactic halo," *Astrophys. J. Lett.* **456** (1996) L49, arXiv:astro-ph/9507097.

[254] D. S. Graff and K. Freese, "The Mass function of low mass halo stars: Limits on baryonic halo dark matter," *Astrophys. J. Lett.* **467** (1996) L65, arXiv:astro-ph/9602051.

[255] C. Alcock *et al.*, "The MACHO Project: Microlensing Results from 5.7 Years of Large Magellanic Cloud Observations," arXiv:astro-ph/0001272 [astro-ph].

[256] T. Lasserre *et al.*, "Not enough stellar mass Machos in the Galactic halo," arXiv:astro-ph/0002253 [astro-ph].

[257] **EROS-2** Collaboration, P. Tisserand *et al.*, "Limits on the Macho Content of the Galactic Halo from the EROS-2 Survey of the Magellanic Clouds," *Astron. Astrophys.* **469** (2007) 387–404, arXiv:astro-ph/0607207.

[258] B. D. Fields, K. Freese, and D. S. Graff, "Chemical abundance constraints on white dwarfs as halo dark matter," *Astrophys. J.* **534** (2000) 265–276, arXiv:astro-ph/9904291.

[259] J. García-Bellido, "Primordial Black Holes," *PoS* **EDSU2018** (2018) 042.

[260] B. Carr and F. Kuhnel, "Primordial Black Holes as Dark Matter: Recent Developments," arXiv:2006.02838 [astro-ph.CO].

[261] S. Tremaine and J. Gunn, "Dynamical Role of Light Neutral Leptons in Cosmology," *Phys. Rev. Lett.* **42** (1979) 407–410.

[262] A. Boyarsky, O. Ruchayskiy, and D. Iakubovskyi, "A Lower bound on the mass of Dark Matter particles," *JCAP* **03** (2009) 005, arXiv:0808.3902 [hep-ph].

[263] G. R. Farrar, "Stable Sexaquark," arXiv:1708.08951 [hep-ph].

[264] C. Gross, A. Polosa, A. Strumia, A. Urbano, and W. Xue, "Dark Matter in the Standard Model?," *Phys. Rev. D* **98** no. 6, (2018) 063005, arXiv:1803.10242 [hep-ph].

[265] E. W. Kolb and M. S. Turner, "Dibaryons cannot be the dark matter," *Phys. Rev. D* **99** no. 6, (2019) 063519, arXiv:1809.06003 [hep-ph].

[266] S. D. McDermott, S. Reddy, and S. Sen, "Deeply bound dibaryon is incompatible with neutron stars and supernovae," *Phys. Rev. D* **99** no. 3, (2019) 035013, arXiv:1809.06765 [hep-ph].

[267] G. R. Farrar, Z. Wang, and X. Xu, "Dark Matter Particle in QCD," arXiv:2007.10378 [hep-ph].

[268] M. Escudero, A. Berlin, D. Hooper, and M.-X. Lin, "Toward (Finally!) Ruling Out Z and Higgs Mediated Dark Matter Models," *JCAP* **12** (2016) 029, arXiv:1609.09079 [hep-ph].

[269] G. Arcadi, M. Dutra, P. Ghosh, M. Lindner, Y. Mambrini, M. Pierre, S. Profumo, and F. S. Queiroz, "The waning of the WIMP? A review of models, searches, and constraints," *Eur. Phys. J. C* **78** no. 3, (2018) 203, arXiv:1703.07364 [hep-ph].

[270] P. W. Graham, I. G. Irastorza, S. K. Lamoreaux, A. Lindner, and K. A. van Bibber, "Experimental Searches for the Axion and Axion-Like Particles," *Ann. Rev. Nucl. Part. Sci.* **65** (2015) 485–514, arXiv:1602.00039 [hep-ex].

[271] I. G. Irastorza and J. Redondo, "New experimental approaches in the search for axion-like particles," *Prog. Part. Nucl. Phys.* **102** (2018) 89–159, arXiv:1801.08127 [hep-ph].

[272] O. Antipin, M. Redi, A. Strumia, and E. Vigiani, "Accidental Composite Dark Matter," *JHEP* **07** (2015) 039, arXiv:1503.08749 [hep-ph].

[273] G. D. Kribs and E. T. Neil, "Review of strongly-coupled composite dark matter models and lattice simulations," *Int. J. Mod. Phys. A* **31** no. 22, (2016) 1643004, arXiv:1604.04627 [hep-ph].

[274] A. Mitridate, M. Redi, J. Smirnov, and A. Strumia, "Dark Matter as a weakly coupled Dark Baryon," *JHEP* **10** (2017) 210, arXiv:1707.05380 [hep-ph].

[275] J. E. Juknevich, D. Melnikov, and M. J. Strassler, "A Pure-Glue Hidden Valley I. States and Decays," *JHEP* **07** (2009) 055, arXiv:0903.0883 [hep-ph].

[276] J. E. Juknevich, "Pure-glue hidden valleys through the Higgs portal," *JHEP* **08** (2010) 121, arXiv:0911.5616 [hep-ph].

[277] K. K. Boddy, J. L. Feng, M. Kaplinghat, Y. Shadmi, and T. M. P. Tait, "Strongly interacting dark matter: Self-interactions and keV lines," *Phys. Rev. D* **90** no. 9, (2014) 095016, arXiv:1408.6532 [hep-ph].

[278] K. K. Boddy, J. L. Feng, M. Kaplinghat, and T. M. P. Tait, "Self-Interacting Dark Matter from a Non-Abelian Hidden Sector," *Phys. Rev. D* **89** no. 11, (2014) 115017, arXiv:1402.3629 [hep-ph].

[279] A. Soni and Y. Zhang, "Hidden SU(N) Glueball Dark Matter," *Phys. Rev. D* **93** no. 11, (2016) 115025, arXiv:1602.00714 [hep-ph].

[280] W. Pauli, "Pauli letter collection: letter to Lise Meitner." https://cds.cern.ch/record/83282.

[281] C. L. Cowan, F. Reines, F. B. Harrison, H. W. Kruse, and A. D. McGuire, "Detection of the free neutrino: a confirmation," *Science* **124** no. 3212, (1956) 103–104, https://science.sciencemag.org/content/124/3212/103.full.pdf. https://science.sciencemag.org/content/124/3212/103.

[282] G. Arnison *et al.*, "Experimental observation of isolated large transverse energy electrons with associated missing energy at s=540 gev," *Physics Letters B* **122** no. 1, (1983) 103 – 116. http://www.sciencedirect.com/science/article/pii/0370269383911772.

[283] M. Banner *et al.*, "Observation of single isolated electrons of high transverse momentum in events with missing transverse energy at the cern pp collider," *Physics Letters B* **122** no. 5, (1983) 476 – 485. http://www.sciencedirect.com/science/article/pii/0370269383916052.

[284] R. Essig *et al.*, "Working Group Report: New Light Weakly Coupled Particles," in *Community Summer Study 2013: Snowmass on the Mississippi*. 10, 2013. arXiv:1311.0029 [hep-ph].

[285] S. Alekhin *et al.*, "A facility to Search for Hidden Particles at the CERN SPS: the SHiP physics case," *Rept. Prog. Phys.* **79** no. 12, (2016) 124201, arXiv:1504.04855 [hep-ph].

[286] J. Alexander *et al.*, "Dark Sectors 2016 Workshop: Community Report," 8, 2016. arXiv:1608.08632 [hep-ph].

[287] J. Beacham *et al.*, "Physics Beyond Colliders at CERN: Beyond the Standard Model Working Group Report," *J. Phys. G* **47** no. 1, (2020) 010501, arXiv:1901.09966 [hep-ex].

[288] V. Gorbenko, S. Rychkov, and B. Zan, "Walking, Weak first-order transitions, and Complex CFTs," *JHEP* **10** (2018) 108, arXiv:1807.11512 [hep-th].

[289] D. B. Kaplan, J.-W. Lee, D. T. Son, and M. A. Stephanov, "Conformality Lost," *Phys. Rev. D* **80** (2009) 125005, arXiv:0905.4752 [hep-th].

[290] S. Hong, G. Kurup, and M. Perelstein, "Conformal Freeze-In of Dark Matter," arXiv:1910.10160 [hep-ph].

[291] M. J. Strassler and K. M. Zurek, "Echoes of a hidden valley at hadron colliders," *Phys. Lett.* **B651** (2007) 374–379, arXiv:hep-ph/0604261 [hep-ph].

[292] H. Georgi, "Unparticle physics," *Phys. Rev. Lett.* **98** (2007) 221601, arXiv:hep-ph/0703260 [hep-ph].

[293] B. Batell, M. Pospelov, and A. Ritz, "Exploring Portals to a Hidden Sector Through Fixed Targets," *Phys. Rev. D* **80** (2009) 095024, arXiv:0906.5614 [hep-ph].

[294] A. Falkowski, J. Juknevich, and J. Shelton, "Dark Matter Through the Neutrino Portal," arXiv:0908.1790 [hep-ph].

[295] S. Kanemura, S. Matsumoto, T. Nabeshima, and N. Okada, "Can WIMP Dark Matter overcome the Nightmare Scenario?," *Phys. Rev. D* **82** (2010) 055026, arXiv:1005.5651 [hep-ph].

[296] A. Djouadi, O. Lebedev, Y. Mambrini, and J. Quevillon, "Implications of LHC searches for Higgs–portal dark matter," *Phys. Lett. B* **709** (2012) 65–69, arXiv:1112.3299 [hep-ph].

[297] A. Djouadi, A. Falkowski, Y. Mambrini, and J. Quevillon, "Direct Detection of Higgs-Portal Dark Matter at the LHC," *Eur. Phys. J. C* **73** no. 6, (2013) 2455, arXiv:1205.3169 [hep-ph].

[298] A. Greljo, J. Julio, J. F. Kamenik, C. Smith, and J. Zupan, "Constraining Higgs mediated dark matter interactions," *JHEP* **11** (2013) 190, arXiv:1309.3561 [hep-ph].

[299] M. A. Fedderke, J.-Y. Chen, E. W. Kolb, and L.-T. Wang, "The Fermionic Dark Matter Higgs Portal: an effective field theory approach," *JHEP* **08** (2014) 122, arXiv:1404.2283 [hep-ph].

[300] A. Freitas, S. Westhoff, and J. Zupan, "Integrating in the Higgs Portal to Fermion Dark Matter," *JHEP* **09** (2015) 015, arXiv:1506.04149 [hep-ph].

[301] M. A. Fedderke, T. Lin, and L.-T. Wang, "Probing the fermionic Higgs portal at lepton colliders," *JHEP* **04** (2016) 160, arXiv:1506.05465 [hep-ph].

[302] H.-C. Cheng, L. Li, E. Salvioni, and C. B. Verhaaren, "Light Hidden Mesons through the Z Portal," *JHEP* **11** (2019) 031, arXiv:1906.02198 [hep-ph].

[303] L. Darmé, S. A. Ellis, and T. You, "Light Dark Sectors through the Fermion Portal," *JHEP* **07** (2020) 053, arXiv:2001.01490 [hep-ph].

[304] H. Banks and M. Mccullough, "Charting the Fifth Force Landscape," arXiv:2009.12399 [hep-ph].

[305] R. Contino, A. Mitridate, A. Podo, and M. Redi, "Gluequark Dark Matter," arXiv:1811.06975 [hep-ph].

[306] **XENON** Collaboration, E. Aprile *et al.*, "Constraining the spin-dependent WIMP-nucleon cross sections with XENON1T," *Phys. Rev. Lett.* **122** no. 14, (2019) 141301, arXiv:1902.03234 [astro-ph.CO].

[307] **XENON** Collaboration, E. Aprile *et al.*, "Dark Matter Search Results from a One Ton-Year Exposure of XENON1T," *Phys. Rev. Lett.* **121** no. 11, (2018) 111302, arXiv:1805.12562 [astro-ph.CO].

[308] **CMS** Collaboration, "Search for a narrow resonance in high-mass dilepton final states in proton-proton collisions using 140 fb$^{-1}$ of data at $\sqrt{s} = 13$ TeV," Tech. Rep. CMS-PAS-EXO-19-019, CERN, Geneva, 2019. http://cds.cern.ch/record/2684757.

[309] **CMS** Collaboration, A. M. Sirunyan *et al.*, "Search for high mass dijet resonances with a new background prediction method in proton-proton collisions at $\sqrt{s} = 13$ TeV," *JHEP* **05** (2020) 033, arXiv:1911.03947 [hep-ex].

[310] **ATLAS** Collaboration, G. Aad *et al.*, "Search for high-mass dilepton resonances using 139 fb$^{-1}$ of $pp$ collision data collected at $\sqrt{s}$ =13 TeV with the ATLAS detector," *Phys. Lett. B* **796** (2019) 68–87, arXiv:1903.06248 [hep-ex].

[311] **ATLAS** Collaboration, G. Aad *et al.*, "Search for new resonances in mass distributions of jet pairs using 139 fb$^{-1}$ of $pp$ collisions at $\sqrt{s} = 13$ TeV with the ATLAS detector," *JHEP* **03** (2020) 145, arXiv:1910.08447 [hep-ex].

[312] *LEPSUSYWG, ALEPH, DELPHI, L3 and OPAL experiments, note LEPSUSYWG/04-01.1 (http://lepsusy.web.cern.ch/lepsusy/Welcome.html).*

[313] Y. G. Kim, K. Y. Lee, and S. Shin, "Singlet fermionic dark matter," *JHEP* **05** (2008) 100, arXiv:0803.2932 [hep-ph].

[314] S. Baek, P. Ko, and W.-I. Park, "Search for the Higgs portal to a singlet fermionic dark matter at the LHC," *JHEP* **02** (2012) 047, arXiv:1112.1847 [hep-ph].

[315] L. Lopez-Honorez, T. Schwetz, and J. Zupan, "Higgs portal, fermionic dark matter, and a Standard Model like Higgs at 125 GeV," *Phys. Lett. B* **716** (2012) 179–185, arXiv:1203.2064 [hep-ph].

[316] L. Randall and R. Sundrum, "A Large mass hierarchy from a small extra dimension," *Phys. Rev. Lett.* **83** (1999) 3370–3373, arXiv:hep-ph/9905221.

[317] K. Agashe, P. Du, S. Hong, and R. Sundrum, "Flavor Universal Resonances and Warped Gravity," *JHEP* **01** (2017) 016, arXiv:1608.00526 [hep-ph].

[318] H. Georgi, "Another odd thing about unparticle physics," *Phys. Lett.* **B650** (2007) 275–278, arXiv:0704.2457 [hep-ph].

[319] B. Webber, "Average Multiplicities in Jets," *Phys. Lett. B* **143** (1984) 501–504.

[320] Y. L. Dokshitzer, V. A. Khoze, and S. Troian, "Inclusive particle spectra from QCD cascades," *Int. J. Mod. Phys. A* **7** (1992) 1875–1906.

[321] **L3** Collaboration, P. Achard *et al.*, "Single photon and multiphoton events with missing energy in $e^+e^-$ collisions at LEP," *Phys. Lett.* **B587** (2004) 16–32, arXiv:hep-ex/0402002 [hep-ex].

[322] **OPAL** Collaboration, G. Abbiendi *et al.*, "Photonic events with missing energy in e+ e- collisions at S**(1/2) = 189-GeV," *Eur. Phys. J.* **C18** (2000) 253–272, arXiv:hep-ex/0005002 [hep-ex].

[323] M. J. Strassler, "Why Unparticle Models with Mass Gaps are Examples of Hidden Valleys," arXiv:0801.0629 [hep-ph].

[324] R. Contino, A. Falkowski, F. Goertz, C. Grojean, and F. Riva, "On the Validity of the Effective Field Theory Approach to SM Precision Tests," *JHEP* **07** (2016) 144, arXiv:1604.06444 [hep-ph].

[325] **ALEPH, DELPHI, L3, OPAL, SLD, LEP Electroweak Working Group, SLD Electroweak Group, SLD Heavy Flavour Group** Collaboration, S. Schael *et al.*, "Precision electroweak measurements on the $Z$ resonance," *Phys. Rept.* **427** (2006) 257–454, arXiv:hep-ex/0509008 [hep-ex].

[326] **Particle Data Group** Collaboration, M. Tanabashi *et al.*, "Review of Particle Physics," *Phys. Rev. D* **98** (Aug, 2018) 030001. https://link.aps.org/doi/10.1103/PhysRevD.98.030001.

[327] **CMS** Collaboration, A. M. Sirunyan *et al.*, "Combined measurements of Higgs boson couplings in proton–proton collisions at $\sqrt{s} = 13\,\text{TeV}$," *Eur. Phys. J. C* **79** no. 5, (2019) 421, arXiv:1809.10733 [hep-ex].

[328] **ATLAS** Collaboration, "Search for invisible Higgs boson decays with vector boson fusion signatures with the ATLAS detector using an integrated luminosity of 139 $\text{fb}^{-1}$," Tech. Rep. ATLAS-CONF-2020-008, CERN, Geneva, Apr, 2020. https://cds.cern.ch/record/2715447.

[329] **ATLAS** Collaboration, "Search for invisible Higgs boson decays with vector boson fusion signatures with the ATLAS detector using an integrated luminosity of 139 $\text{fb}^{-1}$,".

[330] **ATLAS** Collaboration, M. Aaboud *et al.*, "Search for long-lived particles produced in $pp$ collisions at $\sqrt{s} = 13$ TeV that decay into displaced hadronic jets in the ATLAS muon spectrometer," *Phys. Rev. D* **99** no. 5, (2019) 052005, arXiv:1811.07370 [hep-ex].

[331] **ATLAS** Collaboration, G. Aad *et al.*, "Search for long-lived neutral particles produced in $pp$ collisions at $\sqrt{s} = 13$ TeV decaying into displaced hadronic jets in the ATLAS inner detector and muon spectrometer," *Phys. Rev. D* **101** no. 5, (2020) 052013, arXiv:1911.12575 [hep-ex].

[332] **L3** Collaboration, P. Achard *et al.*, "Search for an invisibly-decaying Higgs boson at LEP," *Phys. Lett.* **B609** (2005) 35–48, arXiv:hep-ex/0501033 [hep-ex].

[333] **ATLAS** Collaboration, M. Aaboud *et al.*, "Search for dark matter and other new phenomena in events with an energetic jet and large missing transverse momentum using the ATLAS detector," *JHEP* **01** (2018) 126, arXiv:1711.03301 [hep-ex].

[334] **ATLAS** Collaboration, M. Aaboud *et al.*, "Search for dark matter at $\sqrt{s} = 13$ TeV in final states containing an energetic photon and large missing transverse momentum with the ATLAS detector," *Eur. Phys. J.* **C77** no. 6, (2017) 393, arXiv:1704.03848 [hep-ex].

[335] **ATLAS** Collaboration, M. Aaboud *et al.*, "Search for an invisibly decaying Higgs boson or dark matter candidates produced in association with a $Z$ boson in $pp$ collisions at $\sqrt{s} = 13$ TeV with the ATLAS detector," *Phys. Lett.* **B776** (2018) 318–337, arXiv:1708.09624 [hep-ex].

[336] **ATLAS** Collaboration, G. Aad *et al.*, "Search for new phenomena in final states with an energetic jet and large missing transverse momentum in pp collisions at $\sqrt{s}$ =8 TeV with the ATLAS detector," *Eur. Phys. J.* **C75** no. 7, (2015) 299, arXiv:1502.01518 [hep-ex]. [Erratum: Eur. Phys. J.C75,no.9,408(2015)].

[337] J. Alimena *et al.*, "Searching for Long-Lived Particles beyond the Standard Model at the Large Hadron Collider," arXiv:1903.04497 [hep-ex].

[338] C. Degrande, C. Duhr, B. Fuks, D. Grellscheid, O. Mattelaer, and T. Reiter, "UFO - The Universal FeynRules Output," *Comput. Phys. Commun.* **183** (2012) 1201–1214, arXiv:1108.2040 [hep-ph].

[339] A. Alloul, N. D. Christensen, C. Degrande, C. Duhr, and B. Fuks, "FeynRules 2.0 - A complete toolbox for tree-level phenomenology," *Comput. Phys. Commun.* **185** (2014) 2250–2300, arXiv:1310.1921 [hep-ph].

[340] G. Das, C. Degrande, V. Hirschi, F. Maltoni, and H.-S. Shao, "NLO predictions for the production of a spin-two particle at the LHC," *Phys. Lett.* **B770** (2017) 507–513, arXiv:1605.09359 [hep-ph].

[341] T. Hahn, "Generating Feynman diagrams and amplitudes with FeynArts 3," *Comput. Phys. Commun.* **140** (2001) 418–431, arXiv:hep-ph/0012260 [hep-ph].

[342] G. Pancheri and Y. Srivastava, "Introduction to the physics of the total cross-section at LHC: A Review of Data and Models," *Eur. Phys. J. C* **77** no. 3, (2017) 150, arXiv:1610.10038 [hep-ph].

[343] **CHARM** Collaboration, F. Bergsma *et al.*, "A Search for Oscillations of Muon Neutrinos in an Experiment With $L/E$ Approximately = 0.7-km/{GeV}," *Phys. Lett. B* **142** (1984) 103–110.

[344] **LSND** Collaboration, C. Athanassopoulos *et al.*, "The Liquid scintillator neutrino detector and LAMPF neutrino source," *Nucl. Instrum. Meth. A* **388** (1997) 149–172, arXiv:nucl-ex/9605002.

[345] **NuTeV** Collaboration, T. Adams *et al.*, "Observation of an anomalous number of dimuon events in a high-energy neutrino beam," *Phys. Rev. Lett.* **87** (2001) 041801, arXiv:hep-ex/0104037.

[346] **MINOS** Collaboration, P. Adamson *et al.*, "A Study of Muon Neutrino Disappearance Using the Fermilab Main Injector Neutrino Beam," *Phys. Rev. D* **77** (2008) 072002, arXiv:0711.0769 [hep-ex].

[347] **MiniBooNE** Collaboration, A. Aguilar-Arevalo *et al.*, "Dark Matter Search in a Proton Beam Dump with MiniBooNE," *Phys. Rev. Lett.* **118** no. 22, (2017) 221803, arXiv:1702.02688 [hep-ex].

[348] J. Bjorken, S. Ecklund, W. Nelson, A. Abashian, C. Church, B. Lu, L. Mo, T. Nunamaker, and P. Rassmann, "Search for Neutral Metastable Penetrating Particles Produced in the SLAC Beam Dump," *Phys. Rev. D* **38** (1988) 3375.

[349] E. Riordan *et al.*, "A Search for Short Lived Axions in an Electron Beam Dump Experiment," *Phys. Rev. Lett.* **59** (1987) 755.

[350] A. Bross, M. Crisler, S. H. Pordes, J. Volk, S. Errede, and J. Wrbanek, "A Search for Shortlived Particles Produced in an Electron Beam Dump," *Phys. Rev. Lett.* **67** (1991) 2942–2945.

[351] S. Andreas *et al.*, "Proposal for an Experiment to Search for Light Dark Matter at the SPS," arXiv:1312.3309 [hep-ex].

[352] **LDMX** Collaboration, T. Åkesson *et al.*, "Light Dark Matter eXperiment (LDMX)," arXiv:1808.05219 [hep-ex].

[353] D. Banerjee *et al.*, "Dark matter search in missing energy events with NA64," *Phys. Rev. Lett.* **123** no. 12, (2019) 121801, arXiv:1906.00176 [hep-ex].

[354] J. D. Bjorken, R. Essig, P. Schuster, and N. Toro, "New Fixed-Target Experiments to Search for Dark Gauge Forces," *Phys. Rev.* **D80** (2009) 075018, arXiv:0906.0580 [hep-ph].

[355] K. J. Kim and Y.-S. Tsai, "IMPROVED WEIZSACKER-WILLIAMS METHOD AND ITS APPLICATION TO LEPTON AND W BOSON PAIR PRODUCTION," *Phys. Rev. D* **8** (1973) 3109.

[356] Y.-S. Tsai, "Pair Production and Bremsstrahlung of Charged Leptons," *Rev. Mod. Phys.* **46** (1974) 815. [Erratum: Rev.Mod.Phys. 49, 521–423 (1977)].

[357] Y.-S. Liu and G. A. Miller, "Validity of the Weizsäcker-Williams approximation and the analysis of beam dump experiments: Production of an axion, a dark photon, or a new axial-vector boson," *Phys. Rev. D* **96** no. 1, (2017) 016004, arXiv:1705.01633 [hep-ph].

[358] S. Gninenko, D. Kirpichnikov, M. Kirsanov, and N. Krasnikov, "The exact tree-level calculation of the dark photon production in high-energy electron scattering at the CERN SPS," *Phys. Lett. B* **782** (2018) 406–411, arXiv:1712.05706 [hep-ph].

[359] B. Batell, R. Essig, and Z. Surujon, "Strong Constraints on Sub-GeV Dark Sectors from SLAC Beam Dump E137," *Phys. Rev. Lett.* **113** no. 17, (2014) 171802, arXiv:1406.2698 [hep-ph].

[360] B. McElrath, "Light Higgses and dark matter at bottom and charm factories," *eConf* **C070805** (2007) 19, arXiv:0712.0016 [hep-ph].

[361] A. Badin and A. A. Petrov, "Searching for light Dark Matter in heavy meson decays," *Phys. Rev. D* **82** (2010) 034005, arXiv:1005.1277 [hep-ph].

[362] S. Gninenko and N. Krasnikov, "Invisible $K_L$ decays as a probe of new physics," *Phys. Rev. D* **92** no. 3, (2015) 034009, arXiv:1503.01595 [hep-ph].

[363] D. Barducci, M. Fabbrichesi, and E. Gabrielli, "Neutral Hadrons Disappearing into the Darkness," *Phys. Rev. D* **98** no. 3, (2018) 035049, arXiv:1806.05678 [hep-ph].

[364] M. Hostert, K. Kaneta, and M. Pospelov, "Pair production of dark particles in meson decays," arXiv:2005.07102 [hep-ph].

[365] J. F. Kamenik and C. Smith, "FCNC portals to the dark sector," *JHEP* **03** (2012) 090, arXiv:1111.6402 [hep-ph].

[366] **BESIII** Collaboration, M. Ablikim *et al.*, "Search for invisible decays of $\omega$ and $\phi$ with $J/\psi$ data at BESIII," *Phys. Rev. D* **98** no. 3, (2018) 032001, arXiv:1805.05613 [hep-ex].

[367] C. Bird, P. Jackson, R. V. Kowalewski, and M. Pospelov, "Search for dark matter in b —> s transitions with missing energy," *Phys. Rev. Lett.* **93** (2004) 201803, arXiv:hep-ph/0401195.

[368] C. Bird, R. V. Kowalewski, and M. Pospelov, "Dark matter pair-production in b —> s transitions," *Mod. Phys. Lett.* **A21** (2006) 457–478, arXiv:hep-ph/0601090 [hep-ph].

[369] G. Buchalla *et al.*, "$B$, $D$ and $K$ decays," *Eur. Phys. J. C* **57** (2008) 309–492, arXiv:0801.1833 [hep-ph].

[370] **BaBar** Collaboration, J. P. Lees *et al.*, "Search for $B \to K^{(*)}\nu\overline{\nu}$ and invisible quarkonium decays," *Phys. Rev.* **D87** no. 11, (2013) 112005, arXiv:1303.7465 [hep-ex].

[371] A. J. Buras, "Weak Hamiltonian, CP violation and rare decays," in *Les Houches Summer School in Theoretical Physics, Session 68: Probing the Standard Model of Particle Interactions*, pp. 281–539. 6, 1998. arXiv:hep-ph/9806471.

[372] **E949 Collaboration** Collaboration, A. V. Artamonov *et al.*, "New measurement of the $K^+ \to \pi^+\nu\overline{\nu}$ branching ratio," *Phys. Rev. Lett.* **101** (Nov, 2008) 191802. https://link.aps.org/doi/10.1103/PhysRevLett.101.191802.

[373] R. S. Willey and H. L. Yu, "Neutral higgs boson from decays of heavy-flavored mesons," *Phys. Rev. D* **26** (Dec, 1982) 3086–3091. https://link.aps.org/doi/10.1103/PhysRevD.26.3086.

[374] J. A. Bailey *et al.*, "$B \to Kl^+l^-$ Decay Form Factors from Three-Flavor Lattice QCD," *Phys. Rev. D* **93** no. 2, (2016) 025026, arXiv:1509.06235 [hep-lat].

[375] P. Ball and R. Zwicky, "New results on $B \to \pi, K, \eta$ decay formfactors from light-cone sum rules," *Phys. Rev.* **D71** (2005) 014015, arXiv:hep-ph/0406232 [hep-ph].

[376] G. G. Raffelt, "Particle physics from stars," *Ann. Rev. Nucl. Part. Sci.* **49** (1999) 163–216, arXiv:hep-ph/9903472 [hep-ph].

[377] G. Raffelt and A. Weiss, "Red giant bound on the axion-electron coupling reexamined," *Phys. Rev. D* **51** (Feb, 1995) 1495–1498. https://link.aps.org/doi/10.1103/PhysRevD.51.1495.

[378] H. An, M. Pospelov, and J. Pradler, "New stellar constraints on dark photons," *Phys. Lett. B* **725** (2013) 190–195, arXiv:1302.3884 [hep-ph].

[379] E. Hardy and R. Lasenby, "Stellar cooling bounds on new light particles: plasma mixing effects," *JHEP* **02** (2017) 033, arXiv:1611.05852 [hep-ph].

[380] J. H. Chang, R. Essig, and S. D. McDermott, "Revisiting Supernova 1987A Constraints on Dark Photons," *JHEP* **01** (2017) 107, arXiv:1611.03864 [hep-ph].

[381] J. H. Chang, R. Essig, and S. D. McDermott, "Supernova 1987A Constraints on Sub-GeV Dark Sectors, Millicharged Particles, the QCD Axion, and an Axion-like Particle," *JHEP* **09** (2018) 051, arXiv:1803.00993 [hep-ph].

[382] Y. Zhang, "Supernova Cooling in a Dark Matter Smog," *JCAP* **11** (2014) 042, arXiv:1404.7172 [hep-ph].

[383] H. K. Dreiner, J.-F. Fortin, C. Hanhart, and L. Ubaldi, "Supernova constraints on MeV dark sectors from $e^+e^-$ annihilations," *Phys. Rev. D* **89** no. 10, (2014) 105015, arXiv:1310.3826 [hep-ph].

[384] H. K. Dreiner, J.-F. Fortin, J. Isern, and L. Ubaldi, "White Dwarfs constrain Dark Forces," *Phys. Rev. D* **88** (2013) 043517, arXiv:1303.7232 [hep-ph].

[385] W. DeRocco, P. W. Graham, D. Kasen, G. Marques-Tavares, and S. Rajendran, "Observable signatures of dark photons from supernovae," *JHEP* **19** (2020) 171, arXiv:1901.08596 [hep-ph].

[386] W. DeRocco, P. W. Graham, D. Kasen, G. Marques-Tavares, and S. Rajendran, "Supernova signals of light dark matter," *Phys. Rev. D* **100** no. 7, (2019) 075018, arXiv:1905.09284 [hep-ph].

[387] A. Freitas and D. Wyler, "Astro Unparticle Physics," *JHEP* **12** (2007) 033, arXiv:0708.4339 [hep-ph].

[388] B. Grinstein, K. A. Intriligator, and I. Z. Rothstein, "Comments on Unparticles," *Phys. Lett.* **B662** (2008) 367–374, arXiv:0801.1140 [hep-ph].

[389] K. Blum and D. Kushnir, "Neutrino Signal of Collapse-induced Thermonuclear Supernovae: the Case for Prompt Black Hole Formation in SN1987A," *Astrophys. J.* **828** no. 1, (2016) 31, arXiv:1601.03422 [astro-ph.HE].

[390] N. Bar, K. Blum, and G. D'amico, "Is there a supernova bound on axions?," arXiv:1907.05020 [hep-ph].

[391] S. Hannestad, G. Raffelt, and Y. Y. Y. Wong, "Unparticle constraints from SN 1987A," *Phys. Rev.* **D76** (2007) 121701, arXiv:0708.1404 [hep-ph].

[392] J. S. Lee, "Revisiting Supernova 1987A Limits on Axion-Like-Particles," arXiv:1808.10136 [hep-ph].

[393] G. G. Raffelt, "Astrophysical axion bounds diminished by screening effects," *Phys. Rev. D* **33** (Feb, 1986) 897–909. https://link.aps.org/doi/10.1103/PhysRevD.33.897.

[394] C. Hanhart, D. R. Phillips, S. Reddy, and M. J. Savage, "Extra dimensions, SN1987a, and nucleon-nucleon scattering data," *Nucl. Phys.* **B595** (2001) 335–359, arXiv:nucl-th/0007016 [nucl-th].

[395] G. G. Raffelt, *Stars as laboratories for fundamental physics, p.120ff.* Chicago, USA: Univ. Pr. (1996) 664 p, 1996. http://wwwth.mpp.mpg.de/members/raffelt/mypapers/199613.pdf.

[396] D. S. Dearborn, D. N. Schramm, and G. Steigman, "Astrophysical Constraints on the Couplings of Axions Majorons and Familons," *Phys. Rev. Lett.* **56** (1986) 26.

[397] G. Raffelt and A. Weiss, "Red giant bound on the axion - electron coupling revisited," *Phys. Rev. D* **51** (1995) 1495–1498, arXiv:hep-ph/9410205.

[398] A. Badertscher, P. Crivelli, W. Fetscher, U. Gendotti, S. Gninenko, V. Postoev, A. Rubbia, V. Samoylenko, and D. Sillou, "An Improved Limit on Invisible Decays of Positronium," *Phys. Rev. D* **75** (2007) 032004, arXiv:hep-ex/0609059.

[399] S. Asai, S. Orito, K. Yoshimura, and T. Haga, "Search for longlived neutral bosons in orthopositronium decay," *Phys. Rev. Lett.* **66** (1991) 2440–2443.

[400] A. Czarnecki and S. G. Karshenboim, "Decays of positronium," in *14th International Workshop on High-Energy Physics and Quantum Field Theory (QFTHEP 99)*, pp. 538–544. 11, 1999. arXiv:hep-ph/9911410.

[401] A. Pokraka and A. Czarnecki, "Positronium Decay into a Photon and Neutrinos," *Phys. Rev. D* **94** no. 11, (2016) 113012, arXiv:1611.07645 [hep-ph].

[402] J. A. Wheeler, "Polyelectrons," *Annals N. Y. Acad. Sci.* **48** no. 3, (1946) 219–238.

[403] J. Pirenne, "Le champ propre et l'interaction des particules de Dirac suivant l'electrodynamique quantique. II.," *Arch. Sci. Phys. Nat.* **29** (1947) 265–300.

[404] S. Fichet, "Quantum Forces from Dark Matter and Where to Find Them," *Phys. Rev. Lett.* **120** no. 13, (2018) 131801, arXiv:1705.10331 [hep-ph].

[405] P. Brax, S. Fichet, and G. Pignol, "Bounding Quantum Dark Forces," *Phys. Rev. D* **97** no. 11, (2018) 115034, arXiv:1710.00850 [hep-ph].

[406] E. Salumbides, A. Schellekens, B. Gato-Rivera, and W. Ubachs, "Constraints on extra dimensions from precision molecular spectroscopy," *New J. Phys.* **17** no. 3, (2015) 033015, arXiv:1502.02838 [physics.atom-ph].

[407] G. Altarelli and R. Barbieri, "Vacuum polarization effects of new physics on electroweak processes," *Phys. Lett. B* **253** (1991) 161–167.

[408] G. Altarelli, R. Barbieri, and S. Jadach, "Toward a model independent analysis of electroweak data," *Nucl. Phys. B* **369** (1992) 3–32. [Erratum: Nucl.Phys.B 376, 444 (1992)].

[409] **Gfitter Group** Collaboration, M. Baak, J. Cúth, J. Haller, A. Hoecker, R. Kogler, K. Mönig, M. Schott, and J. Stelzer, "The global electroweak fit at NNLO and prospects for the LHC and ILC," *Eur. Phys. J. C* **74** (2014) 3046, arXiv:1407.3792 [hep-ph].

[410] J. Fan, M. Reece, and L.-T. Wang, "Possible Futures of Electroweak Precision: ILC, FCC-ee, and CEPC," *JHEP* **09** (2015) 196, arXiv:1411.1054 [hep-ph].

[411] J. de Blas, M. Ciuchini, E. Franco, S. Mishima, M. Pierini, L. Reina, and L. Silvestrini, "Electroweak precision observables and Higgs-boson signal strengths in the Standard Model and beyond: present and future," *JHEP* **12** (2016) 135, arXiv:1608.01509 [hep-ph].

[412] L. Borgonovi, S. Braibant, B. Di Micco, E. Fontanesi, P. Harris, C. Helsens, D. Jamin, M. Mangano, G. Ortona, M. Selvaggi, A. Sznajder, M. Testa, and M. Verducci, "Higgs measurements at FCC-hh," Tech. Rep. CERN-ACC-2018-0045, CERN, Geneva, Oct, 2018. http://cds.cern.ch/record/2642471.

[413] D. Curtin and C. B. Verhaaren, "Discovering Uncolored Naturalness in Exotic Higgs Decays," *JHEP* **12** (2015) 072, arXiv:1506.06141 [hep-ph].

[414] K. Cheung and Z. S. Wang, "Probing Long-lived Particles at Higgs Factories," *Phys. Rev. D* **101** no. 3, (2020) 035003, arXiv:1911.08721 [hep-ph].

[415] A. Azatov, R. Contino, and J. Galloway, "Model-Independent Bounds on a Light Higgs," *JHEP* **04** (2012) 127, arXiv:1202.3415 [hep-ph]. [Erratum: JHEP04,140(2013)].

[416] H. Osborn and A. C. Petkou, "Implications of conformal invariance in field theories for general dimensions," *Annals Phys.* **231** (1994) 311–362, arXiv:hep-th/9307010 [hep-th].

[417] F. A. Dolan and H. Osborn, "Conformal four point functions and the operator product expansion," *Nucl. Phys.* **B599** (2001) 459–496, arXiv:hep-th/0011040 [hep-th].

[418] A. Cappelli, D. Friedan, and J. Latorre, "c-theorem and spectral representation," *Nuclear Physics B* **352** no. 3, (1991) 616 – 670. http://www.sciencedirect.com/science/article/pii/0550321391901024.

[419] M. F. Zoller and K. G. Chetyrkin, "OPE of the energy-momentum tensor correlator in massless QCD," *JHEP* **12** (2012) 119, arXiv:1209.1516 [hep-ph].

[420] M. F. Zoller, "OPE of the energy-momentum tensor correlator and the gluon condensate operator in massless QCD to three-loop order," *JHEP* **10** (2014) 169, arXiv:1407.6921 [hep-ph].

[421] M. Becchetti and M. Bochicchio, "OPE and a low-energy theorem in QCD-like theories," *JHEP* **03** (2019) 088, arXiv:1810.08527 [hep-th].

[422] P. A. Baikov and K. G. Chetyrkin, "Top Quark Mediated Higgs Boson Decay into Hadrons to Order $\alpha_s^5$," *Phys. Rev. Lett.* **97** (2006) 061803, arXiv:hep-ph/0604194 [hep-ph].

[423] S. Giombi, G. Tarnopolsky, and I. R. Klebanov, "On $C_J$ and $C_T$ in Conformal QED," *JHEP* **08** (2016) 156, arXiv:1602.01076 [hep-th].

[424] G. M. Tarnopolskiy, *Conformal and Nearly Conformal Theories at Large N*. PhD thesis, Princeton U., 2017-09. http://phy.princeton.edu/sites/physics/files/resource-links/tarnopolskiy_thesis.pdf.

[425] A. C. Petkou, "$C_T$ and $C_J$ up to next-to-leading order in $1/N$ in the conformally invariant O(N) vector model for $2 < d < 4$," *Phys. Lett.* **B359** (1995) 101–107, arXiv:hep-th/9506116 [hep-th].

[426] K. Diab, L. Fei, S. Giombi, I. R. Klebanov, and G. Tarnopolsky, "On $C_J$ and $C_T$ in the Gross?Neveu and O(N) models," *J. Phys.* **A49** no. 40, (2016) 405402, arXiv:1601.07198 [hep-th].

[427] D. Poland and D. Simmons-Duffin, "Bounds on 4D Conformal and Superconformal Field Theories," *JHEP* **05** (2011) 017, arXiv:1009.2087 [hep-th].

[428] R. Rattazzi, S. Rychkov, and A. Vichi, "Central Charge Bounds in 4D Conformal Field Theory," *Phys. Rev.* **D83** (2011) 046011, arXiv:1009.2725 [hep-th].

[429] A. Vichi, "Improved bounds for CFT's with global symmetries," *JHEP* **01** (2012) 162, arXiv:1106.4037 [hep-th].

[430] P. Liendo, I. Ramirez, and J. Seo, "Stress-tensor OPE in $\mathcal{N} = 2$ superconformal theories," *JHEP* **02** (2016) 019, arXiv:1509.00033 [hep-th].

[431] F. Caracciolo, A. Castedo Echeverri, B. von Harling, and M. Serone, "Bounds on OPE Coefficients in 4D Conformal Field Theories," *JHEP* **10** (2014) 020, arXiv:1406.7845 [hep-th].

[432] R. Rattazzi and A. Zaffaroni, "Comments on the holographic picture of the Randall-Sundrum model," *JHEP* **04** (2001) 021, arXiv:hep-th/0012248 [hep-th].

[433] W. D. Goldberger and M. B. Wise, "Modulus stabilization with bulk fields," *Phys. Rev. Lett.* **83** (1999) 4922–4925, arXiv:hep-ph/9907447.